Wolf-Rayet Populations in Local Group Metal Poor Galaxies

Katie A. Tehrani

Department of Physics & Astronomy
The University of Sheffield

A dissertation submitted in candidature for the degree of Doctor of Philosophy at the University of Sheffield

2019

Declaration

I declare that, unless otherwise stated, the work presented in this thesis is my own. No part of this thesis has been accepted or is currently being submitted for any other qualification at the University of Sheffield or elsewhere.

Much of the work presented here has already been published, such that the work in Chapter 2 can be found in Tehrani, Crowther, & Archer I (2017, MNRAS:472:4618) and the work in Chapter 5 can be found in Tehrani, Crowther, Bestenlehner, Littlefair, Pollock, Parker, & Schnurr (2019, MNRAS: 484:2692).

Acknowledgements

There have been highs and lows, and I would like to thank the people that have been there with me through it all. Firstly, to Paul. Without your unwavering calm and patience I imagine this story would end differently, but instead I look back on my four years of research with a smile. Thank you for your support, your reassurance, and the confidence you gave me to rise to the challenge.

To Andy, who invested considerable time and effort sharing X-ray and statistics expertise, and who always made time for a discussion. To Joachim, & Stu for patiently wading through spectral models, or guiding me through radial velocity curve fitting and MCMC. And to Leisa and Pat for sharing their data, taking the time to explain unfamiliar concepts, and offering more help and resources when needed. I've learnt a lot.

To Heloise & Martin who often offered a different perspective to my problems, and were experts at teasing out bugs in my codes. Together you kept spirits high and I'm so grateful I was fortunate enough to be completing this PhD with you. Also to Pablo, who despite my best efforts always managed to restore order to the chaos I had created on my computer.

To Maman & Bobba. There were times when I felt overwhelmed but you kept me grounded and focussed, and always pushed me to do my best. I get my determination from you. And to Caron & Phil, who were always supportive and motivating, especially when I was nervous.

To Joe, who often had to deal with the lows. You've been solid, never once letting me dwell on my anxieties and reminding me to enjoy the experience. You always understood.

And finally to Bella, who patiently sat by me through it all. She's a good girl.

Summary

Wolf-Rayet (WR) stars are curious beasts. Characterised by broad emission line spectra and strong stellar-winds driving huge mass-loss rates, these stars are rare and unusual. Understanding these stars has many implications for massive star evolution and stellar feedback, however numerous obstacles prevent progress, such as incomplete samples and gaps in our knowledge regarding their formation, binary status, stellar properties and final stages.

Within this thesis we have focused on addressing some of these issues through studying the WR population residing in Local Group dwarf galaxies, specifically within IC10 and the 30 Doradus region of the LMC. Using Gemini/GMOS narrow-band optical imaging of IC10 we have completed a thorough search of the region for WR stars, identifying both previously confirmed and new candidates. Follow-up spectroscopy confirmed 3/11 new candidates with the remaining requiring further follow-up. We classified each star and used the spectra to search for evidence of binarity. We update the WC/WN ratio to 1.0±0.4, and using nebular emission lines we also revise the metallicity estimate, finding that IC10 is not as metal poor as previously considered.

We also used X-ray data from the T-ReX Chandra X-ray visionary programme to study the 30 Doradus WR population. Our main focus here was to assess the binary status of these stars by looking for signatures of colliding winds. Our results identify 4 clear binary candidates; Mk34, R140a, R136c and Mk39. Using VFTS data we confirm Mk39 as an SB2.

Finally, an optical follow-up campaign using VLT/UVES to monitor Mk34 revealed an SB2 system with clear radial velocity variations. We derive the orbital parameters and obtain direct mass estimates for each component ($M_A \sin^3(i)$=65±7 $M_\odot$ and $M_B \sin^3(i)$=60±7 $M_\odot$). We also perform spectroscopic and evolutionary modelling, the results of which suggests Mk34 is the most massive binary system known to date.

Contents

List of Figures

List of Tables

Publications

Publication list for works submitted during this PhD include:

Tehrani K., Crowther P.A., Archer I., 2017, MNRAS, 472, 4618

Pollock A. M. T., Crowther P. A., Tehrani K., Broos P. S., Townsley L. K., 2018, MNRAS, 474, 3228

Tehrani K. A., Crowther P. A., Bestenlehner J. M., Littlefair S. P., Pollock A. M. T., Parker R. J., Schnurr O., 2019, MNRAS, 484, 2692

Chapter 1

Introduction

1.1 Introduction

Massive stars (greater than 8 $M_{\odot}$) are an important topic of research within astrophysics. Despite their rarity, they are responsible for contributing to some of the most dramatic and consequential events, such as the re-ionisation of the universe (Sokasian et al., 2004) and emitting mechanical and chemical feedback. Our understanding however, remains incomplete. Hindered by small observable samples, our conclusions often rely on theoretical evolutionary models which, without further investigation, remain uncertain and perhaps controversial.

There are also a number of 'big-picture' outstanding questions which are active areas of research. This includes understanding the formation of these massive stars. For lower mass stars we have a reasonable grasp on the flow of events necessary to form the star, however in the high mass regime, we suspect an alternate formation mechanism is necessary (Tan et al., 2014). For high mass stars, because of the large amount of material involved, it is thought the star is likely to ignite nuclear burning before the formation is complete, introducing feedback and complications to the flow of material onto the star.

Another major focus is understanding the link between massive stars and explosive transients - core collapse supernovae (ccSN) and gamma ray bursts (GRB). We are confident that most massive stars will explode as ccSN, and a subset of ccSN have associated GRBs, but we suspect there is an upper mass limit for ccSN, as well as a metallicity dependence, above which the star may collapse directly to a black hole. It has also been suggested that other stellar properties such as mass-loss and rotation can influence the collapse of massive stars, producing 'islands of explodability', and if these ideal conditions are not satisfied the collapse will fail to produce an explosion (O'Connor & Ott, 2011, 2013; Sukhbold & Woosley, 2014). There is a variety of SN types, and understanding which types of massive stars are responsible for each ccSN, and why, is still under investigation.

Massive stars as gravitational wave (GW) progenitors is another major research topic. With the recent success advanced LIGO has had in discovering merging black hole (BH) and neutron star (NS) binaries (The LIGO Scientific Collaboration & the Virgo Collaboration, 2018) it is becoming a high priority to understand the process leading to these cataclysmic events. Massive star evolution and the role binarity has to play is still not well understood. We know that the progenitors of both BH and NS are massive stars, but to get two of these stars in a binary system suggests the system must survive the very dynamic evolution of these massive stars (Belczynski et al., 2016; Eldridge & Stanway, 2016).

Understanding the effect of binarity is very important. It is commonly quoted that massive stars love company, with high binary fractions of $\sim$70% for O stars in the Milky Way

(MW) (Sana et al., 2012) and ∼50% in the Tarantula nebula, within the Large Magellanic Cloud (LMC) (Sana et al., 2013b). It is therefore critical we recognise the influence a companion star can have, and how this can change the evolutionary path of a massive star.

Within this chapter we introduce massive stars, and in particular Wolf-Rayet (WR) stars. We discuss their origin, evolution and known stellar properties, including observational techniques.

1.2 Massive Stars

The Harvard classification scheme classifies stars based on relative absorption line strengths, which correlate with temperature, or colour. The main spectral classes are O, B, A, F, G, K, and M in order of decreasing temperature as shown in Figure 1.1. These classes are further subdivided, numerically into ionisation classes, and again by luminosity class (Morgan et al., 1943). We consider a massive star to be any star with an initial mass greater than 8 $M_{\odot}$ the lower limit for ccSN for single stars, and these stars span the O and B spectral classes. Very massive stars, have initial masses in excess of 100 $M_{\odot}$ (Vink, 2015).

Most stars are usually assumed to be born in clusters within collapsing molecular clouds (Lada & Lada, 2003), and the initial mass function (IMF) describes the distribution of masses of stars found in a cluster (e.g Kroupa (2001)). It shows low mass stars are much more common with respect to their high mass counter-parts, indeed less than 1% of an initial stellar population would represent high mass stars.

Observing massive stars has advantages and disadvantages. Massive stars are bright, with high bolometric luminosities in the range of $\log(L/L_{\odot})$=3-7, they often dominate galactic observations. This also makes isolated massive stars easier to identify and study. In most cases however, they are found in young star-forming clusters, which are crowded and obscured by gas and dust.

Due to the high mass and bright luminosities of these stars, their lifetimes are short, spending ∼10 Myrs on the main sequence for a star with an initial mass of ∼20 $M_{\odot}$ (Vanbeveren et al., 1998).

1.2.1 OB Stars

O and early-B type stars are hot, massive, main sequence stars which occupy the upper left region of the HR diagram (see Figure 1.1), with initial masses greater than ∼15-20 $M_{\odot}$. Classification of O stars range from ionization classes of 2-9 and luminosity classes of I (supergiants), III (giants) and V (dwarfs). Similarly B stars have ionization classes from

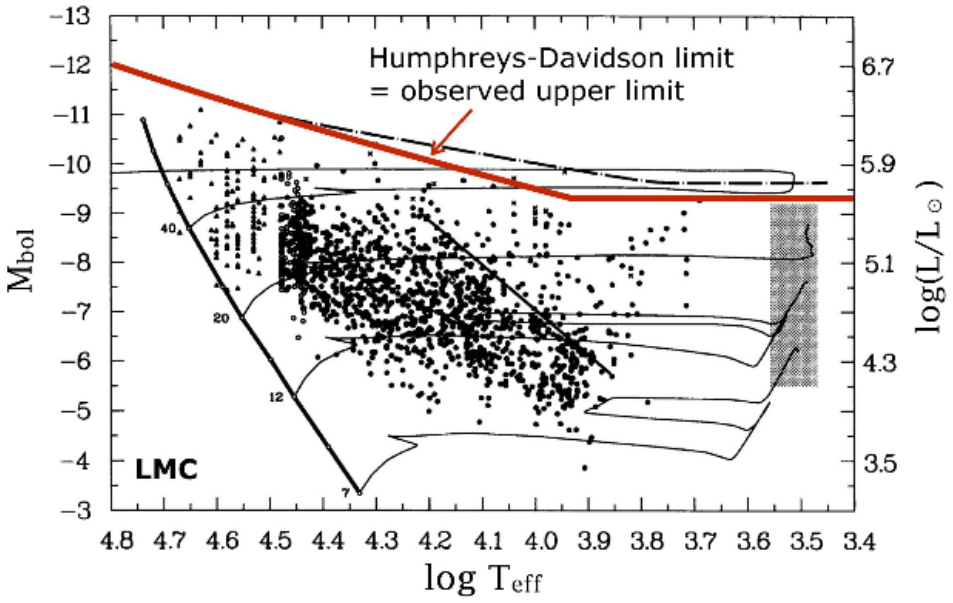

Figure 1.1: HR diagram for the most luminous stars in the LMC. Evolutionary tracks for a 7, 12, 20 and 40 $M_\odot$ star are shown in black. Taken from Lamers & Levesque (2017).

0-9, where early-type B stars (B0-3) have initial masses which bridge the gap from 8 $M_\odot$ (Silverman & Filippenko, 2008).

Our closest massive star forming region is the Orion Nebula, containing ∼20 OB stars (Fukui et al., 2018). Within the H II region lies the Trapezium cluster, host to several O stars, the brightest of which is θ^1 Ori C, a O7-O5.5 eccentric binary system with a combined mass of 44 ± 7 $M_\odot$ (Simón-Díaz et al., 2006; Kraus et al., 2009). θ^1 Ori C is almost solely responsible for producing the ionizing radiation driving the Orion Nebula (Muench et al., 2008).

Typically OB stars have absorption line spectra, however more massive O stars and evolved blue supergiants, with stronger stellar winds, can show emission lines, for example in Hα. O supergiants with He II 4686 and N IV 4058 or N III 4640 emission are designated OIf stars. Spectroscopically, as shown in Figure 1.2, a natural progression from these stars to Wolf-Rayet (WR) stars (discussed in Section 1.2.2) can be observed.

As shown in Figure 1.2 we see the introduction of the OIf/WN classification, first suggested by Walborn (1982) to describe a spectrum in the intermediate stages between OIf and WR stars. The key differentiator between these spectra is the Hβ line, identified in Figure 1.2. In OIf stars we see Hβ in absorption, however in the OIf/WN stars, or hot slash stars as they are sometimes known, Hβ has a P Cygni profile (Crowther & Walborn, 2011). For the WR stars, Hβ is in emission.

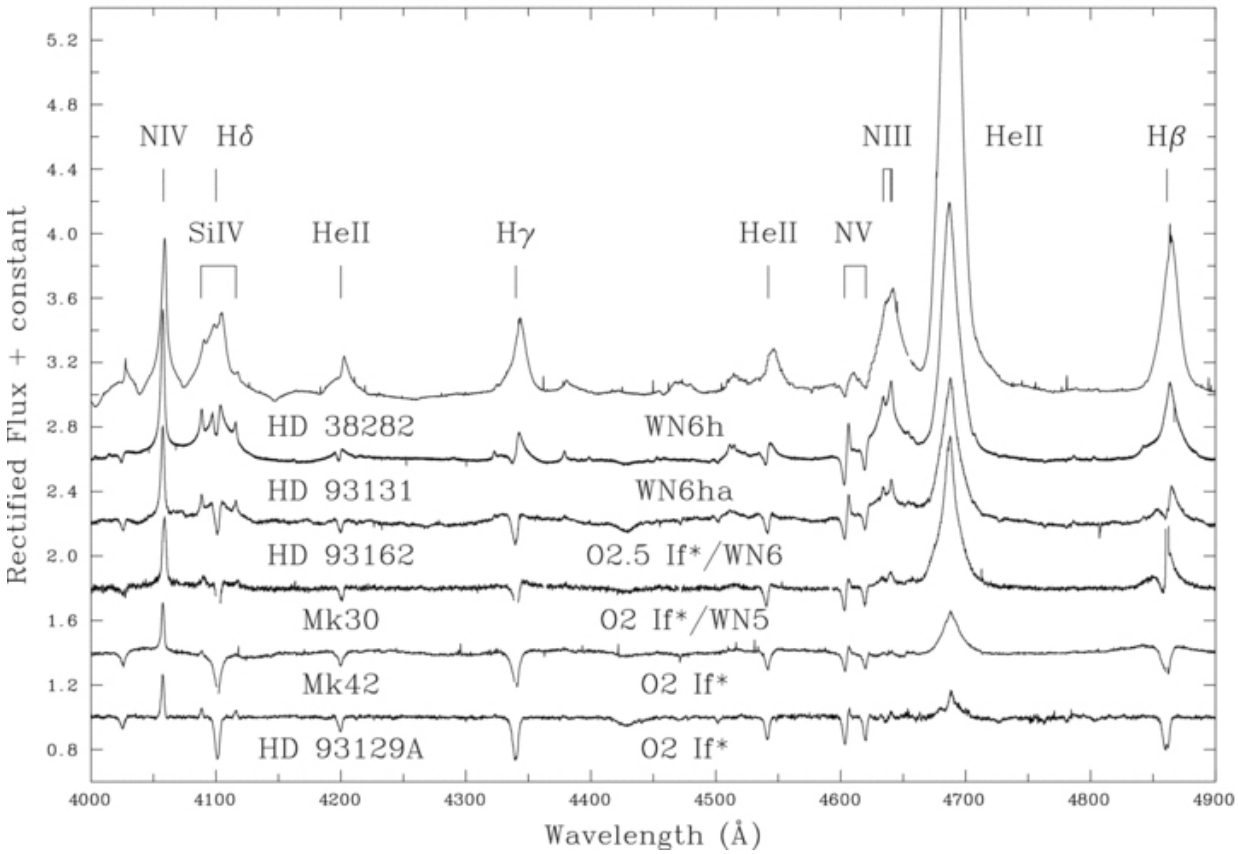

Figure 1.2: Example spectra of OIf, OIf/WN and WNh stars showing the morphological progression through the difference spectroscopic classes. Taken from Crowther & Walborn (2011), where spectra have been offset by a constant of 0.4 for clarity.

1.2.2 WR Stars

At the Paris Observatory, in 1867, Charles Wolf and Georges Rayet published a paper describing three stars in the constellation Cygnus with highly unusual spectra (Wolf & Rayet, 1867). Rather than the regular absorption features present in a stellar spectra, these stars showed strong broad emission lines imposed upon a continuum and became the basis of a new stellar class - Wolf Rayet stars.

It has since been recognised that multiple stellar objects are capable of producing this characteristic broad emission line spectra, such that the WR phenomenon is seen in three different stellar sources:

1. Main-sequence WR stars (WNH or WNh)
2. Classical WR stars (WN + WC + WO)
3. Central stars of planetary nebula WR stars ([WC])

There are significant differences between the stellar properties of these three different WR types. Main-sequence WR stars are essentially an extension of the O star classification to hotter, more massive stars. A star is considered to be in hydrostatic equilibrium when the emitted radiation pressure is balanced by the inwards gravitational force. The classical Eddington luminosity, shown in Equation (1.1), sets the minimum luminosity necessary to break hydrostatic equilibrium, such that radiation pressure from electron scattering overcomes the force of gravity (Crowther et al., 2012). These massive main sequence WR stars have luminosities which approach their Eddington luminosities, and therefore are capable of driving strong stellar winds at young ages.

$$L_{\mathrm{Edd}} = 30000 \frac{M}{M\odot} L \odot \tag{1.1}$$

In contrast, classical WR stars are evolved massive stars which have exhausted most, if not all, of the hydrogen in their core. The strong stellar wind, or a close binary companion, has stripped these stars of the majority of their hydrogen envelope, exposing the helium core, which in turn is responsible for the unusual abundances observed in these stars.

Under rare circumstances, some central stars of planetary nebulae (CSPNe) also exhibit a WR-like spectrum, however these stars originate from much lower mass progenitors. Planetary nebulae represent the end stages of low/intermediate mass star evolution, when the star expels its outer layers to reveal a hot central core. Unusual chemical abundance patterns can arise from thermal pulses within the star which dilute the hydrogen envelope, producing an oxygen/carbon rich spectrum (Herwig et al., 1999).

1.3 Classification of WR Stars

Classical WR stars are recognised as post-main-sequence massive stars progressing through the helium-burning stages of stellar evolution (Lamers et al., 1991). These stars are dominated by strong winds and high mass loss rates, during which they are stripped of their hydrogen, and sometimes helium, envelopes. This distinction lends itself nicely to the criteria for two primary WR spectral types, the nitrogen sequence (WN) and the carbon sequence (WC), both of which can be divided into further ionization subclasses.

Ionization subclasses are denoted by numerical values, where a lower value corresponds to an earlier type star with high ionization and in contrast a high value indicates a later type star with lower ionization.

There is also an oxygen dominated sequence (WO) however it is noted that the abundance of oxygen is not drastically different from the levels observed in early-WC stars,

suggesting that this subclass is an extension of the WC class to higher ionisation levels (Crowther et al., 1998).

1.3.1 WN Sequence

Nitrogen sequence WR stars (WN) have spectra dominated by nitrogen and helium emission lines such that for a hydrogen free WN star, the mass fraction distribution is 98% helium, 1% nitrogen, and ≤1% other elements. The ionization sequence currently ranges from WN2 to WN11, where early-type WNE stars have WN2-WN5 classifications, late-type WNL stars have WN7-WN11 classifications and WN6 is the intermediate stage. Examples of these spectra can be found in the upper panel of Figure 1.5. The classification system of WN stars can be described by three possible criteria outlined in Smith et al. (1996); ionization strength, line strength and width, and hydrogen abundance.

The primary line flux ratio used to define the ionisation state is He II 5411 / He I 5875, where a higher ratio corresponds to more ionisation and therefore an earlier subclass. Ionised nitrogen ratios are also used in a similar manner, and a more complete list of ratios and values can be found in Smith et al. (1996).

The line strength and width criteria are used to distinguish between broad-lined and narrow-lined spectra. For a WN spectra to be designated as broad-lined (WNb), the FWHM of the He II 4686 line should be larger than 30 Å, or the equivalent width of the He II 5412 line should be greater than 40 Å. Generally both of these criteria are satisfied for broad-lined WN stars, however circumstances such as the presence of an OB companion can dilute the equivalent width strength, incorrectly suggesting the particular WN star is weak-lined. For this reason the FWHM criteria is considered the main requirement for broad-line designation.

The presence of hydrogen can be determined through the comparison of H I Balmer lines and He II Pickering lines. Within a WR spectrum, a decline in line flux will be observed along the Pickering series as the excitation level increases, i.e. emission lines at shorter wavelengths will be monotonically weaker than those at longer wavelengths. Every alternate Pickering line however, for example n=8-4 at 4859Å, will coincide with a Balmer line, in this case Hβ at 4861Å, and if the hydrogen abundance is significant it will manifest as a boost in the strength of this coincident line in comparison to the declining 'non-coincident' neighbouring lines. WNo denotes a star with no hydrogen content, WN(h) suggests modest hydrogen content, and WNh indicates hydrogen is substantially present, see Section 1.3.3 for more details.

There are also various other suffixes which can be used to highlight unusual features in

the spectra, such as absorption lines originating from the WR star (a) or absorption lines of unknown origin (abs) (Smith et al., 1996).

1.3.2 WC/WO Sequence

Carbon sequence WR stars (WC) have spectra dominated by carbon, oxygen and helium emission lines with approximate mass fractions of 20–55% for carbon, 15–10% for oxygen and the remainder helium (Crowther, 2007). The WC sequence ranges from WC4 to WC11, where WC4-WC6 are early-type WC stars, WC7-WC9 are late-type WC stars, and the later WC subtypes are observed in CSPNe. The lower panel of Figure 1.5 plots example WC spectra. An exhaustive list of ratios used to quantify the excitation can be found in Crowther et al. (1998), which outlines that, for this sequence, the primary differentiator between ionisation subclasses is the ratio of equivalent widths between C IV 5808 / C III 5696.

As mentioned previously, the WO sequence is considered an extension of the WC sequence, and this is reflected in the ionization numbering, which ranges from WO1 to WO4. The main diagnostic ratio used here is O VI 3811 / O V 5590 (Crowther et al., 1998).

There are some WR stars which have spectra that display characteristics of both WN stars and WC stars, and so consequently have been designated WN/C stars and are thought to be stars transitioning from the WN phase to the WC phase, see Section 1.5.1 for more details (Conti & Massey, 1989).

1.3.3 Main Sequence WR Stars

In contrast to the classical WR stars, main sequence WR stars are thought to be in the core hydrogen burning stage. Their stellar structure is also very different to a classical WR star. In the latter case, the classical WR star has stripped away the outer envelopes to reveal the compact, hot stellar core. For main sequence WR stars however, the central core is much larger, dominating the star such that it is over 80% of the total mass, surrounded by a thin hydrogen envelope (Köhler et al., 2015).

These hydrogen-rich, main sequence, WR stars are only observed within the WN subclass and are unique to young star-forming regions, such as 30 Doradus and NGC3603. Often they resemble mid-type classical WN stars with weak emission lines and the presence of hydrogen lines. To differentiate them, the hydrogen-rich WN stars are sometimes collectively referred to as WNH stars (Smith & Conti, 2008). Individual spectral classifications include an ionisation class and the letter h to denote the hydrogen content.

1.4 Identification of WR Stars

Generally, a combination of photometric and spectroscopic techniques is used to identify WR stars. WR stars are bright, with absolute narrow-band magnitudes in the range of M_v=−2.6 to −7.22 mag (Hamann et al., 2006), and can therefore be observed at large distances. In crowded regions, and in galaxies beyond the Local Group, observations can be challenging due to contamination from nearby sources. In some starburst regions, collections of up to a thousand WR stars can occur. These are known as WR-galaxies and the observations obtained from these regions are a manifestation of all the individual WR stars combined together, exhibiting blue (He II 4686) and/or yellow (C IV 5808) WR bumps (Conti, 1991; Vacca & Conti, 1992).

When searching a region for these stars, narrow-band photometry, sensitive to emission lines and adjacent continuum, is used to identify a number of potential candidates, but spectroscopy is necessary to provide confirmation and assign the star to the correct subclass. The techniques used to search for these stars have been refined over the years as our understanding and technology has progressed, allowing modern surveys to view a much wider field in a single observation, increasing the likelihood of obtaining a complete sample (Neugent & Massey, 2019). Complete samples are hugely important when wanting to make statements applicable to the general population of WR stars. Whilst our confidence in the completeness of local surveys is rising, new WR stars are still being discovered, suggesting that there is still more work to be done. This is especially relevant with regards to the Galactic WR population, where interstellar dust hinders detections, however IR observations have significantly aided discoveries and doubled the sample size in the last decade.

WR stars can be observed at multiple wavelengths, including IR, visual, UV and X-ray, with characteristic WR features present across the full spectrum. Figure 1.3 shows a multi-wavelength spectrum for the Galactic WN4b star WR6. The spectra are primarily dominated by strong broad He I and He II emission, however there is evidence of N IV at 1486, 1718, 4058 and 7116; N V at 1240 and 4603/4620; and C IV at 1550 and 5808.

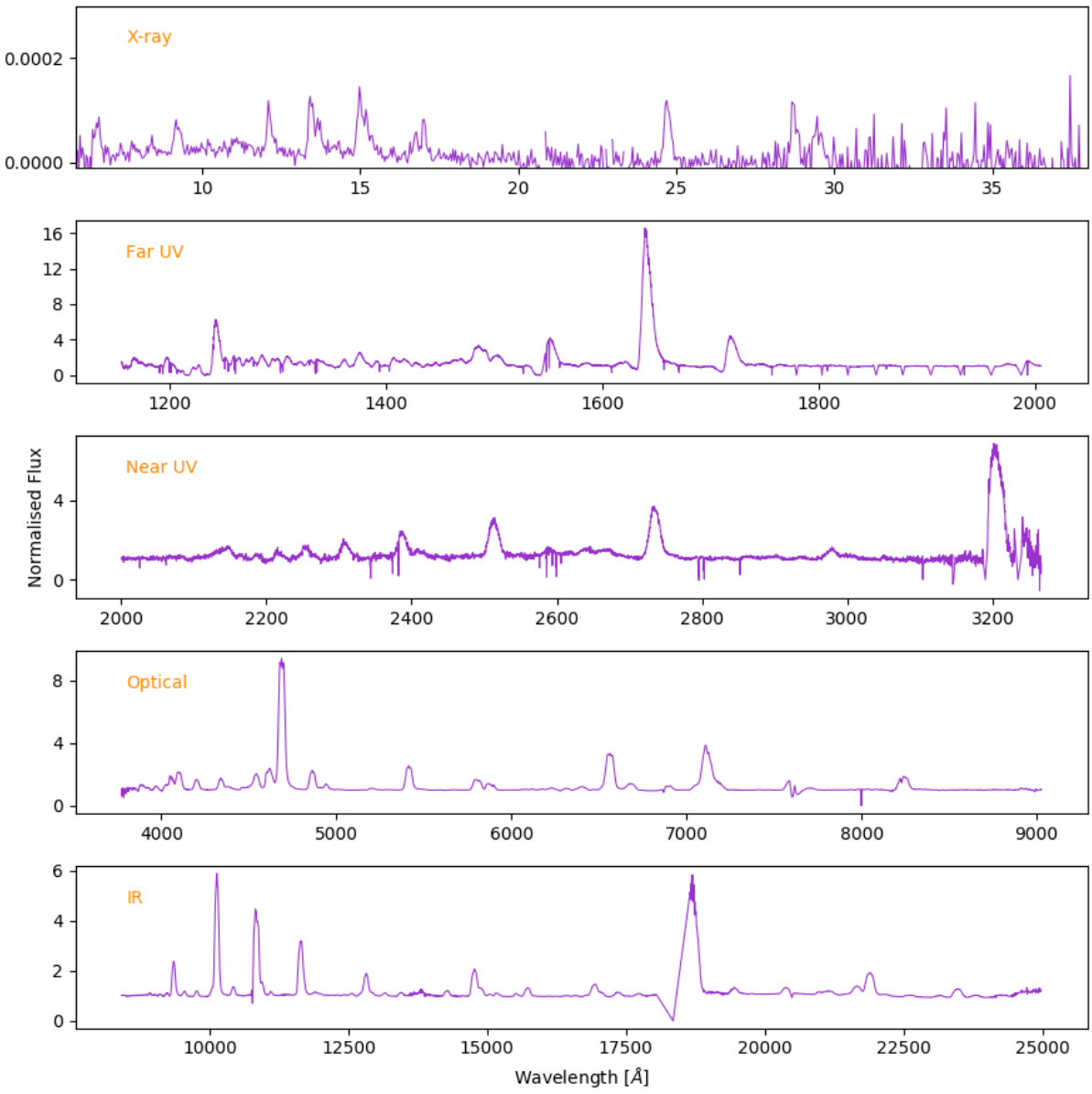

Figure 1.3: X-ray, UV, optical and IR spectrum of WR6, a Galactic WN4b star, showing the presence of emission line features across the full spectral range.

1.4.1 Optical Observations

Due to the ease of obtaining visual observations from ground-based telescopes, optical studies of WR stars are by far the most common. On this basis, the classification system for WR stars is based on emission features observed at optical wavelengths, and photometric filters used to identify these stars have been tailored to optical emission lines.

Photometric Observations

Broad-band filters are unable to distinguish WR stars from other early-type stars, therefore to counter this, imaging surveys often incorporate the use of one, or more, bespoke photometric filters. Wray & Corso (1972) used two narrow interference filters in their search for WR stars in M33. The first filter, known as the continuum filter, was centred at 4450 Å designed to correspond to a region of the WR spectrum with very little line emission. The second filter, located at 4670 Å, was the emission line filter, and was selected to include emission lines present in both WC and WN stars. Images of the same field were taken using both filters and, through blinking the photographic plates, Wray & Corso (1972) were able to observe individual brightening in the emission-line filter in comparison to the continuum filter, therefore signalling a potential WR candidate.

A similar technique was adopted by Azzopardi & Breysacher (1979), who considered the strong emission line nature of WR stars and introduced a filter with a central wavelength of 4650 Å to find WR stars in the SMC. Both WC and WN stars should emit strongly in this region due to the C III 4650 and He II 4686 emission respectively, therefore appearing much brighter than the background population.

Table 1.1: Central wavelengths and bandpasses for the WR emission line and continuum filters used by Armandroff & Massey (1985) to identify and classify WR stars photometrically in NGC 6822 and IC 1613.

Filter	Central Wavelength Å	FWHM Å	Emission Lines
WC	4649	55	C III 4650
			He II 4686
			N III 4634 / N III 4642
WN1	4706	55	He II 4686
WN2	4693	55	He II 4686
CT	4749	55	Continuum

Armandroff & Massey (1985) were amongst the first to attempt to add a quantification element to the interference filter technique in their search for WR stars in NGC 6822 and IC 1613. Here four interference filters were used, outlined in Table 1.1, with the intention of allowing the authors to both identify WR stars and distinguish between WC and WN stars without the need for spectroscopy. Magnitude difference measurements were calculated between the continuum filter and the emission-line filters, with a WR detection defined as difference greater than 0.4 mag.

Although these photometric methods have been successful, they do exhibit some bias

towards specific spectral types. WC stars and early-WN stars exhibit strong emission lines, and therefore appear much brighter within the narrow band emission line filters. Late WN stars however have much weaker emission lines, making discovery of these stars relatively difficult, and sometimes resulting in missed detections. Figure 1.4 shows a comparison in equivalent width strength between the strongest WN emission line (He II 4686) and strongest WC emission line (C III 4650) for WR stars located in the Galaxy and LMC. It can be seen that the C III 4650 emission line in WC stars can be up to 4× stronger than the WN He II 4686 emission line, and therefore making WC detection comparatively easier (Neugent & Massey, 2019).

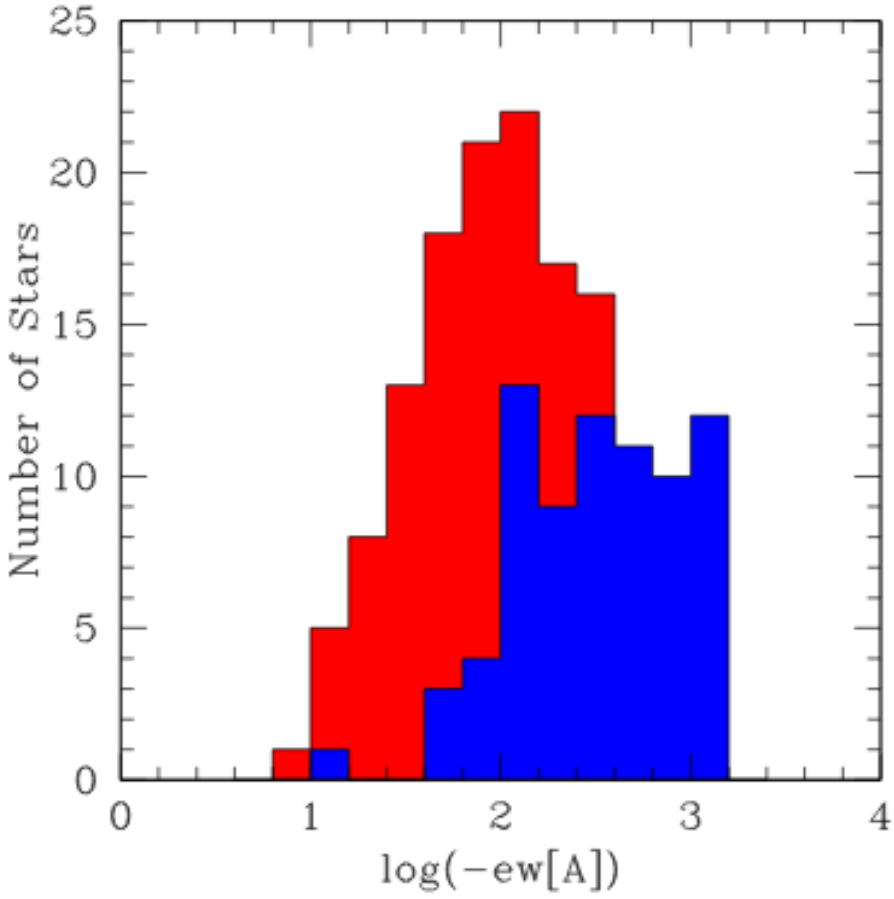

Figure 1.4: Histogram showing a comparison between He II 4686 emission line strengths in WN stars (red) and C III 4650 emission line strengths in WC stars (blue). Includes Galactic and LMC stars. Taken from Neugent & Massey (2019).

Spectroscopic Observations

After identifying candidate WR stars, spectroscopy is necessary to provide confirmation and allocate a spectroscopic class. The general form of a WR spectrum consists of strong broad emission lines imposed upon a weak continuum. Upon closer inspection however, there are significant differences between the WN and WC subclasses.

For comparison, example WN and WC optical spectra are shown in Figure 1.5, with the prominent emission lines labelled. Strong nitrogen and helium lines dominate the WN subclass, whereas the WC spectra show an excess of carbon and helium. Figure 1.5 also demonstrates the spectroscopic differences between early and late ionisation subclasses, as discussed in Section 1.3.1.

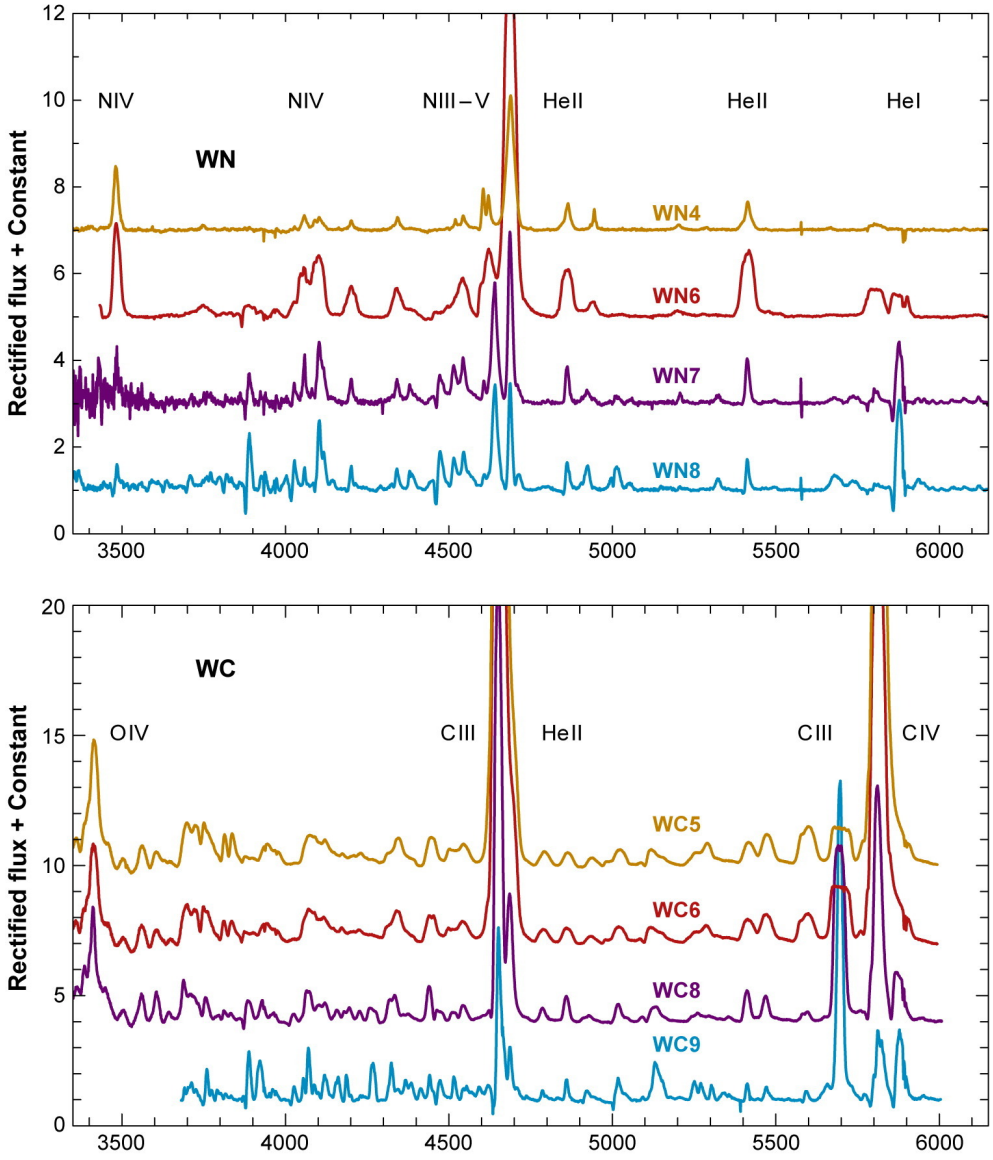

Figure 1.5: WR spectra showing typical emission lines for a WN star (upper) and WC star (lower). (Crowther, 2007)

Spectroscopy is also useful for binary identification, in particular WR stars which reside in binaries with an early-type companion star. The usual weak continuum of a WR star would be enhanced by the contribution from the OB star, which in turn would dilute the strength of the WR emission lines. Low equivalent width measurements of WR emission lines can therefore be suggestive of a binary system.

1.4.2 IR Observations

In regions of high interstellar extinction, using an optical based observing programme to detect WR stars would be unsuccessful. We can, however, adopt an IR observing strategy to identify the WR population instead. An example IR spectrum of a WR star is shown in Figure 1.3, where we can identify clear strong He I and He II emission lines alongside weaker nitrogen emission.

IR surveys are particularly useful when searching for WR stars within the inner Galaxy, where dust obscuration severely limits optical studies (Shara et al., 1999). It does however, introduce additional complications since, unlike optical surveys, there is no pair of bespoke narrowband emission line/continuum filters that can be used together to reveal both WR classes (Crowther et al., 2006). Homeier et al. (2003) carried out an IR survey using 7 narrowband filters, 2 sensitive to WN emission lines, 2 for WC emission lines and 3 for the continuum. They also emphasize the necessity for each emission line filter to have two associated continuum filters, one redward and one blueward, in order to assess the extinction variation that occurs in the IR.

An alternative approach adopted by Hadfield et al. (2007) is to use broadband near IR and mid IR colours to select WR candidates. The stellar winds of WR stars generate free-free emission (Wright & Barlow, 1975), which manifests as an excess in the IR, therefore helping to differentiate them from a general stellar population as shown in Figure 1.6 (Williams & Antonopoulou, 1981; Hadfield et al., 2007).

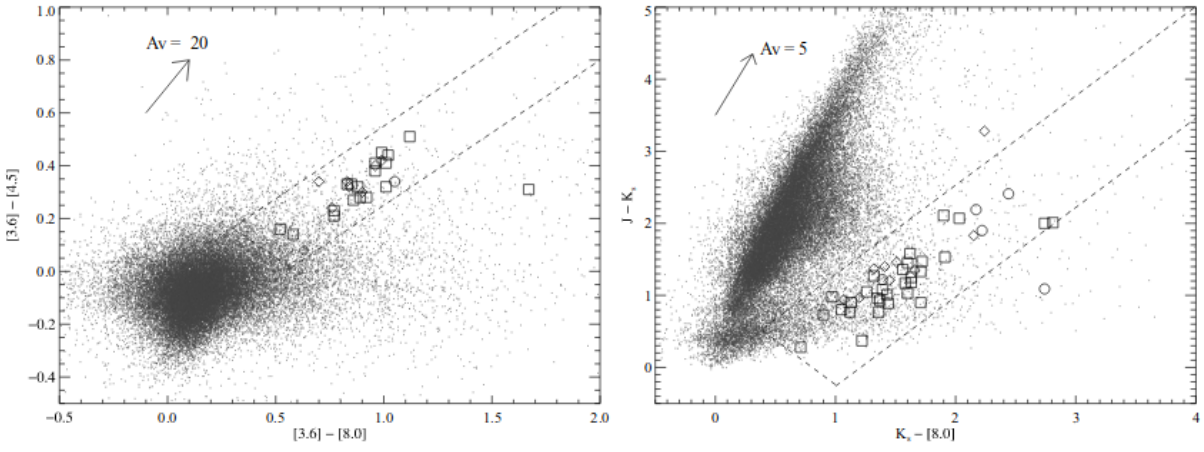

Figure 1.6: IR colour-colour plots for stars within a 1° × 1° area of the galactic plane. WR stars are represented by open symbols, with WN as squares and WC as diamonds and circles. The WR stars are clearly offset from the remainder of the stellar population, which is represented by point symbols. Taken from Hadfield et al. (2007).

Another complication is the strength of WR emission lines fluxes at IR wavelengths. They are much weaker compared to their optical counterparts (Crowther et al., 2006). This is particularly relevant when observing WC stars, as some WC stars are known to form dust (Cohen et al., 1975; Williams et al., 1987b) which can dilute the equivalent width of WR emission lines further.

Like optical WR searches, spectroscopy is necessary to confirm the identified WR candidates. To minimize interstellar dust absorption the most popular IR band for observing WR stars is the K-band (2–2.4 μm). Key emission lines in this range include Brγ 2.17 μm and He II 2.189 μm for WN stars, and C III 2.110 μm and C IV 2.076 μm for WC stars (Crowther et al., 2006). Dusty WC stars however may require J-band observations in order to observe the WR spectral features due to hot dust dominating the spectra at 2 μm (Najarro et al., 2017).

1.4.3 X-ray Observations

X-ray radiation is located in the high energy region of the electromagnetic spectrum, with energies in the range of 0.1–100 keV.

Due to the opaqueness of the Earth's atmosphere to X-ray radiation, observations are strictly limited to high altitude or space-based observatories. This means X-ray astronomy is a relatively new field, with the first cosmic source detection, Sco-X1, in 1962.

Today we understand there are over half a million X-ray sources (Rosen et al., 2016), ranging from active galactic nuclei to high mass X-ray binaries. Here we are particularly interested in massive stars as X-ray sources.

The Origin of X-rays

There are a number of processes capable of generating either a continuous or discrete spectrum of X-ray photons. Below we discuss some of these mechanisms.

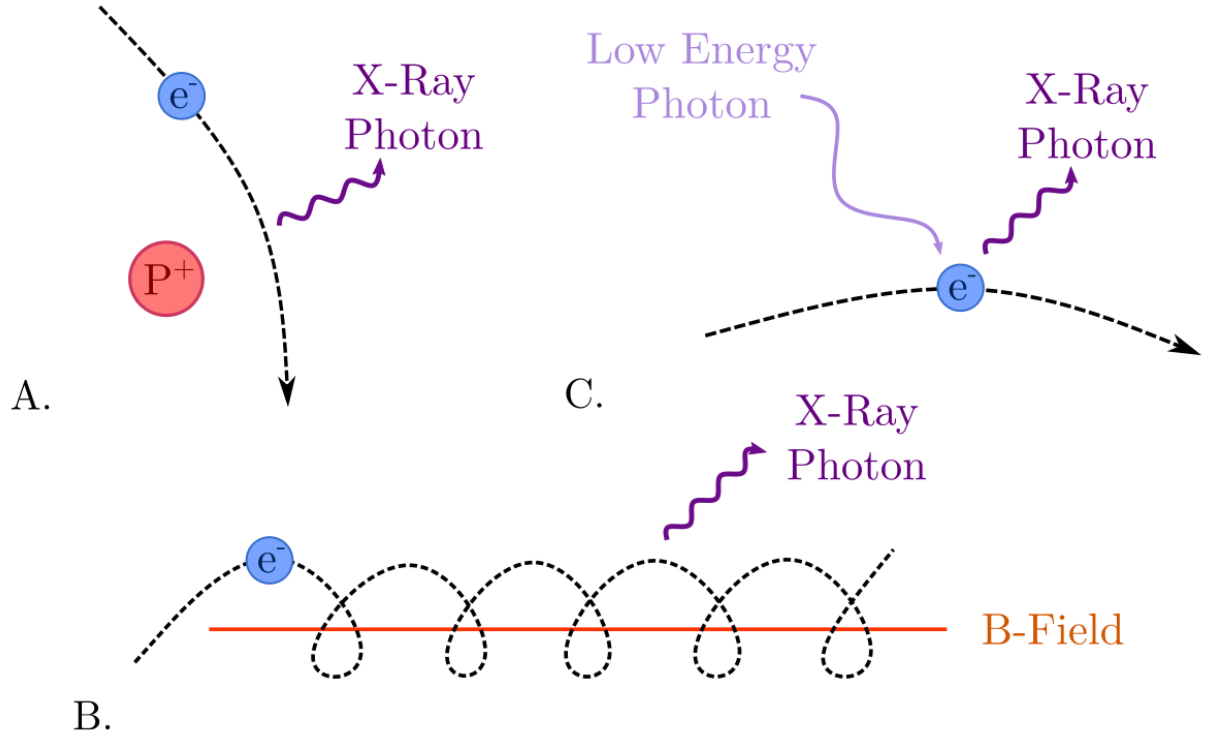

Figure 1.7: Schematic diagrams showing the sources of continuous X-ray emission. A. Bremsstrahlung emission, B. Synchrotron Emission, and C. Inverse Compton scattering.

Sources of X-ray emission which contribute to the continuum are described below, with a schematic of these processes shown in Figure 1.7.

A. **Bremsstrahlung Radiation**, also known as braking radiation, or free-free radiation, is generated in hot ionized gasses. When a liberated electron comes within the vicinity of an electric field surrounding a charged ion it is deflected, causing an acceleration. Any electron that is accelerated or decelerated within a Coulomb potential will emit a photon. The energy of the photon is dictated by the electron velocity and electromagnetic field strength.

B. **Synchrotron Radiation**, is similar to Bremsstrahlung radiation, however the free electrons are deflected around magnetic field lines in a circular motion. This acceleration causes the emission of X-ray photons with energies dependent on the magnetic field strength and initial velocity of the electron.

C. **Inverse Compton Scattering**, is where a low energy photon scatters off a high energy electron, allowing a fraction of the electron energy to be transferred to the photon, producing X-ray emission.

In contrast, discrete emission sources which produce emission lines are described here:

D. **Atomic Emission:** the de-excitation of a bound electron, that has previously been excited to a higher energy level, through a collision with another particle or photon can release an X-ray photon.

E. **Fluorescence:** a secondary emission process where a high energy photon liberates an electron from an inner shell. To stabilize the atom an outer shell electron falls down to take its place, releasing X-ray radiation. This re-processing allows cooler sources to emit X-ray radiation.

F. **Charge Exchange:** the transfer of an electron between ions after a collision can release an X-ray photon as the captured electron settles into the lowest available energy level.

WR Stars in X-rays

Single O stars are known soft X-ray sources (Berghoefer et al., 1997), thought to generate X-ray emission through shocks within their radiatively-driven winds (Lucy & White, 1980; Lucy, 1982). They follow an observed X-ray luminosity to bolometric luminosity relationship such that $L_X/L_{bol} \sim 10^{-7}$ (Pallavicini et al., 1981; Nazé et al., 2011). It is therefore, not unreasonable to assume WR stars would also have some intrinsic X-ray emission if they too have radiatively driven winds. Indeed, WR stars were first discovered to be X-ray emitters by Seward et al. (1979) using observations of the Carina Nebula from the Einstein Observatory. Since then, many more WR sources, both single and binary, have been detected in X-rays, however, the origin of their X-rays remain uncertain.

Single WR stars are currently thought to produce X-rays from line-driven instabilities within the winds. WR winds, which are powered by the absorption and scattering of stellar photons, were originally thought to be smooth and steady (Lucy & Solomon, 1970; Castor et al., 1975). Further analysis however, revealed it was more likely these winds had structure and were prone to instabilities (Owocki et al., 1988; Feldmeier et al., 1997). These instabilities within the winds are capable of forming shocks when fast moving clumps collide with slow moving clumps, which in turn can produce soft X-ray emission.

Binary WR systems are still expected to produce this intrinsic X-ray emission, however they could have additional X-ray production from the colliding wind region between the two stars (Prilutskii & Usov, 1976; Cherepashchuk, 1976). Colliding wind binaries (CWB) however, are only possible if the stars approach close enough to one another, and their stellar winds have achieved a sufficiently high velocity (Stevens et al., 1992).

The first attempt to collectively analyse a WR population in X-rays was by Pollock (1987), who gathered the 48 Milky Way WR stars observed with the Einstein Observatory and directly compared the X-ray properties of the WR sample. This uniform approach revealed that, on average, WN stars were brighter than WC stars, and Pollock (1987) attributed this to their varying abundances. The X-ray faintness of WC stars has also been confirmed in later studies, such as Skinner et al. (2006, 2010) who selected a sample of Galactic WR stars and failed to detect any of the apparently single WC sources despite clear WN detections.

Pollock (1987) also concluded that the massive binaries were brighter than the apparently single stars. This emphasizes the theory that the colliding winds of massive stars in binaries are capable of generating additional X-ray emission, resulting in higher X-ray luminosities.

A classic example of a CWB is WR140, which comprises of a WC7 and an O4-5 star, orbiting on a 7.94 yr highly eccentric (e=0.9) path (Williams et al., 1987a; Marchenko et al., 2003; Fahed et al., 2011). Figure 1.8 shows the observed light curve for this system. At X-ray maximum WR140 achieves an X-ray luminosity of 4.1×10^{34} erg s^{-1} (Pollock et al., 2018), which with a bolometric luminosity of $\log(L_{bol}/L_{\odot})=6.33$ (Williams, 2011) gives a high L_X/L_{bol} of 5.1×10^{-6}. The high eccentricity of this system leads to a large variation in the orbital separation of the two components, ranging from 2–30 AU (Dougherty et al., 2005), and this is key for producing the characteristic X-ray variability observed in a CWB.

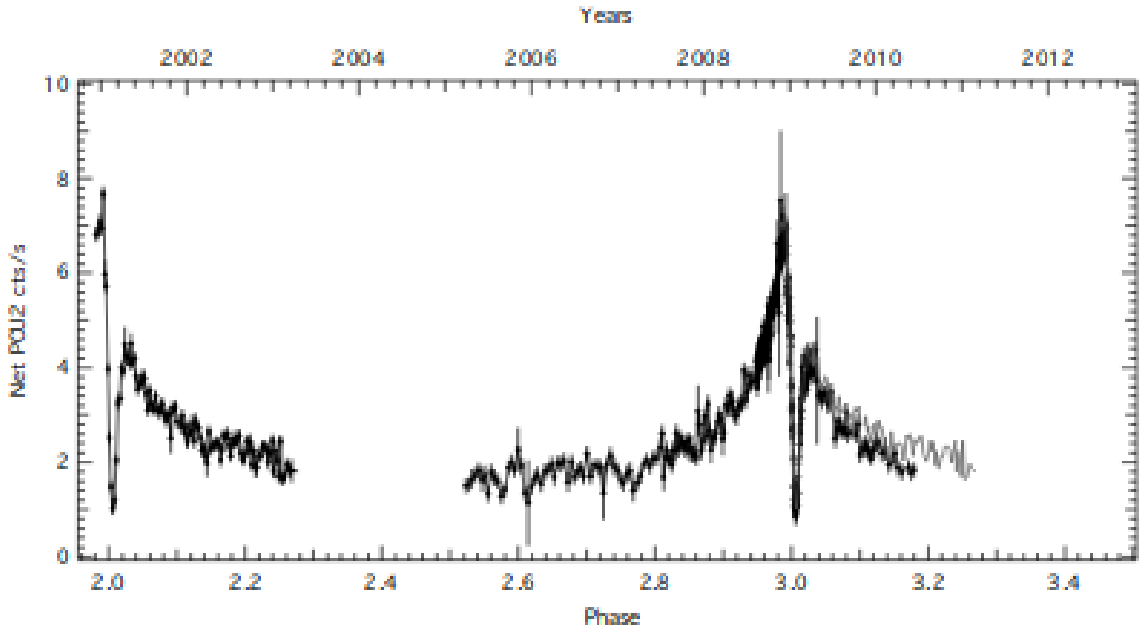

Figure 1.8: WR140 X-ray light curve showing the swift variation between X-ray minimum and maximum at periastron, when the two stars are close to one another, characteristic of a CWB. Taken from Corcoran et al. (2011).

1.5 Massive Star Evolution

The understanding of massive star evolution is still an ongoing process, however there are broad themes that have been identified, such that many of the massive star types discussed in this chapter are thought to be connected through evolutionary chains.

1.5.1 Single Star Origin of WR Stars

Conti Scenario

Classical WR stars are thought to be linked to the post-main-sequence evolution of massive stars. The current favoured explanation for single WR stars is known as the Conti scenario and it attributes the observed over abundance of carbon, nitrogen and oxygen to mass loss of the outer layers as the O star progenitor evolves through the WR phase. This thinking was encouraged as intermediate stars were found with characteristics typical of both Of stars and WR stars (Walborn, 1977, 1982).

The Conti scenario also suggests the two WR spectral types are linked through an evolutionary chain by varying the amount of mass loss each star undergoes (i.e. the WC phase is more advanced than the WN phase). Before reaching the WR phase the O stars

are thought to progress though a luminous blue variable (LBV) stage discussed further below. Here is an outline of the Conti scenario, which has since been adapted by Crowther (2007) to take into consideration initial stellar mass at solar composition.
Initial mass greater than 75 $M_\odot$

$$\text{O} \rightarrow \text{WNL(H-rich)} \rightarrow \text{LBV} \rightarrow \text{WNE(H-poor)} \rightarrow \text{WC} \rightarrow \text{SN Ic.}$$

Initial mass from 40 - 75 $M_\odot$

$$\text{O} \rightarrow \text{LBV} \rightarrow \text{WNE(H-poor)} \rightarrow \text{WC} \rightarrow \text{SN Ic.}$$

Initial mass in the range 25 - 40 $M_\odot$

$$\text{O} \rightarrow \text{LBV/RSG} \rightarrow \text{WNE(H-poor)} \rightarrow \text{SN Ib.}$$

LBV & RSG

Prior to the WR phase, an O star may become either a luminous blue variable (LBV) or red supergiant (RSG).

RSGs are post-main sequence stars, thought to originate from single stars with initial masses up to 25–30 $M_\odot$ (Levesque, 2010). They are cool stars, with temperatures in the range of ∼4000 K, however their large radii (500-1500 $R_\odot$) result in bright luminosities (Mauron & Josselin, 2011). The mass-loss rates for RSG, however, are very uncertain (Beasor & Davies, 2018). There are a number of empirically derived prescriptions available for use, although often they fail to agree, as shown in Figure 1.9 for the de Jager et al. (1988) and van Loon et al. (2005) prescriptions. For some massive stars, the RSG phase will be the final stage before exploding as a type II (hydrogen-rich) SN (Smartt, 2009) . The more massive RSG however, are predicted to lose their hydrogen envelope, and evolve back across to the blue side of the HR diagram (Georgy et al., 2015).

LBVs refer to another type of post-main sequence massive star (Conti, 1984). Characteristically bright, they have luminosities close to their the Eddington limit, see Section 1.2.2, which in turn makes them unstable and prone to erupt (Humphreys & Davidson, 1994). Mass-loss rates of LBV stars are generally high, ranging from 10^{-6} to 10^{-4} $M_\odot$ yr^{-1}, however during giant eruption events the mass-loss rates rise even higher, reaching 10^{-2} to 1 $M_\odot$ yr^{-1}, as shown in Figure 1.9 (Smith, 2014). These eruption events are irregular, occurring on variable timescales, and can last for decades.

If considered single, LBV stars are thought to originate from stars with an initial mass above 25 $M_\odot$ (Smith, 2014), and represent a transitional phase between the main sequence and classical WR star as outlined in the Conti Scenario. This view however has since been

challenged by Smith & Tombleson (2015) who analysed the spatial distribution of LBVs in the Galaxy and Magellanic Clouds and found they were generally in isolation, rather than in clusters similar to their supposed O star progenitors. Instead they argue LBVs are a consequence of close binary evolution, where mass transfer has rejuvenated these evolved stars, as discussed in Section 1.5.2.

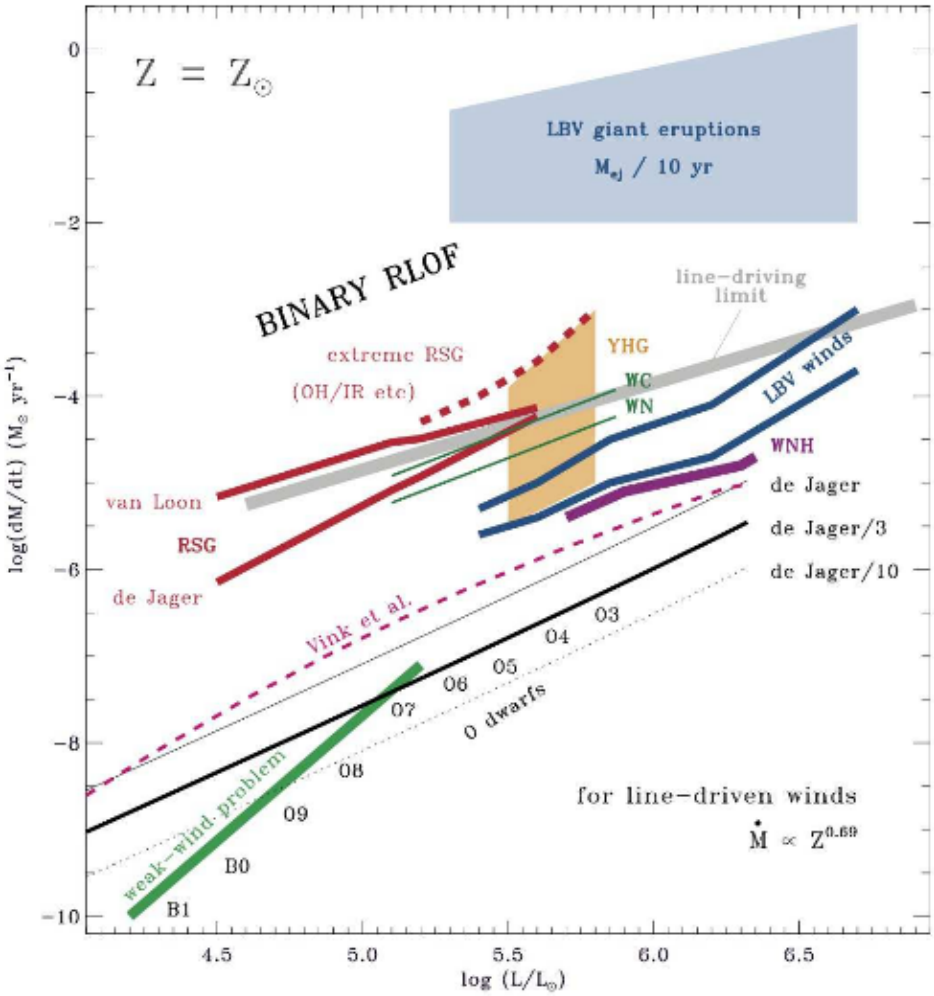

Figure 1.9: Mass-loss prescriptions and observed mass-loss rates for various massive star types. Taken from Smith (2014).

WR Stars

As an O star progresses along the main sequence, hydrogen fusion occurs via the CNO cycle. Once the majority of hydrogen is exhausted, and the core temperature is high enough, helium fusion proceeds via the triple-α process. The nuclear material formed through these processes builds up in concentric layers, with hydrogen in the outer shell and

heavier metals towards the centre. During the WR phase, strong winds remove the outer layers of the star. For a WN star, the wind removes the hydrogen envelope, revealing the products of the CNO cycle below. For a star in equilibrium, the rate limiting step in the CNO cycle is the ^{14}N proton capture, hence the high abundance of nitrogen and helium in these stars. WC stars have experienced a much greater mass loss, stripping the star of more layers and revealing the products of the triple-α process, which results in an excess of carbon and helium.

This process can be seen in the Conti scenario evolutionary tracks outlined above. As shown in the evolutionary sequence for a 75 $M_\odot$ star, an O star born with an exceptionally high initial mass will become a main sequence WR star, still burning hydrogen in its core, see Section 1.3.3. After exhausting the hydrogen core the star will then progress through the LBV stage to a classical hydrogen poor WN star, and after further mass loss will reach the WC phase, before eventually exploding as a hydrogen and helium deficient type Ic SN.

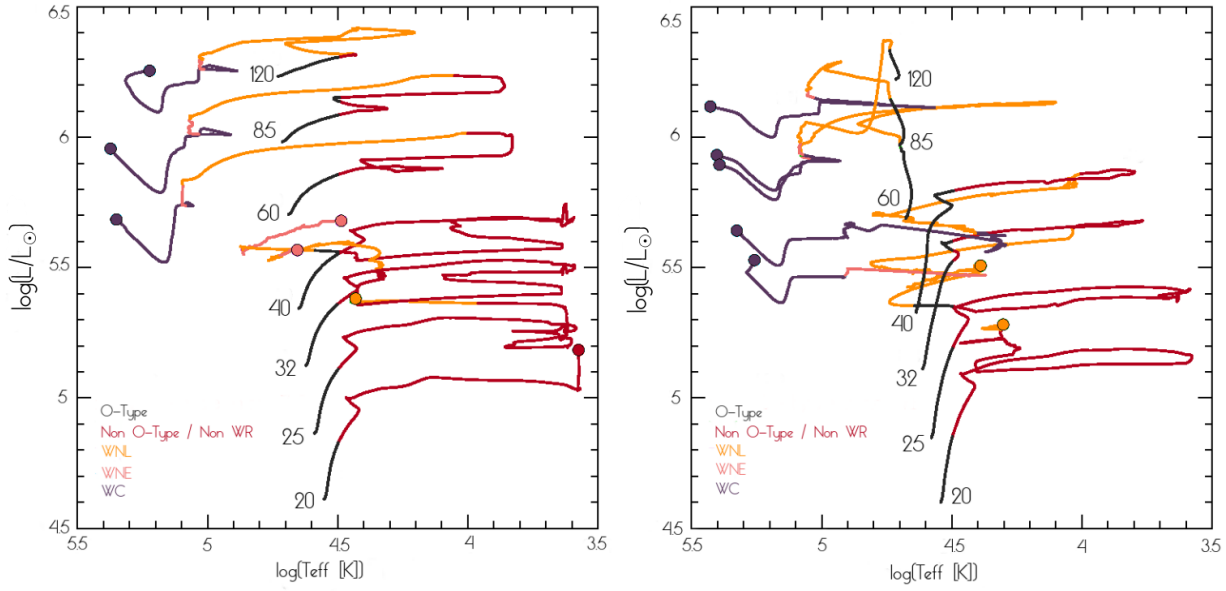

Figure 1.10: HR diagram showing the evolutionary tracks from the main sequence to the WR phase for solar composition stars with initial masses ranging from 20 $M_\odot$to 120 $M_\odot$, with different evolutionary phases highlighted in various colours. The filled circles indicate the end of the evolutionary track. Left: evolutionary models without rotation; Right: evolutionary models with rapid rotation, where v_{rot}=0.4$v_{critical}$. Taken from Georgy et al. (2012).

Figure 1.10 shows the evolutionary tracks of various initial mass stars on a Herzsprung-Russell (HR) diagram, demonstrating how a massive star can evolve from the main sequence to the WR phase. Various evolutionary phases have been highlighted in different colours to demonstrate the differences in evolution for different mass stars, and during which stage

the star is likely to terminate (indicated by the filled circle). Amongst other factors, stellar rotation rates can also greatly influence the evolution of a star as shown in Figure 1.10, where the left panel shows evolutionary tracks for stars with no rotation, and the right panel shows the models with rapid rotation included. Stars with rotation tend to progress further along the evolutionary chain in comparison to their non-rotating counterparts because the rotation drives additional mixing, which feed the core with extra hydrogen and therefore extends the main sequence lifetime.

1.5.2 Binary Origin of WR Stars

Many factors influence a star's evolution, but a strong influential factor is the presence of a close companion. As shown in Figure 1.11, the binary fraction amongst Galactic O stars is thought to be high (Sana et al., 2012, 2013b). Therefore, knowledge of the star's binary status is of great importance when trying to predict how the future will unfold.

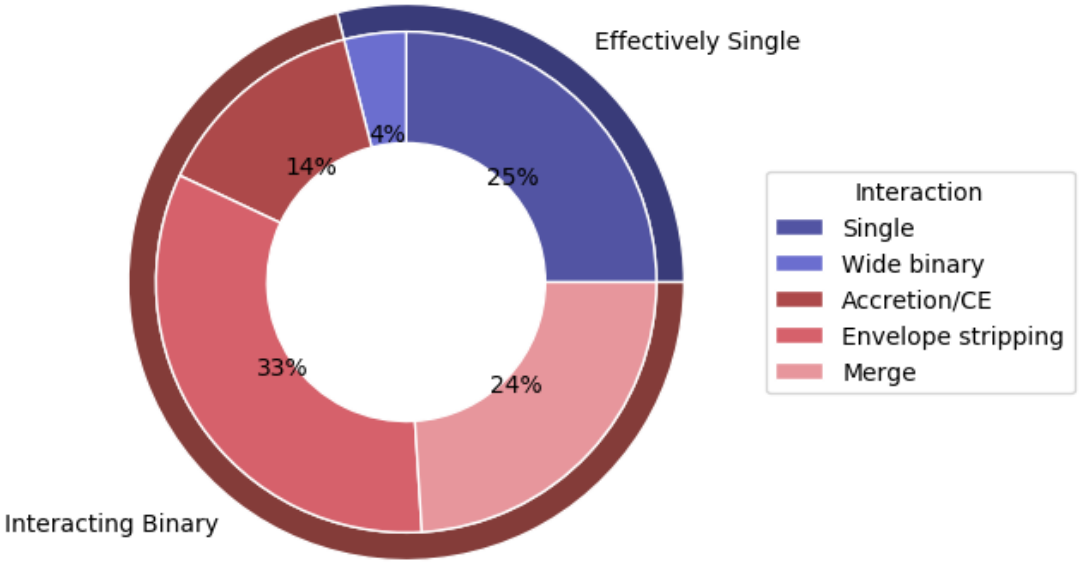

Figure 1.11: Pie chart showing the fraction of O stars expected to evolve in isolation (blue) either as single stars or wide binaries, or with interaction from a companion (red). Approximate fractions have been indicated on the chart. Adapted from Sana et al. (2012) who used observations of young stellar clusters in the Milky Way and theoretical models to correct for observation bias and predict interaction type.

From Figure 1.11, approximately 29% of massive stars will evolve in apparent isolation,

that is without interaction with a companion star (Sana et al., 2012). For these single stars the evolutionary path is likely to be dependent on the initial mass of the star, and follow the routes outlined in the Conti scenario, discussed in Section 1.5.1. The metallicity of the local environment governs the initial mass requires to enter to the WR phase. Table 1.2 compares the minimum masses needed for a single star to reach various milestones in massive star evolution, for MW and LMC metallicities. We see that metal-poor environments require higher mass progenitors to become WR stars, and this is a direct consequence of their weaker winds, as explained in Section 1.6.

Table 1.2: The minimum mass required for single stars to reach O star, WNL, WNE and WC phases at MW and LMC metallicities. Data taken from Georgy et al. (2012, 2015) for rotating stars.

	Metallicity	O star	WNL	WNE	WC
	$Z_\odot$	$M_\odot$	$M_\odot$	$M_\odot$	$M_\odot$
MW	1	16	20	25	27
LMC	0.4	14	32	61	63

Binarity can add an additional level of complication to massive star evolution. For extremely wide separation binaries, the system will evolve as two single stars, but as the separation decreases, the stars will become within range such that at some point during their lifetimes the two stars will interact. This is especially relevant because, for the MW O star population, Sana et al. (2012) predict an intrinsic binary fraction of over 70%, shown in Figure 1.11, meaning the majority of massive stars evolve in a binary.

Within the ∼70% of interacting binaries there are varying degrees of interaction predicted. 33% are thought to undergo envelope stripping, where the hydrogen envelope from the primary is stripped by the secondary through Roche lobe overflow (RLOF) (described below and illustrated in Figure 1.12). RLOF stripping can result in either conservative or non-conservative mass transfer, depending on whether the mass from the primary is accreted onto the secondary or lost to the system respectively. A further 14% of binaries experience accretion/common envelope (CE) following RLOF. The CE phase occurs when the secondary is incapable of accreting matter at the same rate the primary is losing it. This excess matter contributes to the filling of the secondarys Roche lobe, and subsequent RLOF. With both stars filling their Roche lobes, a common envelope of material surrounds the system (Iben & Livio, 1993; Podsiadlowski, 2001). Systems which undergo accretion experience an increase of the rotational velocity of the secondary, known as spin-up. Com-

ponents of a CE system however experience drag from the envelope of material they are orbiting through, and this causes the orbit to shrink. 24% of binaries will result in a merger, either whilst on the main sequence (case A) or for longer period binaries, between core hydrogen and core helium burning (case B) or later phase (case C). For massive stars, the majority of mergers are expected to occur whilst on the main sequence (case A) (Paczyński, 1967; Sana et al., 2012).

Binary fractions for WR stars are lower than their O star counterparts. For a sample of 227 Galactic WR stars of varying spectral types, van der Hucht (2001) find a binary fraction of ∼40%. At lower metallicities, Bartzakos et al. (2001) investigate the binary population of the 23 known WO/WC stars within the LMC. They find an observed binary fraction of 13% when considering definite binaries, however when including an additional 5 potential binary systems, the binary fraction rises to 35%. The LMC WNE population was considered by Foellmi et al. (2003b), who derive a binary frequency of ∼30%, and similarly the WNL population revealed a 20% binary fraction (Schnurr et al., 2008). These results are reasonably consistent, suggesting binarity of WR stars is independent of metallicity. We should, however, note that the WR binary fractions discussed here are derived observationally, and therefore represent lower limits since no adjustment has been made to correct for observational biases.

Figure 1.12 is a schematic outlining WR formation through the binary channel. To start we have two massive stars orbiting within the system, initially detached. As the primary evolves it will expand, filling its Roche lobe and triggering Roche lobe overflow (RLOF), which is when material from the expanding star flows onto the companion through an accretion disk (Paczyński, 1971). For the primary mass donor this results in a stripped, helium-rich star - a WR star. The secondary mass gainer has been rejuvenated, extending its lifetime on the main sequence and is spun-up, potentially altering its evolutionary path too.

Using a grid of spectral models Götberg et al. (2018) investigate the properties of stripped stars with initial masses in the range of 2-20 $M_\odot$. At solar metallicities they find the lowest initial mass progenitor capable of producing a WR spectrum is ∼15 $M_\odot$, which post-interaction results in a 5 $M_\odot$ stripped star. Lower initial mass stars which undergo mass transfer with a companion can also form a stripped helium star, however due to their weaker winds their (absorption line) spectra resemble hot subdwarfs.

It is thought both single and binary evolutionary routes to the WR phase are applicable, however the local environment can influence which route is dominant, as discussed in Section 1.6.

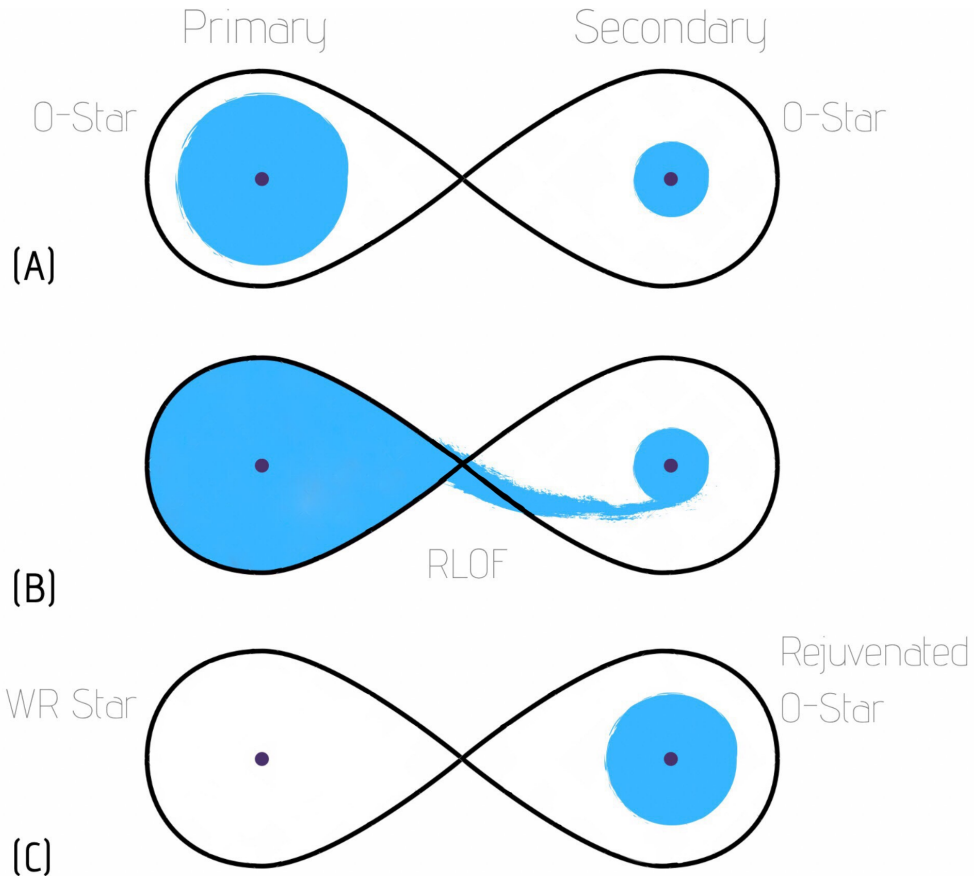

Figure 1.12: A schematic diagram showing the binary evolution to WR phase. (A) depicts two detached O stars in orbit with the primary on the left and secondary on the right. As the primary evolves it fills its Roche Lobe and the secondary begins to accrete material from the primary (B). After the envelope has been stripped from the primary, a hot helium rich core remains, the WR star, and the secondary is rejuvenated due to the accretion of more mass (C).

1.5.3 Supernovae

Supernovae (SN) are classified based on their spectroscopic and photometric properties (Filippenko, 1997). Type I SN are hydrogen deficient and can be subdivided as Ia, Ib and Ic, based on the presence of silicon, helium, or neither, in their spectra respectively. The spectra of type II SN contain hydrogen features, however further classification can be introduced based on their lightcurve shape, such as the linear class (-L) which shows a linear decline in magnitude from peak brightness, and the plateau class (-P) which maintains a similar magnitude for a period of time before declining. The lightcurves of type I SN are generally very similar.

Type Ia SN originate from an accreting white dwarf whose mass exceeds the Chan-

drasaker limit of $\sim$1.4 $M_\odot$. Above this mass the electron degeneracy pressure within the white dwarf can no longer support the star against the gravitational collapse. This triggers a runaway thermonuclear reaction and explosion, leading to the disruption of the white dwarf. They are therefore known as thermonuclear SN and are unrelated to massive stars. The remaining SN subtypes are referred to as core collapse supernovae (ccSN) and are caused by the depletion of fuel in the stellar core. In the final stages of a massive star's life, the stellar core is fusing silicon to form nickel, which decays to iron. Fusion of nickel and iron however is an endothermic process, requiring the input of energy, therefore upon exhaustion of silicon in the core, the star can no long sustain hydrostatic equilibrium and the core collapse begins. As material falls inwards, the density in the star rises and protons and electrons start to combine through inverse β-decay, forming neutrons and neutrinos. The core is transparent to neutrinos, which therefore escape carrying energy away. The collapse continues until the density is such that neutron degeneracy pressure halts and stabilises the core. The origin of the SN explosion remains unclear, however current theories suggest it could potentially be neutrino driven, (Janka, 2017).

As can be seen in the evolution sequences, shown in Section 1.5.1, the current consensus is that the WR phase of a star ends as a ccSN. The type of supernova depends on the helium abundance remaining within the star, which in turn depends on the WR subclass associated with the star prior to the collapse. WN stars have lost most, if not all, of their hydrogen envelopes, but the helium shell below remains, resulting in a type Ib or IIb supernova. On the other hand, due to further mass loss, WC stars are lacking in both hydrogen and helium, hence ending as a type Ic supernova. There is also evidence to suggest that a significant proportion of Ib/c SN cannot be accounted for by single stellar evolution. From a volume limited study of ccSN rates from the Lick Observatory Supernova Search (LOSS) survey, Smith et al. (2011) find that the minimum initial mass necessary to reproduce the observed Ib/c SN fraction is 22 $M_\odot$. Assuming the initial mass required to enter the WR phase to be 35 $M_\odot$, they conclude that approximately 50% of Ib/c SN originate from stars with lower initial masses than WR single star progenitors. To address this, they suggest that lower mass helium stars, stripped through RLOF within a binary, could account for the extension of Ib/c progenitors to lower initial masses, see Section 1.5.2.

There has also been evidence that WR stars are the progenitors of long duration Gamma-Ray Bursts (GRBs). Stars with an initial mass greater than approximately 35 $M_\odot$ are more likely to collapse directly to a black hole rather than explode as supernovae. Woosley (1993) proposed that these 'failed supernovae' could be the origin of extragalactic long GRBs, and this was expanded by MacFadyen & Woosley (1999), who introduced the

collapsar model, describing a rotating helium core rapidly collapsing to a black hole, producing the GRB. There have been observations which substantiate this link between SN and GRBs, the first recorded being GRB 980425, which was found to be coincident with SN 1998bw, a luminous broad lined type Ic SN (Galama et al., 1998). Another significant event was GRB 030329, the second closest GRB event after GRB 980425. Extensive multi-wavelength follow up campaigns revealed the association of another very luminous type Ic SN - SN 2003dh (Hjorth et al., 2003). A luminous Ic SN is associated with higher outflow masses, which in turn suggests a more massive progenitor core. These observations of GRBs accompanying exceptionally bright, hydrogen deficient SN is therefore good evidence GRBs are associated with WR star progenitors.

1.6 Properties of WR Stars

In general, WR stars are characteristically hot, bright, massive objects, however on closer inspection it has been noted that the properties of WR stars are highly dependent on their environment, or more specifically, the local metallicity.

Here we discuss the differences between WR stars in the Milky Way (MW), compared with those in the Large Magellanic Cloud (LMC), a nearby satellite galaxy, approximately 50 kpc away (Pietrzyński et al., 2013). Whilst the composition of young stellar populations in our Galaxy is considered solar due to the modest O/H gradient within the disk (Esteban et al., 2015), the present day metallicity of the LMC is much lower at $\sim$0.4 $Z_{\odot}$. This has significant consequence on a number of WR properties, including stellar winds, mass-loss rates, initial masses, lifetimes, luminosities and evolutionary routes.

1.6.1 Deriving Stellar Properties

The properties of WR stars are usually derived through spectroscopic modelling. Stellar atmosphere codes such as PoWR (Gräfener et al., 2002; Hamann & Gräfener, 2003; Sander et al., 2015) and CMFGEN (Hillier & Miller, 1998) permit grids of model spectra to be calculated, which can be compared to observed data to infer stellar properties such as temperatures, luminosities and mass-loss rates. These codes are tailored to hot, massive stars with strong winds. They assume non-LTE (local thermodynamic equilibrium) atmospheres, necessary when considering hot stars with strong radiation fields, spherical geometry, and include the effects of line blanketing.

Temperatures and wind properties are usually inferred from fitting pairs of emission lines from adjacent ionization stages, for example He I 5876 and He II 5412, or N III 4640

and N IV 4058, or N IV 4058 and N V 4603-20 lines.

Stellar temperatures of WR stars vary with spectral type, with the coolest being WNL stars at ∼30000 K (Crowther et al., 1995), and the hottest corresponding to WO stars at over 100000 K (Tramper et al., 2013). Typical mass-loss rates for Galactic WR stars range from $10^{-4.7}$ to $10^{-5.3}$ $M_\odot$ yr^{-1}, however those of LMC WR stars are somewhat lower (Hainich et al., 2014; Sander et al., 2019; Hamann et al., 2019). It should also be noted that the stellar winds are thought to contain inhomogeneities, or clumps, rather than being smooth, and the degree of clumpiness is quantified through the clumping factor. Mass-loss rates derived without considering wind clumping result in an over-estimation of the true mass-loss rate (Hillier, 1991). To derive individual stellar wind velocities requires tailored models, and typical values fall in the range of 500–3000 km s^{-1} for WN stars and 1000–4000 km s^{-1} for WC stars.

There are also alternative methods available to infer wind properties of OB and WR stars. At longer wavelengths stellar winds are identifiable through the presence of a free-free IR or radio excess, which in turn can be converted to a mass-loss rate when assuming a wind velocity (Panagia & Felli, 1975; Wright & Barlow, 1975). Wind velocities can also be measured from observations of UV P Cygni resonance lines, such as C IV 1550 (Prinja et al., 1990), or IR He I lines (Eenens & Williams, 1994).

A luminosity estimate is derived from a model spectral energy distribution (SED) which, after correcting for reddening, is matched to the observed flux. Integrating the SED and correcting for distance reveals the bolometric luminosity. Bolometric luminosities for classical WR stars in the MW cover the range $\log(L/L_\odot)$=4.9–6.0, and for main sequence WNh stars can achieve $\log(L/L_\odot)$=6.2–6.8 (Hamann et al., 2019).

Nugis & Lamers (2000) investigate the correlation between observed mass-loss rates and luminosities in order to derive an empirical relationship. Using a sample of 64 Galactic WR stars across all spectral types, they find the mass-loss rates are dependent on both luminosity and abundance. Hamann et al. (2006, 2019) investigate the apparently single Galactic WN population using the POWR code to derive updated stellar parameters. Figure 1.13 summarizes their mass-loss rate results and also includes the Nugis & Lamers (2000) empirical relation for reference. Whilst there is evidence for a positive trend between luminosity and mass-loss rate, there also appears to be significant scatter, perhaps suggesting the requirement of additional parameters to fully describe this dependence. Similarly, Sander et al. (2019) investigate the mass-loss rate and luminosity relation within the Galactic WC population. As shown in Figure 1.14, they find a tighter relation. They also plot the results from LMC WC stars from Crowther et al. (2002) in grey for comparison, which highlights

the weaker winds present in LMC WC stars in comparison to their Galactic counterparts. The WO stars are shown in yellow, and the winds of these stars are weaker still.

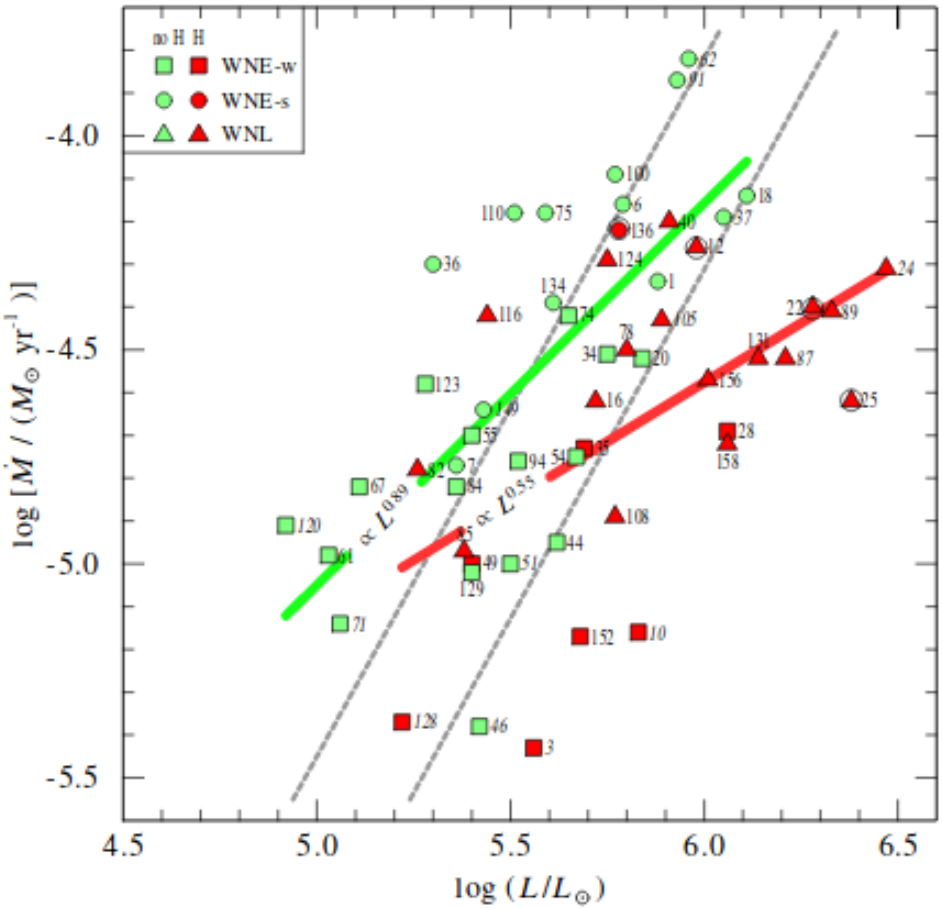

Figure 1.13: The relationship between luminosity and mass-loss rates for Galactic WN stars. Hydrogen-rich WN stars are shown in red and hydrogen-poor are shown in green, with solid lines indicating their respective regression fits. The dashed lines highlight the empirical mass-loss relation from Nugis & Lamers (2000) for hydrogen-free (left) and hydrogen-rich (right) WN stars. Taken from Hamann et al. (2019).

Deriving stellar masses of WR stars is often a difficult process, and direct measurements are rare, since reliable model-independent masses can only be obtained from either astrometric binaries, for nearby objects with a known distance, or spectroscopic binary systems in which the orbital inclination is known, i.e. from double-eclipsing binary systems or polarimetry.

In the absence of an observable companion, masses can be inferred from a theoretical mass-luminosity relationship. Using grids of stellar evolution models for various initial mass stars, theoretical predictions for the mass and luminosities of these stars as they reach

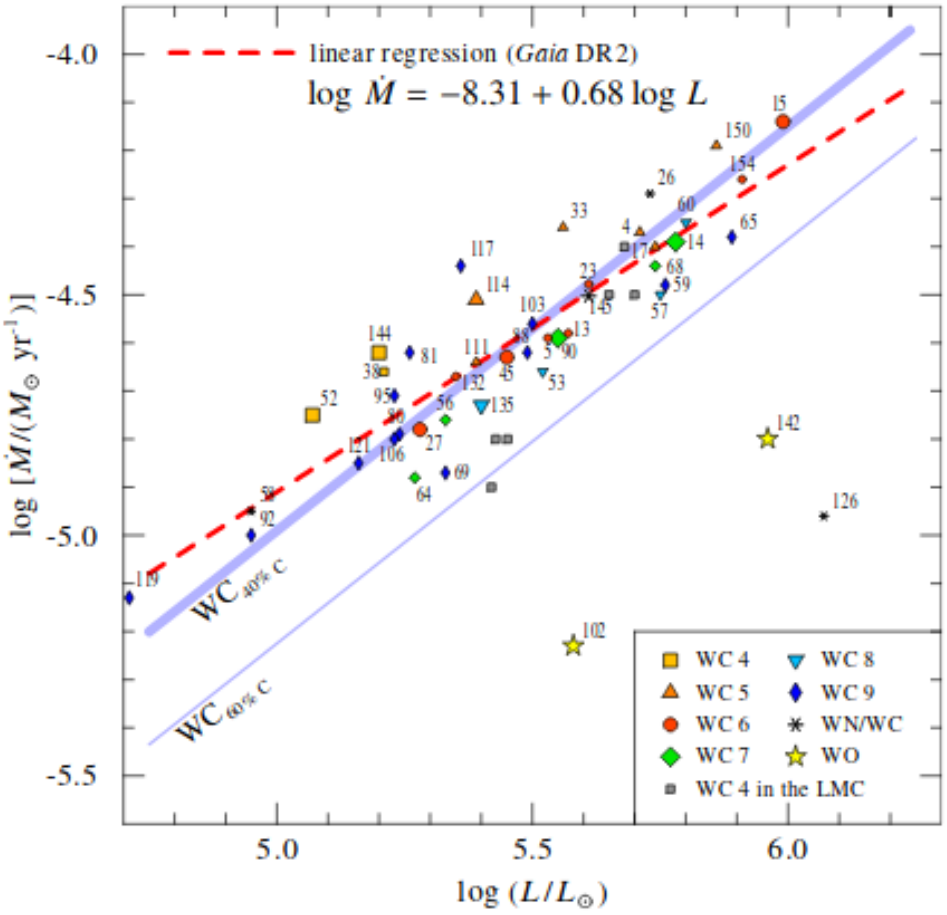

Figure 1.14: The relationship between luminosity and mass-loss rates for Galactic WC stars. Red dashed line shows the best fit to the data, and the grey thick and thin lines show the empirical mass-loss relation from Nugis & Lamers (2000) for 40% and 60% carbon abundances respectively. LMC WC stars from Crowther et al. (2002) are shown in grey. Taken from Sander et al. (2019).

the WR phase can be estimated and compared to one another, deriving the relationship (Langer, 1989; Schaerer & Maeder, 1992).

The difficulty is amplified when working in the high stellar mass range, since massive stars are inherently rare and therefore contribute very little to constraining the empirical M/L relationship. It has also been claimed that an upper stellar mass limit of ∼150 $M_\odot$ exists for the formation of single stars (Weidner & Kroupa, 2004; Figer, 2005; Oey & Clarke, 2005), however this argument is based on interpretation of observations rather than physical constraints restricting a maximum mass. Whilst higher mass stars may be possible, it has been suggested that these stars stem from mergers of lower mass stars rather than the formation of very massive stars (Banerjee et al., 2012).

Due to these complications, we often turn to spectroscopic and evolutionary modelling (e.g. Yusof et al. 2013; Köhler et al. 2015) to determine stellar masses. In the high mass regime however, we must continue to test these theoretical results against directly measured masses to avoid ambiguous and controversial results (Crowther et al., 2010; Schneider et al., 2018).

An example of a well studied classical WR star is γ Velorum, a WC8 + O7.5 spectroscopic binary located in the Galaxy. Orbital monitoring reveals a 78.53 day orbit and mass ratio of 0.31, leading to masses of 9 $M_\odot$ and 29 $M_\odot$ for the WR star and O star respectively (Schmutz et al., 1997). Using the theoretical M/L relation from Schaerer & Maeder (1992), the WR mass suggests a bolometric luminosity of 1.5×10^5 $L_\odot$, which is similar to the luminosity of 10^5 $L_\odot$ found by De Marco et al. (2000) when fitting the optical spectra of the WR component using CMFGEN models.

We also note the distance to γ Vel, adopted as 258 $\pm$ 41 pc by De Marco et al. (2000), may require updating as recent estimates suggest a distance of 336 $\pm$ 8 pc (North et al., 2007). This alteration will impact parameters dependent on distance, such as luminosity and mass-loss rates.

For main sequence WR stars, the double-lined eclipsing binary NGC3603-A1 located in the Galactic cluster NGC 3603 is the most extreme case to have had a direct mass estimation. This system comprises two WN6ha stars orbiting with a 3.772 day period (Moffat & Niemela, 1984), and radial-velocity monitoring from Schnurr et al. (2008) found direct mass estimates of M_A=116 $\pm$ 31 $M_\odot$ and M_B=89 $\pm$ 16 $M_\odot$ for the primary and secondary, respectively. Crowther et al. (2010) use predictions from the Geneva evolutionary code to infer masses. Assuming no rotation and a solar metallicity they find current masses of 120^{+26}_{-17} $M_\odot$ for the primary and 92^{+16}_{-15} $M_\odot$ for the secondary, which are in good agreement with the direct mass estimates.

1.6.2 Milky Way Environment

With a metallicity of Z=0.013 (1 $Z_\odot$) (Asplund et al., 2009), the Solar neighbourhood is considered a metal rich environment. It is host to 662 known WR stars (correct as of July 2019[1]), and the properties of these WR stars are heavily influenced by the MW abundances.

[1]Taken from the Galactic WR Catalogue http://pacrowther.staff.shef.ac.uk/WRcat/index.php

Stellar Winds & Mass-loss Rates

Perhaps the most critical relationship for evolutionary predictions is the dependence of mass-loss rates on metallicity. The stellar winds of massive stars are driven by radiation pressure on highly ionized atoms. Hot stars emit most of their emission in the UV, which is also the region where C, N, O and Fe ions have their strongest spectral lines. These ions are, therefore, accelerated via the repeated absorption/scattering of these continuum UV photons (Lamers & Cassinelli, 1999). Massive stars in a higher metallicity environment are capable of generating stronger, denser stellar winds due to the higher metal content. This directly impacts the mass-loss rates.

Mokiem et al. (2007) derive an empirical relationship between mass-loss rates and metallicity for OB stars in the MW and Magellanic Clouds and, assuming a smooth wind, they find the relationship shown in Equation (1.2). Vink & de Koter (2005) model the metallicity dependence of WR winds and find that WN stars follow a similar trend to OB stars, however the mass-loss to metallicity relationship for WC stars is predicted to be shallower, as shown in Figure 1.15.

$$\dot{M} \propto Z^{0.83\pm0.16} \tag{1.2}$$

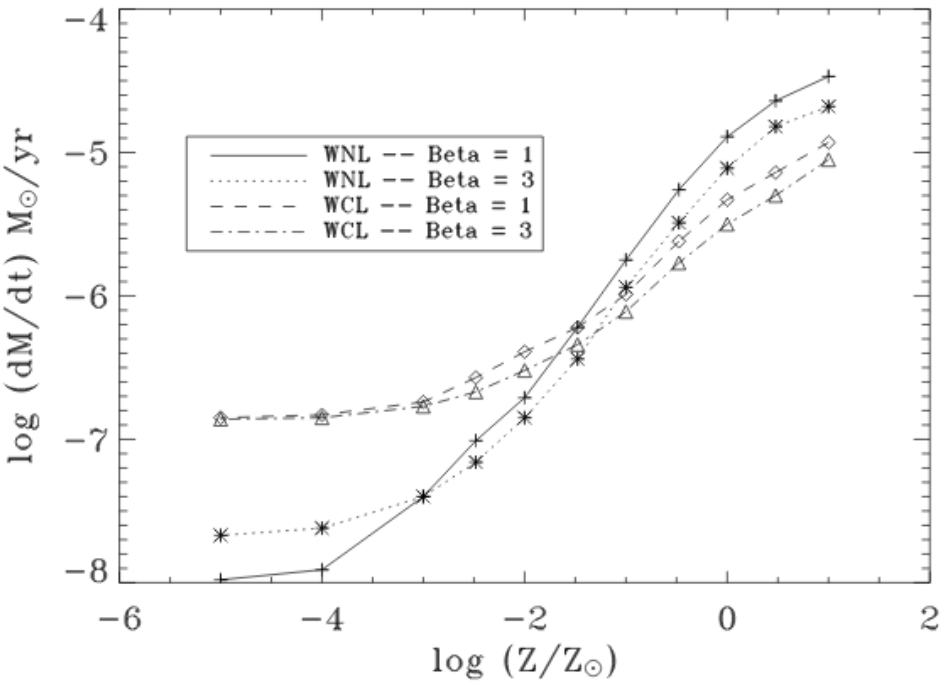

Figure 1.15: Predicted mass-loss to metallicity dependence for WNL and WCL stars, for varying values of β, taken from Vink & de Koter (2005).

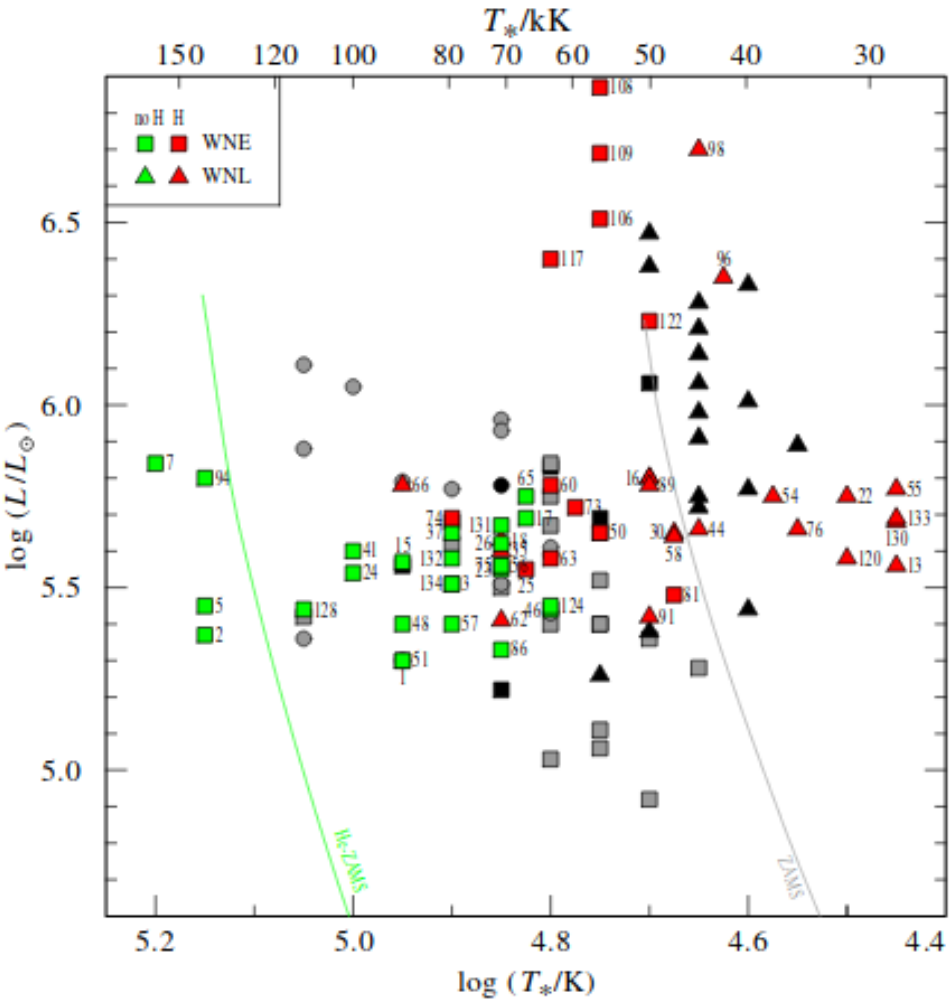

Figure 1.16: HR diagram showing the positions of the LMC WN stars, green for hydrogen free and red for with hydrogen, where the square symbols are WNE stars and the triangles are WNL. For comparison the MW WN stars, grey for hydrogen free and black for with hydrogen, are also plotted. Here the square symbols are weak-lined WNE stars, the circle symbols are strong-lined WNE stars, and the triangle symbols are WNL stars. Taken from Hamann et al. (2019).

Initial Mass & Luminosity

The bolometric luminosity of WR stars is directly connected to stellar mass, however there is also a metallicity dependence, as demonstrated in Figure 1.16. This shows the position of both MW (grey/black) and LMC (red/green) WN stars on a Hertzsprung-Russell (HR) diagram (taken from Hamann et al. (2019)). The black (MW) and red (LMC) points represent hydrogen rich WN stars, and we can see these are distributed at higher temperatures and luminosities than their hydrogen poor counterparts.

The interesting feature of this comparison is the group of MW WNE stars (grey squares) located at low luminosities, and the absence of equivalent LMC stars. This is a consequence of the metallicity effect on WR star evolution. At solar metallicity, a single star may become a WR star if it has sufficient mass to drive the strong stellar winds necessary to strip the outer envelopes of the star. The same mass star at lower metallicity however will have a weaker wind, due to insufficient metals available to drive the wind, so will be incapable of achieving the mass-loss rates required to progress to the WR stage, see Equation (1.2). The lack of low luminosity LMC WR stars is therefore real, and represents how the lower mass limit needed to become a WR star varies with metallicity (Maeder, 1991; Meynet & Maeder, 2005), at least for single stars.

WR Lifetime

Meynet & Maeder (2005) demonstrate the effect of metallicity on WR lifetime for single stars. Using evolutionary models they show that single WR stars located in low metallicity environments spend less time in the WR phase than an equivalent initial mass WR star in a metal-rich location. Their results are shown in Figure 1.17. They link these findings to the mass-loss dependence on metallicity, and argue that since metal poor stars suffer lower mass-loss rates, they take longer to reach the WR phase and therefore have reduced WR phase lifetimes in comparison to their metal-rich counterparts.

1.6.3 Low Metallicity Environment

The LMC is considered a metal poor galaxy (Z=0.006, or 0.4 $Z_{\odot}$) and therefore with its known distance and relatively complete WR sample, it is a useful analogue to study the effects of low metallicity on massive star evolution.

Formation channel

The formation of WR stars is discussed in detail in Section 1.5, however it is important to highlight the role metallicity has to play. There are two potential formation routes an O star can follow to reach the WR phase; the single star route and the binary star route. For an O star to become a WR star following the single star channel it must be of sufficient initial mass such that it is capable of driving the stellar wind, necessary to strip the outer envelope. Formation through the binary channel however, can lower the initial mass required for a star to reach the WR phase, and this becomes particularly relevant in metal-poor environments.

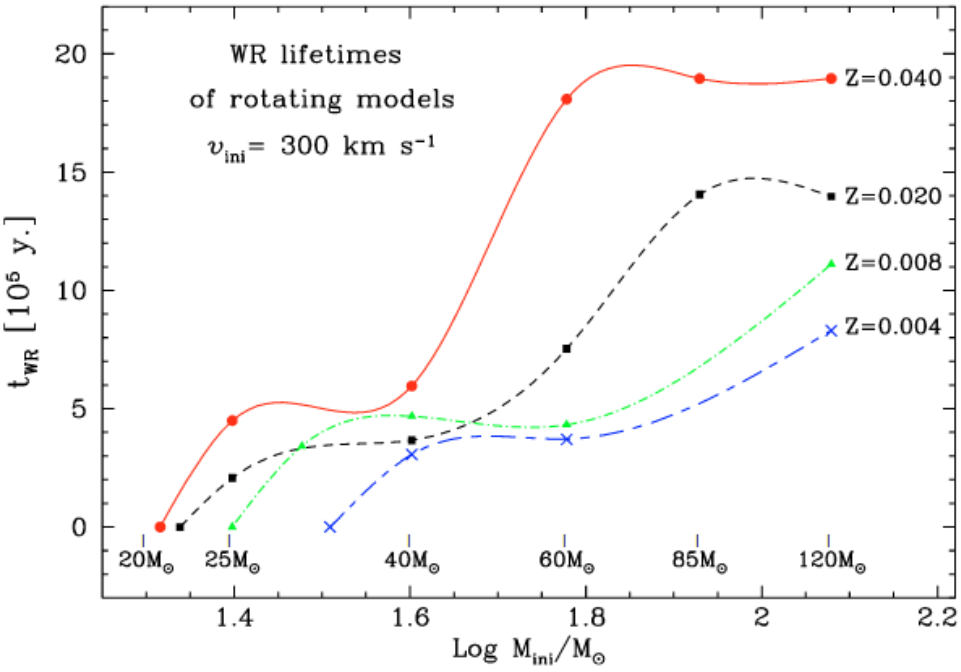

Figure 1.17: The relationship between WR lifetime and initial mass for various metallicity environments, as indicated on the plot. Taken from Meynet & Maeder (2005).

At low metallicities, the winds of massive stars are weaker when compared to their metal-rich counterparts (Mokiem et al., 2007). To compensate for this weaker wind, the initial mass required to reach the WR phase is greater in metal-poor locations (Maeder, 1991). Using the binary route however, a lower initial mass star is capable of reaching the WR phase through mass-stripping.

If we consider a massive star, with an initial mass such that it would be incapable of reaching the WR phase through single star evolution, and place the star in a close binary, we can alter its evolutionary path. As the star evolves off the main sequence and expands, it will fill its Roche lobe and begin transfer of mass on to the secondary through RLOF (discussed in Section 1.5.2, see Figure 1.12). The companion star will strip the hydrogen envelope from the primary, which it would otherwise have been unable to remove through stellar winds alone, and eventually only the helium-rich core will remain, creating a WR, or helium, star.

Since the binary channel provides a route for lower mass stars to reach the WR phase, it is thought that this mechanism would be the dominant formation route in metal-poor environments. Foellmi et al. (2003b,a) investigated the binary WR population in the LMC and SMC respectively. From theory they anticipate WR binary fractions of ∼40% (LMC) and ∼100% (SMC), however observationally they detected much lower binary fractions of

∼30% and ∼40%.

WC/WN Ratio

Another property dependent on the metallicity of the environment is the ratio of WC to WN subtypes. From the Conti scenario, discussed in Section 1.5.1, we expect that only the most massive initial mass stars are capable to generating enough mass-loss to reach the WC phase. Also, as described in Section 1.6.2, as we go to lower metallicities, the mass-loss rates for a comparable mass star decrease. This means that to achieve the same mass-loss necessary to progress to the WC phase in a low metallicity environment requires a higher initial mass star. Observing the WC/WN ratio can therefore give some insight into the local metallicity of these stars.

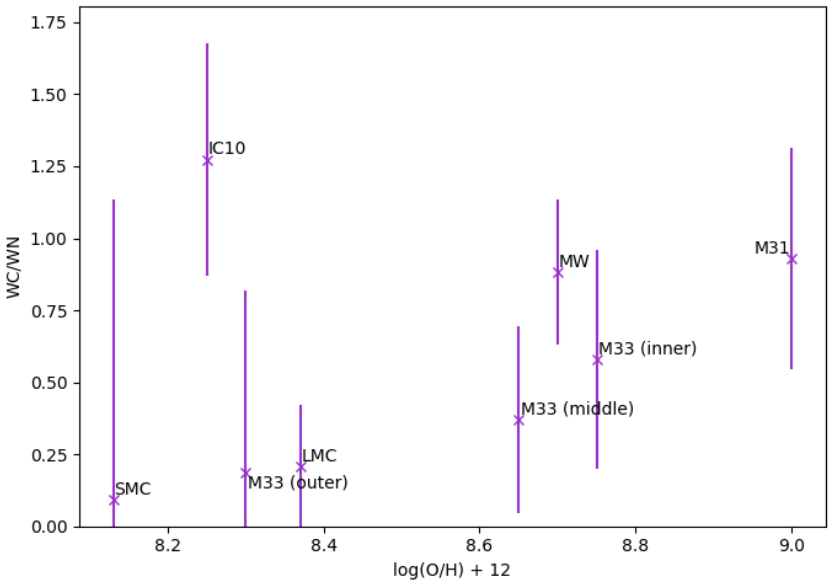

Figure 1.18: The observed WC/WN ratio and metallicity relationship for Local Group galaxies. LMC data from Neugent et al. (2018), SMC data from Massey et al. (2014), IC10 data taken from Crowther et al. (2003), and all other data are from Massey & Johnson (1998).

Figure 1.18 gives an overview of the WC/WN ratio against metallicity relationship observed in regions of the Local Group. As expected, we see an upwards trend, with metal-rich locations generally hosting a higher proportion of WC stars. There are however some outliers, such as IC10, which despite its low metallicity has an anomalously high WC/WN ratio of 1.3. This galaxy and its properties, including its peculiar WC/WN ratio are discussed further in Chapter 2.

1.7 This Thesis

Some of the key questions outlined in this chapter involve metal-poor WR stars. We therefore aim to expand upon our knowledge and investigate metal poor WR populations further.

Our first aim is to study the binary frequency of WR stars in metal poor environments. The single and binary WR formation channels have been discussed in Sections 1.5.1 to 1.5.2, where it was noted that the binary formation channel is anticipated to play a more dominant role at lower metallicities due to the weaker stellar winds. To assess this we compute binary fractions in two low metallicity regions.

In Chapter 2 we focus on the Local Group dwarf galaxy IC10. Currently undergoing star-formation, the WR content of IC10 is relatively high in comparison to other metal poor dwarf galaxies, making it a clear choice to study. We perform a thorough search for new WR stars using optical photometry and follow-up spectroscopy, before highlighting likely binary systems to compute a binary fraction estimate. Whilst examining the WR content of IC10 we also probe the unusual WC/WN ratio shown in Figure 1.18 to determine if this is real or a result of an incomplete sample.

We also investigate a complementary approach to identifying binaries, focussed on X-ray characteristics. In Chapter 3 we introduce a 2 Ms X-ray monitoring survey of the Tarantula nebula region (PI Townsley) and the methods by which we aim to characterise the binary nature of the 30 Dor WR stars. Following this, Chapter 4 discusses the implications of our findings in the context of current literature results and assesses the binary status of each WR star.

Another major issue is the lack of direct mass estimates for very massive stars at low metallicities. We aim to address this through our study of Mk34, outlined in Chapter 5, where we use a tailored optical monitoring programme designed to confirm the binary status of this star and reveal the component stellar masses.

Finally, a summary of these findings, and suggestions for future work, are discussed in Chapter 6.

Chapter 2

The Wolf-Rayet Population of IC10

Much of the work presented in this Chapter is taken from Tehrani et al. (2017), with additional details added with regards to the data reduction and nebular results.

2.1 Introduction to IC10

IC10 is a barred irregular galaxy in the Local Group, considered by some as a blue compact dwarf (Richer et al., 2001). Situated close in projection to the plane of the Milky Way (b=−3.3°), attempts to study this galaxy are hindered by a high Galactic foreground reddening of E(B-V) = 0.77 (Richer et al., 2001). Recent distance determinations range from 660 kpc (Gonçalves et al., 2012) to 817 kpc (Sanna et al., 2008), however for this chapter we adopt an IC10 distance of 740 ± 20 kpc[1]. McConnachie (2012) derived a stellar mass of 7.5 × 10^7 $M_\odot$ for IC10, an order of magnitude lower than the Small Magellanic Cloud (SMC). IC10 is gas rich with an atomic hydrogen content of 4.4 × 10^7 $M_\odot$, adjusted to our adopted distance. The galaxy is also metal-poor, with an oxygen abundance measurement of log(O/H) + 12 = 8.26 (Garnett, 1990). This metallicity is intermediate between those of the Magellanic Clouds, making them good comparative galaxies.

The recent star formation history of IC10 is very uncertain. Studies of the neutral hydrogen content by Wilcots & Miller (1998) revealed that the gas distribution has been shaped by stellar winds rather than supernovae explosions, suggesting the observed interstellar medium features are relatively young. From this it was suggested that the galaxy is currently undergoing a starburst episode which began approximately 10 million years ago. The current star formation rate was found to be 0.07 $M_\odot$ $yr^{-1}$by Gregory et al. (1996), which again is between those of the Magellanic Clouds (Kennicutt et al., 2008). The star formation intensity however, is much greater than both at 0.049 $M_\odot$ yr^{-1} kpc^{-2}(Crowther & Bibby, 2009), due to the small physical size of IC10.

Previous surveys of IC10 have been successful at finding WR stars within this galaxy, despite the high foreground extinction. Massey et al. (1992) first began the search after suspecting a large population of massive stars would be likely when considering the number of H II regions identified within the galaxy (Hodge & Lee, 1990). Further studies such as Massey & Armandroff (1995), Royer et al. (2001), Massey & Holmes (2002) and Crowther et al. (2003) led to the confirmation of 26 WR stars, hereafter referred to as M#, and R# depending on which collaboration initially identified the candidate. The discovery of these WR stars was curious. Not only does IC10 now have the highest surface density of WR

[1]Taken from an average of four different methods; RR Lyrae 820 ± 80 kpc (Sanna et al., 2008), PNLF 660 ± 25 kpc (Gonçalves et al., 2012), tip of the Red Giant Branch 740 ± 60 kpc and Cepheids 740 ± 60 kpc (Tully et al., 2013).

stars in the Local Group, the ratio of WC/WN spectral types does not agree with that expected from evolution models for a galaxy of such a low metallicity (see Section 1.6).

Work by Massey & Holmes (2002) derived the WC/WN ratio to be 2. More recent work by Crowther et al. (2003) updated this ratio to 1.3, as shown in Figure 1.18, which is still an order of magnitude higher than other metal poor star forming galaxies such as the LMC (0.2) and SMC (0.1) (Breysacher et al., 1999; Neugent et al., 2012a; Massey et al., 2014, 2015b; Foellmi et al., 2003a). It has been proposed that either a recent starburst has occurred, or there are further WN stars residing unnoticed within IC10 (Massey & Holmes, 2002). Therefore, to confidently verify the WR content of IC10 we must first be satisfied the search is complete, especially in the context of the recent discovery of unusually faint WN stars in the LMC (Massey et al., 2014; Neugent et al., 2017).

In this chapter we use deep narrow-band imaging to establish whether a hidden population of WR stars is a plausible explanation for the apparently abnormal WC/WN ratio. Since the metallicity of IC10 is intermediate between the LMC and SMC, we also look to compare the properties of WR stars found in each galaxy. Finally we aim to identify the fraction of IC10 WR stars residing in binary systems. The new photometric and spectroscopic data to achieve these aims are presented in Section 2.2. Section 2.3 focuses on the results from nebular emission including an update of the metallicity and star formation rate (SFR). Section 2.4 we present the stellar results from these observations, a discussion of these results in Section 2.5, and a brief summary in Section 2.6.

2.2 Observations

2.2.1 Imaging

We obtained deep imaging observations of IC10 on the 24 September 2009 using the GMOS instrument (Hook et al., 2004) on the 8m Gemini North telescope at Mauna Kea (ID GN-2009B-Q-9, PI Crowther), with clear/photometric conditions. Due to the emission line nature of WR stars, narrow-band filters are more suited to identify potential candidates, therefore four narrow-band filters and one broadband filter were selected, with details outlined in Table 2.1. Two of the narrow-band filters were centred on strong emission lines, and the remaining two were continuum filters, denoted by the suffix C. The He II 4686 emission line is particularly strong within all WR subtypes, therefore to identify He II excess candidates both continuum and emission-line imaging is necessary. The $330''$ × $330''$ field of view on GMOS-N is composed of three CCDs separated by a $2.8''$ gap. To compensate for this gap, IC10 was observed three times through each filter, with each

Table 2.1: Characteristics of the five filters used with GMOS and the imaging quality of IC10 observations.

Filter	λ_c [nm]	FWHM [nm]	T_{exp} [s]	FWHM ["]
He II	468	8	3 x 1750	0.59
He IIC	478	8	3 x 1750	0.56
Hα	656	7	3 x 60	0.53
HαC	662	6	3 x 60	0.52
g	475	154	3 x 30	0.59

subsequent image shifted by 5″. The resultant field of view can be seen in the colour composite image shown in Figure 2.1, where the positions of all confirmed WR stars have also been highlighted.

The reduction of these images was performed by Isabelle Archer. Bias subtraction and flat field procedures were performed, and images in the same filter were aligned and combined in IRAF by Isabelle Archer prior to obtaining the data. Using the DAOPHOT package (Stetson, 1987) we proceeded to identify the position of all sources which satisfied the defined detection limits, and extracted this list using aperture photometry and the PHOT command. We then selected bright, unsaturated, isolated stars to model the point spread function (PSF). ALLSTAR applies our model PSF by fitting it to the extracted sources. It can then derive relative magnitudes for each source.

To convert DAOPHOT narrow-band values to apparent magnitudes a zero point (ZP) correction was applied per filter, derived from observations of the standard star BD +28 4211 and using Equation (2.1), where $m_{\rm std}$ and $m_{\rm std}^{\rm DAO}$ are the apparent magnitude and DAOPHOT magnitude of BD +28 4211 respectively, $t_{\rm exp}$ is the exposure time, A_λ is an extinction coefficient, sec(Z) is the airmass and ZP is the zero point. Using Equation (2.2) we can apply the zero points derived for each filter to the remainder of the sources identified through DAOPHOT.

$$\mathrm{ZP} = m_{\rm std} - m_{\rm std}^{\rm DAO} - 2.5\log(t_{\rm exp}) + \mathrm{A}_\lambda \sec(Z) \tag{2.1}$$

$$m_* = m_*^{\rm DAO} + 2.5\log(t_{\rm exp}) - \mathrm{A}_\lambda \sec(Z) + \mathrm{ZP} \tag{2.2}$$

We also obtained broad g-band imaging which was reduced using a similar method, however standard star observations were unavailable. Instead, isolated sources were selected from within the GMOS field of view for which apparent magnitudes were obtained from PanSTARRS1 g-band observations (Chambers et al., 2016). These standard stars provided

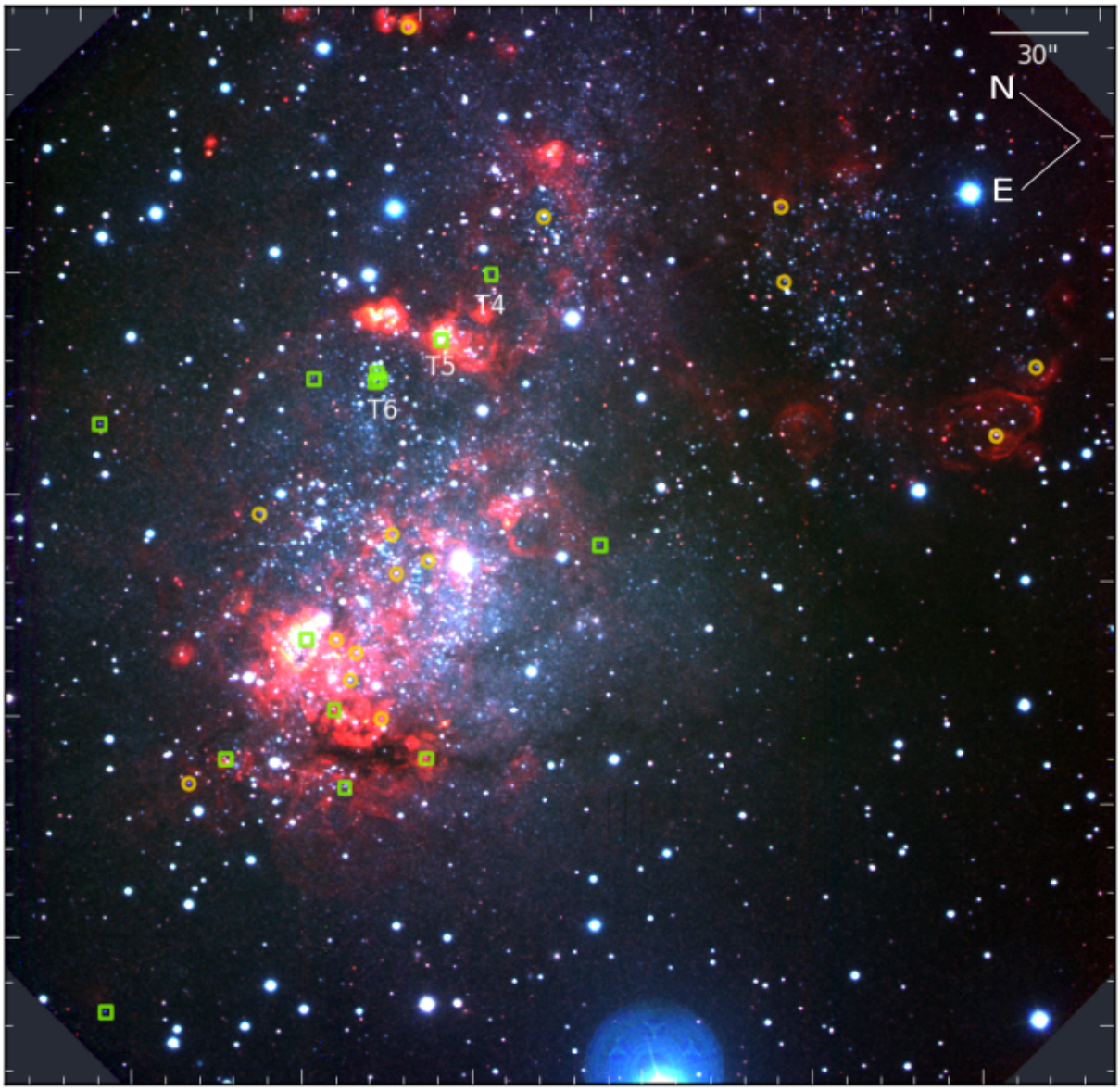

Figure 2.1: Gemini GMOS colour composite image of IC10 showing the relative positions of previously confirmed WN stars (green squares) and WC stars (yellow circles), with the 3 new WN stars labelled (T4–T6). Field of view shown in image is $300'' \times 314''$, corresponding to 1.1 × 1.1 kpc at a distance of 740 kpc. RGB image generated from red-Hα(λ656nm), green-g(λ475nm), and blue-He II(λ468nm) filter images.

an average g-band zero point correction for the remainder of the GMOS data.

New WR candidates were selected from a combination of image subtraction techniques, blinking of the He II and He IIC images, and quantitative relative magnitude comparisons to reveal an excess of He II 4686 emission. A visual inspection of all He II excess sources with a greater than 3 sigma detection was completed to remove spurious sources, and 11 new emission candidates were revealed with their photometric properties outlined in Table 2.2. We note that T8 appears extended with FWHM measurements of $0.64'' \times 0.98''$, compared to the average FWHM of $0.66'' \times 0.63''$ for point sources. We therefore advise that, although this source exhibits a He II excess, it is unlikely to be confirmed a WR star. Figure 2.2 shows the He II excesses as a function of continuum magnitude for the potential WR candidates, along with a comparison including all DAOPHOT sources.

Of the 37 previous WR candidate stars, 36 were located and identified within our field of view. The exception, M22, had previously been dismissed as a potential WR by Massey & Armandroff (1995), and of the 37 candidates, 26 have been confirmed as WR stars by Crowther et al. (2003). Spectral types and photometric results for confirmed WR stars are shown in Tables 2.3 to 2.4, where positions have been astrometrically corrected based on PanSTARRS data.

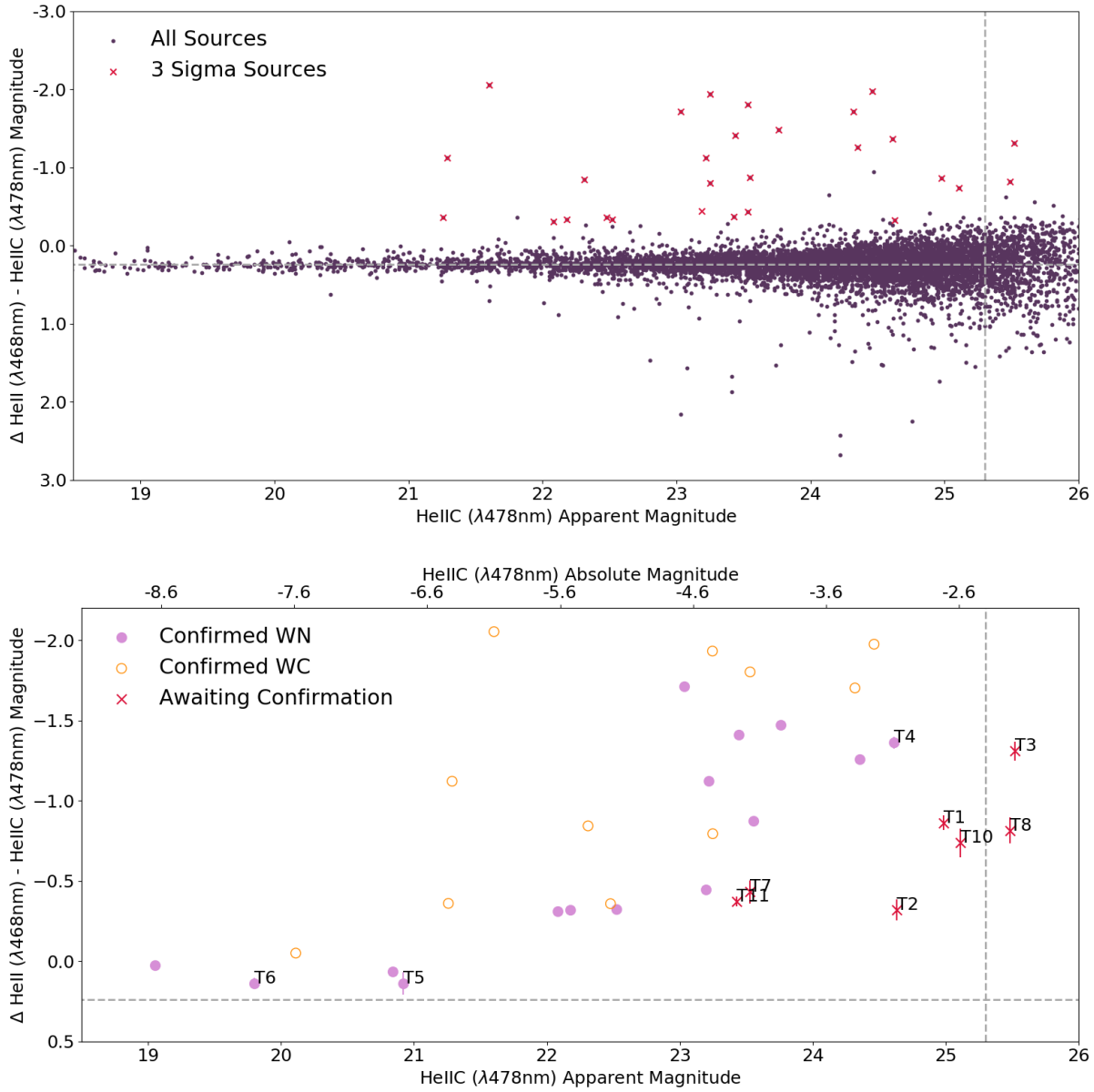

Figure 2.2: Upper panel shows the relationship between continuum magnitude and He II 4686 excess magnitude for all sources identified by DAOPHOT in IRAF. The He II emission zero-point lies at -0.24, as shown by the horizontal dashed line, due to the high extinction towards IC10. The vertical dashed line corresponds to the survey magnitude limit. The majority lie below the zero-excess line indicating no He II emission line excess, and a considerable proportion of the data points are also below the detection limits of this survey, therefore too faint to be considered robust. The red crosses correspond to sources which were found to have a He II detection greater than 3σ. The lower panel is restricted to confirmed WR candidates (WN - closed green circles, WC - open purple circles) and those awaiting confirmation (red crosses). Note that the majority of unconfirmed candidates are much fainter than others in the sample, and there are no candidates included which exceed our He IIC survey limit of 25.3 mag. Both apparent magnitude and absolute magnitudes axis are shown, with absolute magnitudes derived from A_{4780}=3.39 mag and a distance modulus of 24.3 mag.

Table 2.2: He II 4686 emission candidates identified from GMOS He II and He IIC filter images, using blinking and subtraction techniques to search for He II excesses. Candidates listed in increasing RA order.

ID	RA	Dec	He II	He IIC	Hα	HαC	g	Δ He II-He IIC	Status
	[J2000]		[mag]	[mag]	[mag]	[mag]	[mag]	[mag]	
T1	00:20:04.54	59:18:05.4	24.119 ± 0.030	24.983 ± 0.035	22.312 ± 0.060	23.621 ± 0.117	24.213 ± 0.091	-0.86 ± 0.05	
T2	00:20:05.60	59:19:45.7	24.312 ± 0.036	24.633 ± 0.053			24.476 ± 0.168	-0.32 ± 0.06	
T3	00:20:06.99	59:17:47.1	24.211 ± 0.028	25.521 ± 0.053	22.406 ± 0.055		24.489 ± 0.162	-1.31 ± 0.06	
T4	00:20:14.47	59:18:49.9	23.249 ± 0.016	24.612 ± 0.034	22.765 ± 0.123	23.377 ± 0.121	23.958 ± 0.093	-1.36 ± 0.04	WNE
T5	00:20:17.43	59:18:39.2	21.054 ± 0.044	20.918 ± 0.054		19.532 ± 0.069		0.14 ± 0.07	WNE
T6	00:20:20.34	59:18:37.3	19.939 ± 0.019	19.801 ± 0.027	18.125 ± 0.022	18.561 ± 0.018	19.222 ± 0.018	0.14 ± 0.03	WNE
T7	00:20:23.35	59:17:31.2	23.098 ± 0.027	23.530 ± 0.065		22.205 ± 0.064	22.231 ± 0.037	-0.43 ± 0.07	
T8	00:20:27.70	59:19:15.1	24.671 ± 0.056	25.487 ± 0.059				-0.82 ± 0.08	extended
T9	00:20:32.74	59:15:46.4	22.570 ± 0.011	22.537 ± 0.008	19.214 ± 0.011	19.931 ± 0.012	21.635 ± 0.011	0.03 ± 0.01	non WR
T10	00:20:32.98	59:18:24.1	24.373 ± 0.042	25.111 ± 0.077		23.467 ± 0.089		-0.74 ± 0.09	
T11	00:20:35.90	59:18:49.8	23.055 ± 0.019	23.428 ± 0.022	21.894 ± 0.060	22.888 ± 0.088		-0.37 ± 0.03	

Figure 2.3 shows the logarithmic number count distribution of He IIC magnitudes across all sources located by DAOPHOT within our field of view with a least squares polynomial fit applied to the region in which this relationship is linear. The point at which this relationship breaks down, and the slope turns over indicates the faintest magnitude we consider this survey to be complete to within a 3σ error, which for He IIC corresponds to an apparent magnitude of 25.3 mag. Using the same principle for the He II photometry results in a faint magnitude limit of 24.7 mag. From our compiled list of 11 WR candidates, two fall outside this completeness limit (T3 and T8).

The He IIC apparent magnitude was corrected for interstellar extinction using an average E(B-V) of 0.92, discussed in Section 2.4.3, so A_{4780}=3.4 mag when adopting A_{4780}/A_V=1.194 from the Galactic extinction law (Seaton, 1979). We adopt a distance modulus of 24.3 $\pm$ 0.07 mag, corresponding to a distance of 740 $\pm$ 20 kpc, and from that we reach an absolute magnitude survey limit of -2.4 mag for the He II continuum. For comparison, the faintest WR stars detected in the LMC have slightly higher absolute magnitudes of $M_V = -2.5$ mag (Massey et al., 2014, 2015b; Neugent et al., 2017).

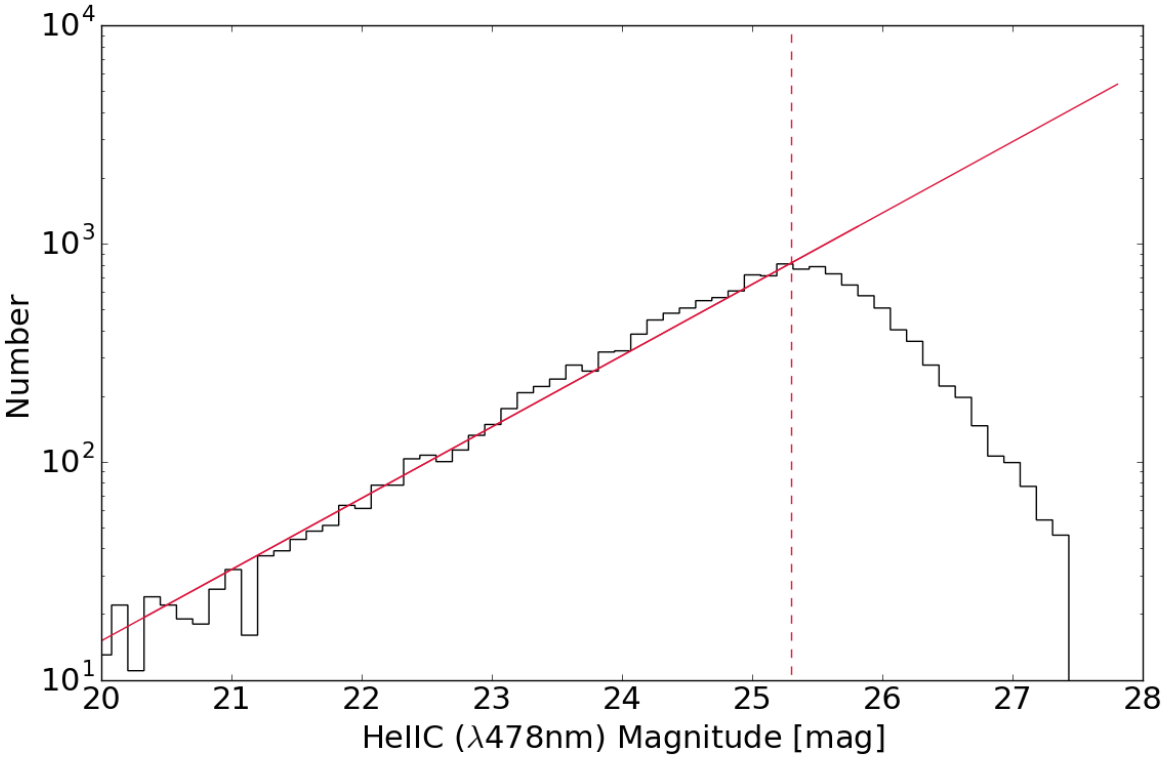

Figure 2.3: Logarithmic histogram showing the He IIC(λ478nm) magnitude for all sources within the field of view. The peak of the curve indicates this survey is complete to an apparent He IIC magnitude of 25.3, or absolute magnitude of -2.4 for an adopted E(B-V) = 0.917, A_{4780} = 1.194 A_V = 3.4, and distance modulus of 24.3 mag.

Table 2.3: Spectral types of all currently confirmed WR stars residing within IC10, listed in increasing RA order. HL# refers to the H II region each star is associated with, outlined in Hodge & Lee (1990). Old spectral types are taken from Massey & Armandroff (1995); Royer et al. (2001); Massey & Holmes (2002); Crowther et al. (2003). New spectral classes have been determined from GMOS spectroscopic data (discussed in Section 2.4.1).

ID	HL #	RA [J2000]	Dec	Old Spectral Type	ref	New Spectral Type
M1	2/3	00:19:56.96	59:17:07.6	WC4-5	c	WC4-5
M2	6	00:19:59.62	59:16:54.7	WC4	c	WC4
R6	10	00:20:02.99	59:18:26.9	WC4	c	WC4
R5		00:20:04.27	59:18:06.2	WC4-5	c	WC4-5
M4		00:20:11.55	59:18:57.6	WC4-5	c	WC4-5
M5	29	00:20:12.83	59:20:08.0	WNE/C4	c	WNE/C4
T4		00:20:14.47	59:18:49.9			WNE
R13		00:20:15.62	59:17:21.4	WN5	c	WN5
T5	45	00:20:17.43	59:18:39.2			WNE
R9	60	00:20:20.31	59:18:39.5	WNE	c	WNE
T6	60	00:20:20.34	59:18:37.3			WNE
R8	60	00:20:20.55	59:18:37.1	WN10	c	WN10
M7	66	00:20:21.95	59:17:41.0	WC4-5	c	WC4-5
M9		00:20:22.67	59:18:46.6	WN3	c	WN3
R11	(71)	00:20:22.74	59:17:53.2	WC4	c	WC4
M10		00:20:23.31	59:17:42.0	WC7	c	WC7
R12	97	00:20:25.65	59:16:48.1	WNE	c	WNE
M12	100	00:20:26.19	59:17:26.2	WC4	c	WC4
R10	106	00:20:26.51	59:17:04.9	WC4	c	WC4
M13	111	00:20:26.66	59:17:32.6	WC5-6	c	WC5-6
M14	(111)	00:20:26.90	59:17:19.7	WC5	c	WC5
M15		00:20:27.06	59:18:17.4	WC6-7	a	WC4
M24	111c	00:20:27.70	59:17:37.1	WN/OB	c	O2.5 If/WN6
R2	(106/115)	00:20:28.03	59:17:14.1	WN7-8	c	WN7-8
M17		00:20:29.09	59:16:51.7	WNE +BH	c	WNE +BH
M19		00:20:31.04	59:19:04.5	WN4	c	WN4
M23	139	00:20:32.76	59:17:16.2	WN7-8	b	WN7
M20		00:20:34.49	59:17:14.4	WC5	c	WC5
M21		00:20:41.62	59:16:24.4	WN4	c	WN4

Parentheses around HL regions indicate the WR star is in the close vicinity of, but not necessarily within, the H II region in question.
Note the minor revisions to the spectral type of M15 - updated from WC6-7 (Massey & Armandroff, 1995), M23 - updated from WN7-8, and M24 - updated from WN/OB (Massey & Holmes, 2002; Crowther et al., 2003).
References as follows: a: Massey & Armandroff (1995); b: Massey & Holmes (2002); c: Crowther et al. (2003);

Table 2.4: Photometric magnitudes taken from GMOS narrow-band filter images of all currently confirmed WR stars residing within IC10, listed in increasing RA order. Interstellar extinction magnitudes were derived using the method outlined in Section 2.4.3 using both photometric data shown here and spectral classifications. M_v absolute v-band magnitudes are derived from spectroscopically measured magnitudes and an adopted distance of 0.74 Mpc.

ID	He II [mag]	He IIC [mag]	Hα [mag]	HαC [mag]	g [mag]	E(B-V) [mag]	M_v [mag]
M1	21.624 ± 0.024		21.028 ± 0.047	21.597 ± 0.019	21.560 ± 0.037	*0.92 ± 0.26*	-5.62 ± 0.87
M2	21.235 ± 0.020		19.908 ± 0.053	20.764 ± 0.050		*0.92 ± 0.26*	-5.86 ± 0.87
R6	22.453 ± 0.014	23.248 ± 0.020	20.723 ± 0.033	21.690 ± 0.041	22.441 ± 0.022	1.28 ± 0.04	-5.75 ± 0.14
R5	22.120 ± 0.027	22.479 ± 0.026	20.951 ± 0.035	21.346 ± 0.036	21.822 ± 0.024	0.94 ± 0.04	-5.36 ± 0.14
M4	20.060 ± 0.007	20.111 ± 0.005	18.718 ± 0.007	19.169 ± 0.011	19.510 ± 0.006	0.91 ± 0.01	-7.67 ± 0.07
M5	21.323 ± 0.008	23.035 ± 0.008	19.665 ± 0.062	21.783 ± 0.032	21.804 ± 0.027	1.04 ± 0.03	-4.86 ± 0.11
T4	23.249 ± 0.016	24.612 ± 0.034	22.765 ± 0.123	23.377 ± 0.121	23.958 ± 0.093	1.03 ± 0.10	-3.48 ± 0.35
R13	23.092 ± 0.018	24.351 ± 0.025	22.238 ± 0.063	23.306 ± 0.136	23.662 ± 0.061	0.81 ± 0.11	-3.04 ± 0.38
T5	21.054 ± 0.044	20.918 ± 0.054		19.532 ± 0.069		1.27 ± 0.07	-8.41 ± 0.25
R9	21.854 ± 0.020	22.176 ± 0.011	20.572 ± 0.022	21.225 ± 0.022	21.412 ± 0.024	0.80 ± 0.02	-4.94 ± 0.09
T6	19.939 ± 0.019	19.801 ± 0.027	18.125 ± 0.022	18.561 ± 0.018	19.222 ± 0.018	1.15 ± 0.03	-9.15 ± 0.11
R8	20.903 ± 0.010	20.839 ± 0.015	18.308 ± 0.012	19.714 ± 0.020	20.191 ± 0.009	0.80 ± 0.02	-6.37 ± 0.09
M7	20.033 ± 0.017			20.887 ± 0.049		*0.92 ± 0.26*	-6.80 ± 0.87
M9	22.284 ± 0.007	23.758 ± 0.013	21.622 ± 0.026	22.822 ± 0.065	22.969 ± 0.030	0.79 ± 0.05	-3.24 ± 0.19
R11	22.615 ± 0.012	24.318 ± 0.030			23.385 ± 0.064	*0.92 ± 0.26*	-2.71 ± 0.87
M10	19.548 ± 0.010	21.602 ± 0.011	19.261 ± 0.013	20.012 ± 0.017	20.481 ± 0.007	1.26 ± 0.02	-7.03 ± 0.09
R12	22.677 ± 0.016	23.552 ± 0.017	20.251 ± 0.041	21.920 ± 0.041	22.587 ± 0.025	1.34 ± 0.04	-5.44 ± 0.14
M12	21.466 ± 0.014	22.310 ± 0.010	19.858 ± 0.052	20.302 ± 0.039	21.256 ± 0.028	1.63 ± 0.03	-8.09 ± 0.13
R10	22.486 ± 0.014	24.462 ± 0.027	19.115 ± 0.081		22.726 ± 0.049	*0.92 ± 0.26*	-2.31 ± 0.87

ID	He II [mag]	He IIC [mag]	Hα [mag]	HαC [mag]	g [mag]	E(B-V) [mag]	M_v [mag]
M13	20.898 ± 0.012	21.259 ± 0.009	19.903 ± 0.036	20.577 ± 0.020	20.713 ± 0.014	0.59 ± 0.02	-5.22 ± 0.09
M14	20.165 ± 0.007	21.287 ± 0.006	20.266 ± 0.059	20.117 ± 0.025	20.569 ± 0.008	0.97 ± 0.02	-6.59 ± 0.09
M15	21.726 ± 0.006	23.529 ± 0.031	21.672 ± 0.044	22.923 ± 0.079	22.477 ± 0.021	0.53 ± 0.07	-3.04 ± 0.24
M24	19.077 ± 0.019	19.052 ± 0.020	18.240 ± 0.039	18.438 ± 0.022	18.486 ± 0.014	0.65 ± 0.02	-8.36 ± 0.10
R2	21.770 ± 0.013	22.083 ± 0.012	19.834 ± 0.013	20.867 ± 0.013	21.477 ± 0.016	0.97 ± 0.01	-5.98 ± 0.08
M17	22.747 ± 0.012	23.194 ± 0.011	22.164 ± 0.098	22.119 ± 0.034	22.590 ± 0.031	0.90 ± 0.03	-5.66 ± 0.12
M19	22.095 ± 0.007	23.220 ± 0.011	21.288 ± 0.025	22.616 ± 0.055	22.467 ± 0.018	0.53 ± 0.05	-3.28 ± 0.17
M23	22.195 ± 0.009	22.521 ± 0.014	19.432 ± 0.022	20.164 ± 0.010	21.660 ± 0.013	*0.92 ± 0.26*	-5.41 ± 0.87
M20	21.313 ± 0.005	23.246 ± 0.014	21.153 ± 0.031	22.186 ± 0.042	22.223 ± 0.013	0.88 ± 0.04	-4.62 ± 0.14
M21	22.031 ± 0.007	23.445 ± 0.017	21.262 ± 0.021	22.424 ± 0.033	22.666 ± 0.023	0.86 ± 0.03	-4.21 ± 0.12

Italics denote a WR star with an E(B-V) value derived from an average, rather than individually calculated (see Section 2.4.3).

Table 2.5: Properties of the IC10 masks used with GMOS instrument for multi-object spectroscopy, where mask 1 and 2 correspond to the most recent data set and mask 3 and 4 are from Crowther et al. (2003). For all cases the slit length was set at 5″.

Mask	Slit Width ["]	Observation Date	FWHM ["]
1	0.75	10 Sept 2010	0.5
2	0.75	10 Sept 2010 - 11 Sept 2010	0.6
3	0.8	22 Dec 2001 - 16 Jan 2002	0.7
4	0.8	22 Dec 2001 - 15 Jan 2002	0.8

2.2.2 Spectroscopy

We obtained follow-up multi-object spectroscopic observations, which took place on 10-11 September 2010, again using GMOS on Gemini-North with the program ID GN-2010B-Q-44 (PI Crowther). Two masks were constructed, (mask 1 and 2), each containing 20 targets, with their properties detailed in Table 2.5. Of the 9 potential candidates identified in Table 2.2, four were included (T4,T5,T6 and T9) across the two masks.

Four exposures per mask were obtained, each for a duration of 2600s. The slit width was fixed at 0.75″ and the B600 grating was used in all cases, and the spectral resolution of the data was found to be 3.4 Å from arc lines. To compensate for the gaps present in the GMOS detector, the central wavelength was shifted by 20nm from 510nm to 530nm for one pair of exposures for each mask. Signal to noise was improved by merging the four exposures per target, and targets common to both masks were also combined.

GMOS spectra were reduced in IRAF using the Gemini package and GMOS sub-package. The science files were bias subtracted and flat-field corrected before being cut into individual spectra using GSREDUCE. Each spectrum was then extracted using the APALL function in IRAF. Figure 2.4 shows an example 2D GMOS spectrum for the WR source M14, where the star can clearly be seen in the centre of the image. To extract the spectrum, for each source we define a single aperture and background region. Working interactively within the program allows us to resize the position and width of the aperture and sky/background as shown in Figure 2.5. Once satisfied, the program will then trace the apertures along the full spectrum, and a trace function is defined by applying a polynomial fit to the data.

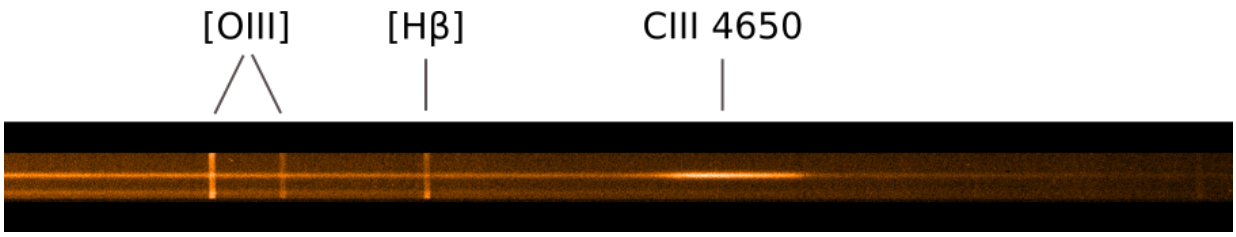

Figure 2.4: The 2D GMOS spectrum of M14 (WC5), prior to extraction using APALL. Spectral coverage shown ranges from ∼5200–4300 Å, with wavelength decreasing towards the right.

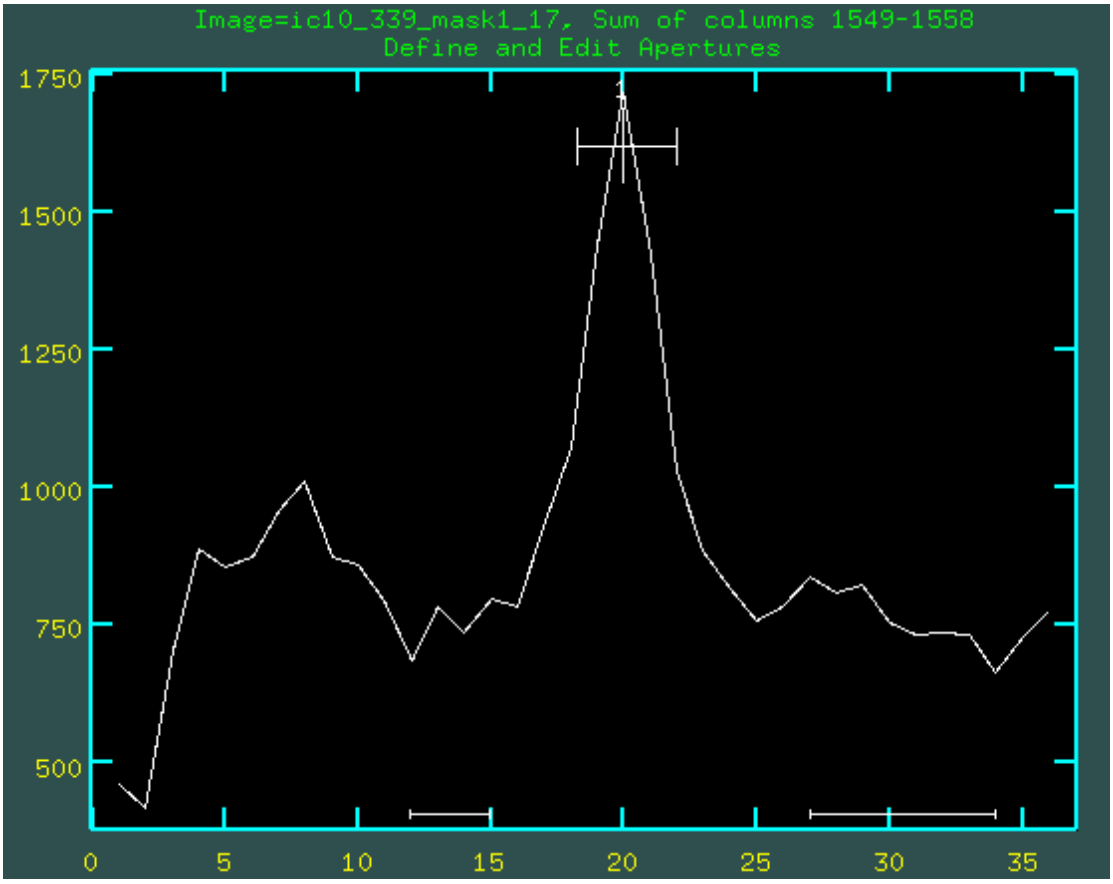

Figure 2.5: Defining the aperture and background regions interactively within APALL for M14. Aperture can be seen positioned across the peak and background regions are indicated by the white bars located at the bottom of the plot.

The wavelength calibration was completed using an internal CuAr arc lamp. Arc lamp spectra are obtained prior to the science observations, whilst using the same instrumental configuration. The spectrum comprises narrow emission lines with well known wavelengths which, once identified, can then be used to calibrate the science spectra by generating a pixel to wavelength conversion. To achieve this we use the IDENTIFY package within IRAF

to determine a number of observed emission lines in the arc spectra, and then use the REFSPEC and DISPCOR packages to apply the wavelength calibration.

For the flux calibration, the white dwarf standard star G191B2B was observed through the same B600 grating with a slit width of 0.75″. Total integration time was 3 × 30s with a shift in central wavelength between exposures from 410nm, 510nm, and 610nm to ensure the generated response function covered the necessary wavelength range. This standard star also has a published flux calibrated spectrum available at www.eso.org/sci/observing/tools/standards/spectra/g191b2b. For each of the 3 spectra, we divided the calibrated spectrum by the observed spectrum, corrected for exposure time, and fit a polynomial to the result to generate a response function. The 3 response functions were combined to create one final response function. To convert our science spectra from counts to flux units we first divided each science spectrum by exposure time and then multiplied by the response function.

Slit loss corrections were also applied to each mask. For each source we derived the photometric magnitude and spectroscopic magnitude in each of the four filters. We then calculated the difference and combined the data to derive a weighted average Δmagnitude for each mask.

$$\frac{F_{phot}}{F_{spec}} = 2.512^{\,m_{spec}-m_{phot}} \tag{2.3}$$

Using Equation (2.3) we can determine the flux factor (F_{phot}/F_{spec}). To obtain photometrically calibrated fluxes we therefore multiplied the spectroscopic flux by the flux factor.

This dataset was combined with previous GMOS observations, GN-2001B-Q-20 (mask 3) and GN-2001B-Q-23 (mask 4), which were obtained between 21 December 2001 and 16 January 2002 (Crowther et al., 2003) (see Table 2.5). Those WR observed in multiple masks underwent further merging to produce a single spectrum for each candidate.

2.3 Nebular Results

Although classical WR stars involve the late stages of massive star evolution, they are still relatively young in comparison to the general population of stars and therefore frequently reside within gas-rich star-forming regions. In these cases, when performing spectroscopy on these stars it is not unusual to note nebular emission from the surrounding HII region, which in turn can allow us to deduce properties of the local environment, such as temperatures, densities and chemical composition.

There are two types of emission lines present in a nebular spectrum, permitted lines and forbidden lines, and their differences originate from the process by which their ions interacted. The gaseous nebula is heated through absorption of the UV radiation from the central massive star(s). The UV radiation ionizes the gas, creating free electrons, which are free to interact with the surrounding ions. Some ions will capture the free electrons, which will subsequently de-excite to a lower energy state, emitting a photon. This process generates permitted emission lines of hydrogen. Forbidden emission lines are generated when a free electron collisionally excites a bound electron from a heavy ion, which in turn de-excites through the emission of a photon. It is these collisionally excited ions that are the primary source of cooling in a nebula.

To obtain a metallicity measurement there are two main approaches; the direct method, and the strong line method.

The direct method exploits the relationship between the energy level structure of [O III] and electron temperature, since a lower electron temperature arises from higher cooling, which in turn is governed by a higher metal abundance in the [H II] region. Temperatures are found using the [O III] 4363, 4959, and 5007 emission lines. Although these lines all occupy a similar wavelength region, they originate from different energy level transitions, such that [O III] 4363 emission arises from the excited ^{1}S–^{1}D transition, whereas the [O III] 4959 and 5007 emission comes from the lower energy level ^{1}D–^{3}P transition, as shown in Figure 2.6. At higher temperatures a larger proportion of electrons will be excited to the ^{1}S energy level with respect to the ^{1}D energy level, i.e. as temperature increases, ^{1}S/^{1}D increases. We would therefore expect to see a relatively stronger [O III] 4363 emission compared to the [O III] 4959 and 5007 emission lines, such that for a line ratio of (5007+4959)/4363=1000, the derived temperature is approximately 7000 K, however with a factor of 10 increase in the [O III] 4363 line strength the approximate temperature is 12500 K (Osterbrock & Ferland, 2006).

Calculating the density requires a measurement of the [S II] 6716 and 6731 emission lines. Unlike the temperature diagnostic lines which involve a large separation in energy, the density diagnostic lines should be of similar excitation energies and therefore relatively temperature independent. Instead, to investigate density we need to investigate whether radiative (low density) or collisional (high density) de-excitation dominates. Again we measure the relative proportion of electrons in each state and use the intensity ratio and density relationship plotted in Figure 2.7 to estimate the density of the region.

Once temperatures and densities are known we can then estimate emissivity, ϵ, and use Equations (2.4) to (2.6) to find an oxygen abundance via the direct method. Abundances,

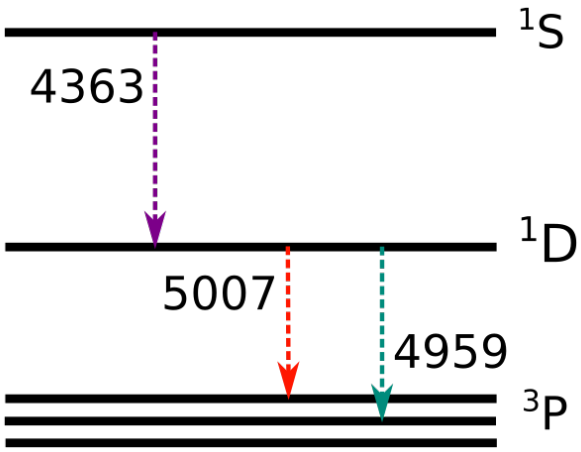

Figure 2.6: Energy level diagram for the [O III] transitions used to measure nebula temperature. Adapted from Osterbrock (1989)

however, can still be derived in the absence of density measurements, as emissivity is relatively insensitive to density.

$$\frac{\mathrm{I[O\,III]5007}}{\mathrm{I(H}\beta)} = \frac{\mathrm{N(O^{2+})}}{\mathrm{N(H)}} \times \frac{\epsilon\mathrm{[O\,III]5007}}{\epsilon(\mathrm{H}\beta)} \tag{2.4}$$

$$\frac{\mathrm{I[O\,II]3727}}{\mathrm{I(H}\beta)} = \frac{\mathrm{N(O^{+})}}{\mathrm{N(H)}} \times \frac{\epsilon\mathrm{[O\,II]3727}}{\epsilon(\mathrm{H}\beta)} \tag{2.5}$$

$$\frac{\mathrm{N(O)}}{\mathrm{N(H)}} = \frac{\mathrm{N(O^{2+})}}{\mathrm{N(H)}} + \frac{\mathrm{N(O^{+})}}{\mathrm{N(H)}} \tag{2.6}$$

In the absence of a robust [O III] 4363 detection, we often turn to empirical methods. Pettini & Pagel (2004) describe the observed linear relationship between metallicity and N2 or O3N2 ratios as shown in Equation (2.7) and Equation (2.9) respectively, for a sample of 137 extra-galactic H II regions spanning a broad range of metallicities. These empirical methods however are associated with a large scatter, which introduces large systematic uncertainties of 0.25 dex and 0.41 dex for the O3N2 and N2 methods respectively.

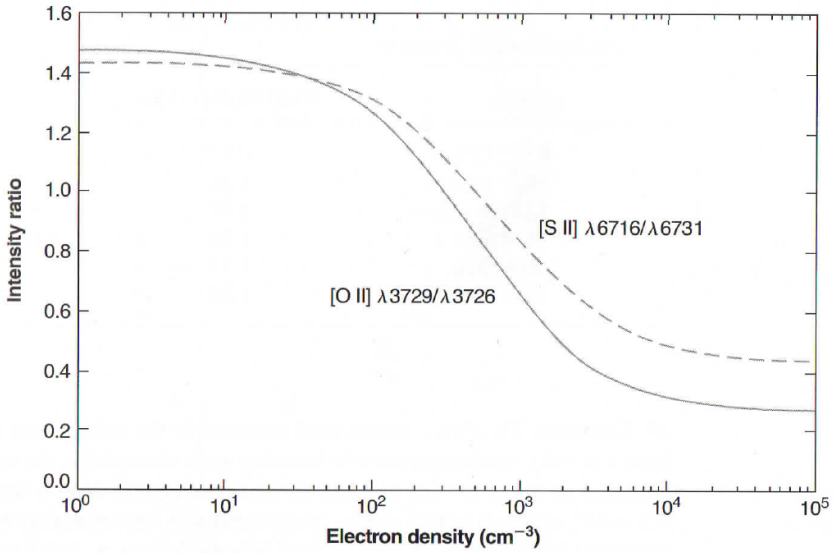

Figure 2.7: Relationship between electron density and [S II] (or [O II]) intensity ratio taken from Osterbrock & Ferland (2006).

$$12 + \log\left(\frac{\mathrm{O}}{\mathrm{H}}\right) = 8.90 + 0.57 \times \mathrm{N2} \tag{2.7}$$

$$\mathrm{N2} = \log\left(\frac{\mathrm{I[N\,II]6583}}{\mathrm{I(H}\alpha\mathrm{)}}\right) \tag{2.8}$$

$$12 + \log\left(\frac{\mathrm{O}}{\mathrm{H}}\right) = 8.73 - 0.32 \times \mathrm{O3N2} \tag{2.9}$$

$$\mathrm{O3N2} = \log\left(\frac{\mathrm{I[O\,III]5007/I(H}\beta\mathrm{)}}{\mathrm{I[N\,II]6583/I(H}\alpha\mathrm{)}}\right) \tag{2.10}$$

A number of spectra within the datasets exhibited prominent nebular emission, prompting a separate analysis to investigate the gaseous properties of IC10. These spectra were extracted again using IRAF, however this time there was no background subtraction to prevent removing the nebula emission. Known H II regions were identified using the maps produced by Hodge & Lee (1990), and we also include data from candidate H II regions suggested by P. Royer (private communication). Table 2.6 shows which regions were included and provides an overview of the available emission line fluxes measured for each region, relative to Hβ= 100.

Table 2.6: Nebular emission line flux measurements relative to Hβ=100 for various H II regions. HL# refer to H II regions outlined by Hodge & Lee (1990) and H II# refer to candidate H II regions suggested by Royer et al. (2001). Final column indicates the reddening correction derived for that region using Balmer emission line ratios as described in the text.

Nebular Region	Mask	[O II] 3727	Hγ 4340	[O III] 4363	Hβ 4861	[O III] 4959	[O III] 5007	[N II] 6548	Hα 6562	[N II] 6584	10^{-17} F$_{H\beta}$ [erg cm^{-2} s^{-1}]	c(Hβ)
HL 6	2				100 ± 17	251 ± 22	801 ± 25	64 ± 15	1035 ± 16	172 ± 15	1.89 ± 0.31	1.06
HL 10	2				100 ± 8	64 ± 8	217 ± 9	41 ± 8	1117 ± 11	117 ± 8	2.51 ± 0.21	1.53
HL 20	3		39 ± 4		100 ± 5			33 ± 6	960 ± 8	72 ± 6	16 ± 0.76	1.29
HL 22	4				100 ± 1	116 ± 3	350 ± 3	9 ± 4	640 ± 5	26 ± 4	109 ± 0.89	0.99
HL 45	3				100 ± 1	174 ± 2	508 ± 3	10 ± 3	628 ± 3	29 ± 3	45 ± 1.1	0.96
HL 45	1	21 ± 1	26 ± 0.2	2.2 ± 0.2	100 ± 2	222 ± 2					381 ± 5.8	1.62
H II 04	4		42 ± 5		100 ± 3	115 ± 3	367 ± 4		555 ± 31	27 ± 23	6.56 ± 0.21	0.61
H II 07	3		30 ± 3		100 ± 1	135 ± 2	449 ± 3	10 ± 3	731 ± 3	28 ± 3	127 ± 1.71	1.18
H II 07	4				100 ± 3	132 ± 2	413 ± 3	11 ± 3	719 ± 4	36 ± 3	137 ± 3.72	1.16
H II 08	3				100 ± 1	135 ± 1	428 ± 2	13 ± 3	809 ± 3	42 ± 3	148 ± 0.80	1.31
H II 08	4	41 ± 2	29 ± 0.4		100 ± 1	141 ± 1	439 ± 2				213 ± 2.83	1.36
H II 11	3		7 ± 1		100 ± 2	150 ± 6	500 ± 7	37 ± 5	2041 ± 7	113 ± 5	22 ± 0.36	-

RA and DEC (J2000) co-ordinates for Royer et al. (2001) H II regions as follows: H II 04 (00:20:15.48, +59:18:40.6) H II 07 (00:20:18.51, +59:17:40.4) H II 08 (00:20:24.41, +59:16:55.2) H II 11 (00:20:19.36, +59:18:02.9)

2.3.1 Nebular Extinction

Individual reddening corrections, based on Balmer emission line ratios, were computed for each H II region. Depending on the available wavelength range, Hα/Hβ or Hγ/Hβ ratios were used in conjunction with an intrinsic intensity ratio to obtain a measure of c(Hβ). Observed emission flux measurements were measured in DIPSO and corrected for underlying stellar absorption using Equation (2.11) where f_0 refers to the observed flux, $f_{\lambda corr}$ is the corrected flux and values for W_{abs} were taken from González Delgado et al. (1999), for an instantaneous burst with Salpeter IMF, mass range of 1-80 $M_\odot$ and age of 2 Myrs.

$$f_{\lambda corr} = f_0 \frac{W_\lambda + W_{abs}}{W_\lambda} \tag{2.11}$$

By interpolating between varying metallicity intervals, the W_{abs} parameter was determined to be 2.5 Å, 2.4 Å and 2.5 Å for Hα, Hβ and Hγ respectively. Measured equivalent widths (W_λ) for all Balmer emission lines are included in Table 2.7.

$$\frac{f_{\lambda corr}}{f_{\beta corr}} = \frac{I_\lambda}{I_\beta} 10^{c(H\beta)[X_\lambda - X_\beta]} \tag{2.12}$$

The corrected fluxes were then used with Equation (2.12), where $X_{H\alpha}$, $X_{H\beta}$ and $X_{H\gamma}$ are 0.82, 1.17 and 1.32 respectively, determined from a Galactic extinction law (Seaton, 1979), and the intrinsic intensity ratios are I(Hα)/I(Hβ)=2.86 and I(Hγ)/I(Hβ)=0.47 at low densities for a temperature of 10000 K. Table 2.6 shows the derived c(Hβ) measurements for each H II region, which when combined give an average nebular extinction of c(Hβ)=1.19 $\pm$ 0.28, or E(B-V) $\sim$ 0.7 c(Hβ) = 0.83 $\pm$ 0.20. Schlafly & Finkbeiner (2011) find the Milky Way foreground contribution in the direction of IC10 to be E(B-V)=1.39, however note the low Galactic latitude of the galaxy translated to a highly uncertain extinction estimate.

2.3.2 Metallicity

Metallicity measurements are important for providing information about the local environment, and the star formation history of the galaxy. A previous metallicity determination for two H II regions, IC10-1 and IC10-2, outlined by Lequeux et al. (1979) and later catalogued as HL111 and HL45 respectively (Hodge & Lee, 1990), suggested oxygen abundance measurements of log(O/H) + 12 = 8.17 and log(O/H) + 12 = 8.45 respectively (for reference, the solar oxygen abundance is log(O/H) + 12 = 8.69$\pm$0.05 (Asplund et al., 2009)). Unfortunately the quality of the [O III] 4363 intensity measurement was flagged as uncertain by Lequeux et al. (1979). Garnett (1990) performed a second analysis of HL45, obtaining a

Table 2.7: Balmer emission line equivalent widths for the H II regions outlined in Section 2.3.1. As before, HL# refer to H II regions outlined by Hodge & Lee (1990) and H II# refer to candidate H II regions suggested by Royer et al. (2001).

Nebular Region	Mask	Log $W_{H\gamma}$ [Å]	Log $W_{H\beta}$ [Å]	Log $W_{H\alpha}$ [Å]
HL 6	2		0.469 ± 0.067	1.205 ± 0.006
HL 10	2		1.043 ± 0.034	1.759 ± 0.004
HL 20	3		0.960 ± 0.020	1.773 ± 0.004
HL 22	4		1.988 ± 0.004	2.685 ± 0.003
HL 45	3		1.940 ± 0.010	>3.00
HL 45	1	1.613 ± 0.004	2.176 ± 0.006	
H II 04	4		0.952 ± 0.014	1.661 ± 0.023
H II 07	3		2.654 ± 0.006	3.248 ± 0.002
H II 07	4		2.892 ± 0.012	3.521 ± 0.002
H II 08	3		2.565 ± 0.002	3.447 ± 0.002
H II 08	4	2.407 ± 0.006	2.695 ± 0.006	
H II 11	3		>3.00	

RA and DEC (J2000) co-ordinates for Royer et al. (2001) H II regions as follows: H II 04 (00:20:15.48, +59:18:40.6) H II 07 (00:20:18.51, +59:17:40.4) H II 08 (00:20:24.41, +59:16:55.2) H II 11 (00:20:19.36, +59:18:02.9)

Table 2.8: Oxygen abundance measurements for H II regions within IC10, derived using the N2 and O3N2 strong line methods outlined in Pettini & Pagel (2004)

Nebular Region	Mask	N2	log(O/H) + 12	O3N2	log(O/H) + 12
HL 6	2	-0.78	8.46 ± 0.41	1.68	8.19 ± 0.26
HL 10	2	-0.98	8.34 ± 0.41	1.32	8.31 ± 0.26
HL 22	4	-1.39	8.11 ± 0.42	1.93	8.11 ± 0.26
HL 45	3	-1.34	8.14 ± 0.41	2.04	8.08 ± 0.25
H II 04	4	-1.31	8.15 ± 0.55	1.87	8.13 ± 0.45
H II 07	3	-1.42	8.09 ± 0.41	2.07	8.07 ± 0.25
H II 07	4	-1.31	8.16 ± 0.41	1.92	8.11 ± 0.25
H II 08	3	-1.29	8.17 ± 0.41	1.92	8.12 ± 0.25
H II 11	3	-1.26	8.18 ± 0.41	1.96	8.10 ± 0.25

metallicity of log(O/H) + 12 = 8.26±0.10, again based on the observations from Lequeux et al. (1979). Richer et al. (2001) also report metallicity measurements for the H II regions HL111b and HL111c located within the IC10-1 region and find log(O/H) + 12 = 7.84±0.25 and log(O/H) + 12 = 8.23±0.09 respectively.

Using the nebular emission present in the regions outlined in Table 2.6, oxygen abundance measurements based on strong line methods using the N2 and O3N2 ratios from Pettini & Pagel (2004) were determined and are shown in Table 2.8. Unfortunately, the linear relationship between oxygen abundance and the O3N2 ratio only holds true for O3N2 measurements within the range of -1 to 1.9, and for IC10 our measured O3N2 ratios (1.3–2.1) suggest we are at the limit of this calibration beyond which this linear relationship breaks down. Nevertheless, using our O3N2 ratio we find an average metallicity of log(O/H) + 12 = 8.14 ± 0.09, with a systematic uncertainty from the method of 0.25. For completeness we also compute oxygen abundance measurements using the N2 ratio, for which we find log(O/H) + 12 = 8.22 ± 0.14, however we note that the N2 method produces results with a large dispersion, therefore introducing a systematic uncertainty on the metallicity of ± 0.41. Overall the O3N2 and N2 metallicity measurements agree within their uncertainties.

To produce a more robust determination of the oxygen content we also derive an updated metallicity measurement for IC10 using the nebular emission spectra of the newly confirmed WR star T5, which is associated with the HL45 H II region (Hodge & Lee, 1990) and is shown in Figure 2.8. Whilst nebular emission was present in a number of spectra, solely T5 provided a robust [O III] 4363 flux measurement (10σ), as shown in Table 2.6, necessary when calculating metallicity using the direct method.

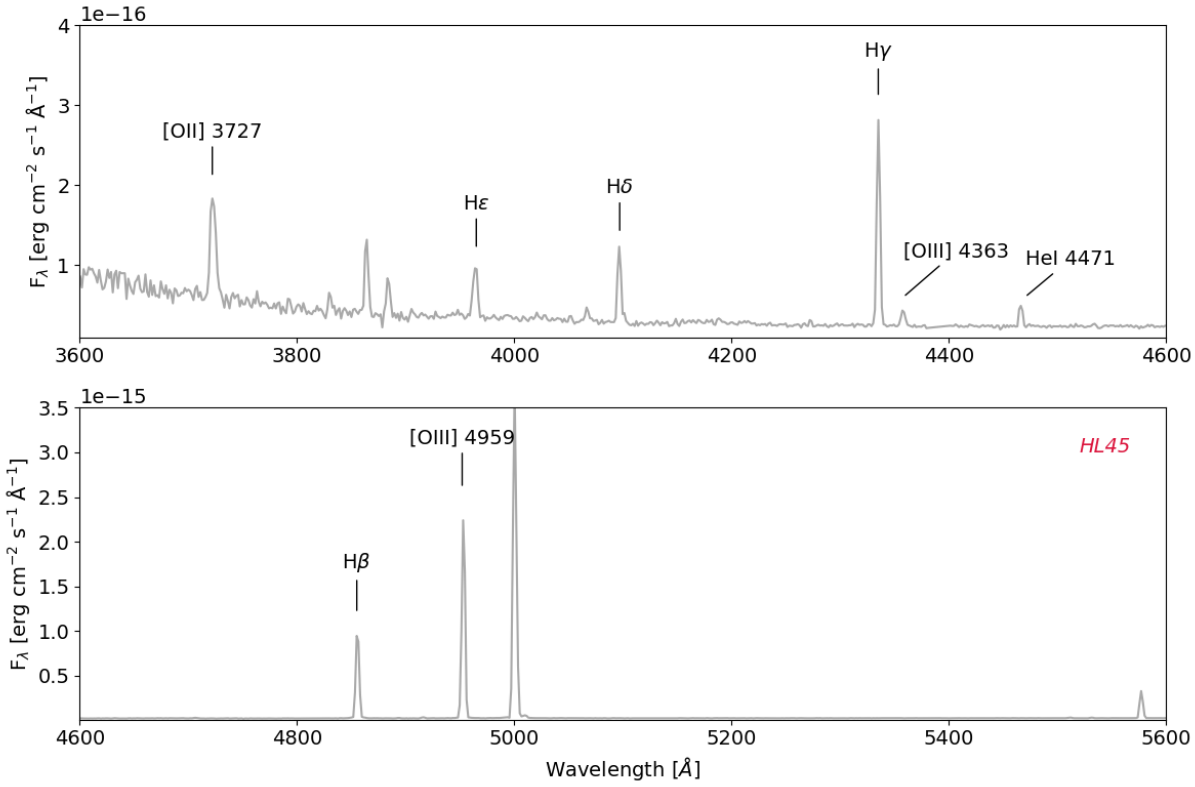

Figure 2.8: Flux calibrated optical nebular spectra of the H II region HL45, associated with the WR star T5. Labels highlight the Balmer series and other forbidden lines important for metallicity measurements, including a clear [O III] 4363 emission line.

HL45 was corrected for an extinction of c(Hβ)=1.62 $\pm$ 0.05 found using the method outlined in Section 2.3.1 before appropriate emission line intensities were measured in DIPSO. An [O III] electron temperature of 9700$\pm$250 K was found using the TEMDEN package in IRAF, and the same temperature was adopted for the [O II] gas temperature. This approximation should be sufficient, since the contribution from the [O III] region dominates the final oxygen abundance measurement, as shown in Table 2.9. A change in $\pm$ 1000 K in [O II] gas temperature corresponds to a $\pm$ 0.03 adjustment in log(O/H) + 12.

As discussed in Section 2.3, a density estimate requires a measurement of the [S II] lines, however our spectra did not extend far enough to cover this wavelength range. We therefore assumed a typical value for a low density H II region of 100 cm^{-3} (Kennicutt, 1984).

Ionic abundances were then derived using the IONIC package in IRAF, which when provided with a temperature and intensity ratio relative to Hβ, calculated the emissivity and ionic abundance for the specified ion. To find the total oxygen abundance we sum the relative contributions from the [O III] and [O II] ions.

This gave an oxygen abundance of log(O/H) + 12 = 8.40 $\pm$ 0.04, following Equations (2.4) to (2.6) outlined in Section 2.3. Present results are included in Table 2.9. It is apparent that our updated oxygen abundance for HL 45 is similar to Lequeux et al. (1979) although is somewhat higher than both Garnett (1990) and Richer et al. (2001). We consider this oxygen measurement to be a good representation of the global metallicity of IC10 because the oxygen content distribution for other dwarf galaxies has been shown to be relatively uniform. Integral field studies of blue compact dwarf (BCD) galaxies (García-Lorenzo et al., 2008; Cairós et al., 2015) find that for a BCD with a metallicity greater than 8.1, the variation in log(O/H) + 12 across the galaxy does not exceed $\sim$0.1 dex. A slightly higher metallicity for IC10 is still consistent with the luminosity-metallicity relationship from Shi et al. (2005) for $M_B = -16.3$ mag[2]. The oxygen content of this galaxy is therefore more similar to the LMC (log(O/H) + 12 = 8.37) than the SMC (log(O/H) + 12 = 8.13), and IC10 is not as metal-poor as previously considered.

2.3.3 Star Formation Rate

Using the Hα and HαC imaging discussed in Section 2.2.1 we also re-determine the star formation rate (SFR) of IC10. Figure 2.9 shows the Hα image of IC10, and we include the positions of known WR stars for reference. Using aperture photometry to obtain a total Hα count rate, we apply a conversion derived from standard star measurements to find the

[2]Absolute blue magnitude for IC10 obtained from $m_B = 11.8$ mag, $A_B = 4.1 \times$ E(B-V) = 3.8 mag and a distance modulus of 24.3 mag.

Table 2.9: Overview of previously derived [O III] temperatures and metallicity measurements for two different H II regions within IC10 (IC10 1 and IC10 2), outlined by Lequeux et al. (1979), and present results from mask1 observations of HL45

Lequeux Region	HL	$T(O^{2+})$ [$\times 10^4$ K]	(O^+/H) [$\times 10^5$]	(O^{2+}/H) [$\times 10^4$]	log(O/H) + 12	Ref
IC10 1	111	1.16	3.98	1.10	8.17	a
IC10 1	111b	1.40 ± 0.30			7.84 ± 0.25	b
IC10 1	111c	1.00 ± 0.06			8.23 ± 0.09	b
IC10 2	45	1.06	6.03	2.19	8.45	a
IC10 2	45	1.08			8.26 ± 0.10	c
IC10 2	45	0.97 ± 0.03	2.28 ± 0.19	2.30 ± 0.21	8.40 ± 0.04	d

a: Lequeux et al. (1979); b: Richer et al. (2001); c: Garnett (1990); d: This work;

integrated Hα flux. A similar exercise for the HαC filter permits the stellar contribution to be subtracted. This approach was preferred to producing a net Hα - HαC image, which introduced subtraction artefacts due to bright stars within the field of view. To correct for [N II] 6548 and [N II] 6584 emission within the GMOS Hα filter bandwidth, we apply the correction:

$$\frac{\mathrm{F([N\,II]6548+6584)}}{\mathrm{F(H}\alpha)} = 0.09 \pm 0.02,$$

derived from average flux measurements of the [N II] 6548, [N II] 6584 and Hα emission lines across all available H II regions (shown in Table 2.10).

The average gas extinction of c(Hβ)=1.19 ± 0.28 was applied and adopting a distance of 740 ± 20 kpc we find $L_{H\alpha}$=5.64 ± 2.93$\times 10^{39}$ erg s^{-1}. To convert this to a SFR we used:

$$\mathrm{SFR} = 7.94 \times 10^{-42} L_{H\alpha},$$

which assumes a Salpeter function IMF over a mass range of 0.1-100 $M_\odot$. This resulted in SFR=0.045 ± 0.023 $M_\odot$ yr^{-1} (Kennicutt, 1998). We also derive a SFR for the dominant giant H II region of IC10 comprising the complex centred on HL111/106 (Hodge & Lee, 1990). An elliptical aperture with semi-major/minor axes of 17″ × 27″ reveals a Hα luminosity of 1.4$\times 10^{39}$ erg s^{-1}, typical of the brightest H II regions of local star forming galaxies (Kennicutt, 1988). These results are shown in Table 2.15.

A summary of the current and previous SFR determinations, using both Hα and radio flux measurements, are shown in Table 2.10. Kennicutt et al. (2008) find a lower SFR

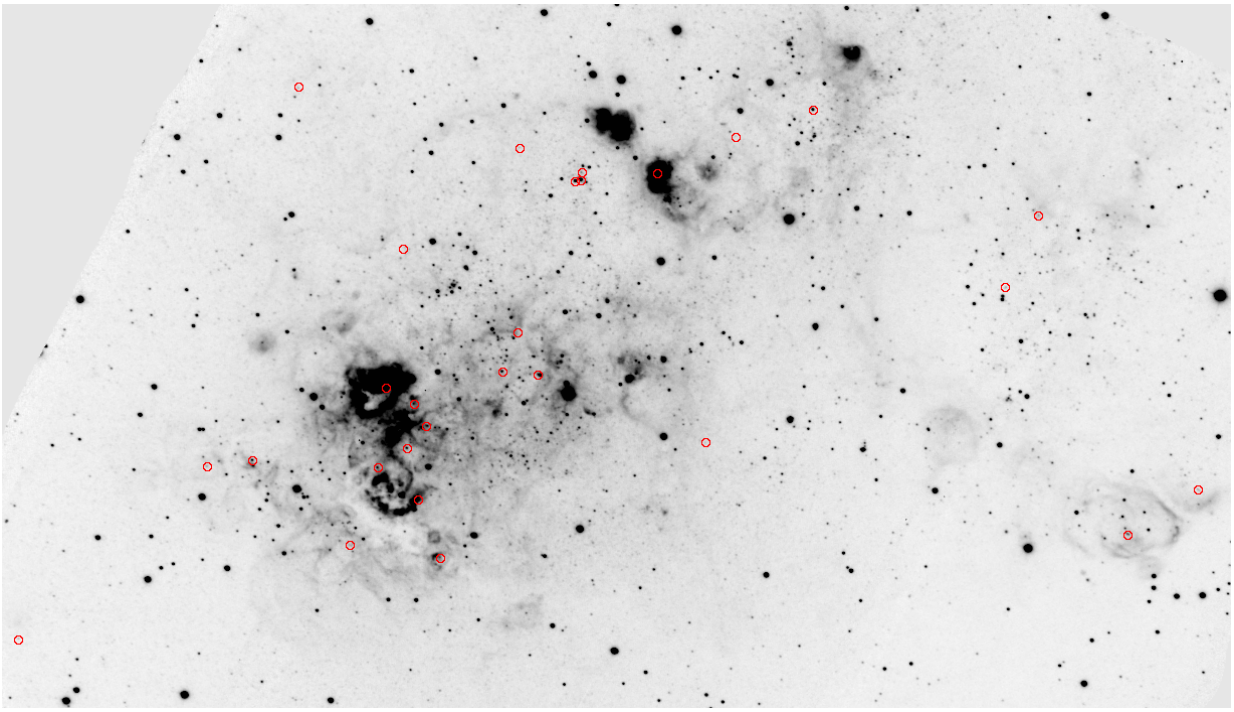

Figure 2.9: Gemini GMOS Hα image of IC10, north is up and east is left, showing the distribution of ionized gas and the relative positions of confirmed WR stars (red circles) with the exception of M5 which is out of the field of view but is associated with the H II region HL29. The bright star forming complex HL106/111 (left of centre) contains 6 WR stars. The total field of view is 384″ × 210″, corresponding to 1.4 × 0.8 kpc at a distance of 740 kpc.

using a similar method, owing to a lower Hα flux and smaller dust extinction correction. In contrast, our SFR lies intermediate between the radio derived SFRs by Gregory et al. (1996) and Chyży et al. (2016). The comparison to radio-derived SFRs is useful, because at radio wavelengths dust extinction is non-existent, and therefore does not effect the measured radio flux. We do, however, note that contributions from non-thermal radio sources such as synchrotron emission from supernova remnants can skew results, especially at longer radio wavelengths. The radio SFRs shown from Gregory et al. (1996) and Chyży et al. (2016) have not been corrected for this contribution.

Table 2.10: Comparison of the IC10 star formation rates derived using both radio flux measurements and Hα luminosity measurements, including a new attempt from this work. All values have been scaled to a distance of 740 kpc. Radio SFRs assume all flux measured is free-free radio emission and there is no contribution from non-thermal sources.

Method	ν [GHz]	F_λ [mJy]	10^{-12} $F_{H\alpha}$ [erg cm^{-2} s^{-1}]	$A_{H\alpha}$ [mag]	N II/Hα	10^{39} $L_{H\alpha}$ [erg s^{-1}]	SFR [$M_\odot$ yr^{-1}]	Ref
Radio	4.85	137 ± 12					0.030 ± 0.003	a
Radio	1.43	377 ± 11					0.073 ± 0.005	b
Hα			103 ± 28	1.90	0.080 ± 0.008	3.89 ± 0.86	0.031 ± 0.007	c
Hα			130 ± 33	2.06 ± 0.49	0.092 ± 0.023	5.64 ± 2.93	0.045 ± 0.023	d

a: Gregory et al. (1996); b: Chyży et al. (2016); c: Kennicutt et al. (2008); d: This work

2.4 Stellar Results

2.4.1 New Wolf-Rayet Stars

The spectra of three newly confirmed WR stars in IC10 are presented in Figure 2.10. All three have been assigned early-WN (WNE) spectral types. Both T5 and T6 are associated with star clusters which is evident from both the photometry and the presence of a strong continuum. Also, as discussed in Section 2.3.2, T5 is located within the H II region HL45. Spectroscopy for T9 was also performed, and analysis concluded that it was not a WR star. The presence of molecular TiO bands suggested it is most likely to be a foreground early M-dwarf star instead.

The number of spectroscopically confirmed WR stars in IC10 has increased from 26 to 29 stars, and a summary of their spectral properties can be found in Tables 2.12 to 2.13. Of the previously confirmed WR stars, we suggest some changes to prior spectral classifications, including the revision of M15 from WC6-7 (Massey & Armandroff, 1995) to WC4 due to the absence of C III 5696 and presence of O III 5592 shifting the equivalent width ratios outlined in Smith et al. (1990) and Crowther et al. (1998) into the WC4 category; the adjustment of M24 from a WNE/OB (Massey & Holmes, 2002) to a O2.5 If/WN6 due to its similarity to HD93162 (Crowther & Walborn, 2011); and finally, the minor adjustment to the subclass of M23 from WN7-8 (Massey & Holmes, 2002) to WN7 based on the strengths of He I 5876 to He II 5411. Tables 2.3 to 2.4 include a complete census of the WR population and their classifications.

As mentioned previously, the WC/WN ratio in IC10 is peculiar, and since the addition of three new WN stars only reduces the ratio from 1.3 to 1±0.4, IC10 is still regarded as an anomaly given the WC/WN ratio of ∼0.2 for the LMC and 0.1 for the SMC.

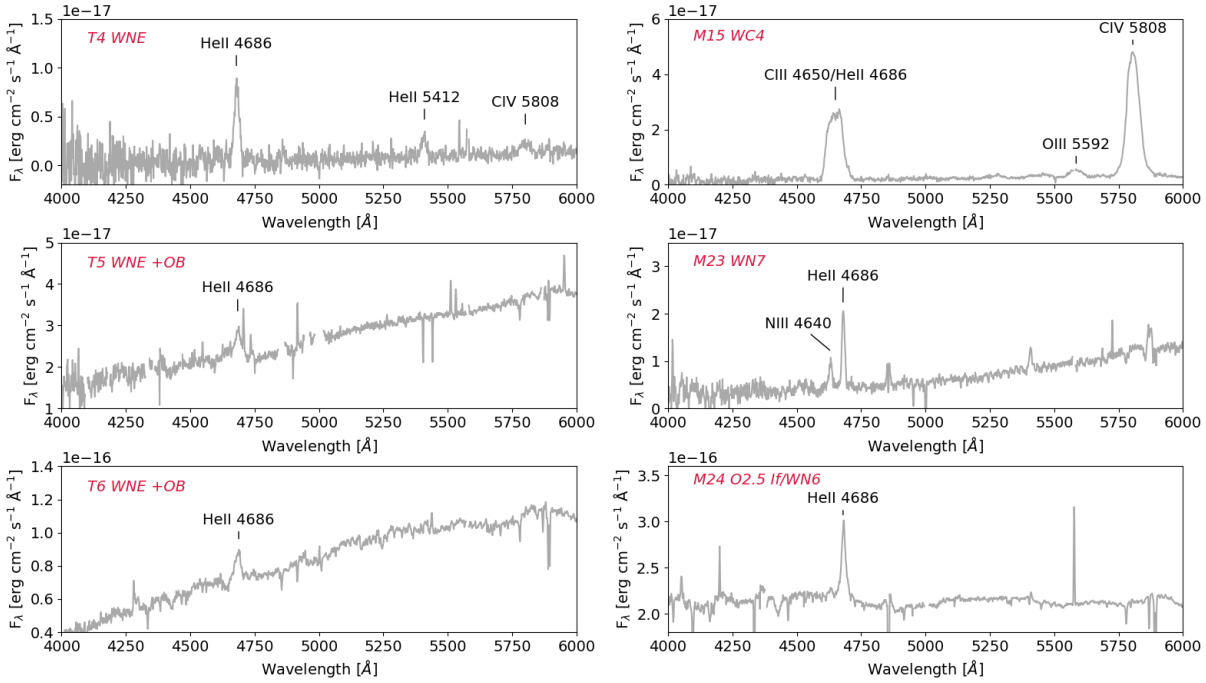

Figure 2.10: On the left we show the flux calibrated optical spectra of 3 newly confirmed WR stars within IC10, all belonging to the WN subclass. On the right we show the optical spectra for 3 previously confirmed WR stars, which were not included in the Gemini/GMOS datasets presented by Crowther et al. (2003) and therefore providing a complete set of spectra for all IC10 confirmed WR stars. Some nebular emission has been removed for clarity. The strong, broad absorption feature at λ4430 in T6 and M24 is a prominent Diffuse Interstellar Band (Herbig, 1995).

2.4.2 Binary Fraction

Recent evidence suggests the local OB binary frequency is high (see Section 1.5.2). Analysis of radial velocity variations in O-stars within the 30 Doradus region of the LMC by Sana et al. (2013b) revealed a lower limit intrinsic binary fraction of 51 ± 4%. Similarly, using O stars residing in young Galactic clusters, Sana et al. (2012) found a lower limit binary fraction of 69 ± 9%. The initial binary fractions for 30 Dor most likely will have been higher, but will have been disrupted over time due to the mixed age population and past stellar evolution (Schneider et al., 2018).

If we assume a similar scenario for IC10, we would expect that some of these OB binaries would have survived the transition to WR stars, and therefore we expect a relatively high WR binary frequency. To assess this, we outline a number of criteria used to identify potential binary candidates, and compare the resultant binary fraction with that of WR stars in other Local Group galaxies.

The simplest method involves identifying absorption features from OB companions in the spectrum of each WR star. There is however, some ambiguity in this approach, since WR stars may contain intrinsic absorption features. There is also the potential that the observed absorption is from a neighbouring star which is not necessarily bound to the system. This technique alone therefore, is insufficient to confidently suggest a binary system.

Another method involves searching for unusual radial velocities, resulting from orbital motion, in the strongest emission line features present in the spectrum. Radial velocity measurements were found for those WR stars with nebular emission available, and heliocentric corrections were found for each mask using the BCVcor task in IRAF. For those WR without nebular emission an average heliocentric radial velocity of -347 ± 75 km s^{-1} was assumed, where the error reflects the range in the upper and lower observed radial velocities. This agrees well with the expected radial velocity of -348 ± 1 km s^{-1} (Huchra et al., 1999) and takes into consideration the average dispersion velocity of the gas, found to be 34 ± 5 km s^{-1} (McConnachie, 2012). By measuring the radial velocity for He II 4686 (WN) and C IV 5808 (WC) emission lines in each spectrum and comparing with the expected radial velocity measurement, the WR stars with shift excesses greater than 2σ were identified as potential binary candidates or runaway stars.

Finally, the continuum of an O-star companion can also dilute the emission line strength of the WR, therefore the presence of a companion would result in low equivalent width measurements and small ΔHe II-He IIC excesses. These stars are easily identifiable in Figure 2.11 (a) and (b), in which emission line widths are compared against line strengths in IC10 and Magellanic Cloud WN and WC stars respectively. It is however, important to

note that nearby sources or line-of-sight contaminations can also enhance the continuum and falsely suggest a binary system.

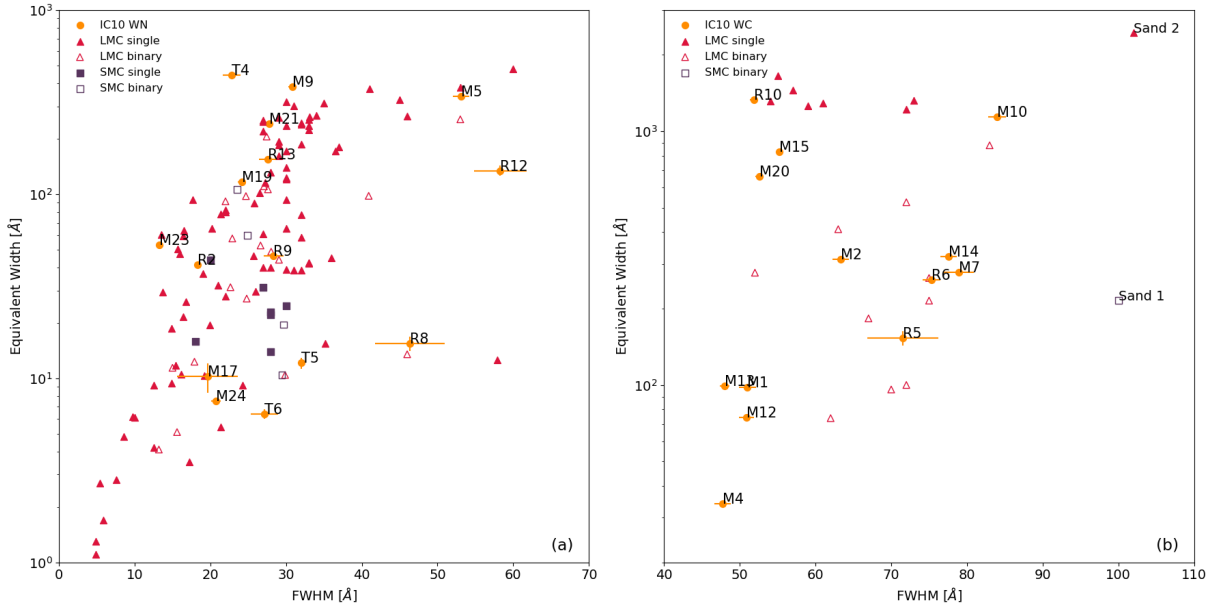

Figure 2.11: Shows the relationship between FWHM and equivalent width for (a) WN stars and (b) WC stars in the LMC (red triangles), SMC (blue squares), and IC10 (yellow circles). For the Magellanic cloud WR stars, binary and single stars can also be distinguished between by open and filled plot symbols respectively. The two known Magellanic WO stars have also been included (Sand 1,2). LMC data taken from Crowther & Hadfield (2006), Schnurr et al. (2008), and Foellmi et al. (2003b). SMC data from Foellmi et al. (2003a) and Crowther & Hadfield (2006).

Taking all these indicators into consideration, those WR stars which meet a minimum of two out of the three requirements were deemed likely to be part of a binary system, and have been indicated in Tables 2.12 to 2.13, giving a coarse binary fraction of 41%. Of these potential binary systems, four WR stars (M1, M4, T5 and T6) successfully fulfilled all three of the binary system criteria. This estimated binary fraction is in good agreement with the observed WR binary fraction in both the LMC (Breysacher et al., 1999; Neugent et al., 2012a; Massey et al., 2014, 2015b) and SMC(Foellmi et al., 2003a), which again are lower limits, suggesting the mechanism for producing binaries is metallicity independent (Shenar et al., 2016).

2.4.3 Stellar Extinction

Interstellar extinction studies of IC10 have previously been attempted using H II regions, from which an E(B-V) = 0.83 ± 0.20 was obtained (Section 2.3.1). Here we derive new

E(B-V) values of individual WR stars based on photometric magnitudes and spectral types. We consider the extinction in two continuum bands, He II C at 478 nm, and HαC at 662 nm as follows:

$$\begin{aligned} \mathrm{E(He\,II C - H}\alpha\mathrm{C)} &= \mathrm{(He\,II C - H}\alpha\mathrm{C)} - \mathrm{(He\,II C - H}\alpha\mathrm{C)}_0; \\ &= A_{\mathrm{He\,II C}} - A_{\mathrm{H}\alpha\mathrm{C}}. \end{aligned}$$

The conversion from reddening to E(B-V) was achieved using the Galactic extinction law (Seaton, 1979). Assuming $R_\lambda = 3.1$, A_λ/E(B-V), ratios at wavelengths of 478 nm(He II C) and 662nm(HαC) were determined to be $A_{\mathrm{He\,II C}} = 3.7$ E(B-V) and $A_{\mathrm{H}\alpha\mathrm{C}} = 2.44$ E(B-V) respectively, resulting in:

$$E(B-V) = 0.79[\mathrm{(He\,II C - H}\alpha\mathrm{C)} - \mathrm{(He\,II C - H}\alpha\mathrm{C)}_0].$$

Intrinsic He II C-HαC values are dependent on WR subtype, therefore for each class, the He II C and HαC magnitudes were determined from model spectra, free from extinction, to find the intrinsic colour. Where possible we used LMC template WR stars, however there are no late-type WC stars within the LMC so for this case we used a model for a Milky Way WC star. For cases where the WR spectra are dominated by OB stars we used Starburst99 population synthesis models at an age of 5Myr, since this is the typical age of stellar clusters hosting WR stars (Leitherer et al., 1999). Table 2.11 lists these results along with their associated model references.

Where possible we have attempted to derive individual extinction values tailored to each star. A comparison between the nebular and photometrically derived extinctions for T5 (HL45) gives E(B-V)=1.13 $\pm$ 0.04 and E(B-V)=1.15 $\pm$ 0.03 respectively, showing the two methods are in agreement. For the remainder of the sample, where robust magnitude measurements were unavailable, an average extinction value of E(B-V) = 0.92 $\pm$ 0.26 was applied, obtained from both the stellar extinction (E(B-V)=0.95 $\pm$ 0.27), and nebular extinction (E(B-V)=0.83 $\pm$ 0.20) results. The E(B-V) values applied for each star are included in Table 2.4.

Table 2.11: The (He II C-HαC)$_0$ intrinsic colour of WR stars for different ionization subclasses, determined from the spectral model indicated by the reference column.

Spectral type	Template Star	(He II C-HαC)$_0$	Ref
WN3-4	LMC-AB9	-0.06	a
WN6	HD 38282	0.03	a
WN7	HDE 269883	-0.01	a
WN8	LMC-AB11	0.00	a
WN10	BE 294	0.12	a
WC4-5	HD 37026	-0.05	b
WC6	HD 97809	-0.06	c
WC7	HD 156385	0.00	d
WR +OB		-0.21	e

a: Doran et al. (2013); b: Crowther et al. (2002); c: Smartt et al. (2001); d: Dessart et al. (2000); e: Leitherer et al. (1999)

Table 2.12: Emission line properties of the strongest spectral features found in the confirmed WN stars of IC10. Line luminosities derived using the individual interstellar extinction values outlined in Table 2.4 and discussed in Section 2.4.3, along with a distance of 740 ± 20 kpc. Mask column refers to the mask the star was observed through. Multiple masks indicate that the star was observed more than once, therefore these spectra were combined to improve signal to noise. For WN stars the strongest lines usually refer to He II 4686 and He II 5411 emission (with the exception of the WNE/C star M5). Binary column indicates stars that successfully met two out of the three binary criteria outlined in Section 2.4.2. Note this only suggests and does not confirm binary status of a star.

		He II 4686				He II 5411						
ID	Spectral Type	FWHM [Å]	Log W_λ [Å]	10^{-17} f_λ [erg cm^{-2} s^{-1}]	10^{35} L_λ [erg s^{-1}]	FWHM [Å]	Log W_λ [Å]	10^{-17} f_λ [erg cm^{-2} s^{-1}]	10^{35} L_λ [erg s^{-1}]	Mask	Radial Velocity [kms^{-1}]	Binary
T4	WNE	23 ± 1	2.65 ± 0.02	19 ± 1	4.5 ± 1.6	22 ± 3	1.73 ± 0.05	5 ± 1	0.6 ± 0.2	1	-317 ± 30	
R13	WN5	28 ± 1	2.19 ± 0.02	18 ± 1	1.9 ± 0.8	28 ± 3	1.66 ± 0.04	4 ± 0	0.3 ± 0.1	2,3	-80 ± 27	
T5	WNE	32 ± 0	1.08 ± 0.03	20 ± 3	10.9 ± 3.2					1,2	-30:	b?
R9	WNE	28 ± 1	1.67 ± 0.02	18 ± 1	2.0 ± 0.2	31 ± 3	0.98 ± 0.04	6 ± 1	0.4 ± 0.1	2,3	-222 ± 36	
T6	WNE	27 ± 2	0.81 ± 0.03	46 ± 3	16.6 ± 2.1					1	-82 ± 46	b?
R8	WN10	46 ± 5	1.19 ± 0.04	28 ± 2	2.9 ± 0.4					4	-19 ± 111	b?
M9	WN3	31 ± 0	2.58 ± 0.01	47 ± 1	4.8 ± 0.9	29 ± 6	1.85 ± 0.07	9 ± 1	0.6 ± 0.1	3	-251 ± 12	
R12	WNE	58 ± 3	2.13 ± 0.03	24 ± 1	16.7 ± 2.5					4	259 ± 98	
M24	O2.5 If/WN6	21 ± 1	0.88 ± 0.01	163 ± 4	10.4 ± 1.1					2	-204 ± 14	
R2	WN7-8	18 ± 0	1.62 ± 0.01	31 ± 1	5.9 ± 0.5	17 ± 4	0.79 ± 0.08	6 ± 1	0.6 ± 0.1	2,3	-117 ± 9	b?
M17	WNE + BH	20 ± 4	1.01 ± 0.07	8 ± 1	1.2 ± 0.2					4		var.
M19	WN4	24 ± 1	2.07 ± 0.01	44 ± 1	1.8 ± 0.3	29 ± 1	1.52 ± 0.01	10 ± 0	0.3 ± 0.04	1,3,4	-260 ± 15	
M23	WN7	13 ± 0	1.72 ± 0.01	23 ± 1	3.7 ± 3.3	12 ± 1	0.83 ± 0.04	6 ± 0	0.5 ± 0.4	2	-286 ± 10	
M21	WN4	28 ± 0	2.38 ± 0.00	54 ± 1	7.0 ± 0.8	29 ± 1	1.66 ± 0.01	12 ± 0	0.9 ± 0.1	2,3	-117 ± 9	

M17 is a known X-ray binary, involving a WR and black hole orbiting with a 34.93 ± 0.04 hr period. (Prestwich et al., 2007; Silverman & Filippenko, 2008).
The : refers to an uncertain measurement.

Table 2.13: Emission line properties of the strongest spectral features found in the confirmed WC stars of IC10. Line luminosities derived using the individual interstellar extinction values outlined in Table 2.4 and discussed in Section 2.4.3, along with a distance of 740 ± 20 kpc. Mask column refers to the mask the star was observed through. Multiple masks indicate that the star was observed more than once, therefore these spectra were combined to improve signal to noise. For WC stars the strongest features are C IV 5808 and, due to the broad nature of the emission lines, a C III 4650/He II 4686 blend. Binary column indicates stars that successfully met two out of the three binary criteria outlined in Section 2.4.2. Note this only suggests and does not confirm binary status of a star.

		C III 4650/He II 4686 blend				C IV 5808					Radial	
ID	Spectral Type	FWHM [Å]	Log W_λ [Å]	10^{-17} f_λ [erg cm^{-2} s^{-1}]	10^{35} L_λ [erg s^{-1}]	FWHM [Å]	Log W_λ [Å]	10^{-17} f_λ [erg cm^{-2} s^{-1}]	10^{35} L_λ [erg s^{-1}]	Mask	Velocity [kms^{-1}]	Binary
M5	WNE/C4	53 ± 1	2.53 ± 0.01	89 ± 2	21.8 ± 2.4	79 ± 1	3.09 ± 0.01	370 ± 6	38.4 ± 3.6	3,4	-422 ± 30	
M1	WC4-5	65 ± 3	1.86 ± 0.02	46 ± 2	7.5 ± 6.8	51 ± 1	1.99 ± 0.01	84 ± 2	6.3 ± 4.3	4	239 ± 23	b?
M2	WC4	69 ± 1	2.17 ± 0.01	138 ± 2	22.5 ± 20.3	63 ± 1	2.50 ± 0.01	322 ± 5	24.0 ± 16.4	2	-460 ± 23	
R6	WC4	73 ± 2	2.29 ± 0.01	45 ± 1	25.9 ± 3.7	75 ± 1	2.41 ± 0.01	95 ± 2	18.4 ± 2.1	2,4	-158 ± 27	b?
R5	WC4-5	74 ± 1	2.16 ± 0.01	64 ± 1	11.3 ± 1.6	72 ± 5	2.18 ± 0.03	99 ± 6	7.9 ± 1.0	2,4	-183 ± 100	b?
M4	WC4-5	67 ± 1	1.65 ± 0.01	204 ± 3	32.9 ± 2.4	48 ± 1	1.53 ± 0.01	183 ± 4	13.6 ± 0.9	1	-163 ± 22	b?
M7	WC4-5	81 ± 1	2.73 ± 0.01	836 ± 12	137 ± 123	79 ± 2	2.44 ± 0.01	1002 ± 27	75 ± 51	1	-205 ± 44	
R11	WC4	83 ± 4		69 ± 4	11.3 ± 10.2	82 ± 1		274 ± 3	20.4 ± 14.0	1	-445 ± 18	
M10	WC7	68 ± 0	3.06 ± 0.00	904 ± 7	496 ± 41.2	84 ± 1	3.06 ± 0.01	1128 ± 15	203 ± 18	4	-47 ± 24	
M12	WC4	53 ± 2	1.96 ± 0.02	40 ± 2	80.9 ± 10.9	51 ± 1	1.87 ± 0.01	99 ± 2	49.1 ± 5.2	3	10 ± 20	b?
R10	WC4	61 ± 2	3.39 ± 0.01	84 ± 2	13.7 ± 12.4	52 ± 1	3.13 ± 0.00	118 ± 1	8.8 ± 6.0	1	-279 ± 11	
M13	WC5-6	59 ± 1	2.07 ± 0.01	161 ± 3	8.3 ± 0.7	48 ± 1	1.99 ± 0.01	163 ± 2	5.1 ± 0.4	4	-59 ± 13	b?
M14	WC5	77 ± 1	2.64 ± 0.00	588 ± 6	115 ± 10.7	78 ± 1	2.51 ± 0.01	622 ± 9	53.1 ± 4.4	1,3	-32 ± 25	b?
M15	WC4	65 ± 1	3.00 ± 0.01	180 ± 3	7.5 ± 1.8	55 ± 0	2.92 ± 0.00	269 ± 2	7.1 ± 1.3	1,2	-274 ± 6	
M20	WC5	61 ± 0	2.94 ± 0.00	272 ± 2	39.2 ± 5.4	53 ± 1	2.82 ± 0.00	269 ± 3	18.2 ± 2.0	1,3	-232 ± 10	

Table 2.14: Average line luminosities of the He II 4686, and C IV 5808 emission lines for the WN and WC/O spectral classes respectively, where the errors represent the standard error in the mean. Both the WN and WC class have been further divided using ionization classifications into early and late subgroups. To avoid confusion, the WNE/C star M5 has not been included in any category. For comparison, the mean line luminosities obtained for the LMC and SMC have been included from Crowther & Hadfield (2006) data.

		IC10		LMC		SMC	
Spectral Type	Emission line [Å]	WR [#]	$L_\lambda \times 10^{35}$ [erg s^{-1}]	WR [#]	$L_\lambda \times 10^{35}$ [erg s^{-1}]	WR [#]	$L_\lambda \times 10^{35}$ [erg s^{-1}]
WN2-5 (WNE)	He II 4686	10	6.73 ± 1.90	45	9.27 ± 1.30	6	0.62 ± 0.13
WN6-9 (WNL)	He II 4686	4	5.71 ± 1.69	15	13.3 ± 3.9	1	7.79
WC4-6 (WCE)	C IV 5808	13	23.6 ± 6.03	17	32.5 ± 3.8		
WC7 (WCL)	C III 5696	1	87 ± 8				
WC7 (WCL)	C IV 5808	1	203 ± 18				
WO	C IV 5808			1	10.2	1	14.9

2.4.4 WR Line Luminosities

Average WR emission line luminosities are very useful for interpreting extragalactic observations of young star forming regions. Significant WR populations can be found in distant galaxies which have recently undergone a burst of massive star formation, however individual WR stars will be unresolved. To probe the WR content we must rely on integrated WR emission line luminosities from the galaxy, calibrated using nearby resolved populations (Schaerer & Vacca, 1998; Sidoli et al., 2006), such as those in IC10.

Here we present the average WR line luminosities obtained for IC10. We divide the WR population into five categories based on spectral type and determine the luminosities of the strongest emission lines associated with that WR class. The individual stellar extinctions applied for each star are shown in Table 2.4. Individual line luminosities can be found in Tables 2.12 to 2.13 and the average results are summarised in Table 2.14. For comparison, we also include Magellanic Cloud WR line luminosity data taken from Crowther & Hadfield (2006). Figure 2.12 provides a visual representation for the comparison of individual line luminosities between IC10 and Magellanic Cloud WN, WC and WO stars.

WN stars, using the He II 4686 emission line, appear to show conflicting results. For WN2-5 (WNE) stars the average line luminosity of 6.7 ± 6.0 $\times 10^{35}$ erg s^{-1} for IC10 is similar to LMC counterparts, whereas for WN6-9 (WNL) stars however, the IC10 average of 5.7 ± 3.4 $\times 10^{35}$ erg s^{-1} is somewhat lower than both the Magellanic Clouds. We note however, that the sole late-WN star in the SMC is the unusual system HD5980 (Koenigsberger

et al., 2014), and the LMC statistics include the very massive WN stars in 30 Doradus (see Section 1.3.1).

The similarities between IC10 and LMC WN stars can been seen in Figure 2.12, while SMC WN stars can be seen to have lower luminosities than their LMC and IC10 counterparts.

WCE stars in IC10 and the LMC, which all belong to the WC4 class, have comparable C IV 5808 emission line averages, however there is no counterpart for the IC10 late-WC (WCL) star in either of the Magellanic Clouds. This provides an opportunity to extend the local line luminosity calibrators to include WC7 stars at LMC metallicity. However, our WCL sample consists of only M10. Smith et al. (1990) find that Galactic late-WC stars have lower C IV 5808 fluxes than WC4 stars, with an average emission line luminosity of $3.81 \pm 0.46 \times 10^{35}$ erg s^{-1}, therefore suggesting M10 is unusually luminous and may not be typical.

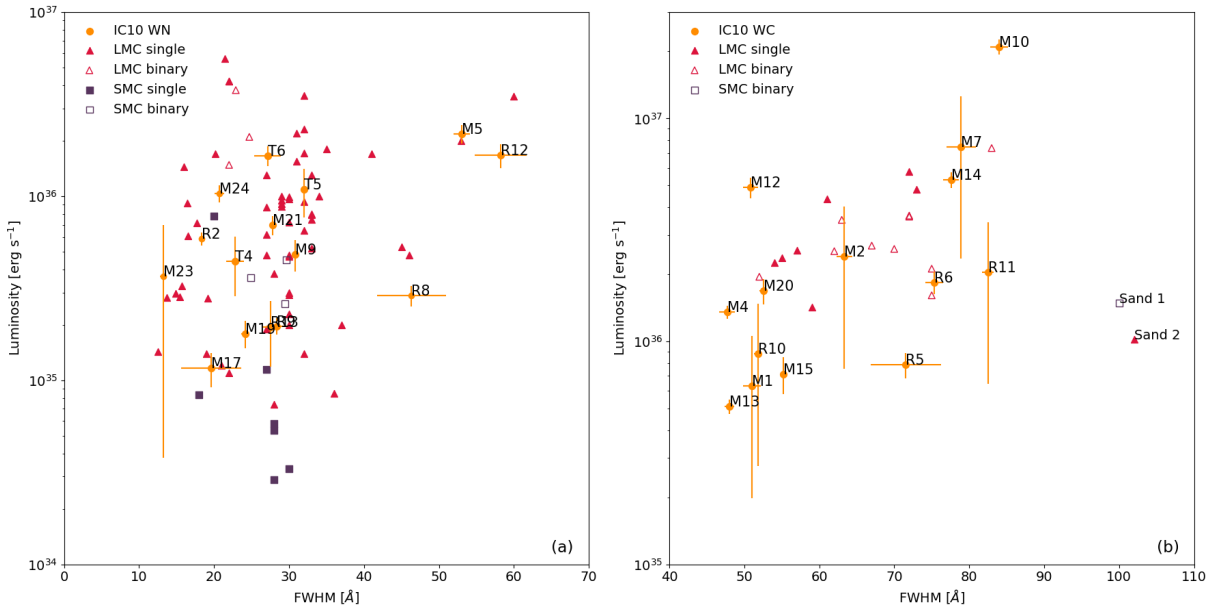

Figure 2.12: Shows the relationship between FWHM and line luminosity for (a) WN stars using the He II 4686 emission line, and (b) WC and WO stars using the C IV 5808 emission line. The corresponding host galaxy for each WR can be identified from plot symbol and colour using the following; LMC (red triangles), SMC (blue squares), and IC10 (yellow circles). For the Magellanic cloud WR stars, binary and single stars can also be distinguished between by open and filled plot symbols respectively. LMC data taken from Crowther & Hadfield (2006), Schnurr et al. (2008), and Foellmi et al. (2003b). SMC data from Foellmi et al. (2003a) and Crowther & Hadfield (2006).

2.5 Discussion

2.5.1 WR Content

Table 2.15 provides a comparison between IC10 and Magellanic Cloud global properties. The size and low metallicity of IC10 has meant that it had previously been considered as a SMC-like galaxy, however when considering the revised metallicity, the presence of WC stars, and average line luminosity comparisons, IC10 bears closer resemblance to the LMC than the SMC.

The total number of spectroscopically confirmed WR stars in IC10 has increased to 29, with a WC/WN ratio of 1.0±0.4, putting aside the intermediate WN/C star M5. From Table 2.15, if we take the LMC WR content, which one can consider to be essentially complete (Massey et al., 2015b), and scale this to the IC10 SFR of 0.045 $M_\odot$ yr^{-1} we find the expected number of WR stars is ∼28, which agrees well with our result and suggests that the IC10 WR survey is also relatively complete.

The WC/WN ratio of IC10 is substantially higher than the LMC value of ∼0.2, suggesting an excess of WC stars. Deep imaging reveals a further 6 potential candidates, and if all 6 remaining candidates were confirmed as WN stars, the WC/WN ratio would fall again to 0.70±0.24.

Whilst we acknowledge that the method outlined here has limitations regarding the identification of WR stars located in dense local stellar environments, we consider this survey near complete. It should also be noted that a recent survey of the LMC has identified weak emission line WN3 stars, with characteristically faint magnitudes of -2.5 ± 0.5 mag (Massey et al., 2014, 2015b). The He II C sensitivity limit of our survey however is -2.4 mag for a 3σ detection, which should be sufficient to identify some of the faint stars belonging to this class. Considering these faint WN3 +abs stars comprise ∼ 6% of the LMC WR population, we are confident a huge hidden population of WR stars does not remain undiscovered within IC10.

Table 2.15: Comparing galactic and individual star forming region properties of Local Group members with similar metallicity to IC10. Distances to the LMC and SMC were taken as 50 kpc and 60 kpc respectively (Westerlund, 1990). 30 Dor. refers to the 30 Doradus star forming region within the LMC, HL 111/106 refers to the central star forming region of IC10. Bracketed values reflect potential changes to the WR number and WC/WN ratio in IC10 should all 6 potential WR candidates be successfully confirmed as WN stars.

Galaxy	Distance [kpc]	Log$\frac{O}{H}$+12	*Ref*	10^{39} $L_{H\alpha}$ [erg s^{-1}]	SFR [$M_\odot$ yr^{-1}]	*Ref*	R_{25} [′]	Σ_{SFR} [$M_\odot$ yr^{-1} kpc^{-2}]	*Ref*	WR [#]	WC/WN [#]	Binary Fraction [%]	*Ref*
LMC	50	8.37	a	31	0.260	c	646	0.0036	e,f	154	0.19±0.22	29	g,h,i,j
SMC	60	8.13	a	4.68	0.046	c	316	0.0016	e	12	0.1±1.0	42	k
IC10	740	8.40	b	5.64	0.045	b	6.3	0.049	e	29 (35)	1.0±0.4 (0.70±0.24)	41:	b
30 Dor.	(LMC)			14	0.108	d	15*	0.722	d	27	0.25±0.50	20	l
HL 111/106	(IC10)			1.44	0.011	b	0.30×0.46*	0.559	b	6	2.0±0.7	67	b

a: Garnett (1990); b: this work; c: Kennicutt et al. (2008); d: Kennicutt et al. (1995); e: Crowther & Bibby (2009); f: de Vaucouleurs et al. (1991) g: Breysacher et al. (1999); h: Neugent et al. (2012a); i: Massey et al. (2014); j: Massey et al. (2015b); k: Foellmi et al. (2003a); l: Doran et al. (2013);

*R_{25} radius used for all galaxies (de Vaucouleurs et al., 1991) excluding 30 Doradus (Kennicutt et al., 1995) and the ellipse used for HL 111/106 complex.

The colon following the binary fraction highlights the uncertainty in this measurement since a robust method has not been used to confirm potential binary candidates.

2.5.2 WC/WN Ratio

The evolution of single WR stars from the WN phase to the WC phase is due to mass loss, which is primarily dictated by metal-driven winds, as seen in the clear trend of increasing WC/WN ratio with metallicity in the Local Group (Massey et al., 2015a; Crowther, 2007). For IC10, however, with an LMC-like metallicity, the high WC/WN ratio remains peculiar, suggesting this relationship also depends on another parameter. From Table 2.15 we see that the SFR in IC10 is unremarkable, however the star formation surface density ($\Sigma_{\rm SFR}$) far exceeds those of the Magellanic Clouds. We therefore consider the $\Sigma_{\rm SFR}$ as a second parameter in our understanding of WC/WN ratios.

Massive stars are generally formed in clusters (Portegies Zwart et al., 2010), for which it is known from the cluster mass function that high mass clusters are rare and low mass clusters are common (Whitmore et al., 1999; Zhang & Fall, 1999). Increasing the star formation intensity extends the cluster mass function to higher masses, such that the truncation of the upper cluster mass increases for starburst regions with respect to their quiescent star forming counterparts (Gieles, 2009). A second relationship exists between cluster mass and its most massive star, proposed by Weidner & Kroupa (2006). Combining these two results allows us to draw the conclusion that regions of more intense star formation are capable of producing higher mass stars, fully sampling the IMF, whereas quiescent star forming regions would exhibit a deficit of high mass stars. This result is significant because the initial mass of the O-star can play a crucial role in the future evolution of the WR star through the WN and WC phases.

When observing LMC WN stars, Hainich et al. (2014) found that the stellar evolution tracks modelled using the Geneva group stellar evolution models (Meynet & Maeder, 2005) show that the majority of WN stars had initial masses within the range of 25-40 $M_{\odot}$. Meanwhile the progenitors of LMC WC stars are likely to have had initial masses greater than 40 $M_{\odot}$(Crowther et al., 2002; Meynet & Maeder, 2005). Therefore higher initial masses are required for single stars to progress to the WC stage.

Comparing IC10 to the LMC, with similar host metallicity environments, we see the global SFR of IC10 is lower but the star formation surface density is an order of magnitude higher (see Table 2.15). The high $\Sigma_{\rm SFR}$ will extend the stellar mass limit to higher masses, in turn increasing the frequency of higher mass stars. If IC10 has been host to a higher proportion of massive O-stars, the percentage of WR stars capable of achieving the mass-loss rates necessary to reach the WC phase would also increase and the WC/WN ratio would rise to reflect this, as is observed. Indeed, the WC/WN ratio of the dominant star-forming complex of IC10, comprising of HL106/111 (Hodge & Lee, 1990) is especially high,

as summarised in Table 2.15.

Within the Local Group, the closest analogue to the high $\Sigma_{\rm SFR}$ of IC10 is the 30 Doradus region in the LMC. A census of the WR content of 30 Doradus, within 15′ of R136, implies a ratio of WC/WN = 0.25 (Breysacher et al., 1999; Doran et al., 2013). However, putting aside main sequence very massive WN5h(a) stars, the WC/WN ratio rises to 0.42. Again, this increased ratio arises from the high $\Sigma_{\rm SFR}$ of 30 Doradus, leading to an increased frequency of high mass stars in this region and consequently a higher WC/WN ratio. Similarly, a low $\Sigma_{\rm SFR}$ at high metallicity would produce a low WC/WN ratio. By way of example, the super-solar metallicity galaxy M31 has a relatively low $\Sigma_{\rm SFR}$ and a modest WC/WN = 0.67 ratio (Neugent et al., 2012b).

2.6 Summary

In this chapter we have used deep narrow-band imaging to search IC10 for a He II 4686 magnitude excess as a proxy for WR star candidates. We identify 11 new potential WR stars and spectroscopically confirm 3 of these as WN stars, whilst rejecting one as an early M-dwarf and suggesting another is unlikely to be a WR star due to the dispersed nature of the source. The total number of WR stars in IC10 has now been raised from 26 to 29, and the WC/WN ratio has lowered to 1.0±0.4. We review previous spectral classifications and suggest updates for 3 previously confirmed WR stars, M15, M23 and M24.

We also derive an updated SFR measurement of 0.045 ± 0.023 $M_\odot$ yr^{-1} from the Hα luminosity, an increase from the previous result of 0.031 ± 0.007 (Kennicutt et al., 2008). This updated Hα SFR is intermediate between radio-derived SFRs, however we note the radio fluxes have not been corrected to eliminate non-thermal radio sources.

Using nebular emission from the H II region HL45, associated with the WR star T5, the oxygen abundance for IC10 has also been updated from 8.26 to 8.40 ± 0.04, suggesting IC10 has an LMC-like metallicity. Comparison of emission line luminosities also revealed similar results for WNE and WCE stars in IC10 and the LMC, emphasising the similarities, however the WNL and WCL results were less consistent, most likely due to the small number of stars in these categories.

Photometry revealed a further 7 potential WR candidates which have yet to be investigated, 1 of which was dismissed after visual inspection revealed the source was extended and therefore unlikely to be stellar. Despite the potential addition of these 6 new unconfirmed candidates, which would lower the WC/WN ratio to 0.70±0.24, the WC/WN ratio observed for IC10 remains peculiar. We propose the most likely explanation is due to the

high star formation surface density of the galaxy, which extends the cluster upper stellar mass limit to higher values. Assuming the WC initial mass limit is higher than for WN stars, the higher WC/WN ratio observed in IC10 would be expected as a result of the higher star formation intensity observed in this galaxy.

Chapter 3

The X-ray Properties of Wolf-Rayet Stars in 30 Doradus

3.1 Introduction

30 Doradus (30 Dor) is the brightest giant H II region in the LMC, indeed the richest star forming region in our Local Group (Kennicutt, 1984). Consequently, 30 Dor is a popular choice for multi-wavelength studies of star forming regions, and its low metallicity ($\sim$0.4 $Z_{\odot}$) means that it is perhaps our closest analogue of star-forming regions in distant galaxies, and our best opportunity to understand these regions.

At the centre resides R136, a young, compact, massive star cluster host to some of the most massive stars known (Massey & Hunter, 1998; Crowther et al., 2010). Its position far above the disk of the MW reduces the effect of Galactic dust extinction, and its relative proximity (50 kpc) allows a complete sample of the brightest stars to be obtained from X-ray to IR wavelengths

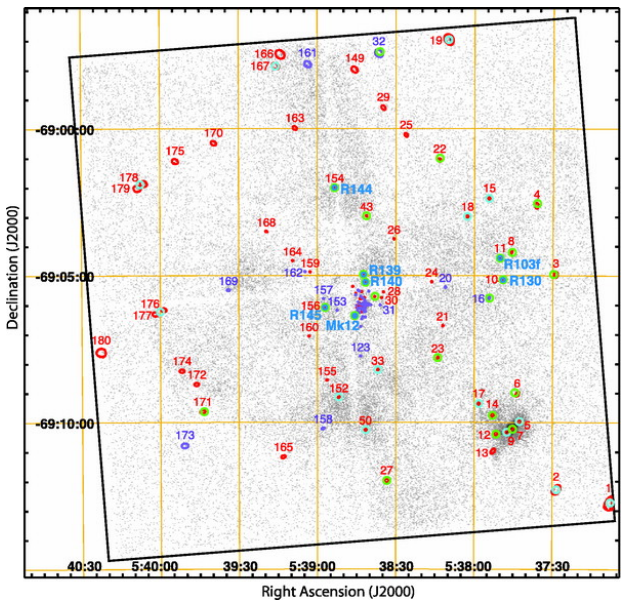

Figure 3.1: Reliable (red) and tentative (purple) point sources identified using the September 1999 Chandra observation, taken from Townsley et al. (2006b) (their Figure 1). Counterparts from 2MASS are shown in green, and previously known X-ray sources in cyan, however for clarity, sources within R136 have been omitted. The field of view shown is 20′ $\times$ 20′, or 300 $\times$ 300 pc.

Prior to 2014, X-ray observations of 30 Dor were limited, and the most complete catalogue of 30 Dor X-ray sources could be found in Townsley et al. (2006a,b) based on a $\sim$26 ks exposure centred on R136, using Chandra in September 1999. Townsley et al. (2006b) reveal 180 X-ray point sources, classifying 117 of these as reliable sources (red) and the remaining 63 as tentative sources (purple) as shown in Figure 3.1. Net counts range from 1.3 – 950 counts in the 0.5-8 keV energy band.

X-ray observations are useful probes of hot massive stars. Instabilities within their radiatively driven stellar winds result in intrinsically bright X-ray emission. Observations also help to identify massive binaries owing to their colliding winds generating additional X-ray emission. Sources which are unusually bright with respect to their bolometric luminosities are prime candidates for colliding wind binaries (CWB, see Section 1.4.3). The time-domain aspect of X-ray astronomy is also critical when monitoring the variability of massive stars. Periodic variability in X-ray lightcurves is often another clear indication of a binary system.

In this chapter we introduce the Tarantula Revealed by X-rays (T-ReX) survey, a 2 Ms Chandra survey of the Tarantula nebula (PI Townsley) which was designed to expand upon the minimal collection of archival X-ray observations. We use these data sets to discuss the X-ray properties of 30 Dor WR stars in this chapter. In Chapters 4 to 5 these findings are combined with archival observations and literature results to further our understanding of the WR stars of 30 Dor.

3.1.1 Chandra X-ray Observatory

The Chandra X-ray observatory was launched on July 23rd 1999. It follows a highly elliptical path around the Earth, taking approximately 64 hours to complete one orbit (Weisskopf et al., 2002). The detectors are capable of observing X-ray photons in the 0.1–10 keV energy band.

Unlike optical astronomy, an unconventional telescope design is required to collect incoming X-rays. High energy photons travelling perpendicular to the mirror are either transmitted through the mirror or absorbed, rather than reflected towards the focal point. Instead, to observe X-rays we must use grazing incidence to bend the photon path towards the detector.

The Chandra telescope was built using pairs of mirrors, one parabolic mirror and one hyperbolic mirror, in what is known as a Wolter-1 configuration (Wolter, 1952). These mirrors are aligned almost parallel to the incoming radiation, such that the angle of incidence (θ) is close to 90°, shown in Figure 3.2. This significantly reduces the collecting surface area (Schwartz, 2014), therefore to help combat this, X-ray telescopes usually have many nested pairs of mirrors. Chandra has four, as shown in Figure 3.2.

Whilst the nested mirrors increase the collecting area of the Chandra telescope, the effective area is slightly lower due to reflectivity. The reflectivity of each mirror is dependent on both the angle of incidence and energy of the incoming photon, as shown in Figure 3.3. Here we see that lower energy photons maintain a higher reflectivity for a high angle of

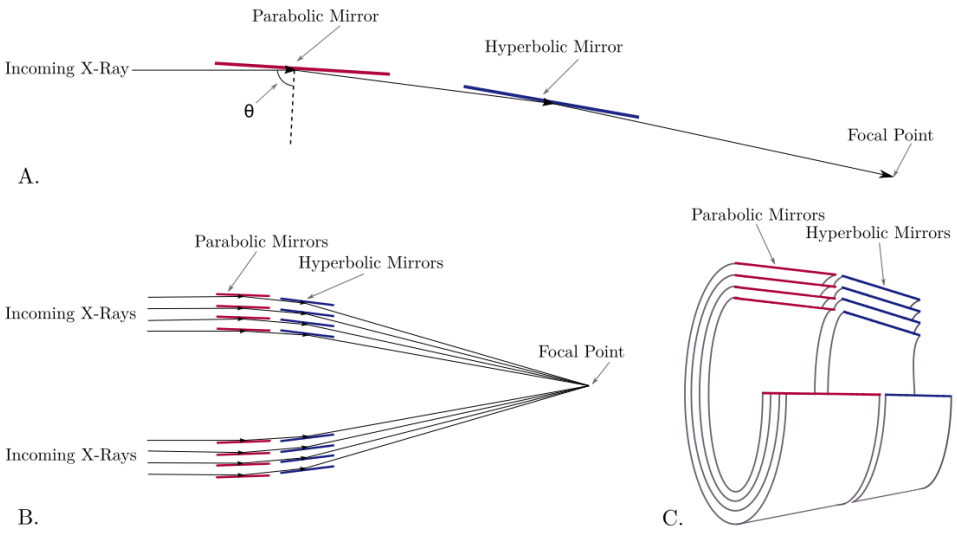

Figure 3.2: (A.) Shows the incoming X-ray light path through a single pair of parabolic (red) and hyperbolic (blue) mirrors. The angle of incidence, θ must be large to allow the X-ray photon to graze the mirrors. (B.) A schematic showing a slice through the Chandra telescope and the four mirror pairs. After two reflections the X-rays are focussed at the focal point onto the detector. (C.) Another schematic showing how the mirrors are nested within the telescope to increase the collecting surface area.

incidence compared to higher energy photons.

The varying mirror diameters correspond to different angles of incidence, therefore different energy photons will be reflected towards the detector by different amounts. Figure 3.4 shows how the effective area varies with energy for the ACIS-I instrument.

There are four instruments aboard Chandra; The Advanced CCD Imaging Spectrometer (ACIS), the High Resolution Camera (HRC), and two grating instruments (LETG & HETG). In this work, we use ACIS instrument in the ACIS-I configuration, which is a collection of 4 CCDs arranged in a 2x2 configuration.

ACIS-I records position, energy and arrival time of each incoming X-ray photon during the exposure. Since the ACIS-I detector is comprised of 4 chips, the telescope moves slightly during the exposure in a process known as dithering. This allows the detector to compensate for the gaps between these chips.

X-ray detectors are also sensitive to optical photons, therefore to remove this source, the telescopes introduce an optical blocking filter. Over time, astronomers have noted a decrease in sensitivity at low energies, which has been attributed to a build up of material on the optical blocking filters. The current consensus is that this contamination layer has been accumulating over the lifetime of the telescope, however the source is unknown

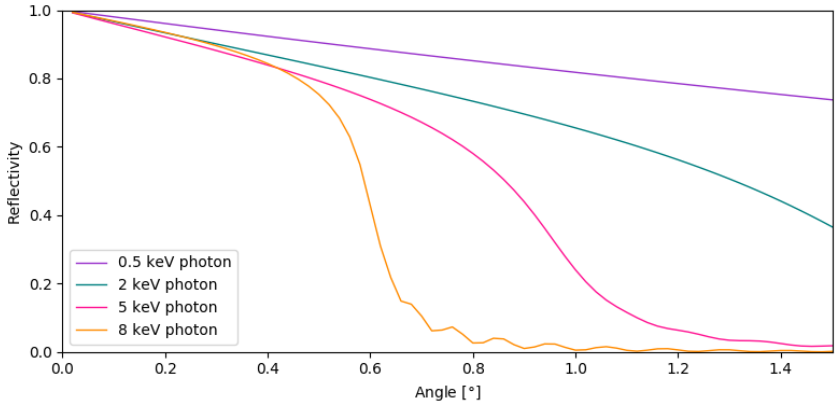

Figure 3.3: Reflectivity as a function of angle of incidence for varying incoming photon energies; 0.5 keV (purple), 2 keV (teal), 5 keV (pink), and 8 keV (orange). Data were produced using the Berkeley Laboratory's Center for X-ray Optics X-ray (CROX) interactive reflectivity tool, using an Iridium layer coating of 33nm thickness to mimic the Chandra mirror.

(Plucinsky et al., 2018). The accumulation rate has been monitored over time using known constant astronomical sources, as shown in Figure 3.5 for the ACIS-I optical blocking filter. The most recent measurements suggest a plateau in the build-up rate, however it is unsure as to whether this is due to a decrease in deposition or an increase in vaporization.

Another potential problem to address when undertaking X-ray observations is pile up. Pile up refers to the phenomenon where two or more incoming photons arrive at the same time, causing the CCD to register only one event, and therefore leading to an underestimation of the X-ray flux. Pile-up is instrument dependent and generally affects bright X-ray sources, since the higher count rate increases the likelihood of multiple photons simultaneously arriving within the same pixel. Also, the energy recorded during a simultaneous arrival event will be overestimated, as the two photons will both contribute to the measured energy. As a result, sources suffering from pile up will appear to have a fainter, harder spectrum than in reality. The effect of pile up among LMC WR stars is 10% in the worst cases (Mk34 and R140a), however for the majority of the WR sources included in this work, the effect of pile up is negligible.

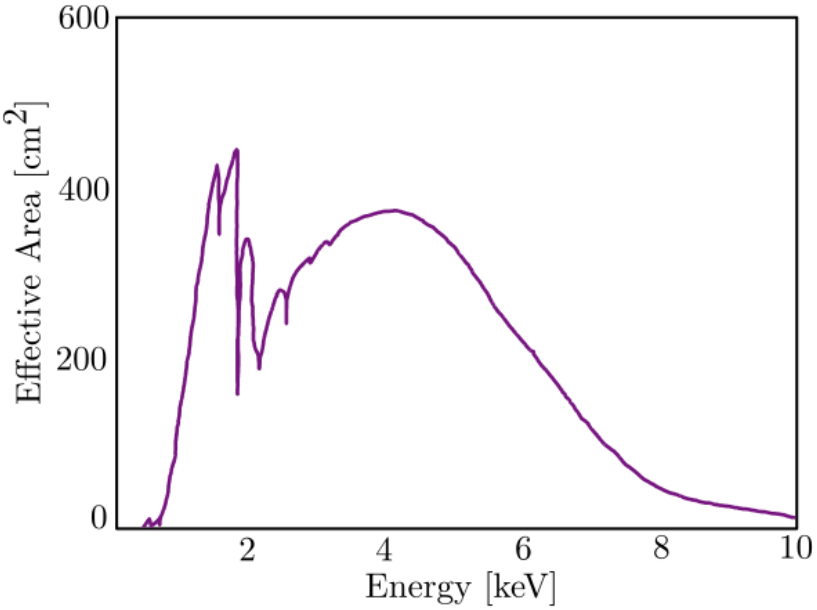

Figure 3.4: Chandra effective area as a function of energy for the ACIS I3 CCD, adapted from the Chandra Proposer's Observatory Guide.

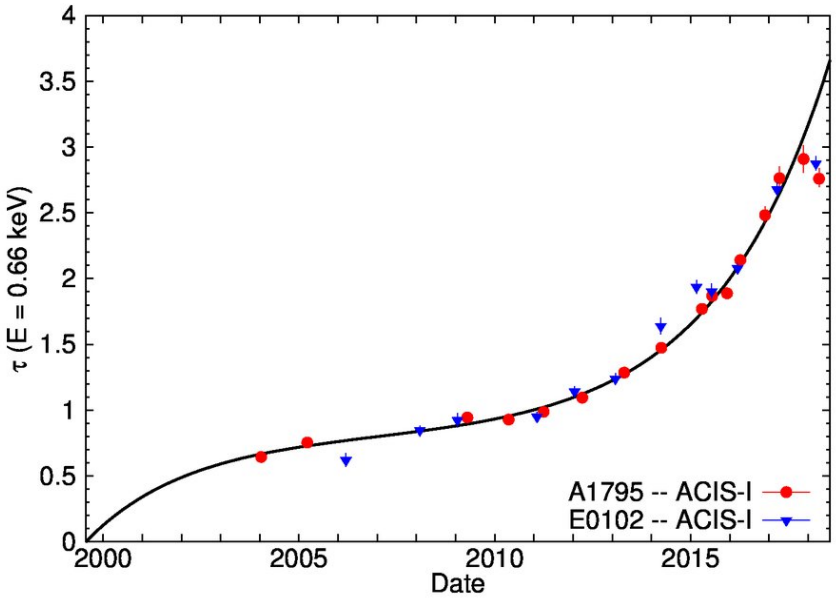

Figure 3.5: The variation in optical depth over time for ACIS-I optical blocking filter, taken from Figure 2 of Plucinsky et al. (2018). Red points show measurements derived from observations of Abell 1795, a bright cluster of galaxies, blue points use observations of E 0102.2-7219, a supernova remnant.

3.2 T-ReX Survey

As discussed in Section 3.1, prior to 2015, X-ray observations of 30 Dor were limited to relatively short, shallow exposures revealing only the brightest X-ray sources. To rectify this, the 2 Ms Tarantula Revealed by X-rays (T-ReX, PI Townsley) Chandra X-ray visionary programme was obtained. It was tasked with producing deep X-ray observations of 30 Dor, with the intention of revealing a more complete picture in the high energy regime.

Table 3.1: A log of the Chandra observations of 30 Dor showing the 3 archival epochs, and 51 T-ReX epochs.

Observation ID	MJD	Exposure Time [s]	Observation ID	MJD	Exposure Time [s]
5906	53756.79	12317	17486	56995.57	33541
7263	53757.70	42528	17555	56997.69	55247
7264	53765.63	37593	17561	57011.72	54567
16192	56780.17	93764	17562	57016.63	42031
16193	56785.43	75997	16444	57018.96	41440
16612	56788.09	22672	16448	57067.50	34599
16194	56789.83	31336	17602	57072.58	51705
16615	56792.35	45170	16447	57107.23	26868
16195	56801.59	44405	16199	57108.85	39461
16196	56807.00	67112	17640	57112.55	26318
16617	56808.06	58857	17641	57116.82	24638
16616	56811.94	34530	16445	57169.01	49310
16197	56814.52	67799	17660	57171.62	38950
16198	56819.85	39465	16446	57175.49	47547
16621	56822.62	44396	17642	57181.22	34438
16200	56834.83	27360	16449	57293.23	24631
16201	56859.93	58390	18672	57334.04	30574
16640	56862.47	61676	18706	57336.72	14776
16202	56888.65	65128	18720	57358.45	9832
17312	56891.27	44898	18721	57364.72	25598
16203	56902.53	41422	17603	57365.64	13778
17413	56908.64	24650	18722	57367.38	9826
17414	56913.52	17317	18671	57369.99	25617
16442	56955.57	48343	18729	57377.92	16742
17545	56958.18	34530	18750	57407.03	48318
17544	56962.70	25636	18670	57408.87	14565
16443	56975.97	34527	18749	57409.68	22153

Using the ACIS-I instrument on-board the Chandra Observatory, 51 observations were

obtained between May 2014 and January 2016. These 51 epochs from T-ReX are complemented with 3 further archival Chandra observations from ∼8 years prior to produce a catalogue of 54 observations across a 10 year baseline, shown in Table 3.1. Each image has a $16' \times 16'$ field of view, centred on R136, corresponding to ∼235×235 pc at the distance of the LMC. Chandra is well suited for observing this dense region. Its high spatial resolution (∼$0.5''$) is capable of differentiating individual sources, and its low background noise will help the detection of faint sources.

The raw data were processed by Patrick Broos and Leisa Townsley using the ACIS-Extract pipeline (Broos et al., 2010). The data for the extracted WR sample were then provided to us for analysis.

3.3 T-ReX WR Sample

Overall, the T-ReX catalogue comprises nearly 4000 X-ray point sources (Townsley, in prep), however for the purpose of this study we restrict our sample to the 21 WR stars within 30 Dor, identified using the Breysacher et al. (1999) catalogue and supplemented by VFTS 682, from the VLT Flames Tarantula Survey by Evans et al. (2011), with additional information sourced from Doran et al. (2013). T-ReX successfully detects 20/21 WR sources (see Table 3.2), the exception being R136b. Two of the 20 sources host multiple WR stars, R140a and R136a, and we also note that R136a is detected as two X-ray sources, R136a1/a2 and R136a3/a6, again see Table 3.2.

Table 3.2: Basic properties of the 20 WR sources detected in T-ReX. Source counts refer to the total number of counts detected between 0.5-8 keV. Background counts refer to the total number of counts detected within the background aperture. Area scale describes the ratio between the background aperture size and source aperture size. Sources highlighted in pink were also present in the Townsley et al. (2006b) catalogue.

CXOU J	Source	BAT99	VFTS	Spectral Type	Ref	Total Counts	Background Counts	Area Scale	Net Counts
053749.06-690508.1	R130	92		WN/C+B1I	(1)	1293±36	877±30	7.59±3.90	1178±70
053833.62-690450.4	R135	95	402	WN7h	(1)	159±13	539±23	27.62±0.84	139±13
053836.40-690657.5	VFTS427	96	427	WN8(h)	(1)	83±9	879±30	55.17±0.54	67±9
053838.82-690649.6	Mk51	97	457	O3.5If/WN7	(2)	63±8	512±23	40.09±0.56	50±8
053839.15-690621.2	Mk49	98		WN6(h)	(1)	83±9	509±23	29.52±0.76	66±9
053840.22-690559.8	Mk39	99	482	O2.5If*/WN6	(2)	8126±90	839±29	5.72±5.06	7979±158
053840.54-690557.1	R134	100	1001	WN7h	(1)	58±8	357±19	15.25±1.24	35±8
053841.59-690513.4	R140a1/a2	101/102	507	WC4+WN6+O	(1)	54393±233	565±24	1.71±13.90	54062±2696
053841.62-690515.1	R140b	103	509	WN6+O5(h)	(1)	705±27	2862±53	9.24±5.79	395±196
053842.38-690602.8	R136a[1 2 4 5 7 8]	108/109		WN5h+WN5h+O2-3V+ O2If+O3III+O2-3V	(1,3) (3)	5457±74	1054±32	0.97±33.47	4369±37493
053842.32-690603.4	R136a3/a6	106		WN5h+O2If	(1,3)	1063±33	958±31	1.68±18.42	492±6254
053842.90-690604.9	R136c	112	1025	WN5h	(1)	7460±86	495±22	0.99±22.47	6960±11351
053843.09-690546.9	Mk30	113	542	O2If*/WN5	(2)	252±16	623±25	13.33±1.87	205±17
053843.20-690614.4	Mk35	114	545	O2If*/WN5	(2)	227±15	464±22	18.01±1.20	201±15
053844.25-690605.9	Mk34	116		WN5h+WN5h	(4)	71607±268	(495±22)	(0.99±22.47)	71107±11353
053847.48-690025.1	R146	117	617	WN5ha	(1)	855±29	1038±32	6.56±4.91	697±122
053853.36-690200.9	R144	118		WN5-6h+WN6-7h	(5)	1402±37	1426±38	10.24±3.69	1263±63
053855.52-690426.7	VFTS 682		682	WN5h	(1)	314±18	820±29	72.75±0.39	303±18
053857.06-690605.6	R145	119		WN6h+O3.5If*/WN7	(6)	806±28	771±28	36.71±0.76	785±28
053911.27-690201.2	R147	122	758	WN5h	(7)	143±12	615±25	15.30±1.62	103±13

For brevity, R136a[1 2 4 5 7 8] shall be referred to as R136a1/a2.
For Mk34 we adopt the background counts and aperture size from the closest neighbour, R136c, shown in parenthesis.
1. Doran et al. (2013); 2. Crowther & Walborn (2011); 3. Crowther et al. (2016); 4. This work (Chapter 5); 5. Sana et al. (2013a); 6. Shenar et al. (2017)

Table 3.2 lists the 20 WR sources, and their spectral types (Sana et al., 2013a; Crowther & Walborn, 2011; Doran et al., 2013; Crowther et al., 2016; Shenar et al., 2017), detected in the T-ReX survey. It also shows the number of counts between 0.5-8 keV detected from each source over the full 2 Ms exposure, however to determine the net number of counts we must correct for the background. Total counts were determined using a circular aperture which aimed to encompass 90% of the psf. Since the psf varies across the source of the detector, this results in aperture sizes ranging from $\sim$0.8″ on axis, up to $\sim$10″ on the periphery. Background counts are determined by defining an aperture near to the source in a region void of other sources. The background counts column in Table 3.2 shows the total number of background counts between 0.5-8 keV detected for each source. Since the source aperture and background aperture are defined as different sizes, before applying the background correction we must first scale the background counts. The area scale column shows the ratio between the size of the background aperture and source aperture, such that net counts can be derived as Equation (3.1).

$$\text{Net Counts} = \text{Total Counts} - \frac{\text{Background Counts}}{\text{Area Scale}} \tag{3.1}$$

16″ × 16″ X-ray images of all 20 WR sources can be found in Figures 3.6a to 3.6c. From these figures we can assess the strength of the X-ray source and the local environment. We can see that most WR stars appear to be relatively isolated from other X-ray sources. Some notable exceptions include R136a and R140a1/a2.

R136a resides within a crowded X-ray region, indeed Figure 3.7a shows a HST WFC3 F555W optical image (De Marchi et al., 2011) of the R136a region, with the Chandra X-ray contours overlaid for the same field of view. We can see the X-ray contours include multiple bright sources in addition to R136a, such as R136c (WN5h, Doran et al. (2013)), H36 (O2If, Crowther et al. (2016)) and H42 (O3V+O3V, Massey et al. (2002)). The X-ray image is not, however, capable of resolving this region to the same extent as HST. It is important to note therefore, that the source we refer to as R136a1/a2 and R136a3/a6 actually contain a multitude of sources.

On a similar tone, shown in Figure 3.7b is the same HST F555W optical image for the R140 region. We can see that R140a1/a2 and R140b lie in close proximity, and whilst distinguishable in the optical image, the sources are more blended in X-rays. Care is therefore needed when distinguishing X-ray photons between R140a, the brighter star, and R140b, the fainter star.

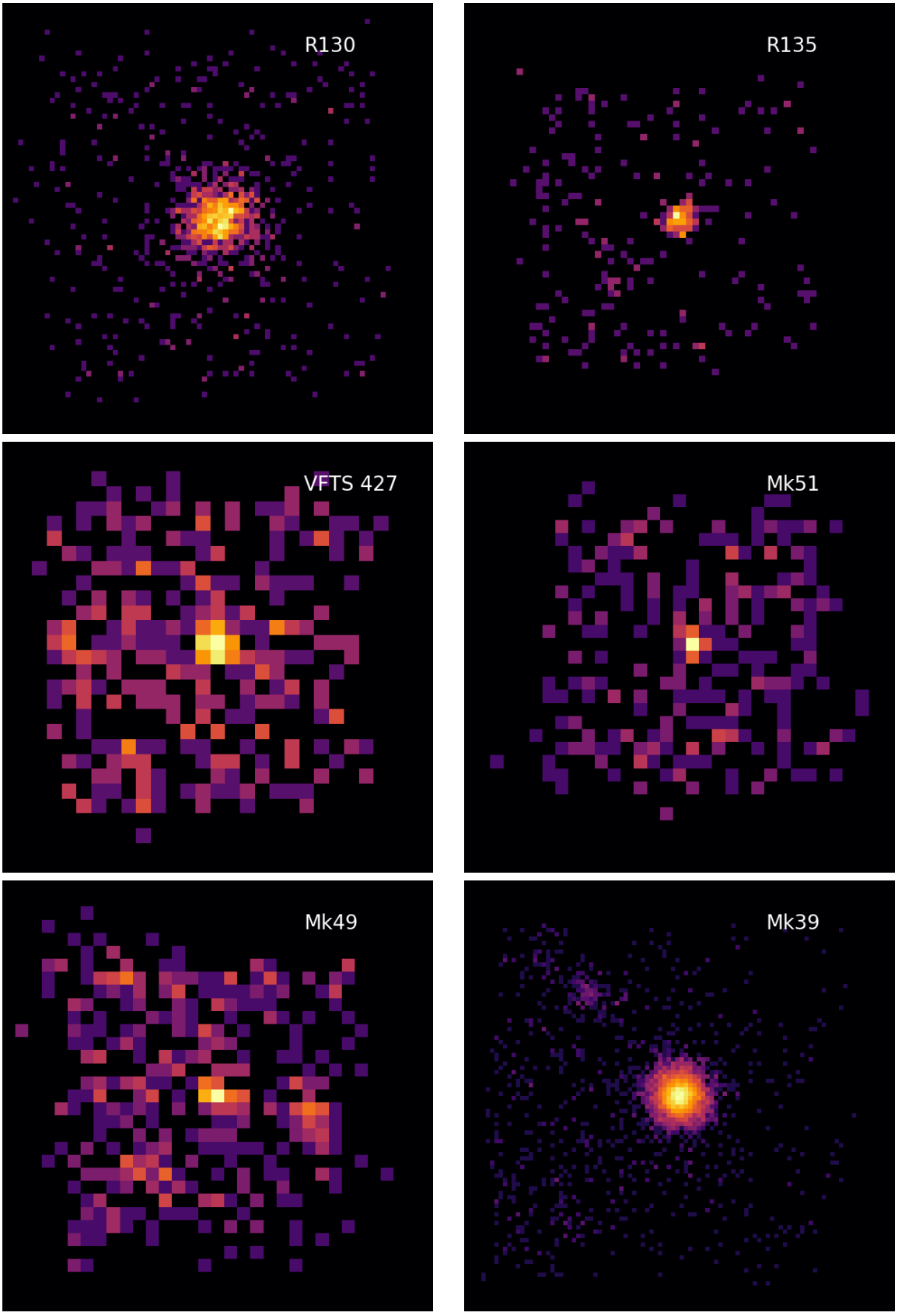

Figure 3.6a: Co-added X-ray images of each WR source. Images are centred on the source and show a ∼16x16″ field of view, ∼4x4 pc for a distance of 50 kpc. North is up and East is to the left.

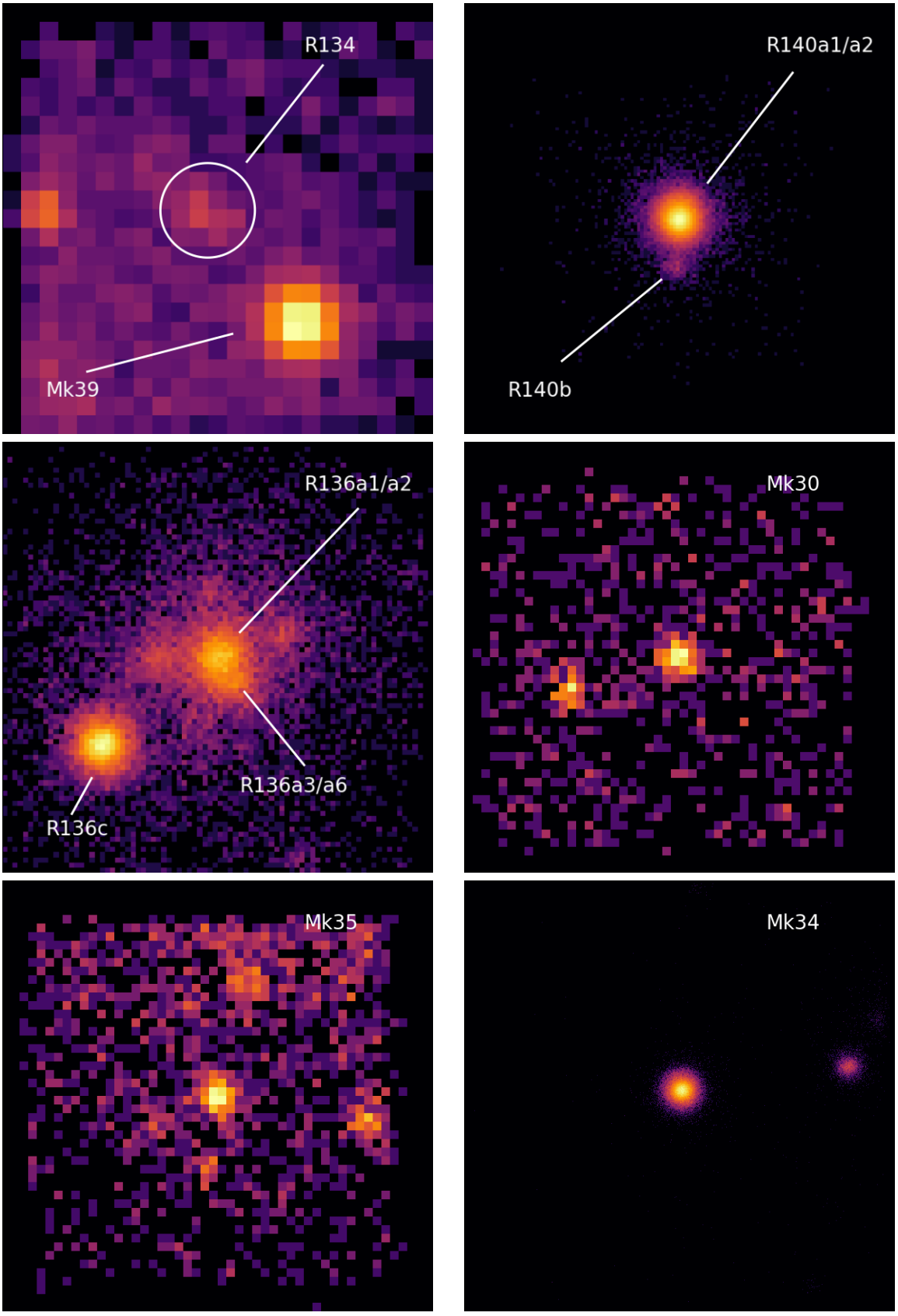

Figure 3.6b: Co-added X-ray images of each WR source. Images are centred on the source and show a ∼16x16″ field of view, ∼4x4 pc for a distance of 50 kpc. North is up and East is to the left.

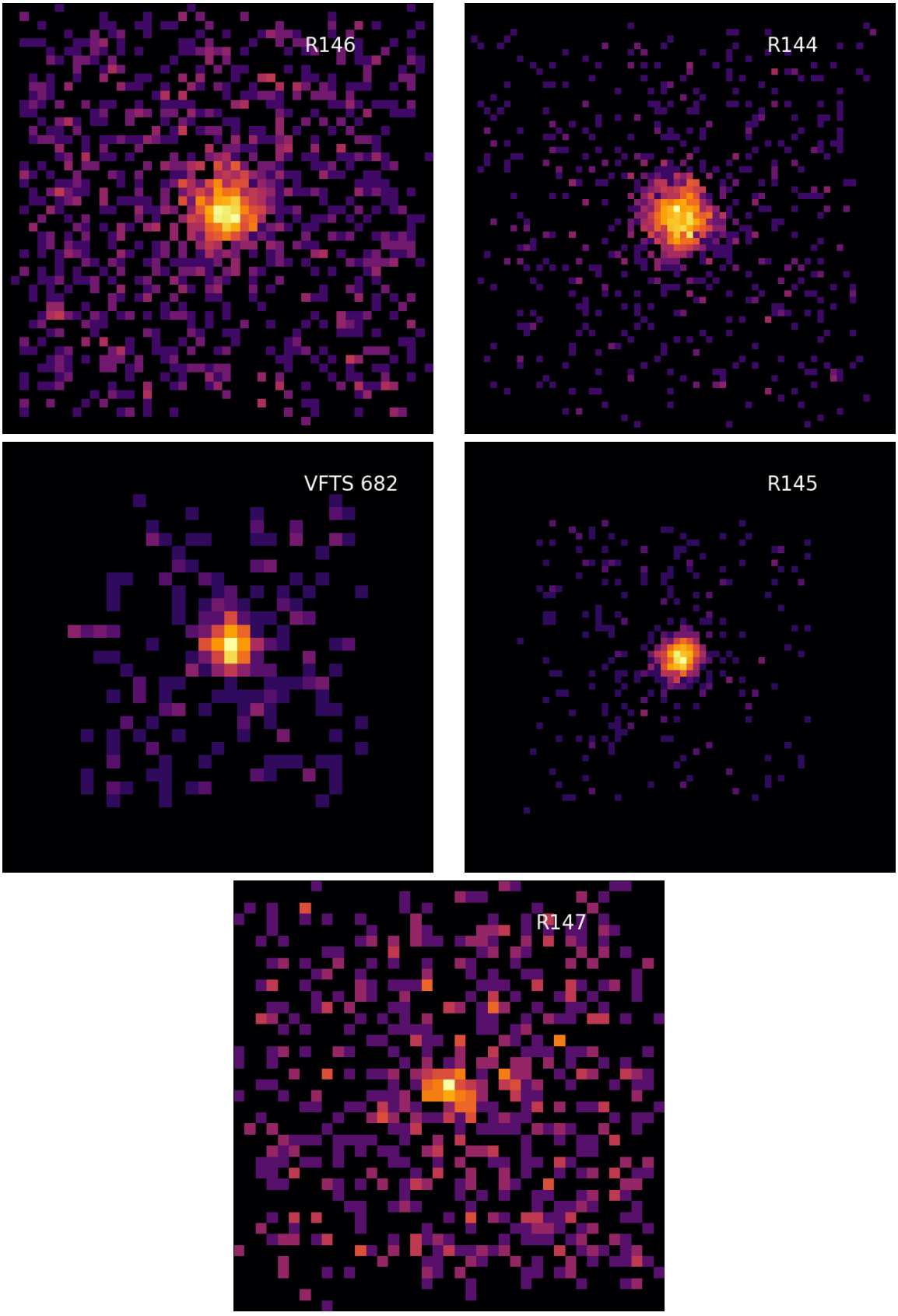

Figure 3.6c: Co-added X-ray images of each WR source. Images are centred on the source and show a ∼16x16″ field of view, ∼4x4 pc for a distance of 50 kpc. North is up and East is to the left.

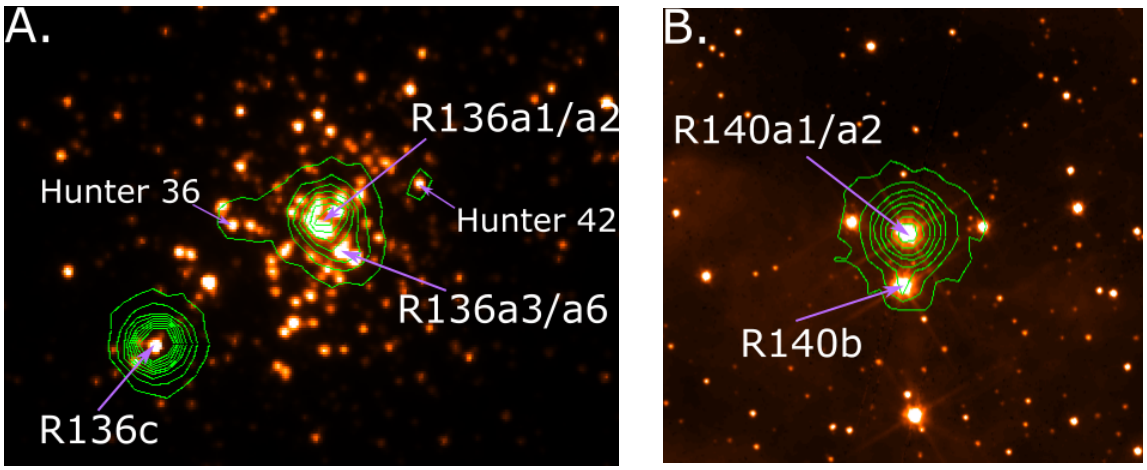

(a) R136a/R136c (b) R140a/R140b

Figure 3.7: HST F555W optical image of (a) R136a/R136c central region and (b) R140 stars, with Chandra X-ray contours overlaid in green. North is up and East is left. In panel (a) the separation between R136a1/a2 and R136c is $\sim 4''$, or ~ 1 pc. In panel (b) the separation between R140a1/a2 and R140b is $\sim 1.5''$, or ~ 0.4 pc. Bright X-ray sources have been labelled, including Hunter 36 (O2If) and Hunter 42 (pair of O3V).

3.4 X-ray Variability

Our first objective was to assess the variability of each source. To achieve this we monitored how count rate varied with time. The number of counts received between 0.5–8 keV is stored within the 'source.photometry' file for each epoch.

Due to the variation of the position of the source on the detector between epochs, the recorded number of counts is not directly comparable between epochs. The sensitivity across the detector changes with position, therefore we must account for this using the associated response function (ARF), which quantifies the effective area as a function of energy.

For each epoch we store the maximum spectral response value. From this list of maximum spectral responses across all epochs we then identify the maximum spectral response again, which we refer to as the ARF-standard. Finally, we scale the remaining maximum spectral response values for all other epochs relative to the ARF-standard to derive the sensitivity factor for each epoch. The corrected count rates are then derived using Equation (3.2).

$$\text{Corrected Count Rate} = \frac{\text{Counts}}{\text{Exposure Time} \times \text{Sensitivity Factor}} \tag{3.2}$$

Plots demonstrating how the count rate varies with time can be found in Figures A.1a to A.1h in Appendix A. To quantify the variability we used multiple techniques described in the subsections below, however discussion of variability is deferred until Chapter 4. The variability results for each source are shown on the plots in Figures A.1a to A.1h and summarised in Table 3.3

Table 3.3: Variability parameters of WR sources detected in T-ReX. The mean count rates are derived using the corrected exposure times. The critical value for χ^2_ν, taking 53 degrees of freedom and a significance of 5%, is 70.99. -log(P_{KS}) refers to the log probability of the Kolmogorov-Smirnov (KS) variability test.

CXOU J	Source	Mean Count Rate [counts/ks]	Max Count Rate [counts/ks]	χ^2_ν	χ^2_{red}	C	MAD [%]	-log(P_{KS})
053749.06-690508.1	R130	0.669 ± 0.019	1.146	66.7	1.259	33.9	17.9	0.79
053833.62-690450.4	R135	0.092 ± 0.008	0.320	79.9	1.507	25.7	53.2	0.82
053836.40-690657.5	VFTS 427	0.042 ± 0.005	0.131	57.3	1.082	15.9	118.2	0.05
053838.82-690649.6	Mk51	0.036 ± 0.005	0.152	53.1	1.003	13.9	140.5	0.05
053839.15-690621.2	Mk49	0.047 ± 0.006	0.276	55.8	1.053	15.2	76.7	0.17
053840.22-690559.8	Mk39	4.478 ± 0.050	10.036	1792.8	33.827	852.0	27.1	260.65
053840.54-690557.1	R134	0.028 ± 0.005	0.244	117.8	2.223	20.8	–	1.91
053841.59-690513.4	R140a1/a2	38.309 ± 0.165	45.514	270.8	5.109	136.2	5.2	8.71
053841.62-690515.1	R140b	0.314 ± 0.016	1.362	247.9	4.678	69.8	49.9	0.88
053842.38-690602.8	R136a1/a2	2.373 ± 0.036	3.550	198.7	3.749	98.0	18.1	1.93
053842.32-690603.4	R136a3/a6	0.293 ± 0.013	0.927	285.7	5.391	100.2	67.9	0.16
053842.90-690604.9	R136c	3.776 ± 0.045	7.363	338.5	6.387	148.2	8.4	10.62
053843.09-690546.9	Mk30	0.116 ± 0.008	0.435	74.8	1.412	31.2	43.6	0.45
053843.20-690614.4	Mk35	0.111 ± 0.008	0.240	50.6	0.954	21.3	36.8	0.60
053844.25-690605.9	Mk34	39.218 ± 0.147	79.124	6941.1	130.965	4023.8	7.4	16.57
053847.48-690025.1	R146	0.396 ± 0.015	0.732	68.6	1.294	34.8	31.5	4.54
053853.36-690200.9	R144	0.674 ± 0.019	1.992	138.1	2.605	63.7	23.7	2.62
053855.52-690426.7	VFTS 682	0.173 ± 0.010	0.401	59.2	1.116	29.4	35.4	1.95
053857.06-690605.6	R145	0.457 ± 0.016	1.127	217.5	4.103	116.6	38.3	4.46
053911.27-690201.2	R147	0.066 ± 0.007	0.268	74.4	1.404	21.6	74.5	0.81

3.4.1 Chi-squared (χ^2) - Gaussian Variability Statistic

Chi-squared (χ^2) is a Gaussian method for measuring variability. Deriving χ^2 requires both an expected, μ, and observed, n, value, therefore here we use expected and observed counts.

To derive the expected number of counts, μ, we find the mean count rate across all epochs for each WR source following Equation (3.3), where t and F are the exposure time and sensitivity factor for each epoch respectively. We then use the mean count rate with the corrected individual epoch exposure times to find an expected number of counts for each observation. The observed number of counts, n, is found from taking the net counts between 0.5–8 keV.

$$\text{Mean Count Rate} = \frac{\sum \text{Counts}_i}{\sum t_i \times F_i} \tag{3.3}$$

The Pearson's χ^2 statistic can be calculated as shown in Equation (3.4) using the values we have defined earlier. χ^2 is a useful statistic to test a hypothesis. Here we define our null hypothesis H_0 as: 'The number of counts are constant per unit time' and our alternative hypothesis H_1 as: 'The number of counts will vary per unit time'. To determine whether our null hypothesis is valid, we must first know the number of degrees of freedom, ν. We can calculate this by taking the number of independent points we are fitting, 54, and subtracting the number of fitting parameters we use, 1, to find ν=53. We must also choose our significance level, α, which we set at 5%.

$$\chi^2_\nu = \sum \frac{(n_i - \mu_i)^2}{\mu_i} \tag{3.4}$$

Figure 3.8 shows the shape of the χ^2 distribution for ν=53. Also shown, shaded in orange, is the rejection region, which corresponds to our 5% significance level. The rejection zone begins at the critical value, which can be derived using probability tables, and here we find it to be 70.993[1].

We can now derive χ^2 values for each WR source. Should the result be less than the critical value, 70.993, we can say our null hypothesis is true, and the source would be considered constant. If, however, our χ^2 value is greater than the critical value, it would fall in the rejection zone, and therefore our null hypothesis is false and the source is variable.

A similar statistic is the reduced χ^2, χ^2_{red}, shown in Equation (3.5). This value has also been derived for each source and is shown in Figures A.1a to A.1h and Table 3.3. A $\chi^2_{\text{red}} >> 1$ indicates a poor fit to the data, and so would suggest the source is variable. In contrast, a $\chi^2_{\text{red}} < 1$ implies the data is being over-fitted, perhaps due to an over estimation

[1] χ^2 probability table found at: https://www.medcalc.org/manual/chi-square-table.php

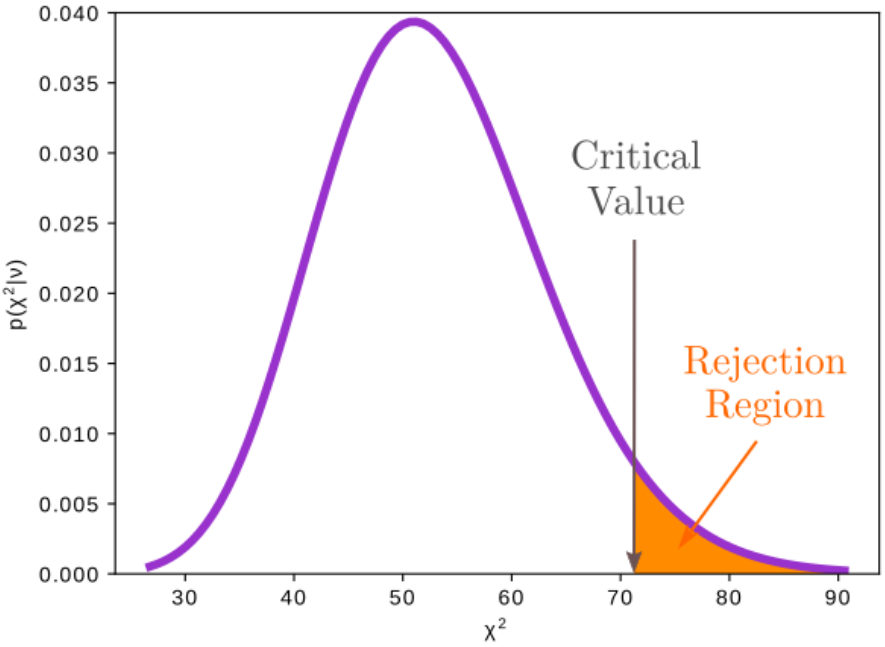

Figure 3.8: χ^2 distribution for 53 degrees of freedom. The orange shaded region shows the rejection zone at the 5% significance level, α=0.05. The critical value is 70.993.

of the errors. When $\chi^2_{\rm red} = 1$, we can infer that the model and the data agree, and so the source is not variable.

$$\chi^2_{\rm red} = \frac{\chi^2}{\nu} \tag{3.5}$$

A summary of the χ^2 and reduced χ^2 results can be found in Table 3.3 and these findings are discussed for individual WR stars in Section 3.7.

3.4.2 C - Poisson Variability Statistic

An alternative method would be to use a Poissonian approach to determine variability. The Poisson probability distribution is shown in Equation (3.6), with the log likelihood function shown in Equation (3.7). The C-statistic (C) is the difference between two log likelihood functions, one in which the expected value assumes a constant count rate, and the other where the expectation is variable and equal to the observed count rate (Cash, 1979). The equation for C is shown in Equation (3.8).

$$\mathrm{P}(n|\mu) = \frac{e^{-\mu}\ \mu^n}{n!} \tag{3.6}$$

$$\ln(\mathrm{P}) = \sum_i \ln(\frac{e^{-\mu_i}\ \mu_i^{n_i}}{n_i!}) = \sum_i \ln(e^{-\mu_i}) + \ln(\mu_i^{n_i}) - \ln(n_i!) \tag{3.7}$$

$$\mathrm{C} = \ln(\mathrm{P}) = \sum_i n_i - n_i \ln(n_i) - \mu_i + n_i \ln(\mu_i) \tag{3.8}$$

The calculated C for each source can be found in Table 3.3, where a larger C suggests the source is more variable compared to those with smaller C.

3.4.3 Median Absolute Deviation

The median absolute deviation, MAD, is another useful statistic which can assess the amplitude of variability of the source count rates, without being heavily influenced by extreme outliers.

$$\mathrm{MAD} = \mathrm{median}|Y_i - \mathrm{median}(Y_i)| \tag{3.9}$$

The MAD is derived following Equation (3.9). Taking the corrected count rates (Y_i) for each epoch, we find the median value (median(Y_i)). We then continue by calculating the absolute difference between the corrected count rate and median value for each epoch, and finally we compute the MAD by finding the median value of these differences. Again the MAD values for each epoch can be found in Figures A.1a to A.1h and Table 3.3, where we convert the median values to percentages for ease.

It is clear that sources with a low count rate tend to have high MAD values. This is expected because statistical fluctuations in the count rate for weak sources correspond to a fractionally large proportion of the total count rate, and therefore will translate to a large MAD. This highlights the danger in solely using the MAD values to identify variable sources.

3.5 Spectra

For each photon, Chandra records the time, position and the channel value (pi), which is synonymous to the energy of the photon. To convert pi to an energy we can use Equation (3.10).

$$\mathrm{Energy\ [eV]} = \mathrm{pi} \times 14.6 \tag{3.10}$$

Using this information, it is possible to construct a spectrum for each WR source, as shown in Figures 3.9a to 3.9d. Here we can see number of counts against energy in the 0.5-

8 keV range, summed across all epochs, where the red and grey lines show the total counts and background counts respectively. The spectra of the WR sources vary significantly, showing huge differences in the number of counts accumulated, the peak energy values and the distribution shapes. We can describe a spectrum as hard or soft depending on the relative proportion of high energy and low energy photons observed in the spectrum. To quantify this we can use the hardness ratio as shown in Equation (3.11).

$$\text{Hardness} = \frac{\text{Number of photons with energies between 2–8 [keV]}}{\text{Number of photons with energies between 0.5–2 [keV]}} \tag{3.11}$$

Another important point to note is that Mk34 (053844.25-690605.9) and R140a1/a2 (053841.59-690513.4) suffer from pile-up. As discussed in Section 3.1.1, pile-up affects bright sources and can have implications on the shape of the spectra, making it fainter and harder. Pile up corrections are determined using reconstructed spectra generated by ACIS-Extract and were provided by Patrick Broos.

An empirical model is used to generate photons, which are then passed through a detailed operational model of the Chandra satellite, detectors and data analysis procedures to simulate the observed X-ray source spectrum. Since the photon production follows a Poisson distribution, pile-up naturally occurs within this simulation. The model spectrum is then compared with the observed spectrum, and the parameters of the operational model are adjusted until a good fit is achieved. Once completed, the simulation is repeated whilst prohibiting the simultaneous arrival of multiple photons, effectively disabling pile-up. The resulting spectrum represents a reconstruction of the X-ray source spectrum without pile-up (Broos et al., 2011).

The affect of pile up on Mk34 was considered by Pollock et al. (2018) and the results are presented in Figure 3.10. Using the observed spectra and reconstructed spectra for each epoch, Pollock et al. (2018) derive the X-ray luminosity (red) and column density (blue). The filled and open symbols demonstrate the difference between the data with and without the influence of pile-up, respectively.

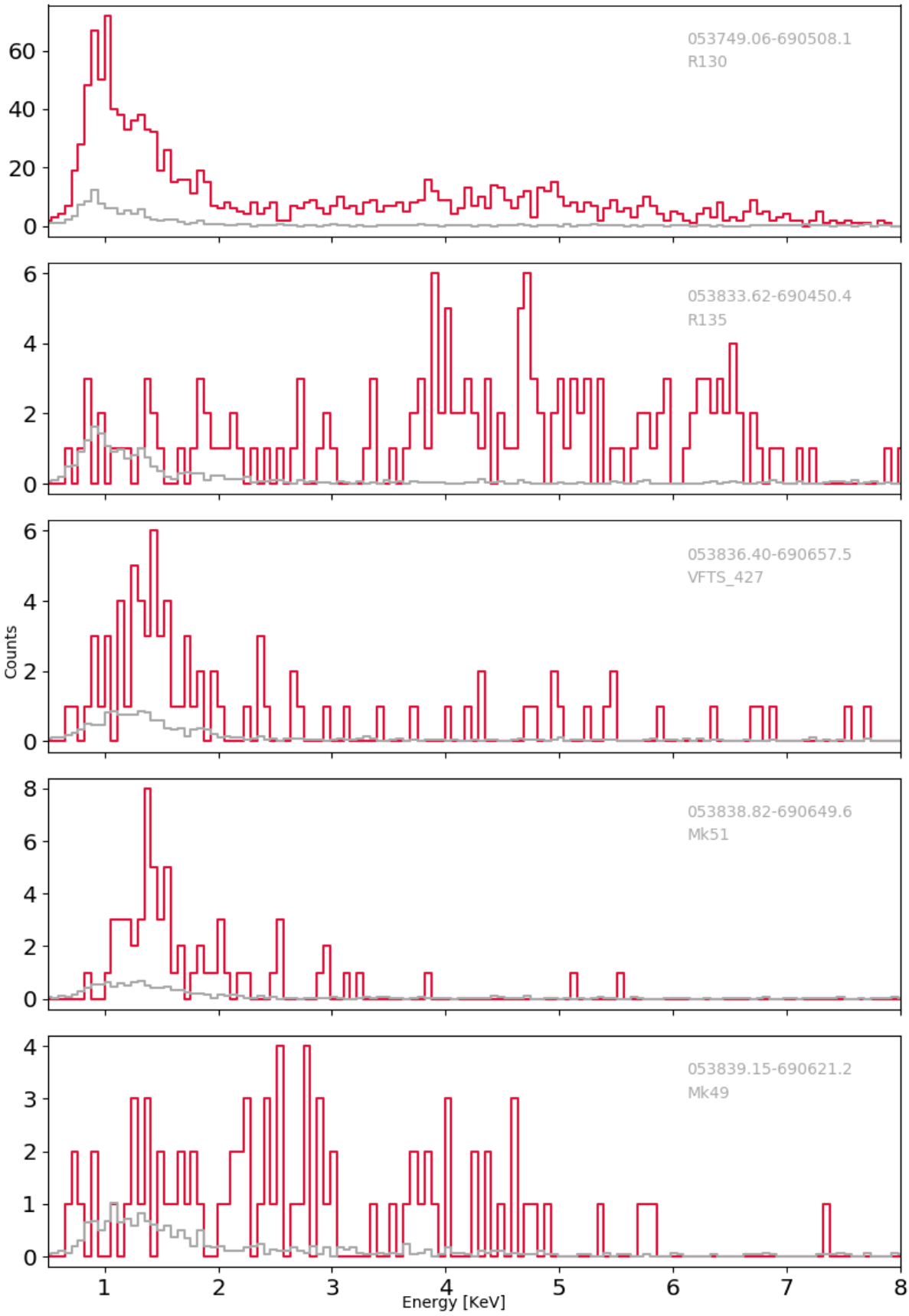

Figure 3.9a: X-ray spectra for all WR sources in the sample. Red line shows the total counts and the grey line shows the scaled background counts.

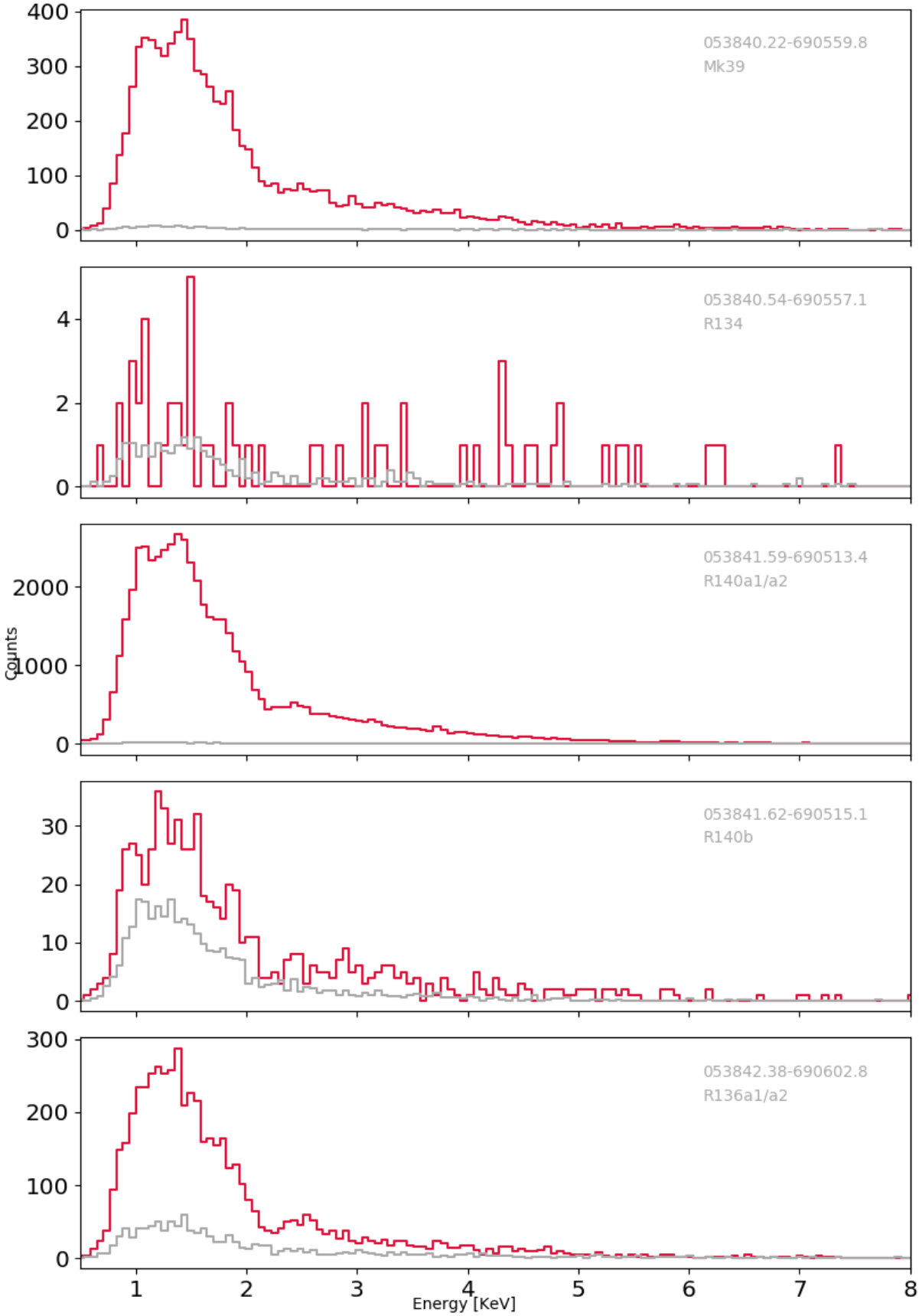

Figure 3.9b: X-ray spectra for all WR sources in the sample. Red line shows the total counts and the grey line shows the scaled background counts.

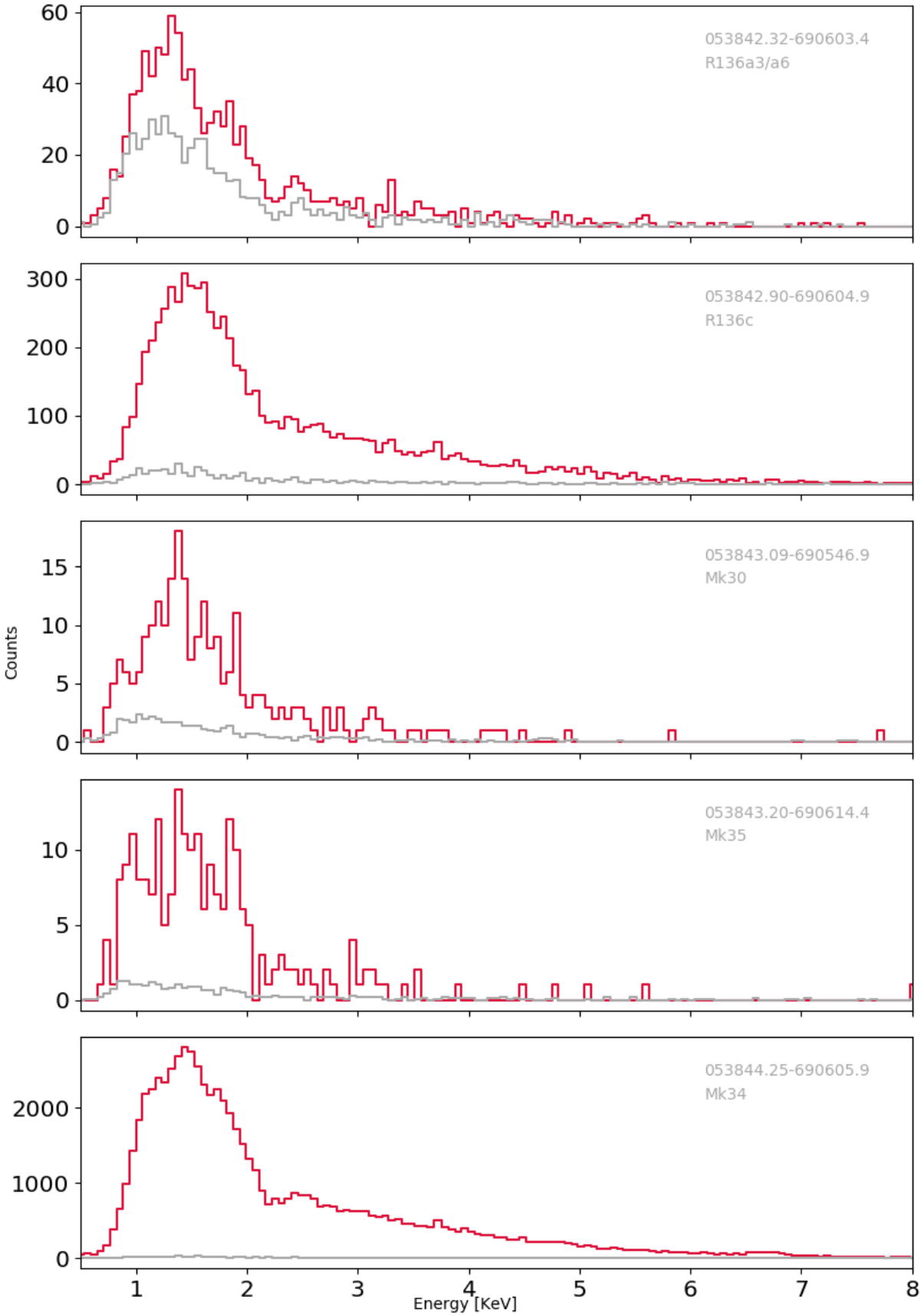

Figure 3.9c: X-ray spectra for all WR sources in the sample. Red line shows the total counts and the grey line shows the scaled background counts.

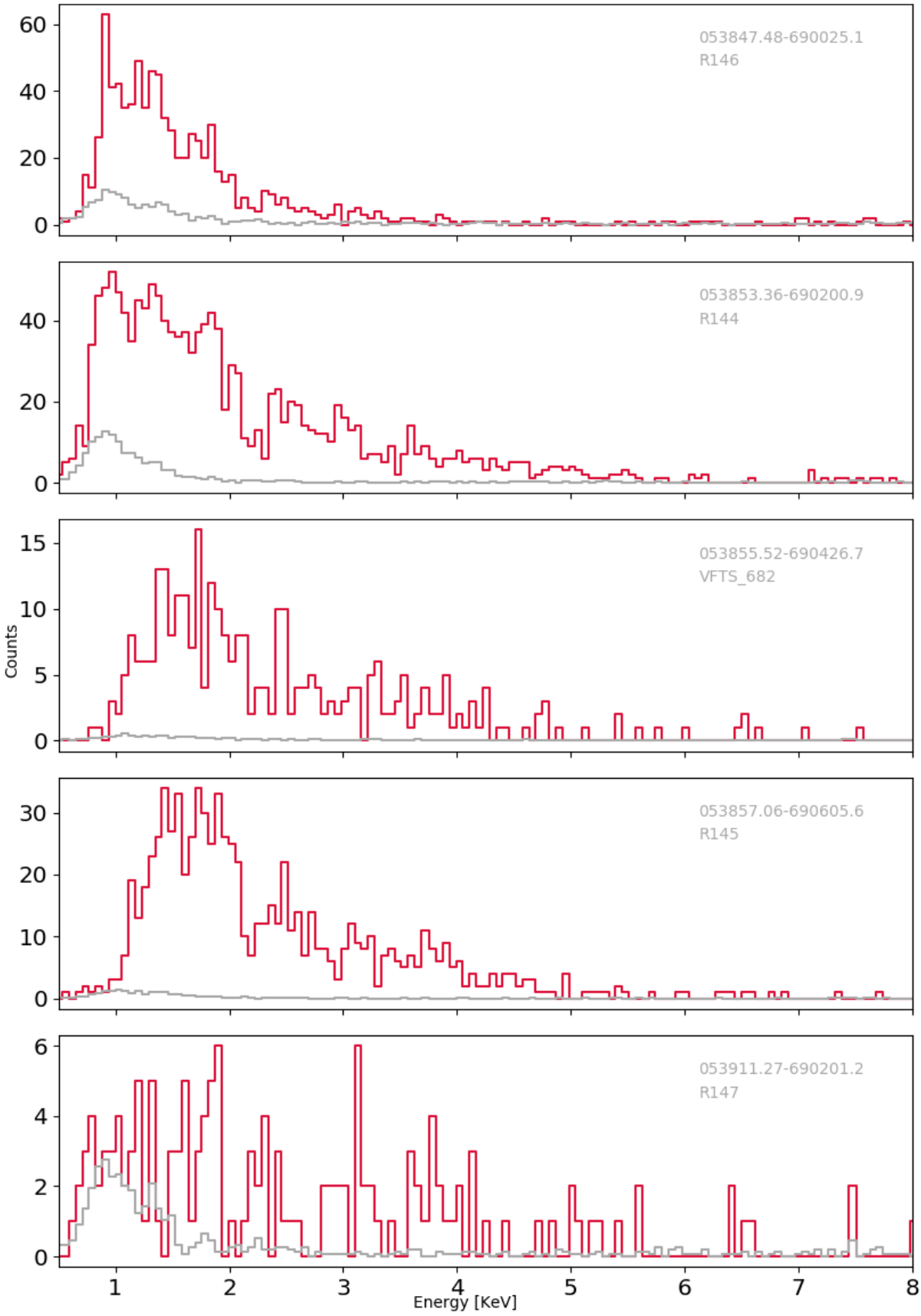

Figure 3.9d: X-ray spectra for all WR sources in the sample. Red line shows the total counts and the grey line shows the scaled background counts.

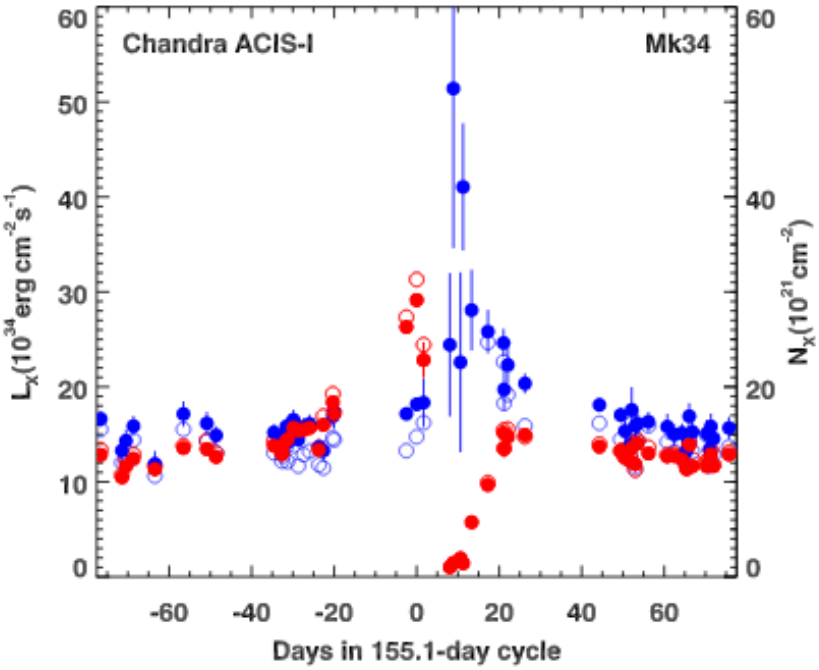

Figure 3.10: The X-ray luminosity (red) and column density (blue) variations of Mk34 folded on a 155.1 day period. The filled symbols represent results derived from the observed data, and the open symbols correspond to results which have taken the effect of pile-up into consideration. Taken from Pollock et al. (2018).

3.6 XSPEC

Spectral fitting is necessary to extract information regarding the X-ray flux, abundances and X-ray absorption towards the source.

To do this we use XSPEC, an X-ray spectral fitting program developed by Arnaud (1996). In particular, for this work we use PyXspec[2], a python wrapper for XSPEC.

From the previous Tarantula X-ray survey by Townsley et al. (2006b), 49 out of the 180 X-ray point sources have XSPEC fits, including 11 of the WR sources in this sample. Townsley et al. (2006b) use single thermal plasma models for the hot star sources and power-law models for the binaries and background active galactic nuclei (AGN). We therefore adopt a similar approach and begin our XSPEC fitting with a single thermal plasma model.

3.6.1 1T Model

Our 1 temperature (1T) XSPEC fits comprise four model components: MW foreground absorption (*tbabs*); LMC foreground absorption (*tbvarabs*); stellar absorption (*tbvarabs*); and plasma emission (*vapec*).

The MW absorption model, *tbabs*, requires an input for the column density parameter. The column density describes the amount of hydrogen gas along our line of sight. In this instance, we need a measure for the column density which is contributing to the absorption within the MW. To determine this we can use the gas-to-dust ratio outlined in Vuong et al. (2003) and shown in Equation (3.12). Using the Cardelli et al. (1989) dust extinction law, which with the assumption R_V=3.1 gives a conversion of A_J/A_V=0.282, we find the gas extinction relationship shown in Equation (3.13).

$$N(H)/A_J = 5.57 \times 10^{21} \text{ atoms cm}^{-2} \text{ mag}^{-1} \tag{3.12}$$

$$N(H)_{\text{MW}} = A_V \times 1.6 \times 10^{21} \text{ atoms cm}^{-2} \tag{3.13}$$

Taking A_V=0.22 from Fitzpatrick & Savage (1984) we find the foreground MW column density along the line of sight towards the LMC to be 3.5×10^{20} atoms cm^{-2}. We use this value for all sources in our sample and fix this parameter in our XSPEC fitting.

The LMC absorption model, *tbvarabs* also requires a column density input, however in this case it is the column density attributed to the LMC. Here the MW relationship is inadequate because at lower metallicity there is less dust due to fewer metals. For the

[2]PyXspec was developed by Craig Gordon and Keith Arnaud

LMC column density parameter therefore, we need an N(H)/A_V relationship tailored to the LMC and so for this we use Equation (3.14) from Koornneef (1982).

To find the total hydrogen column density, we must consider both atomic and molecular hydrogen contributions, however the fraction of molecular hydrogen compared to total hydrogen in the LMC was found to be very small (f_{H_2}=0.012 (Tumlinson et al., 2002). We therefore consider Equation (3.14) a good approximation for the total hydrogen column density for 30 Dor.

$$N(H)/E(B-V) = 2 \times 10^{22} \text{ atoms cm}^{-2} \text{ mag}^{-1} \tag{3.14}$$

$$A_V = R_V \times E(B-V) \tag{3.15}$$

Taking the dust reddening relationship shown in Equation (3.15), where R_V is 3.1, and substituting into Equation (3.14), we can find the relationship between column density and dust reddening shown in Equation (3.16).

$$N(H)_{\text{LMC}} = A_V \times 6.5 \times 10^{21} \text{ atoms cm}^{-2} \tag{3.16}$$

To use Equation (3.16) we need a list of appropriate dust extinction coefficients to use for each source. For this we use the literature values cited in Table 3.4 obtained from UV/optical/IR spectroscopic modelling. Table 3.4 also shows the derived LMC column densities used for each source.

Finally, the column density for the stellar absorption model, *tbvarabs*, is left as a free parameter. Absorption within the X-ray emitting region of the star is relatively unknown and specific to each system, therefore we specify soft limits for the column density of 0.018×10^{22} – 27.22×10^{22} atoms cm^{-2} (as advised by Leisa Townsley), and a hard lower limit of 0.0.

The plasma emission model, *vapec*, requires a temperature input, which again is left as a free parameter. The hard and soft limits were adjusted slightly between targets, however the starting range for the soft limits were 0.5 – 9.1 keV.

The LMC foreground absorption model, stellar absorption model, and plasma emission model also require abundance parameters for a range of elements listed in Table 3.5. LMC abundance measurements for elements included within Russell & Dopita (1990), Lebouteiller et al. (2008) and Mokiem et al. (2007) were used, and averaged if included in more than one reference. For remaining elements excluded from these studies we use Z=0.4 $Z_\odot$. The MW foreground absorption model requires no input and is instead fixed at solar abundances.

Table 3.4: Literature values of E(B-V) and R_V used in Equation (3.15) and Equation (3.16) to derive the LMC column density for each WR source

Name	E(B-V)	Ref	Rv	Ref	Av [Mag]	$N(H)_{LMC}$ [$\times 10^{22}$ atoms cm^{-2}]
R130	0.39	1	3.5	2	1.365	0.887
R135	0.575	1	0.85	3	0.489	0.318
VFTS 427	0.534	3	4.16	3	2.221	1.444
Mk51	0.806	3	2.83	3	2.281	1.483
Mk49	0.80	1	3.5	2	2.8	1.82
Mk39	0.436	3	3.85	3	1.679	1.091
R134	0.523	3	2.93	3	1.532	0.996
R140a1/a2	0.7	1	3.5	2	2.45	1.593
R140b	0.295	1	5.37	1	1.584	1.03
R136a1/a2	0.42	4	4.1	4	1.722	1.119
R136a3/a6	0.42	4	4.1	4	1.722	1.119
R136c	0.608	3	4.5	3	2.736	1.778
Mk30	0.408	3	3.71	3	1.514	0.984
Mk35	0.436	3	3.67	3	1.6	1.04
Mk34	0.49	5	4.09	5	2.004	1.303
R146	0.212	3	4.5	3	0.954	0.62
R144	0.16	1	3.5	2	0.56	0.364
VFTS 682	0.941	3	4.74	3	4.46	2.899
R145	0.29	1	3.5	2	1.015	0.66
R147	0.428	3	3.63	3	1.554	1.01

1. Hainich et al. (2014); 2. Doran et al. (2013); 3. Bestenlehner et al. (2014); 4. Crowther et al. (2016); 5. Tehrani et al. (2019)

We focussed our fitting on the spectral energy range of 0.5–8 keV, which corresponds to pi values of 35-548. For each source we used the all-inclusive spectrum, that is the spectrum summed over all observations, and we did not perform any binning. We ran the 1T model to fit the spectrum and the final fitting parameters are summarized in Table 3.6. There are two statistical processes within the XSPEC fitting that must also be specified; the fit statistic and the test statistic. The fit statistic is used to find the best fitting parameters and their associated errors and for this we used the C-statistic, discussed in Section 3.4.2. The test statistic is a measure of the goodness-of-fit between the final XSPEC model and the observed spectrum. For this we used the Pearson χ^2, discussed in Section 3.4.1.

Table 3.5: LMC ISM abundances with respect to solar abundances used in the LMC absorption, stellar absorption and plasma emission components of the 1T XSPEC model. Where possible values are averages taken from Russell & Dopita (1990), Lebouteiller et al. (2008) & Mokiem et al. (2007), however for elements not included within these references we take a standard value of 1.0 $Z_\odot$ for helium and 0.4 $Z_\odot$ for metals, highlighted in pink.

Element	Abundance [$Z_\odot$]
He	1.0
C	0.20
N	0.14
O	0.47
Ne	0.62
Na	0.4
Mg	0.29
Al	0.4
Si	0.48
S	0.50
Cl	0.15
Ar	0.65
Ca	0.4
Cr	0.4
Fe	0.30
Co	0.4
Ni	0.4

Table 3.6: The XSPEC fitting parameters and results using the 1T model for all WR sources. We use C as the fit statistic, χ^2 as the test statistic, and the 1T models had 511 degrees of freedom. The corrected X-ray luminosities refer to the X-ray luminosities corrected for ISM absorption, and the units for these luminosities should be taken to be erg s^{-1}.

Name	N(H) [$\times 10^{22}$ atoms cm^{-2}]	kT [keV]	C	Pearson-χ^2	log(L_X)	log($L_{X\mathrm{cor}}$)
R130	$0.000^{+0.009}$	$9.10_{-0.13}$	1010	1797	33.44 ± 0.01	33.53 ± 0.04
R135	$51.596^{+15.804}_{-9.596}$	$9.10_{-2.40}$	427	9241	32.97 ± 0.04	32.97 ± 0.09
VFTS 427	$0.000^{+0.375}$	$6.90^{+13.50}_{-2.25}$	260	1082	32.24 ± 0.06	32.37 ± 0.14
Mk51	$2.088^{+1.146}_{-1.129}$	$1.08^{+0.30}_{-0.54}$	159	1019	32.04 ± 0.06	32.21 ± 0.16
Mk49	$6.168^{+4.198}_{-2.714}$	$2.95^{+3.36}_{-1.17}$	291	1653	32.39 ± 0.06	32.43 ± 0.14
Mk39	$0.000^{+0.008}$	$1.88^{+0.03}_{-0.03}$	536	637	34.09 ± 0.01	34.30 ± 0.03
R134	$37.472^{+82.528}_{-31.472}$	$2.16_{-1.80}$	223	18717	32.22 ± 0.09	32.23 ± 0.26
R140a1/a2	$0.000^{+0.003}$	$1.44^{+0.01}_{-0.01}$	2475	3730	34.97 ± 0.01	35.31 ± 0.04
R140b	$0.000^{+0.062}$	$3.52^{+0.76}_{-0.53}$	428	879	33.10 ± 0.03	33.24 ± 0.09
R136a1/a2	$0.000^{+0.012}$	$1.53^{+0.03}_{-0.03}$	564	1582	33.85 ± 0.01	34.10 ± 0.05
R136a3/a6	$2.427^{+0.399}_{-0.614}$	$0.87^{+0.20}_{-0.11}$	361	19228	33.10 ± 0.03	33.26 ± 0.13
R136c	$0.000^{+0.080}$	$2.73^{+0.09}_{-0.06}$	521	674	34.17 ± 0.01	34.38 ± 0.03
Mk30	$2.199^{+0.303}_{-0.188}$	$0.71^{+0.09}_{-0.09}$	263	50956	32.42 ± 0.03	32.59 ± 0.08
Mk35	$1.673^{+0.265}_{-0.302}$	$0.78^{+0.11}_{-0.04}$	248	1291	32.52 ± 0.03	32.72 ± 0.09
Mk34	$0.000^{+0.002}$	$3.16^{+0.03}_{-0.03}$	738	789	35.12 ± 0.01	35.29 ± 0.03
R146	$1.443^{+0.156}_{-0.164}$	$0.86^{+0.04}_{-0.04}$	396	103625	33.00 ± 0.02	33.14 ± 0.07
R144	$0.000^{+0.201}$	$4.16^{+0.43}_{-0.55}$	521	736	33.41 ± 0.01	33.48 ± 0.03
VFTS 682	$1.259^{+0.577}_{-0.591}$	$1.91^{+0.31}_{-0.24}$	375	755	32.81 ± 0.03	33.00 ± 0.08
R145	$4.332^{+0.442}_{-0.478}$	$1.60^{+0.15}_{-0.12}$	417	677	33.22 ± 0.02	33.25 ± 0.05
R147	$5.487^{+2.258}_{-2.231}$	$2.89^{+2.77}_{-0.89}$	337	2772	32.53 ± 0.05	32.55 ± 0.12

Errors for the column density and plasma temperature were derived based on their C-Statistic distribution. For each parameter XSPEC derives the best result as when the C-Statistic reaches a minimum. We can then identify the lower and upper bounds of this result by identifying the values which correspond to a C-Statistic change of 1. An example of this is shown in Figure 3.11 for Mk39. The left panel shows the delta C-Statistic change with stellar column density, where we can see the minimum sits at a column density of 0. The dashed line is positioned at delta C-Statistic = 1, and corresponds to a column density of 0.008×10^{22} atoms cm^{-2}, giving the upper limit. In this case there is no lower limit since the column density cannot fall below 0. The right panel shows how the delta C-Statistic changes with plasma temperature. The minimum sits at kT=1.88 keV and again the dashed line highlights a C-Statistic change of 1. As before, the position at which this dashed line intersects the curve reveals the upper, kT=1.91 keV, and lower, kT=1.85 keV, bounds. This technique was used to derive the errors for the stellar column densities and plasma temperatures for all WR sources.

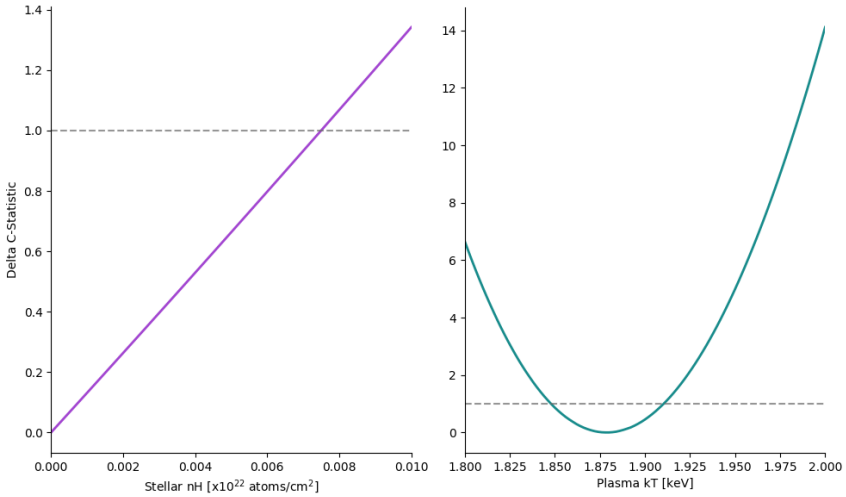

Figure 3.11: Plots showing the delta C-Statistic change with stellar absorption (left panel) and plasma temperature (right panel) for Mk39. Dashed line highlights a delta C-Statistic change of 1, which was used to identify the upper and lower bounds for each parameter. For Mk39 we find a column density N(H) $\leq 0.008\times10^{22}$ atoms cm^{-2}, and a plasma temperature of 1.88 $\pm$ 0.03 keV.

Examples of the 1T XSPEC fits are shown in Figures B.1a to B.1k (Appendix B). In some cases the 1T model is not sufficient, such as for R130 and R140a1/a2. For these sources we proceed to alternate model combinations to find improvements, as discussed in Section 3.6.2.

For some sources we derive a stellar column density of 0 which, whilst possible, could

Table 3.7: Updated LMC ISM column densities (XSPEC LMC nH) for sources that derived a stellar column density of 0 during 1T plasma emission spectral modelling. Literature values for E(B-V) initially used are shown alongside the updated E(B-V) values found from spectral fitting.

Name	Literature LMC N(H) [$\times 10^{22}$ atoms cm^{-2}]	XSPEC LMC N(H) [$\times 10^{22}$ atoms cm^{-2}]	Literature E(B-V)	Ref.	XSPEC E(B-V)
R130	0.887	0.235	0.39	(1)	0.10
VFTS 427	1.444	0.985	0.53	(2)	0.36
Mk39	1.091	1.047	0.44	(2)	0.42
R140a1/a2	1.593	1.575	0.70	(1)	0.69
R140b	1.030	0.695	0.30	(1)	0.20
R136a1/a2	1.119	1.043	0.42	(3)	0.39
R136c	1.778	1.778	0.61	(2)	0.61
R144	0.364	0.364	0.16	(1)	0.16
Mk34	1.303	1.272	0.49	(4)	0.48

1. Hainich et al. (2014); 2. Bestenlehner et al. (2014); 3. Crowther et al. (2016); 4. This work (See Chapter 5)

also be an indication that the LMC ISM column density was over-estimated because XSPEC will not allow a negative stellar absorption column density. To investigate this we repeat the spectral fitting whilst decreasing the LMC ISM column density in small increments. Through monitoring the C-statistic we can ascertain whether a better model has been calculated with the new column density value until we reach a minimum C-statistic value. Table 3.7 provides a summary of the WR sources which return stellar column densities of 0, and the updated LMC ISM column densities that were found upon further analysis. Using the relationship shown in Equation (3.16) we convert these XSPEC derived column densities to E(B-V) values to compare with the original literature values used. We find in most cases there is very little difference, with the main exceptions being VFTS 427, R140b and R130 (which as already noted was not well fit using the 1T plasma emission model).

3.6.2 2T Models

As shown in Figure B.1a, the 1T model for R130 failed to reasonably reproduce the observed spectrum, despite a reasonable count rate. We see a second broad, hard emission component in the observed spectrum which is neglected during the 1T fit.

Similarly, R140a1/a2, which is the second brightest source in the sample, also struggles to achieve a good fit when using the 1T model. Here we see the model predicts an excess

at softer energies, around 1 keV, that does not match the observed spectrum.

For these sources therefore, we explore a 2 temperature (2T) fit to assess the improvement. We also investigate a 2T fit for Mk34 as we note that Pollock et al. (2018) use a 2T model when analysing this source. We therefore are interested in investigating whether the introduction of further free parameters into the fitting model is justified by producing a better fit.

The adopted 2T model is very similar to the 1T model, with the addition of a second plasma emission (*vapec*) component. The temperature parameter again remains a free parameter, with similar soft limits in the range of 0.5–9.1 keV. The four other model components remain identical to the 1T fitting, with the same frozen parameter inputs.

Table 3.8 gives a summary of the 2T model fitting results for R130, R140a1/a2 and Mk34 and plots of these 2T fits are shown in Figure 3.12.

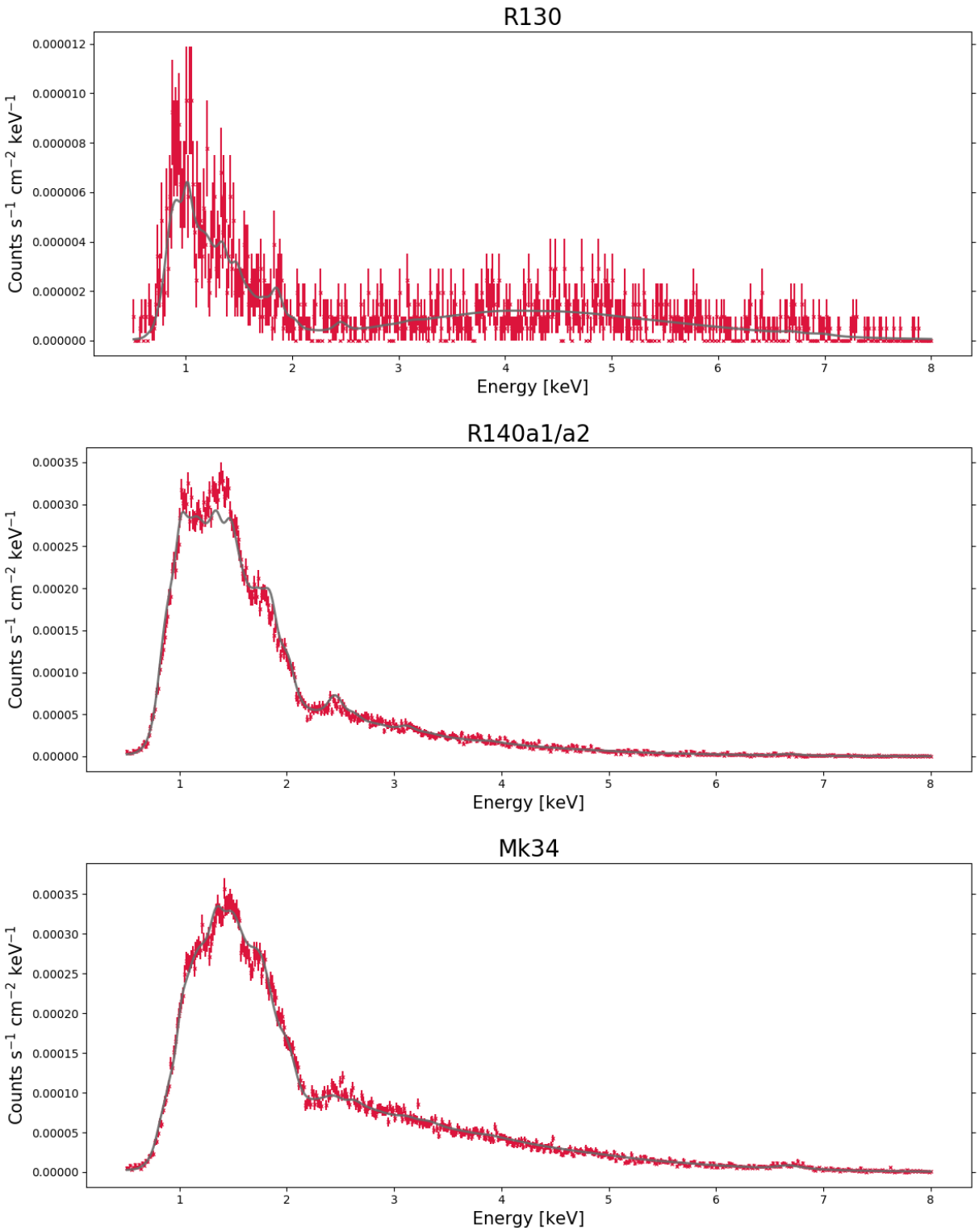

Figure 3.12: 2T thermal plasma XSPEC fits for R130 (upper panel), R140a1/a2 (middle panel), and Mk34 (lower panel)

Table 3.8: The XSPEC fitting parameters and results using the 2T model. Again, we use C as the fit statistic, χ^2 as the test statistic, and the 2T models had 508 degrees of freedom. The corrected X-ray luminosities refer to the X-ray luminosities adjusted for no ISM absorption and the units for these luminosities should be taken to be erg s^{-1}.

Name	nH_1 [$\times 10^{22}$ atoms cm^{-2}]	kT_1 [keV]	nH_2 [$\times 10^{22}$ atoms cm^{-2}]	kT_2 [keV]
R130	$0.000^{+0.032}$	$0.73^{+0.03}_{-0.03}$	$37.067^{+5.183}_{-4.317}$	$10.86^{+5.08}_{-1.64}$
R140a1/a2	$0.397^{+0.013}_{-0.013}$	$0.78^{+0.01}_{-0.01}$	$0.000^{+0.006}$	$2.48^{+0.08}_{-0.08}$
Mk34	$0.753^{+0.069}_{-0.051}$	$0.39^{+0.03}_{-0.02}$	$0.068^{+0.793}_{-0.068}$	$3.55^{+0.10}_{-0.08}$

Name	C-statistic	Pearson-χ^2	$\log(L_X)$	$\log(L_{X\,\mathrm{cor}})$
R130	534	593	33.62 ± 0.013	33.77 ± 0.06
R140a1/a2	736	759	35.01 ± 0.002	35.36 ± 0.07
Mk34	622	665	35.12 ± 0.002	35.34 ± 0.07

3.6.3 X-ray Luminosity

With the spectral fitting complete, XSPEC can calculate the X-ray flux for each source in the 0.5–8 keV range. We can convert this to a luminosity using Equation (3.17), where distance, d, is taken to be 50 kpc (Pietrzyński et al., 2013).

$$L_{\mathrm{x}} = f_{\mathrm{x}} 4\pi d^2 \tag{3.17}$$

XSPEC also calculates a corrected, or intrinsic, X-ray luminosity, equivalent to the luminosity that would be observed if the Milky Way and LMC foreground absorption were set to 0. Both the observed and corrected X-ray luminosities derived using the 1T thermal plasma XSPEC model are summarized in Table 3.6 for every WR source. Similarly, Table 3.8 shows the same luminosity parameters which were derived using the 2T thermal plasma model for R130, R140a1/a2 and Mk34.

Figure 3.13 shows a direct comparison between the observed X-ray luminosities for all the WR sources, using both the 1T (purple) and 2T (blue) thermal plasma models, and their derived plasma temperatures. Since the 2T models consist of 2 plasma components, the temperatures of each component are shown, connected by a dashed line.

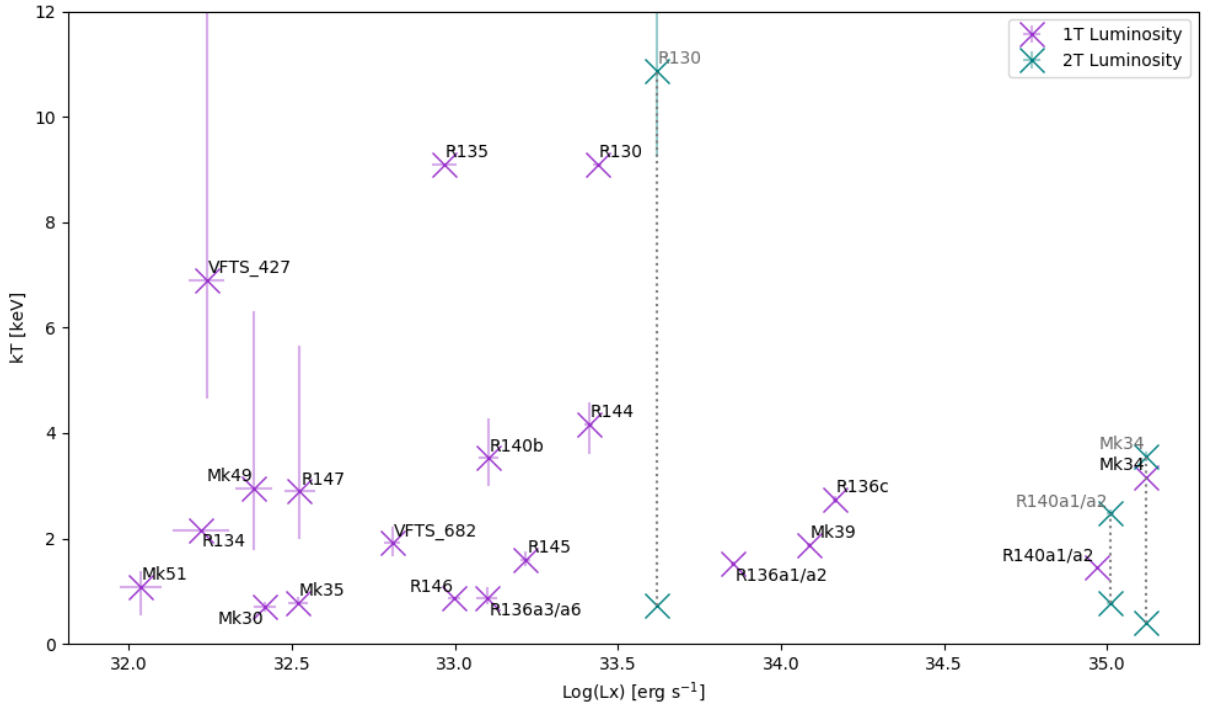

Figure 3.13: Plot showing how the observed X-ray luminosity (L_X) varies with plasma temperature for all WR sources in the sample. Plasma temperatures and X-ray luminosities derived with 1T thermal plasma fits are shown in purple, whereas those derived with 2T thermal plasma fits are shown in blue with a grey dashed line connecting the two temperatures derived for each source.

3.7 Individual Sources

Here we provide some brief comments on the XSPEC results for each of the WR stars in our sample, however we defer discussion on variability until Chapter 4. Some of these sources, highlighted in pink in Table 3.2, were also detected in the X-ray survey conducted by Townsley et al. (2006b) (T2006). Where possible, spectral fits by T2006 were performed in XSPEC using a model composed of an absorption component with solar abundance (*wabs*), and a single temperature thermal plasma component with 0.3 $Z_\odot$ abundances (*apec*). Note that the column densities from T2006 encompass the collective MW ISM, LMC ISM and stellar components, so are therefore not directly comparable with the stellar column densities derived in this work. When referring to X-ray luminosities, the units should be taken to be erg s^{-1}.

3.7.1 R130 (053749.06-690508.1, BAT99 92)

From the T-ReX observations we detect 1178 net counts, and R130 was also detected in T2006 with 9.4 net counts. Spectral modelling by T2006 reveals a column density of 0.32×10^{22} atoms cm^{-2} and plasma temperature of 2.4 keV. As discussed in Section 3.6.2, our 1T spectral modelling yields unsatisfactory results, with a high plasma temperature and poor fitting statistics (reduced χ^2 = 3.52). Our 2T model fit shows an excellent improvement in the fitting statistics with a reduced χ^2 of 1.17, justifying the addition of a second component. We do note, however, that the second plasma component derives a very high plasma temperature, $10.86^{+5.08}_{-1.64}$ keV, and column density, $37.07^{+5.183}_{-4.317}\times10^{22}$ atoms cm^{-2}. Overall the XSPEC fitting finds an X-ray luminosity of $\log(L_{X\mathrm{cor}})$=33.77 ± 0.06, slightly higher than the T2006 corrected X-ray luminosity of $\log(L_{X\mathrm{cor}})$=33.48.

3.7.2 R135 (053833.62-690450.4, BAT99 95, VFTS 402)

R135 was not detected in T2006, whereas we find 139 net counts from T-ReX. We note an unusual spectral shape for R135, showing a small excess of hard emission, at approximately 5 keV, but relatively little soft emission. There is no evidence from optical extinction measurements to suggest this source is highly absorbed. The unusual shape made spectral fitting particularly challenging and therefore our 1T model results of $51.60^{+15.80}_{-9.60}\times10^{22}$ atoms cm^{-2} for stellar column density and $9.1_{-2.4}$ keV plasma temperature are not robust. We find a corrected X-ray luminosity of $\log(L_{X\mathrm{cor}})$=32.97 ± 0.09, which should be used with caution.

3.7.3 VFTS 427 (053836.40-690657.5, BAT99 96, Mk53)

VFTS 427 was not detected in T2006, however we note 67 net counts from T-ReX. Spectral fitting with the T-ReX data reveals a stellar column density of $0^{+0.04}\times10^{22}$ atoms cm^{-2} and a high plasma temperature of $6.9^{+13.5}_{-2.3}$ keV. Considering the low count rate the test statistic suggests an acceptable fit, with a reduced Pearson-χ^2 of 2.1, and from inspection it is difficult to highlight areas for improvement. The stellar column density of 0 was investigated further to ensure this did not arise from an overestimation of the LMC ISM absorption. The LMC ISM column density was lowered in increments and the spectrum re-fit until a minimum C-statistic was found. This corresponded to a reduction in the LMC ISM absorption from 1.44×10^{22} atoms cm^{-2} to 0.99×10^{22} atoms cm^{-2}, translating to an E(B-V) of 0.418. Using the T-ReX data we find a corrected X-ray luminosity of $\log(L_{X\mathrm{cor}})$=32.37 ± 0.14.

3.7.4 Mk51 (053838.82-690649.6, BAT99 97, VFTS 457)

In the T-ReX data we find Mk51 has 50 net counts, however it was not detected in T2006. Our 1T model of the T-ReX data revealed a stellar column density of $2.09^{+1.15}_{-1.13} \times 10^{22}$ atoms cm^{-2} and plasma temperature of $1.08^{+0.30}_{-0.54}$ keV during spectral fitting, however the lack of counts introduces difficulties in gauging the goodness-of-fit. For this source we derive a corrected X-ray luminosity of $\log(L_{X\mathrm{cor}})=32.21 \pm 0.16$.

3.7.5 Mk49 (053839.15-690621.2, BAT99 98)

Mk49 was not detected in T2006. T-ReX reveals a relatively flat spectrum with 66 net counts, which appears to show a small excess at harder energies, with a slight peak at ∼2.5 keV, and very little in the soft energy range. 1T spectral fitting was difficult to improve, with a final test statistic of Pearson-χ^2=1653, corresponding to a reduced χ^2=3.23. We find a stellar column density of $6.17^{+4.20}_{-2.71} \times 10^{22}$ atoms cm^{-2} and a plasma temperature of $2.95^{+3.36}_{-1.17}$ keV, however these results host high uncertainties and, considering the model fit and low count rate, should be used with care. The corrected X-ray luminosity was found to be $\log(L_{X\mathrm{cor}})=32.43 \pm 0.14$.

3.7.6 Mk39 (053840.22-690559.8, BAT99 99, VFTS 482)

Mk39 is the third brightest X-ray source in T-ReX with 7979 net counts, and was also detected in T2006 with 65.9 net counts, a column density of $0.16^{+0.24} \times 10^{22}$ atoms cm^{-2} and plasma temperature of $2.0^{+2.6}$ keV. Our 1T model produces an excellent fit to the data and we also derive a similar plasma temperature of $1.88^{+0.03}_{-0.03}$ keV. A stellar column density of $0^{+0.01} \times 10^{22}$ atoms cm^{-2} was found during initial fitting, and after further investigation we find a minor reduction to the LMC ISM column density from 1.09×10^{22} atoms cm^{-2} to 1.05×10^{22} atoms cm^{-2}. Overall we are satisfied with this fit, which results in a corrected X-ray luminosity of $\log(L_{X\mathrm{cor}})=34.30 \pm 0.03$, slightly higher than the $\log(L_{X\mathrm{cor}})=34.22$ found by T2006.

3.7.7 R134 (053840.54-690557.1, BAT99 100, VFTS 1001)

R134 is the weakest X-ray source in the WR sample with a net counts of 35. Noted as a tentative detection source in T2006 with 2 net counts, and due to this lack of counts, spectral fitting was not attempted in T2006. Considering the faint nature of this star in the T-ReX data, the detection in T2006 is perhaps unlikely, however a third Chandra ACIS-I

study of the 30 Dor region by Portegies Zwart et al. (2002) also notes an X-ray detection, with 9 counts in a 21 ks exposure.

In this work we attempt a 1T fit, but again acknowledge that the low count rate makes this difficult. We find an exceptionally high stellar column density of $37.47^{+82.53}_{-31.47} \times 10^{22}$ atoms cm^{-2}, and a plasma temperature of $2.16_{-1.80}$ keV. When probing the error range of the plasma temperature we were unable to find an upper limit at which the C-statistic reached one, therefore this temperature is also highly uncertain. Based on these results we find $\log(L_{X\mathrm{cor}})=32.23 \pm 0.26$.

3.7.8 R140a1/a2 (053841.59-690513.4, BAT99 101/102, VFTS 507)

R140a1/a2 is the second brightest X-ray source in the whole T-ReX sample, with 54062 net counts, and was a bright detection in T2006 with 377.6 net counts. They report a good spectral fit using their absorbed single temperature thermal plasma model, deriving a column density of $0.79^{+0.16}_{-0.15} \times 10^{22}$ atoms cm^{-2} and plasma temperature of $0.9^{+0.1}_{-0.1}$ keV. In contrast, we do not find a good fit to the observed T-ReX data using the 1T model, as explained in Section 3.6.2. Instead we use a 2T plasma model to fit the spectrum, giving a reduced χ^2 of 1.52. Interestingly, this is a similar result to the 1T model, where the reduced χ^2=1.49, and as shown in Figure 3.12 the data at the peak of the spectrum is not fully reproduced by the model suggesting further investigation is necessary. Nevertheless, using a 2T fit we find $\log(L_{X\mathrm{cor}})=35.36 \pm 0.07$, slightly higher than $\log(L_{X\mathrm{cor}})=35.25$ found by T2006.

3.7.9 R140b (053841.62-690515.1, BAT99 103, VFTS 509)

R140b is detected in T-ReX with 395 net counts, versus 14.6 net counts in T2006. It is important to note R140b lies in very close proximity to R140a1/a2, which is the stronger X-ray source, and therefore contamination from R140a1/a2 in the R140b aperture is possible, as shown in Figure 3.7b. Considering that other sources in T2006 are generally detected with net count values at approximately 1% of that observed in T-ReX it is surprising R140b is detected in the T2006 sample. Nevertheless, spectral fitting in T2006 reveals a column density of $0.16^{+0.47} \times 10^{22}$ atoms cm^{-2} and plasma temperature of 2.5 keV. With the T-ReX data we find a stellar column density of $0^{+0.06} \times 10^{22}$ atoms cm^{-2} and higher plasma temperature of $3.52^{+0.76}_{-0.53}$ keV. This equates to a corrected X-ray luminosity of $\log(L_{X\mathrm{cor}})=33.24 \pm 0.09$, which is slightly lower than T2006 who find $\log(L_{X\mathrm{cor}})=33.57$.

Overall the spectral fit is reasonable, however there is room for improvement at low energies, where it fails to reproduce the dip in the spectrum at ∼1 keV observed in the data. Since the T-ReX data suggested a stellar column density of 0, reductions to the LMC ISM column density were investigated and we find the minimum C-statistic coincides with an LMC ISM column density of 0.70×10^{22} atoms cm^{-2}. This equates to E(B-V)=0.199.

3.7.10 R136a1/a2 (053842.38-690602.8, BAT99 108/109)

R136a1/a2 is the fifth brightest T-ReX source with 4369 net counts, having previously been detected in T2006 with 52.8 net counts. From spectral fitting T2006 find a column density of $0.40^{+0.40}_{-0.27}\times10^{22}$ atoms cm^{-2} and plasma temperature of $1.2^{+0.4}_{-0.4}$ keV. In this work we find a stellar column density of $0^{+0.0}\times10^{22}$ atoms cm^{-2} and a plasma temperature of $1.53^{+0.03}_{-0.03}$ keV. Modifying the LMC ISM column density revealed the best fit occurred when the LMC ISM column density was lowered from 1.12×10^{22} atoms cm^{-2} to 1.04×10^{22} atoms cm^{-2}, resulting in a small change to the E(B-V) derived in Crowther et al. (2016) from 0.42 to 0.39. T2006 find a corrected X-ray luminosity of log($L_{X\mathrm{cor}}$)=34.31, slightly higher than log($L_{X\mathrm{cor}}$)=34.10 ± 0.05 derived here.

3.7.11 R136a3/a6 (053842.32-690603.4, BAT99 106)

R136a3/a6 is detected in T-ReX with 492 net counts, albeit with potential contamination from the brighter R136a1/a2 source nearby, as shown in Figure 3.7a. T2006 also note a detection with 21.9 net counts, and report a column density of 0.20×10^{22} atoms cm^{-2} and plasma temperature of 4.2 keV. With the T-ReX data we find a stellar column density of $2.43^{+0.40}_{-0.61}\times10^{22}$ atoms cm^{-2} and a plasma temperature of $0.87^{+0.20}_{-0.11}$ keV, a huge contrast to the T2006 result. Upon visual inspection however, the 1T model fit struggles to reproduce the observed spectrum, confirmed by the high Pearson-χ^2 test statistic. The low energy absorption edge and high energy tail are both reasonably well matched however the shape of the broad emission peak at ∼1.2 keV has not been well represented. T2006 derive a corrected X-ray luminosity of log($L_{X\mathrm{cor}}$)=33.93, which is higher than the log($L_{X\mathrm{cor}}$)=33.26 ± 0.13 derived in this work.

3.7.12 R136c (053842.90-690604.9, BAT99 112, VFTS 1025)

R136c is the fourth brightest source in T-ReX with 6960 net counts. R136c was previously detected in T2006 with 246.8 net counts, a column density of $0.50^{+0.13}_{-0.10}\times10^{22}$ atoms cm^{-2} and plasma temperature of $3.0^{+1.3}_{-0.8}$ keV. Here we report a stellar column density of $0^{+0.08}$

$\times 10^{22}$ atoms cm^{-2} and a similar plasma temperature of $2.73^{+0.09}_{-0.06}$ keV. The 1T model gives an excellent fit to the observed data with a reduced Pearson-χ^2 of 1.32 and C-statistic of 521 for 511 degrees of freedom. We investigate lowering the LMC ISM column density however we find no improvement to the fit and can therefore conclude that the E(B-V)=0.608 from Bestenlehner et al. (2014) is in agreement with the absorption seen in the X-ray data. T2006 find a corrected X-ray luminosity of $\log(L_{X\mathrm{cor}})$=35.04, slightly higher than $\log(L_{X\mathrm{cor}})$=34.38 $\pm$ 0.03 found using the T-ReX data.

3.7.13 Mk30 (053843.09-690546.9, BAT99 113, VFTS 542)

Mk30 is detected in T-ReX with 205 net counts, having previously been detected in T2006 with 5.0 net counts, but this source was not considered bright enough to proceed to spectral fitting by T2006. In this work we attempt a 1T fit and find a stellar column density of $2.20^{+0.30}_{-0.19} \times 10^{22}$ atoms cm^{-2} and plasma temperature of $0.71^{+0.09}_{-0.09}$ keV. Overall the fit is quite poor, with a high Pearson-χ^2 test statistic of $\sim$51,000, giving a reduced χ^2 of $\sim$100. Visual inspection shows the model struggles at $\sim$1–1.5 keV, failing to reproduce the shape of the absorption edge and underestimating the peak at $\sim$1.2 keV however at higher energies the general shape is good. We find a corrected X-ray luminosity of $\log(L_{X\mathrm{cor}})$=32.59 $\pm$ 0.08.

3.7.14 Mk35 (053843.20-690614.4, BAT99 114, VFTS 545)

Mk35 is detected in T-ReX with 201 net counts. It was previously detected in T2006 with 5.6 net counts, however again there were insufficient counts in the T2006 data to complete a spectral fitting. With the T-ReX data we use the 1T model to derive a stellar column density of $1.67^{+0.27}_{-0.30} \times 10^{22}$ atoms cm^{-2} and plasma temperature of $0.78^{+0.11}_{-0.04}$ keV. The corrected X-ray luminosity was $\log(L_{X\mathrm{cor}})$=32.72 $\pm$ 0.09.

3.7.15 Mk34 (053844.25-690605.9, BAT99 116)

Mk34 is the brightest X-ray source in T-ReX with 71,107 net counts, when assuming the same background counts subtraction as R136c. Mk34 was also detected in T2006 with 948.6 net counts, and their spectral fitting found a column density of $0.40^{+0.07}_{-0.07} \times 10^{22}$ atoms cm^{-2} and plasma temperature of $3.9^{+1.1}_{-0.7}$ keV. In this work using the 1T model we find a stellar column density of $0^{+0.002} \times 10^{22}$ atoms cm^{-2} and plasma temperature of $3.16^{+0.03}_{-0.03}$ keV, very similar to the temperature found by T2006. Since we derived a stellar column density of 0, we repeated the XSPEC fitting whilst lowering the LMC column density and found the minimum C-Statistic coincided with a LMC interstellar column

density of 1.27×10^{22} atoms cm^{-2}. This corresponded to E(B-V)=0.48, which is very similar to the literature value of E(B-V)=0.49 derived in this work (See Chapter 5). Our corrected X-ray luminosity was found to be $\log(L_{X\mathrm{cor}})=35.29 \pm 0.03$, only slightly lower than that found by T2006, where $\log(L_{X\mathrm{cor}})=35.38$.

Pollock et al. (2018) also performed spectral fitting on the T-ReX data with XSPEC, using a two temperature thermal plasma with freely variable abundances. Their approach was to fit all 54 epochs simultaneously, and they find plasma temperatures of $1.20^{+0.04}_{-0.04}$ keV and $4.46^{+0.21}_{-0.21}$ keV. We also perform a 2T fit to the combined Mk34 spectrum and find lower plasma temperatures of $0.39^{+0.03}_{-0.02}$ keV and $3.55^{+0.10}_{-0.08}$ keV. Our 2T model derives an X-ray luminosity of $\log(L_{X\mathrm{cor}})=35.34 \pm 0.07$, higher than that found by Pollock et al. (2018), $\log(L_{X\mathrm{cor}})=35.08$, however very similar to the luminosity derived by T2006. Although there was an improvement in the reduced χ^2 found using the 2T model fit, 1.31, from that found using the 1T model fit, 1.54, we are more inclined to prefer the 1T model results, which produced satisfactory results without the need for additional parameters.

3.7.16 R146 (053847.48-690025.1, BAT99 117, VFTS 617)

R146 was detected in T-ReX with 697 net counts, having not been detected in T2006. Using the T-ReX data we find a stellar column density of $1.44^{+0.16}_{-0.16} \times 10^{22}$ atoms cm^{-2} and plasma temperature of $0.86^{+0.04}_{-0.04}$ keV. The fitting statistics for this star suggest a very poor fit to the data, with a reduced Pearson χ^2 of 203, however upon visual inspection the model is mostly representative of the data with the exception of a sharp dip at ∼1.1 keV which the model appears unable to reproduce. The 1T fit corresponded to a corrected X-ray luminosity of $\log(L_{X\mathrm{cor}})=33.14 \pm 0.07$.

3.7.17 R144 (053853.36-690200.9, BAT99 118)

R144 is a bright X-ray detection in T-ReX with 1263 net counts, whilst also detected be T2006 with 12.0 net counts. Spectral fitting in T2006 reveals a plasma temperature of $2.1^{+6.6}_{-1.5}$ keV with a fixed column density of 0.10×10^{22} atoms cm^{-2}. With the T-ReX data the 1T model provides a good fit, revealing a stellar column density of $0^{+0.20}$ $\times10^{22}$ atoms cm^{-2} and plasma temperature of $4.16^{+0.43}_{-0.55}$ keV, significantly higher than that found by T2006. Lowering the LMC ISM absorption and repeating the spectral fitting did not yield an improved fit, therefore verifying the E(B-V) of 0.16 reported by Hainich et al. (2014). T2006 find a corrected X-ray luminosity of $\log(L_{X\mathrm{cor}})=33.51$, very similar to $\log(L_{X\mathrm{cor}})=33.48 \pm 0.03$ found using the T-ReX data.

3.7.18 VFTS 682 (053855.52-690426.7)

VFTS 682 is detected in T-ReX with 303 net counts, having not been detected in T2006. The 1T model reveals a stellar column density of $1.26^{+0.58}_{-0.59} \times 10^{22}$ atoms cm^{-2} and plasma temperature of $1.91^{+0.31}_{-0.24}$ keV. On visual inspection the 1T model mimics the observed data well, and we find a reduced Pearson-χ^2 of 1.48. The corrected X-ray luminosity was found to be $\log(L_{X\mathrm{cor}})$=33.00 ± 0.08.

3.7.19 R145 (053857.06-690605.6, BAT99 119)

R145 is a clear T-ReX detection with 785 net counts. R145 was previously detected in T2006 with 11.1 net counts, where they report a plasma temperature of $1.6^{+2.8}_{-0.7}$ keV for a fixed column density of 3.16×10^{22} atoms cm^{-2}. With the T-ReX data we find a stellar column density of $4.33^{+0.44}_{-0.48} \times 10^{22}$ atoms cm^{-2} and plasma temperature in agreement with T2006 of $1.60^{+0.15}_{-0.12}$ keV. The 1T model appears to find a good fit to the data, both from visual inspection and from the model and test statistics (reduced Pearson-χ^2=1.32). We find a corrected X-ray luminosity of $\log(L_{X\mathrm{cor}})$=33.25 ± 0.05, which is slightly lower than $\log(L_{X\mathrm{cor}})$=33.99 reported by T2006.

3.7.20 R147 (053911.27-690201.2, BAT99 122, VFTS 758)

R147 is a faint T-ReX detection with 103 net counts, having not been detected in T2006. Here we find a stellar column density of $5.49^{+2.26}_{-2.23} \times 10^{22}$ atoms cm^{-2} and a high plasma temperature of $2.89^{+2.77}_{-0.89}$ keV using the 1T model, however the observed spectrum appears relatively flat and therefore hard to interpret. The high Pearson-χ^2 and low C-statistic emphasizes the point that there is too few counts to produce a reliable fit. The 1T model finds a corrected X-ray luminosity of $\log(L_{X\mathrm{cor}})$=32.55 ± 0.12.

3.7.21 R136b (BAT99 111)

One notable difference between the T-ReX data and the T2006 is the apparent non-detection of R136b in T-ReX, whose absence can also be seen in Figure 3.7a. R136b is an O4If/WN8 star and T2006 report 5.9 net counts from this source, although no spectral fitting is attempted. With T-ReX however, using an automated pipeline with ACIS-Extract, no such source is noted.

3.8 Other T-ReX Early Type Sources

The T-ReX catalogue contains approximately 4000 X-ray point sources (Townsley, in prep). Of these there are 107 targets that are considered early-type stars: 20 WR stars, 72 O stars, 8 B stars, and 7 of unknown spectral type, drawn from the Doran et al. (2013) photometric catalogue and literature spectroscopic results. Table C.1 lists these early-type stars, and their X-ray net count detection in T-ReX, sorted by decreasing X-ray brightness. The WR stars included in this work have been highlighted in pink, comprising 12 of the 20 brightest T-ReX X-ray sources. Although this work focuses on the WR subset, we can use these results to investigate the remainder of the early-type star sample. In particular, we look to approximate the X-ray luminosities of these stars, a parameter which generally requires spectral fitting and can therefore be time-consuming and complicated. Instead we show that a simple approximation can be derived using the net counts detected from each source. Figure 3.14 shows the relationship between net counts and observed/absorption-corrected X-ray luminosities (shown as purple/green crosses respectively) for the WR stars in 30 Dor.

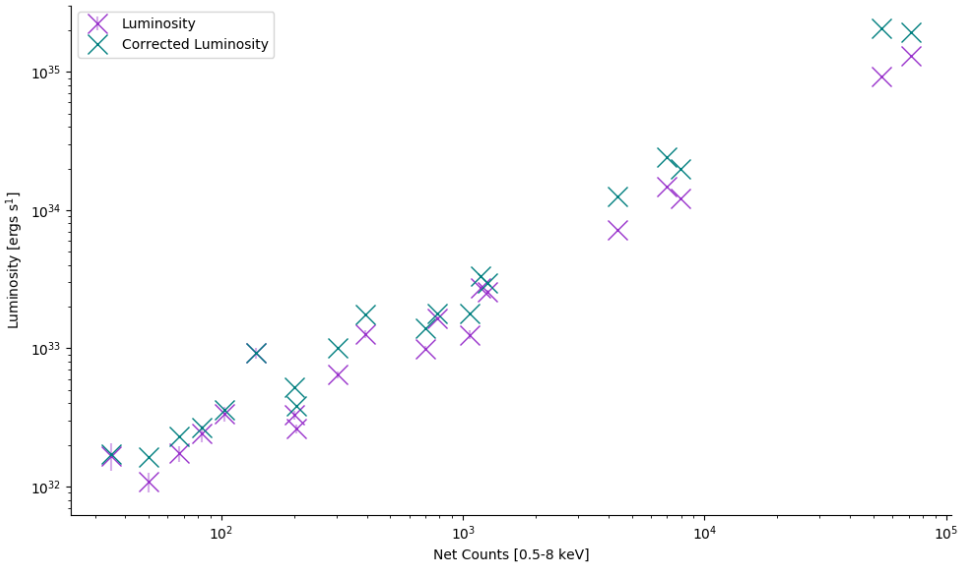

Figure 3.14: Plot showing the linear relationship between X-ray counts against observed X-ray luminosity (purple crosses) and corrected X-ray luminosity (green crosses). X-ray luminosities were predicted by XSPEC using the 1T plasma model fits.

Fitting the net counts against observed X-ray luminosity with a linear regression line using the least-squares method gives the relationship shown in Equation (3.18). We can then use this relationship to obtain an approximation of the X-ray luminosities for the remainder of the early-type population.

$$\log(L_X[\text{erg s}^{-1}]) = 0.905(2)\log(\text{Net Counts}) + 30.61(1) \tag{3.18}$$

To estimate the corrected X-ray luminosity values we can simply calculate the average ratio of $L_{X\text{cor}}/L_X$=1.4 for the WR subset and apply this to the observed X-ray luminosities.

As shown in Table C.1, VFTS 399 is the third brightest X-ray source in the T-ReX sample and is thought to be a rapidly rotating O9III star (Ramirez-Agudelo et al., 2013; Walborn et al., 2014). Using the 3 archival and first 5 T-ReX observations described in this work, Clark et al. (2015) investigated this source further. With XSPEC they use an absorbed power-law model to fit the spectrum and derive a corrected X-ray luminosity of 5.0×10^{34} erg s^{-1}.

In the whole T-ReX survey, VFTS 399 was observed with 22,011 counts. Applying our counts to X-ray luminosity relationship we find an intrinsic X-ray luminosity of 4.89×10^{34} erg s^{-1}, which is in very good agreement with the XSPEC derived result from Clark et al. (2015). Taking the bolometric luminosity of $\log(L_{\text{bol}}/L_\odot)$=4.8 from Ramírez-Agudelo et al. (2017) gives an exceptionally high $L_{Xc}/L_{\text{bol}}=2.04\times10^{-4}$, giving a clear indication VFTS 399 is an exceptional system, which Clark et al. (2015) attribute to a high mass X-ray binary (HMXB).

We can also extrapolate this relationship to accommodate the weakest early-type sources in the T-ReX survey, shown in Table C.1, specifically VFTS 417, a B2Ib star with 2 net counts. Using Equation (3.18) we derive an observed X-ray luminosity of 0.8×10^{31} erg s^{-1}, which correlates to a corrected X-ray luminosity of 1×10^{31} erg s^{-1}. This is pertinent because it defines the upper limit for the intrinsic X-ray luminosity of the undetected early-type stars, including R136b.

3.9 Conclusion

In this chapter we have described the X-ray results derived from the WR star subset of the T-ReX survey. 20 of the 21 WR sources in the field of view were detected, and the majority of these were strong detections, including 6 of the top 10 brightest X-ray sources in T-ReX (see Table C.1). We have analysed the X-ray data in order to derive key X-ray properties such as net counts, variability and hardness, however we defer discussion of these collective properties for individual sources until Chapter 4.

We have also performed X-ray spectral fitting with XSPEC to derive stellar column densities, plasma temperatures and X-ray luminosities, both observed and intrinsic. For all WR stars we performed fits using a 1T thermal plasma model, and for R130, R140a1/a2

and Mk34 we performed additional fits with a 2T model. We discuss these XSPEC fits in this Chapter and, where possible, compare the results to those derived by Townsley et al. (2006b).

For the WR stars we find intrinsic X-ray luminosities ranging from $\log(L_{X\mathrm{cor}})$=32.21 to $\log(L_{X\mathrm{cor}})$=35.31, with a mean $\log(L_{X\mathrm{cor}})$=34.37 for the whole sample (when using the 1T model XSPEC fits, and taking the units of $L_{X\mathrm{cor}}$ to be in erg s^{-1}). Using these intrinsic X-ray luminosities and the recorded net counts we define a net counts to corrected X-ray luminosity relationship, which we can apply to other early-type stars detected in the T-ReX survey. We also derive an upper X-ray luminosity of $\log(L_{X\mathrm{cor}})$=31 for early-type stars in 30 Dor which were not detected.

Chapter 4

The Binary Nature of Wolf-Rayet Stars in 30 Doradus

4.1 Introduction

In this chapter we discuss the more general properties of the WR stars in 30 Doradus. Specifically, we aim to comment on evidence for binarity within the WR sample using literature searches and the X-ray results from the T-ReX survey (discussed in Chapter 3). To inform our decision we use a number of binary indicators, including the hardness ratio (Section 3.5), variability tests (Section 3.4) and the L_{Xc}/L_{bol} ratio (Section 1.4.3). For variability we include the Kolmogorov-Smirnov (KS) test which is useful for assessing long term variations, and the reduced χ^2 which is more suited to highlighting short term variability. When discussing $\log(L_X)$ values, the units of L_X are erg s^{-1}. Also, recall from Section 1.4.3 that the expected L_{Xc}/L_{bol} ratio for isolated stars is $\sim 10^{-7}$, which will be relevant in the following sections when assessing binarity.

For some objects, new observations from other studies such as the VLT Flames Tarantula Survey (VFTS) and the All-Sky Automated Survey for Supernovae (ASAS-SN) have also been included to help establish binary status. The results discussed in the following section are summarized in Table 4.5.

4.2 WR stars in 30 Dor

4.2.1 R130

R130, a WN/C + B1I star, is one of only two stars in this sample to have a carbon rich stellar component (Breysacher et al., 1999).

Using radial velocity monitoring, Moffat & Seggewiss (1986) were the first to derive an orbital solution, finding a 4.309 day period. To reconcile reasonable mass estimates for the WR star and B supergiant, however, they introduced the suggestion of a third component within R130, most likely an O star. This hypothesis has yet to be confirmed but likewise has also not been dismissed. Schnurr et al. (2008) also investigated the radial velocity variations of R130, and found very similar results to Moffat & Seggewiss (1986) with a 4.3125(6) day period, almost circular orbit.

More recently, spectroscopic modelling by Shenar et al. (2019) have found R130 is best described with a composite spectrum, using a WC star and B-type companion. They found a high bolometric luminosity of $\log(L_{bol}/L_{\odot})$=6.34, which they suggested could be interpreted as evidence for additional components within R130. This luminosity is higher than that estimated by Doran et al. (2013), who obtained $\log(L_{bol}/L_{\odot})$=6.0 for the WN/C component of R130. After inspection of the spectrum, we favour the WN/C spectral type

based on its weak C III 4650 emission.

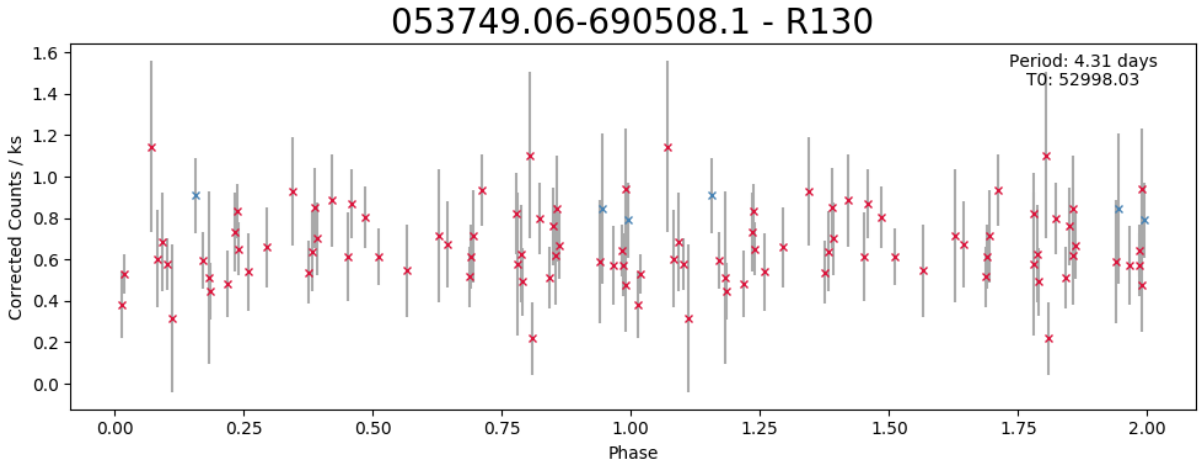

Figure 4.1: The X-ray light curve of R130 folded on a 4.3125 day period as reported by Schnurr et al. (2008). Two full orbital periods have been shown for clarity. Blue crosses refer to the three archival observations taken several years prior to T-ReX.

Despite the reported orbital period, the X-ray data from T-ReX fail to support the claimed binarity. With 1178 net counts, it is a reasonably bright X-ray source and could host a wind-wind collision region. Hints of variability are noted from the reduced χ^2 of 1.26, however the KS probability measurement is low. Folding the light curve with the 4.3125 day period reported by Schnurr et al. (2008) is inconclusive, as shown in Figure 4.1. The hardness ratio is intermediate, 0.86±0.05, which again does not clearly signal binarity, although certainly does not dismiss it.

From 1T XSPEC models we find a corrected X-ray luminosity of $\log(L_{X\mathrm{cor}})$=33.53, however as discussed in Section 3.6.2, a 1T plasma model derives an unsatisfactory fit. Instead a 2T plasma model is favoured, which results in an X-ray luminosity of $\log(L_{X\mathrm{cor}})$=33.77. Using the bolometric luminosities from Shenar et al. (2019) or Doran et al. (2013), we derive high ratios of $L_{Xc}/L_{\mathrm{bol}}=7.08\times10^{-7}$ or $L_{Xc}/L_{\mathrm{bol}}=15.5\times10^{-7}$ respectively.

Based on the X-ray properties of R130, we consider this source to be a good binary candidate. Although the variability and hardness results are inconclusive, the strong detection and high L_{Xc}/L_{bol} favour binarity.

4.2.2 R135

R135 is a WN7h star, designated a binary by Schnurr et al. (2008) who suggested a circular orbit with a 2.1110(18) day period based on radial velocity variations.

Using the VFTS spectroscopic data, Evans et al. (2011) reported the first detection of a massive companion in the spectrum, and updated the spectral type to WN7h + OB. Using the same data, Bestenlehner et al. (2014) noted the spectrum resembled an SB2, however they derived unrealistic radial velocity variations, driven by the uncertainties in the unknown companion. This ultimately resulted in the removal of this source from their discussion, and they noted that the bolometric luminosity, $\log(L_{bol}/L_{\odot})$=5.92, was merely an estimate.

Based on the binary confirmation by Schnurr et al. (2008), spectral modelling by Shenar et al. (2019) cautiously revealed two WR components, a WN5h primary and WN7h secondary, with $\log(L_{bol}/L_{\odot})$=6.20 for the system. They did however, remark a large degree of uncertainty in their results, due a poor model fit, degeneracies in the derived parameters, and a lack of wavelength coverage around key emission lines.

When searching the Chandra ACIS archives, Schnurr et al. (2008) reported a non detection for R135, which would be expected considering the low net counts of 139 we find with the T-ReX survey. This is also evidence for a weaker wind collision region if present. X-ray variability is low/moderate in this source, with a -$\log(P_{KS})$=0.82 and reduced χ^2 of 1.51. We are also unable to confirm the optical period with the X-ray data, as shown in Figure 4.2 which shows the light curve folded with a 2.1110 day period. Whilst there appears to be some periodic variation, there is also a substantial amount of scatter making it difficult to assess and comment on any periodicity.

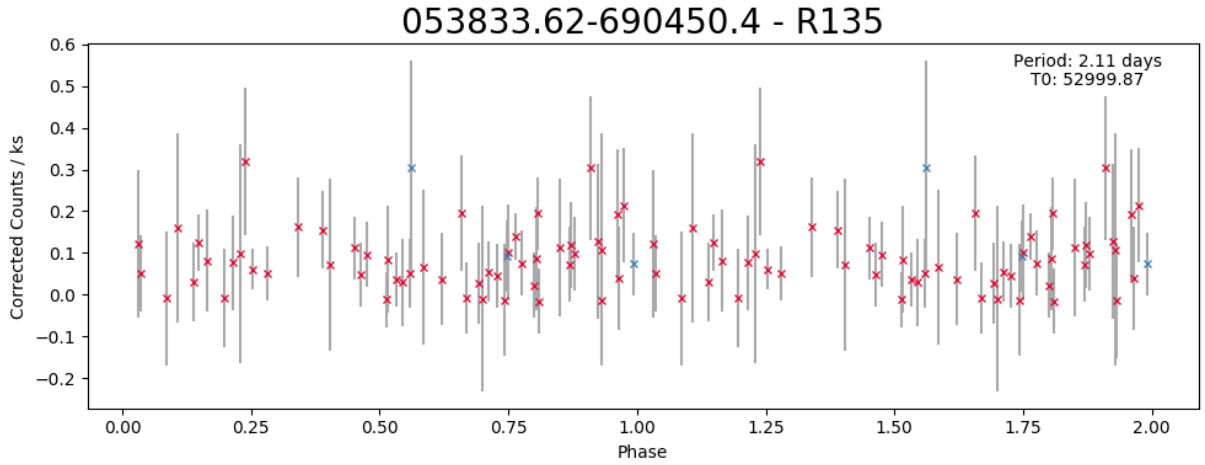

Figure 4.2: The X-ray light curve of R135 folded on a 2.1110 day period as reported by Schnurr et al. (2008). Two full orbital periods have been shown for clarity. Blue crosses refer to the three archival observations taken several years prior to T-ReX.

The hardness of the spectrum does show strong evidence for binarity, with a hardness

ratio of 5.36±1.17. It is the hardest source in the sample by over a factor of 2. From spectral fitting we derived a corrected X-ray luminosity of $\log(L_{X\mathrm{cor}})$=32.97 which, when used with the bolometric luminosities from Bestenlehner et al. (2014) or Shenar et al. (2019), gives $L_{Xc}/L_{\mathrm{bol}}=2.95\times10^{-7}$ or $L_{Xc}/L_{\mathrm{bol}}=1.55\times10^{-7}$ respectively.

Overall the X-ray data give a mixed response to the question of binarity, despite suggestions from optical data.

4.2.3 VFTS 427

Widely reported as a single WN8(h) star (Moffat & Seggewiss, 1986; Doran et al., 2013; Bestenlehner et al., 2014), VFTS 427 was also included in the Schnurr et al. (2008) survey, where they detected no variability in the radial velocity measurements.

A similar conclusion can be drawn from the X-ray data. It is a faint source, with 67 net counts, which suggests either a weakly colliding wind, or single star emission. Variability statistics reveal the source is not variable, with -$\log(P_{\mathrm{KS}})$=0.05 and reduced χ^2 of 1.08, and the hardness ratio was derived to be 0.66±0.15.

Bestenlehner et al. (2014) derived a bolometric luminosity of $\log(L_{\mathrm{bol}}/L_{\odot})$=6.13, which when coupled with the corrected X-ray luminosity of $\log(L_{X\mathrm{cor}})$=32.37 gives $L_{Xc}/L_{\mathrm{bol}}=0.46\times10^{-7}$. This ratio is relatively small, therefore indicative of a single star.

Overall the evidence shows VFTS 427 is a weak, soft, non-variable X-ray source, which implies it is a single star in agreement with the optical data.

4.2.4 Mk51

Mk51 is classified as a O3.5If/WN7 star. Schnurr et al. (2008) found no evidence of significant radial velocity scatter and the source was omitted from Shenar et al. (2019) after being considered a single star by Hainich et al. (2014). The source was included in the VFTS data, and Bestenlehner et al. (2014) found $\log(L_{\mathrm{bol}}/L_{\odot})$=6.20, slightly lower than the $\log(L_{\mathrm{bol}}/L_{\odot})$=6.3 found by Hainich et al. (2014).

In X-rays the source is faint, with 50 net counts, and exhibits a soft spectrum with a hardness ratio of 0.40±0.11. There is no evidence of variability with a reduced χ^2 of 1.00 and KS-test probability of -$\log(P_{\mathrm{KS}})$=0.05. Spectral modelling reveals an X-ray luminosity of $\log(L_{X\mathrm{cor}})$=32.21, which with the bolometric luminosity from Bestenlehner et al. (2014) gives $L_{Xc}/L_{\mathrm{bol}}=0.27\times10^{-7}$. This weak, soft X-ray source, with a low L_{Xc}/L_{bol} ratio, does not show any indication of binarity.

4.2.5 Mk49

Classified as a WN6(h) star, Mk49 is another likely single star. Hainich et al. (2014) considered the star to be single and derived a high luminosity of $\log(L_{bol}/L_{\odot})$=6.70. Although not included in the VFTS sample, Doran et al. (2013) used the data from Schnurr et al. (2008) to make an estimate of the luminosity based on spectral type. They found a considerably lower $\log(L_{bol}/L_{\odot})$=6.1.

From T-ReX we find a weak detection, with 66 net counts, however Mk49 exhibits the second hardest spectrum in the sample, with a hardness ratio of 2.32±0.56. With a reduced χ^2 of 1.05 and KS-test probability of -$\log(P_{KS})$=0.17, there is no trace of X-ray variability in this source.

We find a corrected X-ray luminosity of $\log(L_{Xcor})$=32.43, which gives L_{Xc}/L_{bol}=0.56×10^{-7} when coupled with the luminosity derived by Doran et al. (2013). Based on the results presented here we conclude that Mk49 is a likely single star, despite the hardness of the spectrum.

4.2.6 Mk39

Classified as an O2.5If*/WN6, Mk39 is a suspected binary. Massey et al. (2005) attempted to fit the observed optical spectrum, however were unable to do so with a single model and instead required a composite, so therefore reported this star as a binary. Schnurr et al. (2008) confirmed the binary nature of this source using radial velocity monitoring, where they reported variability with a standard deviation of 58.9 km s^{-1}(22.9 km s^{-1} limit for variability). They also reported a tentative period of 92.60(31) days, however admitted this measurement is at their detection limit. In contrast, Shenar et al. (2019) recorded Mk39 as an SB1 binary, noting that they were unable to find any evidence for a companion in their available spectra.

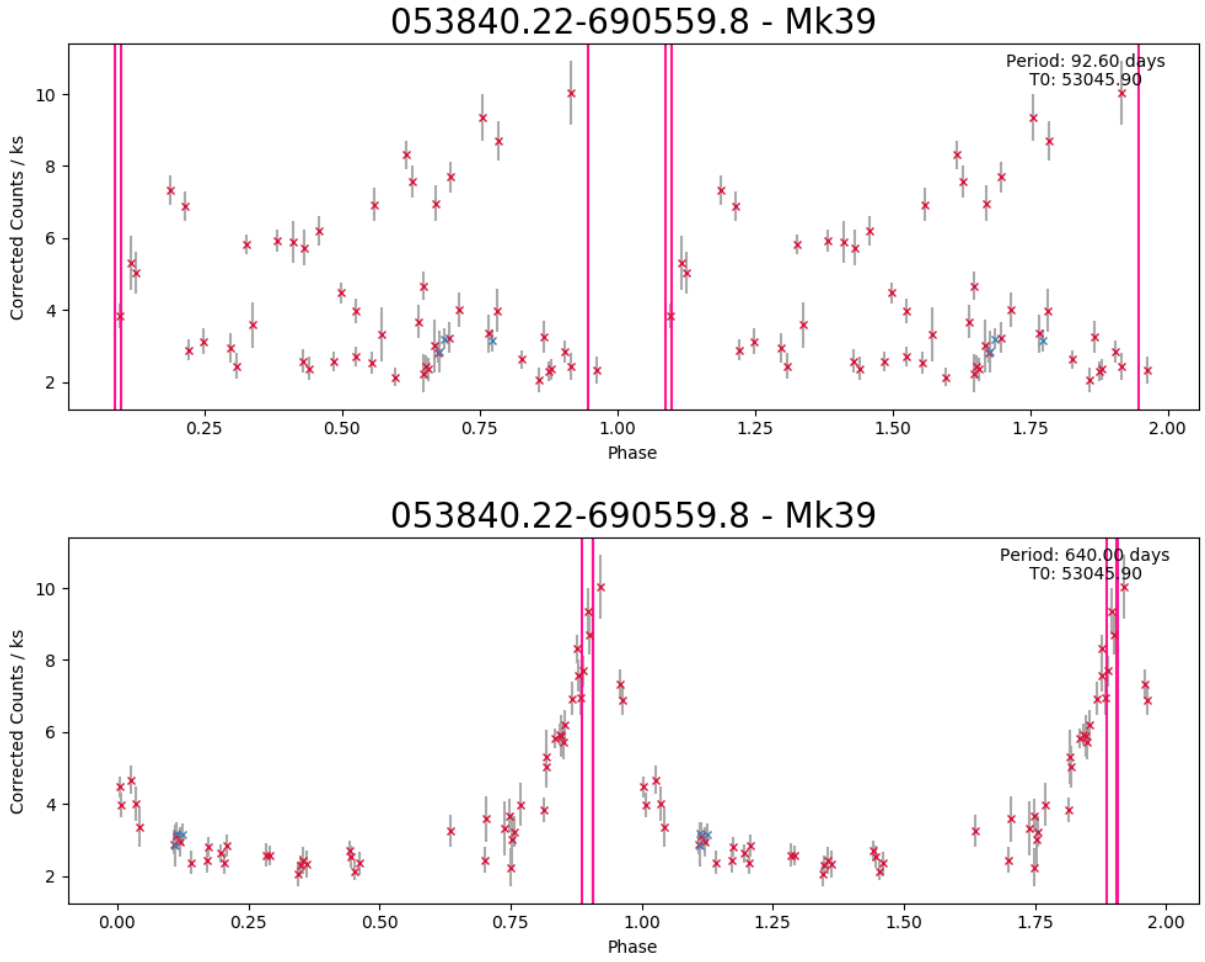

Figure 4.3: The X-ray light curve of Mk39 folded on a 92.60 day period as reported by Schnurr et al. (2008) (upper) compared with the light curve folded on a 640 day period (lower). Two full orbital periods have been shown for clarity. Blue crosses refer to the three archival observations taken several years prior to T-ReX. Pink vertical lines show the phase measurement corresponding to UVES observations thought to be taken close to periastron, such that double emission is observed in the spectra.

Using the X-ray data from T-ReX we also find obvious systematic long-term X-ray variability, as can be seen in light curve for Mk39 shown in Appendix A. It has a high reduced χ^2 of 33.83 and the highest KS-test probability of the sample, -log(P_{KS})=260.65. The periodicities from optical and X-ray data however do not agree. Folding the light curve on a 92.60 day period yields rather unsatisfactory results, as shown in Figure 4.3. Instead we propose a period in the range of 630–660 days, with a 640 day period shown in Figure 4.3 and discussed further below. We note again that Schnurr et al. (2008) commented on the

uncertainty in their optical period, and that their study would only be suitable for finding binaries with a period less than 200 days.

The hardness ratio was found to be 0.41±0.01, which with respect to other WR stars in the sample, the hardness of Mk39 is quite soft. It does however have a high mean L_{Xc}/L_{bol} of 21×10^{-7} using a corrected X-ray luminosity of $\log(L_{X\,cor})$=34.30 and a bolometric luminosity of $\log(L_{bol}/L_{\odot})$=6.4 (Bestenlehner et al., 2014). Overall these X-ray properties strongly suggest Mk39 is a colliding wind binary.

Mk39 in VFTS

The VLT Flames Tarantula Survey (VFTS) (Evans et al., 2011) is an optical spectroscopic survey of 893 massive stars in the 30 Dor region. Using the Fibre Large Array Multi-Element Spectrograph (FLAMES) instrument on the VLT, multi-epoch observations were taken using the mode configurations outlined in Table 4.1.

Table 4.1: Observing modes and properties for VFTS, taken from Evans et al. (2011). Note that due to a detector gap, the UVES mode has a break in wavelength coverage between 5155-5240 Å.

FLAMES Mode	Wavelength Coverage [Å]	Spectral Resolution [Å]	R
Medusa	3960-4564	0.61	7000
Medusa	4499-5071	0.56	8500
Medusa	6442-6817	0.41	16000
ARGUS	3960-4570	0.40	10500
UVES	4175-6200	0.10	53000

Mk39 was included in VFTS, from which there were 5 epochs of UVES (red-arm) optical spectroscopy summarized in Table 4.2. The raw data were reduced by Sergio Simon-Diaz before being distributed. We used these data to search for evidence of an SB2 binary.

Table 4.2: UVES observations of Mk39, collected as part of the VFTS survey.

Epoch	Observation	MJD	Exposure Time [s]
1	a	54803.15	1815
1	b	54803.17	1815
2	a	54803.19	1815
2	b	54803.22	1815
3	a	54851.08	1815
3	b	54851.10	1815
4	a	54907.06	1815
4	b	54907.08	1815
4	c	54893.02	1815
4	d	54893.05	1815
4	e	54905.99	1550
4	f	54906.01	860
4	g	54906.02	173
5	a	55204.12	1815
5	b	55204.14	1815

To increase the S/N ratio we combine observations taken at the same time such that we result in the following 7 spectra, in chronological order: 1ab, 2ab, 3ab, 4cd, 4efg, 4ab and 5ab. Using these spectra we note clear morphological changes between epochs in the He II 4542, N III 4641, He II 5411 and C IV 5807-5812 emission/absorption lines. Figure 4.4 shows the trail plots for the He II 4542, N III 4641 and C IV 5807-5812 emission/absorption lines demonstrating these variations through time. Double peaked/troughed lines can clearly be observed in groups 4cd, 4efg and 4ab, whereas in the remainder of observations these lines are blended. The spectra for these observations can be found in Figure D.1.

We recorded the optical radial velocity variations for the He II 4542 absorption profile using the emission line fitting function in DIPSO, shown in Figure 4.5. A single Gaussian profile was fit to the blended absorption line, or two Gaussian profiles were used when double peaked absorption was visible. The results are shown in Table 4.3. To constrain the orbital period we utilise the UVES and T-ReX data together. As shown in Table 4.3, the UVES observations during which double absorption lines can be measured correspond to phases close to X-ray maximum, which likely corresponds to periastron. Similarly,

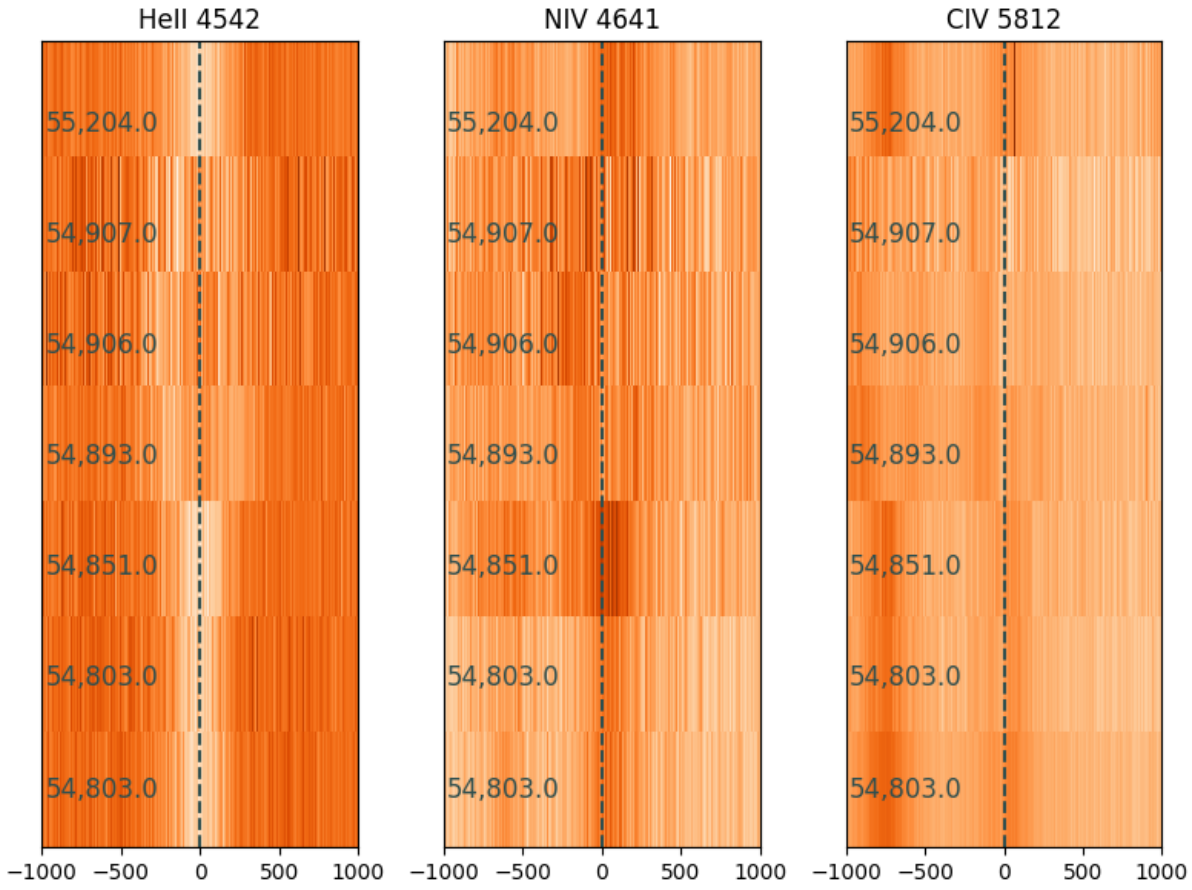

Figure 4.4: Trail plot of the three optical emission/absorption lines shown in Figure D.1, He II 4542, N III 4641 and C IV 5807-5812, using VFTS observations of Mk39. Again the radial-velocity scale is centred such that the reference velocity (240 km s^{-1}) is zero and the dashed line corresponds to the rest wavelength of each emission line.

observations with blended absorption occur at phases away from periastron. By selecting the UVES observations thought to coincide with times close to periastron we can convert the MJD to a phase measurement and combine this data with the folded X-ray light curve, as shown by the pink lines in Figure 4.3. It is only by using both data sets that we have been able to identify a likely period range of 630–660 days.

Table 4.3: He II 4542 radial velocity measurements for Mk39. If only RV1 measurement recorded then the absorption line appeared blended and it was not possible to differentiate between the two components. Phase measurements are derived using a 640 day period, with T_0=53046.

Epoch	MJD [J2000]	RV1 [km s^{-1}]	RV2 [km s^{-1}]	Phase
01ab	54803.1616	235 ± 1		0.7456
02ab	54803.2056	236 ± 1		0.7456
03ab	54851.0882	245 ± 1		0.8205
04cd	54893.0344	105 ± 5	393 ± 6	0.8860
04efg	54906.0079	140 ± 8	367 ± 5	0.9063
04ab	54907.0848	138 ± 4	387 ± 4	0.9079
05ab	55204.1328	242 ± 1		0.3721

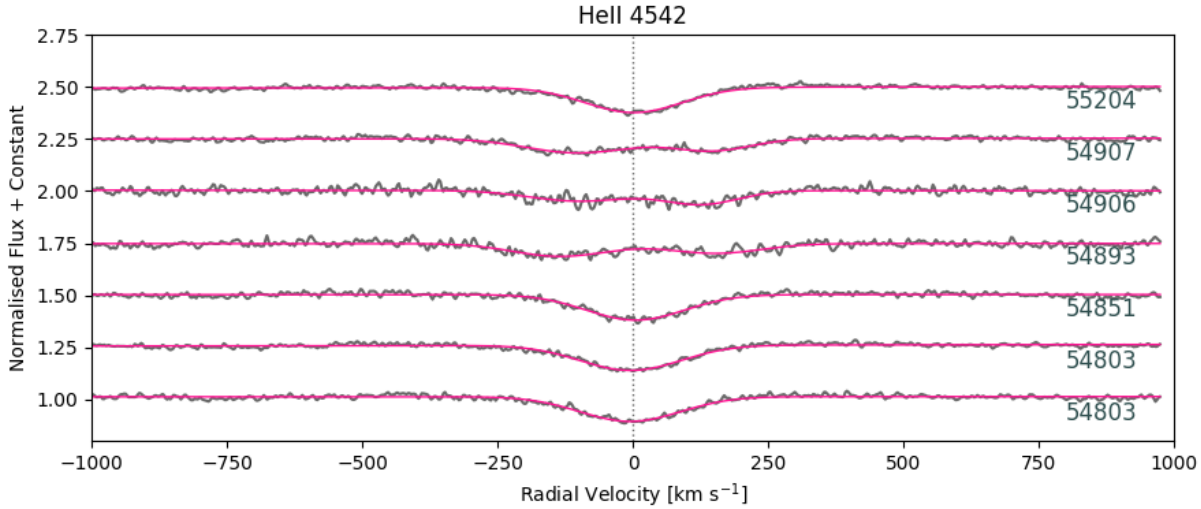

Figure 4.5: He II 4542 absorption line radial velocity measurements, in pink, using VFTS data of Mk39, in grey. Spectra are plotted in chronological order with the observation MJD noted within the figure. Spectra are offset for clarity. The radial-velocity scale is centred such that the reference velocity (taken here to be 240 km s^{-1}) is zero and the dashed line corresponds to the rest wavelength of 4541.59 Å.

T-ReX and VFTS establish Mk39 as a SB2 colliding wind binary with a possible period of 640 days. The shape of the folded light curve also suggests an eccentric orbit, with an eccentricity greater than ∼0.5 when assuming count rate is inversely proportional to separation. We recommend further follow-up with this source to confirm this period and derive a full orbital solution.

4.2.7 R134

Schnurr et al. (2008) found no evidence of significant radial velocity scatter in R134 (WN7h). Shenar et al. (2019) mark R134 as a single star, though note this designation is uncertain. In contrast, Hénault-Brunet et al. (2012) reported the potential detection of line profile variations in the He II 4542 emission line using the VFTS data. They also acknowledged some uncertainty here too, due to problems defining the continuum. Bestenlehner et al. (2014) assigned R134 as a single star and found $\log(L_{bol}/L_{\odot})$=6.2.

In X-rays R134 was the faintest source in the sample, showing 35 net counts in 2 Ms. We find some evidence for variability, with a KS-test probability of -$\log(P_{KS})$=1.91 and reduced χ^2 of 2.22, however given the low count rate it is difficult to assess the robustness of these measurements. As noted in Section 3.7, Townsley et al. (2006b) and Portegies Zwart et al. (2002) report X-ray detections for this source using observations with much shorter exposure times. This could indicate X-ray variability on longer timescales.

The hardness ratio was derived to be 1.07±0.28, meaning that the spectrum of R134 is quite hard. Using the corrected X-ray luminosity for this work, $\log(L_{X\mathrm{cor}})$=32.23, with the bolometric luminosity from Bestenlehner et al. (2014), we find $L_{Xc}/L_{bol}=0.28\times10^{-7}$.

In summary we would argue that the binary status of R134 remains uncertain. The hard spectrum and possible hint of variability indicates there is a companion, however the weakness of the source and low L_{Xc}/L_{bol} suggests otherwise.

4.2.8 R140a1/a2

R140a1/a2 comprises two sources in close proximity, within R140a. Assigned a combined spectral type of WC4 + WN6 + O, R140a1/a2 has long thought to host one, if not two, binary systems, but this has yet to be confirmed. The system also resides close to R140b which can sometimes cause confusion. For example, Moffat et al. (1987) reported a 2.7596(1) day period for R140a2, however Schnurr et al. (2008) attributed this period to R140b. For R140a1/a2 they noted some radial velocity scatter above their significance threshold, however were unable to find any periodicity. Based on the lack of solid evidence, Shenar et al. (2019) considered R140a2 (WN6) as a single star, whereas Hainich et al. (2014) considered R140a1/a2 to be a binary suspect.

The strongest evidence this system is host to at least one binary is in the X-ray data. R140a1/a2 is exceptionally bright in X-rays, with 54,062 net counts. Using our 1T XSPEC fits it has the highest corrected X-ray luminosity in the sample, $\log(L_{X\mathrm{cor}})$=35.31. The 2T XSPEC model returns a slightly higher $\log(L_{X\mathrm{cor}})$=35.36. Using the 2T model corrected

X-ray luminosity combined with a bolometric luminosity of $\log(L_{bol}/L_{\odot})$=6.41 for the WR component (Doran et al., 2013), we find L_{Xc}/L_{bol}=234×10^{-7}. This is exceptionally high and a very strong indication of at least one colliding wind system.

The spectrum for R140a1/a2 is relatively soft, with a hardness ratio of 0.347±0.003. The light curve shows strong evidence for long-term X-ray variability, with a high KS-test probability of -$\log(P_{KS})$=8.71 and reduced χ^2 of 5.11. Based on the light curve shown in Appendix A, this variability appears to occur on the order of ∼100 days. It is however, important to mention that R140a1/a2 was subject to large count rate corrections as a result of its unfavourable location, in close proximity to the edge of the chip, see Section 3.4. These corrections could also generate some of the short-term variability observed in the light curve. As yet, we have been unable to derive a periodicity for the variability. Figure 4.6 shows a comparison of the light curves for R140a1/a2 and R140b folded with the updated 2.75975(27) day period reported by Schnurr et al. (2008). Based on Figure 4.6 we are more inclined to consider that the 2.75975 day period is associated with R140b rather than R140a, although, as shown in Figure 4.6, neither source is compelling.

Despite the lack of period, based on the high L_{Xc}/L_{bol} and evidence for variability, there is strong reason to suspect R140a1/a2 is host to at least one colliding wind binary system.

4.2.9 R140b

As discussed in the section above, R140b is located in close proximity to R140a with ∼0.4 pc between them, see Figure 3.7b in Section 3.3, and has been the source of some confusion in the past. Classified as a WN6 + O5(h) star it is a known binary. Schnurr et al. (2008) attributed the 2.75975(27) day period previously associated with R140a2 to this system, see discussion in the section above. Also, Evans et al. (2011) revealed R140b to host a massive companion using VFTS spectroscopic data.

Shenar et al. (2019) also confirmed R140b as an SB2 system, and successfully disentangled the composite spectrum to reveal a WN5h + O3.5 V system. They reported the presence of artefacts during the disentanglement which they attributed to excesses arising from wind-wind collisions within the binary. Shenar et al. (2019) independently found an orbital solution with a period of 2.7586(4) days, which is in excellent agreement with that derived by Schnurr et al. (2008).

Using the period of 2.7586(4) days derived from optical data (Schnurr et al., 2008; Shenar et al., 2019), Figure 4.6 shows the folded X-ray light curve for R140b (lower panel). There is a reasonable amount of scatter evident in the plot, making it difficult to claim the 2.7586 day period seen in the optical data fully agrees with the X-ray variability. Despite

being unable to verify the periodicity, there is clear X-ray variability evident in R140b with a high reduced χ^2 of 4.68. The KS-test is less definitive with -log(P_{KS})=0.88, however is still suggestive of variability. The hardness ratio is relatively low, 0.45±0.04, giving R140b a soft spectrum.

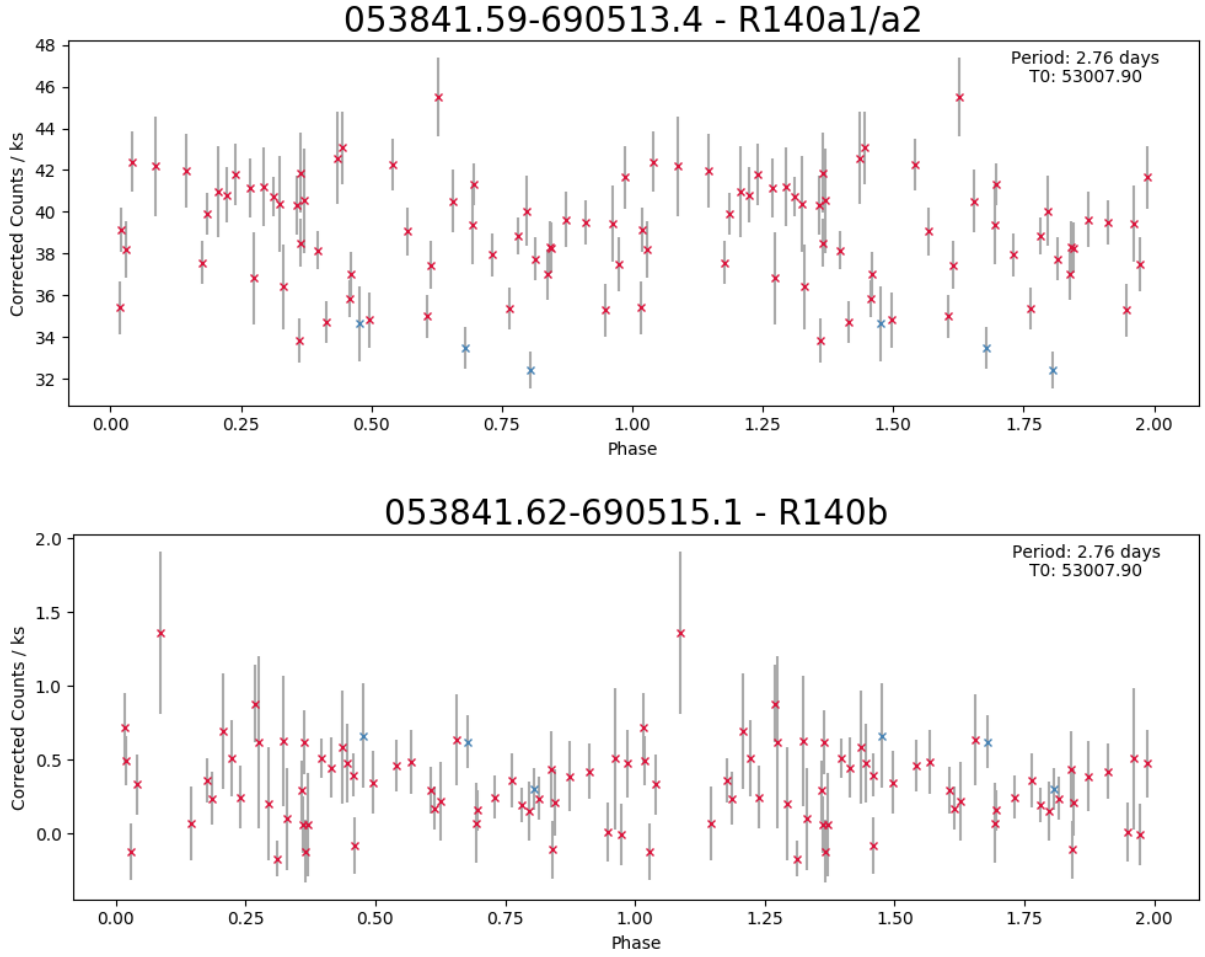

Figure 4.6: The X-ray light curve of R140a1/a2 (upper) and R140b (lower) both folded on a 2.7586 day period as reported by Shenar et al. (2019). Two full orbital periods have been shown for clarity. Blue crosses refer to the three archival observations taken several years prior to T-ReX.

Bestenlehner et al. (2014) derived a luminosity of log($L_{bol}/L_{\odot}$)=6.43 however they comment on the poor quality of the spectral fit, attributed to the presence of the secondary which was unaccounted for. In contrast, Shenar et al. (2019) account for both components (WN5(h) + O3.5 V) in their models, although as discussed above they too noticed

poor fits. Nevertheless, they found a luminosity of $\log(L_{bol}/L_{\odot})$=6.25. Taking the X-ray luminosity to be $\log(L_{Xcor})$=33.24, we find L_{Xc}/L_{bol}=1.70×10^{-7} and L_{Xc}/L_{bol}=2.57×10^{-7} using the bolometric luminosities from Bestenlehner et al. (2014) and Shenar et al. (2019) respectively.

Overall, the high X-ray variability and moderate L_{Xc}/L_{bol} is consistent with a colliding wind binary system, despite the soft spectrum. We therefore consider R140b a good binary candidate.

4.2.10 R136a

The T-ReX survey, discussed in Chapter 3, extracted two sources within R136a, as shown in Figure 3.7a. R136a is a particularly dense region, host to multiple massive stars (Massey & Hunter, 1998), therefore the two X-ray sources in our sample comprise many stars (Crowther et al., 2016). The most massive stars within R136a are listed in Table 4.4, and we have identified those stars which are spatially consistent with X-ray sources. Continuing with the two X-ray defined regions we have; R136a1/a2/a4/a5/a7/a8 (which we refer to as R136a1/a2), and R136a3/a6.

Table 4.4: Properties of the most massive stars located within R136a. Spectral types are taken from Doran et al. (2013) and Crowther et al. (2016). Bolometric luminosities are from Bestenlehner et al. (in prep) with the exception of R136a8, from Crowther et al. (2016).

Star	Spectral Type	$\log(L_{bol}/L_{\odot})$
R136a1	WN5h	6.79
R136a2	WN5h	6.67
R136a3	WN5h	6.63
R136a4	O2-3V	6.24
R136a5	O2If	6.29
R136a6	O2If	6.27
R136a7	O3III	6.25
R136a8	O2-3V	6.28

R136a1/a2

Using VLT spectroscopic observations, and archival HST photometry, Schnurr et al. (2009b) found no evidence for short-period binarity in R136a1, R136a2 or R136a5. If we assume a mass ratio close to unity, which is the easiest configuration to detect as both components

should present strong emission lines, spectroscopic analysis also reveals no evidence for short-period binaries amongst the R136a stars (Crowther et al., 2010).

In X-rays the R136a1/a2 source is strong, with 4,369 net counts, though soft, with a hardness ratio of 0.33±0.01. There is also evidence for variability with a reduced χ^2 of 3.75 and KS-test probability of -log(P_{KS})=1.93.

Using our 1T model in XSPEC we find a corrected X-ray luminosity of log(L_{Xcor})=34.10, which combined with a bolometric luminosity of log($L_{bol}/L_{\odot}$)=7.28 (from Table 4.4) gives $L_{Xc}/L_{bol}=1.74\times10^{-7}$.

In general the X-ray characteristics would suggest R136a1/a2 could be a potential host for a colliding wind binary. Since the aperture encompasses multiple sources however, it would not be possible to identify which source is the most likely binary candidate.

R136a3/a6

R136a3 was also included in the study compiled by Schnurr et al. (2009b) to search for radial velocity and photometric variability, however nothing significant was detected.

The R136a3/a6 source has a much weaker X-ray detection than R136a1/a2, with 492 net counts. The hardness of the spectrum however, is comparable at 0.38±0.03. The variability parameters return mixed results, with a high reduced χ^2 of 5.39 but a low KS-test probability of -log(P_{KS})=0.16. Visual inspection of the light curve indicates some potential variability, however in general is unclear.

The X-ray luminosity was derived to be log(L_{Xcor})=33.26, using the 1T model in XSPEC, and using a bolometric luminosity of log($L_{bol}/L_{\odot}$)=6.79 (from Table 4.4) we derive $L_{Xc}/L_{bol}=0.78\times10^{-7}$.

Although R136a3/a6 exhibits a weak, soft X-ray spectrum, with a low L_{Xc}/L_{bol} ratio, the high variability which is clearly observed in the light curve leads to doubt on its single status. We therefore tentatively suggest that this source could be a potential binary system.

4.2.11 R136c

R136c, a WN5h star, lies close the central core of the R136 cluster, as shown in Figure 3.7a. It has a high X-ray flux (Portegies Zwart et al., 2002; Townsley et al., 2006b), which has long prompted suspicions that R136c is a binary. The companion star however, has never been observed, and there is no evidence of a composite spectra in the available data (Shenar et al., 2019). Schnurr et al. (2009b) used VLT observations to search for radial velocity variability in R136c, and reported a marginal detection with a tentative 8.2 day period. They admit, however, some concerns with regards to this solution, and suggested a longer

period is more likely. Nevertheless, the X-ray literature results indicate that R136c will be confirmed as a multiple system (Crowther et al., 2010), especially since the characteristics of this star are similar to the newly confirmed binary Mk34 (see Chapter 5).

In the T-ReX survey R136c is a bright source with 6,960 net counts. The hardness ratio of 0.72±0.02 suggests a moderate level of hard emission, although this in isolation is not conclusive evidence for a colliding wind system. We do note however, continuing the theme of comparison to Mk34, that the level of hard emission observed in R136c is almost identical to that recorded for Mk34, shown in Table 4.5.

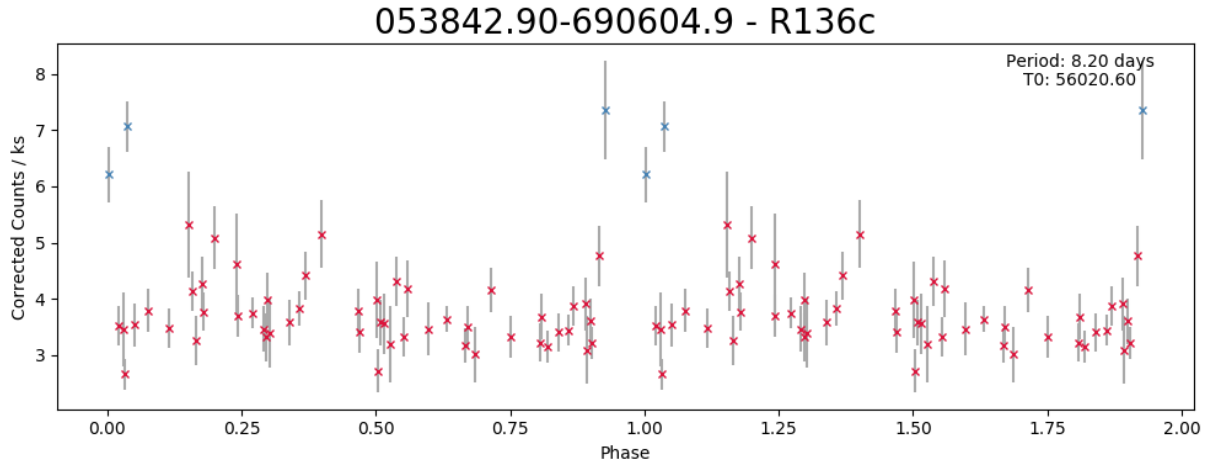

Figure 4.7: The X-ray light curve of R136c folded on a 8.2 day period as reported by Schnurr et al. (2009b). Two full orbital periods have been shown for clarity. Blue crosses refer to the three archival observations taken several years prior to T-ReX.

R136c shows very strong evidence of X-ray variability with a high reduced χ^2 of 6.39 and KS-test probability of -log(P_{KS})=10.62. As Figure 4.7 shows, we are unable to confirm this variability follows the 8.2 day period reported by Schnurr et al. (2009b).

Using our 1T model in XSPEC we find a corrected X-ray luminosity of log(L_{Xcor})=34.38. From spectroscopic modelling Bestenlehner et al. (2014) find a bolometric luminosity of log($L_{bol}/L_{\odot}$)=6.58, giving an L_{Xc}/L_{bol}=16.6×10^{-7}. Spectral analysis from Crowther et al. (2010) suggests a slightly higher temperature, giving log($L_{bol}/L_{\odot}$)=6.75 and L_{Xc}/L_{bol} =11.2×10^{-7}.

Both literature bolometric luminosities result in a high L_{Xc}/L_{bol} ratio, and when coupled with the high count rate, fairly hard spectrum, and strong variability we are confident R136c is a colliding wind binary of uncertain period.

4.2.12 Mk30

Mk30 is classified as an O2If*/WN5 star by Crowther & Walborn (2011). It was first identified as a binary by Schnurr et al. (2008) whilst searching for radial velocity variations and they derived a 4.699(10) day period. Doran et al. (2013) also noted radial velocity variations however mentioned the companion is likely much fainter than the primary. Despite this, Shenar et al. (2019) were able to disentangle the spectra to reveal a B0V secondary, although they remarked the task was challenging and required additional data for improvement. They too derived an orbital solution for Mk30 and found a period of 4.6965(2) days, in excellent agreement with Schnurr et al. (2008).

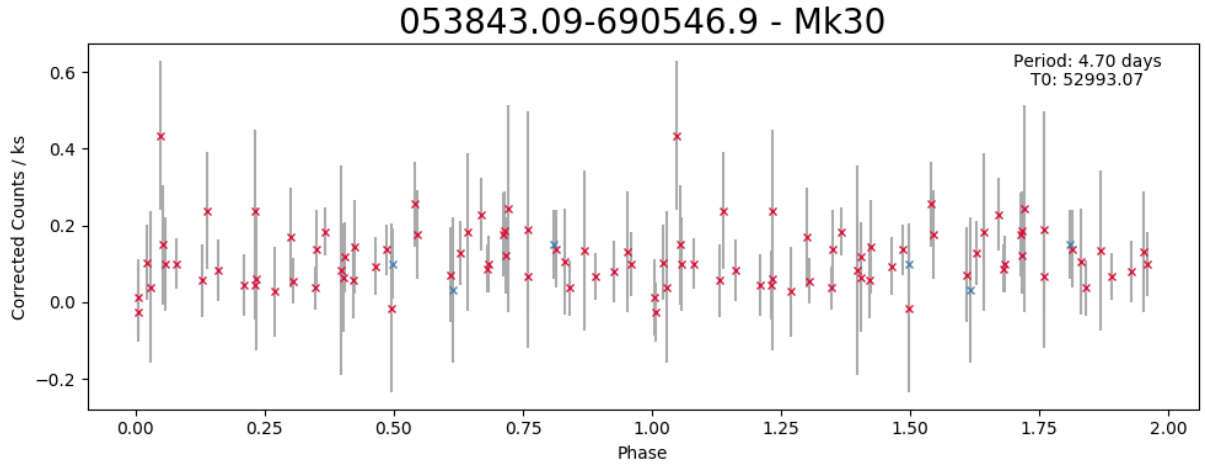

Figure 4.8: The X-ray light curve of Mk30 folded on a 4.6965 day period as reported by Shenar et al. (2019). Two full orbital periods have been shown for clarity. Blue crosses refer to the three archival observations taken several years prior to T-ReX.

In X-rays Mk30 is a relatively weak, soft X-ray source with 205 net counts and a hardness ratio of 0.32±0.05. The source shows little evidence of variability with a reduced χ^2 of 1.41 and KS-test probability of -log(P_{KS})=0.45. When the light curve is folded with the 4.6965(2) day period (Shenar et al., 2019) as shown in Figure 4.8, there is no obvious X-ray periodicity to match.

Both Bestenlehner et al. (2014) and Shenar et al. (2019) found a consistent bolometric luminosity of log($L_{bol}/L_{\odot}$)=6.16. With an X-ray luminosity of log($L_{X\,cor}$)=32.59, found from the 1T model XSPEC fitting, we find a low L_{Xc}/L_{bol} of 0.71×10^{-7}.

Without the optical radial velocity variations it would be difficult to identify Mk30 as a binary system. This could be attributed to the low mass ratio of the system, q=0.32 (Shenar et al., 2019), where a fainter secondary would have a weaker interacting wind and

therefore a weaker X-ray signature.

4.2.13 Mk35

Classified as a O2If*/WN5 star (Crowther & Walborn, 2011), Mk35 was first considered a binary star candidate after Schnurr et al. (2008) found radial velocity variations above their significance threshold. Unfortunately, however, they were unsuccessful in their attempts to identify the period. Based on the lack of binary evidence, Shenar et al. (2019) excluded the source from their sample.

Mk35 is a relatively weak X-ray source with 201 net counts, and a hardness ratio of 0.24±0.04, indicating the softest spectrum of the WR sample. There is no suggestion of X-ray variability, with a reduced χ^2 of 0.95 and KS-test probability of -log(P_{KS})=0.60

Bestenlehner et al. (2014) found a bolometric luminosity of log($L_{bol}/L_{\odot}$)=6.3 using spectral modelling, although they treated the system as a single star. From XSPEC 1T models we find an X-ray luminosity of log(L_{Xcor})=32.72, which in turn gives an L_{Xc}/L_{bol} of 0.69×10^{-7}.

Considering the soft, weak detection, lack of variability and low L_{Xc}/L_{bol} ratio, the X-ray data does not help to confirm the binary status of Mk35 or constrain the unknown orbital period.

4.2.14 Mk34

The brightest X-ray source in the sample, Mk34 has been proposed as a potential binary for some considerable time, based on its exceptionally bright X-ray luminosity (Townsley et al., 2006b) and the large optical variations which were observed for a brief period by Chené et al. (2011). Further attempts to observe a companion or derive an orbital period have, however, been unsuccessful.

Mk34 is discussed extensively in Chapter 5, however to briefly summarize we observe extreme variability, with a reduced χ^2 of 131 and -log(P_{KS})=16.57, that is periodic with a 155.1(1) day cycle, shown in Figure 4.9 (Pollock et al., 2018). The resulting light curve is reminiscent of other known colliding wind binaries, such as WR140, as shown in Figure 1.8. The hardness ratio is moderate, at 0.70 ± 0.01, similar in magnitude to R136c.

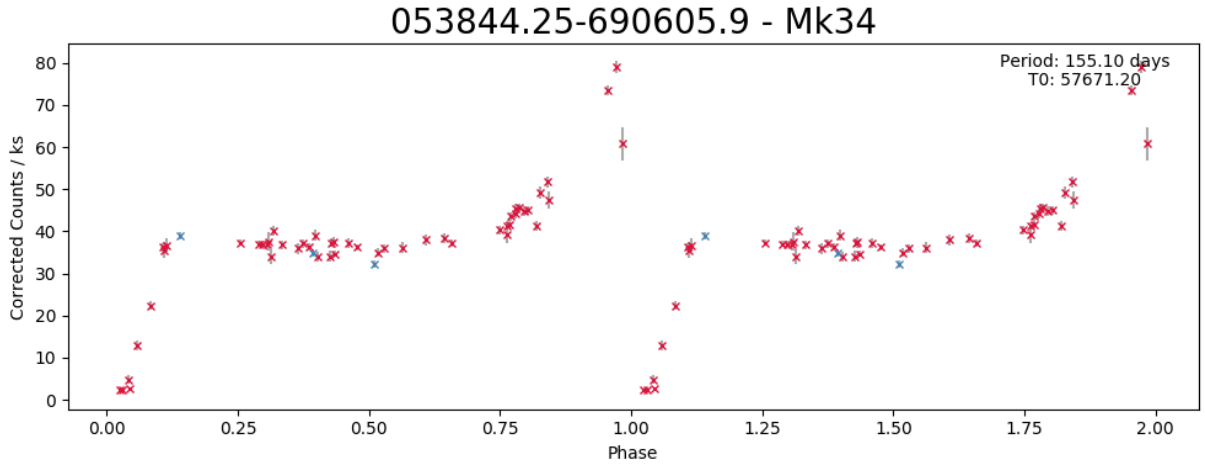

Figure 4.9: The X-ray light curve of Mk34 folded on a 155.1 day period as reported by Pollock et al. (2018). Two full orbital periods have been shown for clarity. Blue crosses refer to the three archival observations taken several years prior to T-ReX.

We also find a particularly high X-ray luminosity of $\log(L_{X\mathrm{cor}})$=35.29 (1T model). Combined with a bolometric luminosity of $\log(L_{\mathrm{bol}}/L_{\odot})$=6.70, found in Chapter 5, we derive an extremely high L_{Xc}/L_{bol} of 102×10^{-7}.

Based on these X-ray results we are strongly in favour of designating Mk34 as a binary and, as discussed in Chapter 5, using additional optical observations we can confirm that Mk34 is a colliding wind binary.

4.2.15 R146

R146 is classified as a WN5ha star and, whilst originally suspected to have a B-star companion (Smith et al., 1996), it is currently thought to be single (Moffat, 1989; Foellmi et al., 2003b).

The X-ray data returns mixed messages with regards to the binarity of R146. The source has a reasonably strong detection with 697 net counts in the T-ReX data, however the spectrum is soft, with a hardness ratio of 0.25±0.02. There is some evidence of variability within the X-ray light curve. Although the reduced χ^2 of 1.29 is inconclusive, the KS-test probability for R146 returns a high value of $-\log(P_{\mathrm{KS}})$=4.54, suggesting some fluctuations. Visual inspection of the light curve, shown in Figure A.1f, reveals some variability may be plausible.

Bestenlehner et al. (2014) considered this star to be single and derived a bolometric luminosity of $\log(L_{\mathrm{bol}}/L_{\odot})$=6.29, similar to that derived by Doran et al. (2013), where $\log(L_{\mathrm{bol}}/L_{\odot})$=6.2. From XSPEC we find an X-ray luminosity of $\log(L_{X\mathrm{cor}})$=33.14 (1T

model) and using the Bestenlehner et al. (2014) bolometric luminosity we derive L_{Xc}/L_{bol} $=1.86\times10^{-7}$.

Overall it is difficult to interpret these results and confidently appoint a binary status for R146, despite the hint of variability, therefore we consider this source single.

4.2.16 R144

Originally thought to be single by Moffat (1989), using radial velocity variations Schnurr et al. (2008) identified R144 as binary candidate. They, however, were unable to find periodicity, even with additional polarimetric data Schnurr et al. (2009a).

Sana et al. (2013a) obtained further multi-epoch X-Shooter spectra which revealed R144 as an SB2 binary, and they assigned the spectral classification WN5-6h + WN6-7h. They were not, however, able to identify the period, but combining this data with the results from Schnurr et al. (2009a) allowed them to place the constraint of a ∼370 day maximum orbit, with potential solutions ranging from integer divisions (i.e. 370/n).

R144 (HD38282) was also observed within the All-Sky Automated Survey for Supernovae (ASAS-SN)[1] (Shappee et al., 2014; Kochanek et al., 2017), allowing periodicity searches using this independent data set. Consisting of 24 telescopes distributed worldwide, ASAS-SN scans the night sky primarily looking for transients. To optimise this the pixel-scale is very large (∼8″per pixel), which means for the majority of our 30 Dor WR stars the ASAS-SN data is unusable due to crowding. R144 however, is relatively isolated.

With 2754 V-band observations and 2635 g-band observations taken over a baseline of 1869 days, the most likely period was derived to be 74.24 days, as shown in the periodogram and folded ASAS-SN light curve in Figure 4.10 (Pollock, private communication). This is in agreement with Sana et al. (2013a) who state P=370/n, and where for ∼74 days, n=5. We should however, note that Sana et al. (2013a) favoured n=1,2,3 & 6 and noted n=4,5 & ≥7 solutions were unlikely as further large radial velocity variations should be present in the current data.

[1] http://www.astronomy.ohio-state.edu/asassn/index.shtml

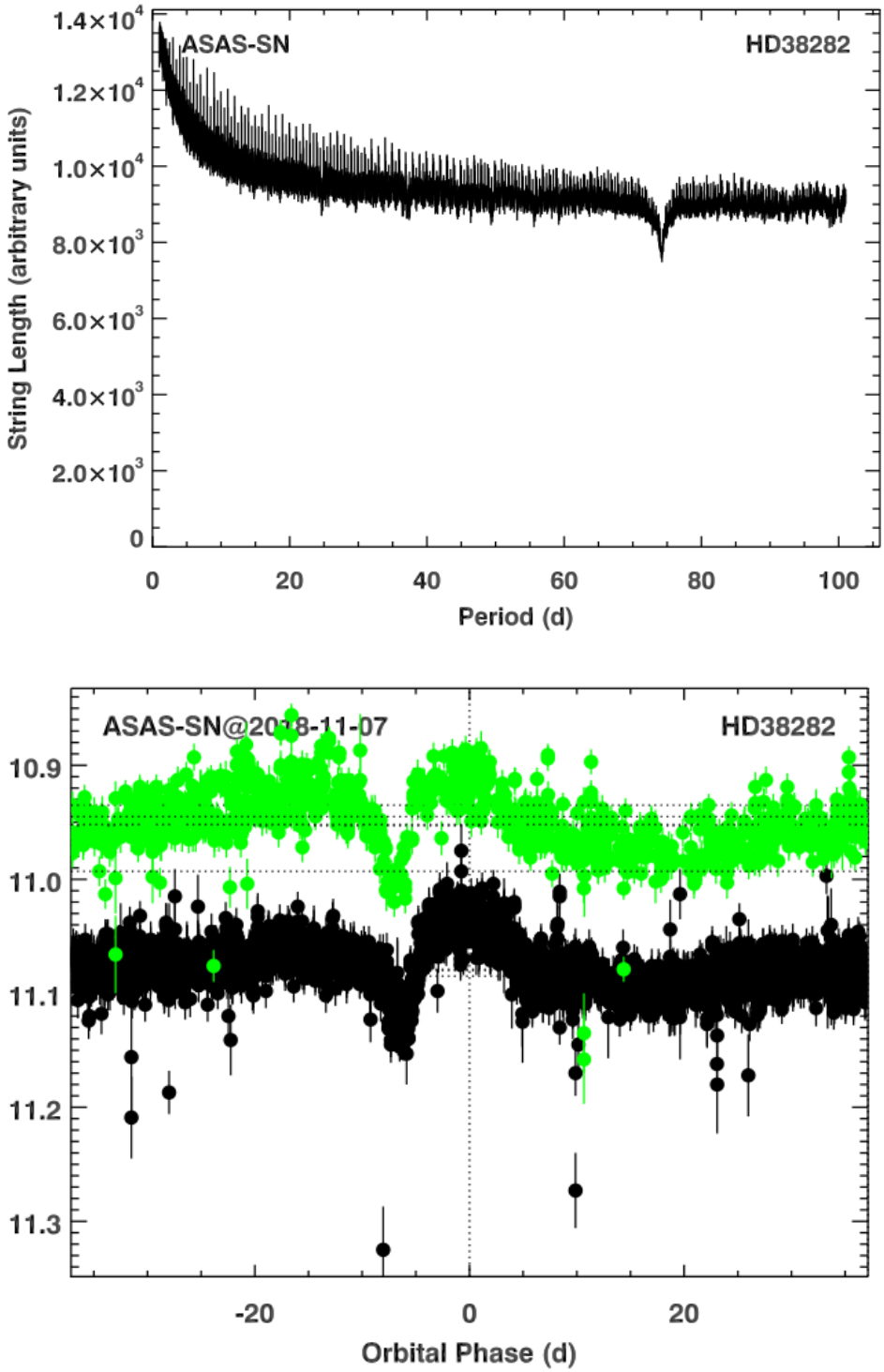

Figure 4.10: Upper: The periodogram for R144 (HD38282) using ASAS-SN data. Lower: ASAS-SN light curve in g-band (green) and V-band (black) folded on a 74.24 day period.

In the T-ReX data R144 is well detected, with 1263 net counts, however the spectrum

is quite soft with a hardness ratio of 0.60±0.03. The source is also noted as variable, with a reduced χ^2 of 2.61 and KS test probability of -log(P_{KS})=2.62. Figure 4.11 shows the X-ray light curve folded on the 74.24 day period derived with the ASAS-SN data. We can see this period is reasonably consistent with the X-ray variability, strengthening the argument for a ∼74 day orbit.

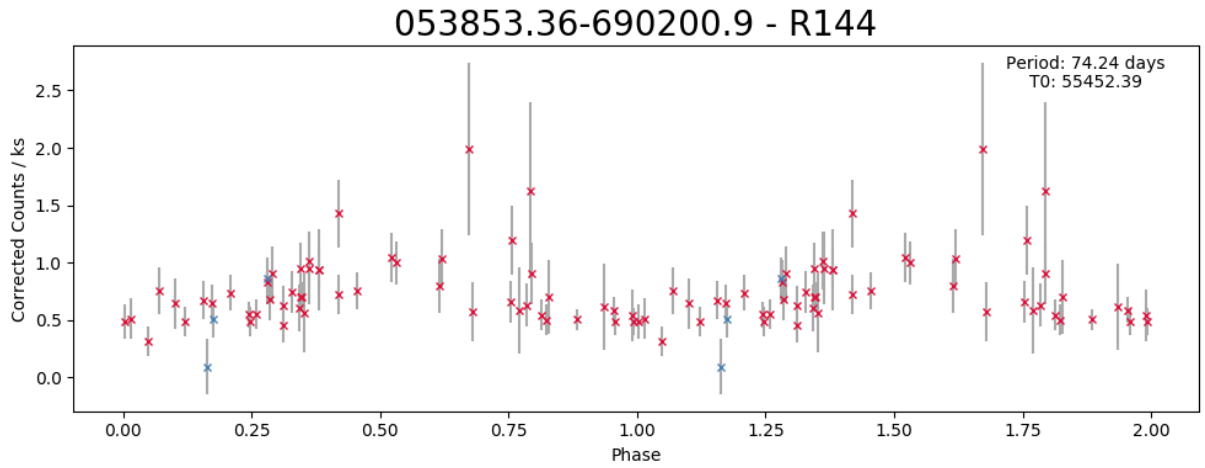

Figure 4.11: The X-ray light curve of R144 folded on a 74.24 day period (Pollock, private communication). Two full orbital periods have been shown for clarity. Blue crosses refer to the three archival observations taken several years prior to T-ReX.

There are various bolometric luminosity estimates for R144. Sana et al. (2013a) found log($L_{bol}/L_{\odot}$)=6.8-7.0, whereas Doran et al. (2013) found a lower log($L_{bol}/L_{\odot}$)=6.4. The X-ray luminosity was derived at log(L_{Xcor})=33.48 (1T model) and combined with the bolometric luminosity from Doran et al. (2013) gives $L_{Xc}/L_{bol}=3.16\times10^{-7}$, or using the bolometric luminosity from Sana et al. (2013a) gives $L_{Xc}/L_{bol}=1.26\text{-}0.79\times10^{-7}$.

Although R144 was a known binary, the period has remained elusive. Some of the results shown here could be the first steps to revealing an orbital solution, and the consistent results between the ASAS-SN and T-ReX data is promising.

4.2.17 VFTS 682

A recently discovered WR star, VFTS 682 lies within a particularly dusty region and suffers from significant reddening which had previously prevented the identification of this source (Evans et al., 2011). Now classified as a WN5h star, the spectrum has been thoroughly analysed by Bestenlehner et al. (2011), who found no evidence of binarity, and their spectral modelling determined a bolometric luminosity of log($L_{bol}/L_{\odot}$)=6.5.

In X-rays, VFTS 682 had a moderate/weak detection with a net count value of 303. The observed spectrum however, was reasonably hard, with a hardness ratio of 1.08±0.12. There is slight evidence of variability with a reduced χ^2 of 1.12 and KS test probability of -log(P_{KS})=1.95. The 1T thermal plasma model derives an X-ray luminosity of log(L_{Xcor})=33.00, which in turn gives a low L_{Xc}/L_{bol} of 0.83×10^{-7}.

Together optical and X-rays unveil a similar result, and we can be reasonably confident that VFTS 682 does not show evidence for binarity.

4.2.18 R145

R145 is a well-studied binary system. First investigated by Moffat (1989), they found R145 was an SB1 binary with a 25.17 day circular orbit. Using additional spectroscopic and polarimetric data Schnurr et al. (2009a) later revised these results to find a 158.8(1) day eccentric orbit, with an inclination of 38°. Shenar et al. (2017) made further progress. Using moderate resolution VLT FLAMES spectra they were able to identify spectroscopic features belonging to the secondary, updating the binary to an SB2. They also found an eccentric orbit with a 158.760(17) day period and inclination of 39°, in agreement with Schnurr et al. (2009a).

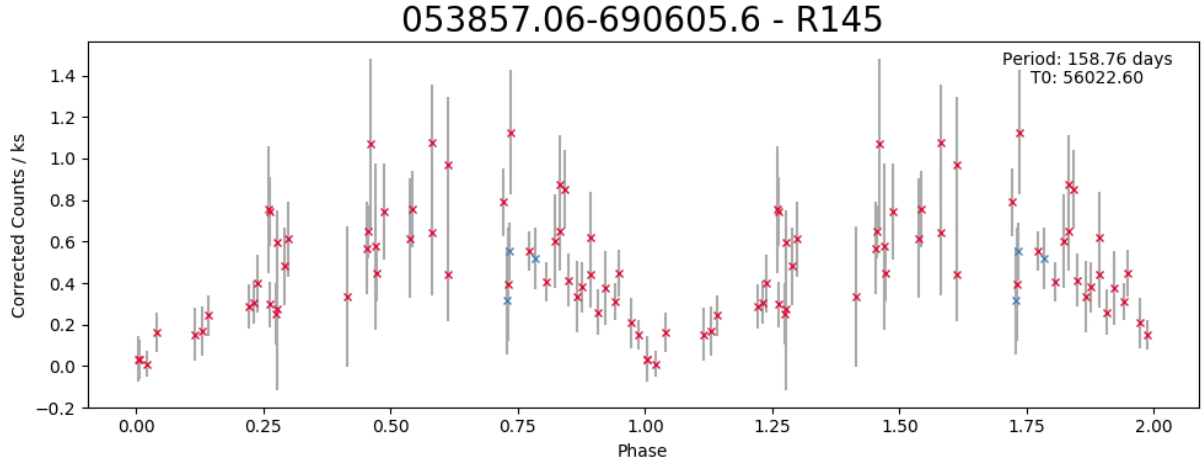

Figure 4.12: The X-ray light curve of R145 folded on a 158.76 day period as reported by Shenar et al. (2017). Two full orbital periods have been shown for clarity. Blue crosses refer to the three archival observations taken several years prior to T-ReX.

We also see evidence for variability in the T-ReX data, with a relatively high reduced χ^2=4.10 and KS-test probability of -log(P_{KS})=4.46. Using the 158.760 day period (Schnurr et al., 2009a; Shenar et al., 2017) we fold the X-ray light curve as shown in Figure 4.12. We

note the period is reasonably consistent with the X-ray variability but there does appear to be slight deviations at certain phases. The X-ray spectrum is moderately bright, with 785 net counts, and quite hard, with a hardness ratio of 0.98±0.07. 1T plasma thermal fits suggest a corrected X-ray luminosity of $\log(L_{X\mathrm{cor}})$=33.25, and Shenar et al. (2017) found a bolometric luminosity of $\log(L_{\mathrm{bol}}/L_{\odot})$=6.64, giving an L_{Xc}/L_{bol} of 1.07×10^{-7}.

Overall, the relatively bright, hard X-ray spectrum, with periodic variability is suggestive that R145 is indeed a binary, however the modest L_{Xc}/L_{bol} ratio could be indicative that this system does not have a colliding wind.

4.2.19 R147

Classified as a WN5h star, Foellmi et al. (2003b) found no evidence of radial velocity variations in R147 and therefore considered this star single. Bestenlehner et al. (2014) also noted no line profile or radial velocity variations, and using spectroscopic modelling derived a bolometric luminosity of $\log(L_{\mathrm{bol}}/L_{\odot})$=6.36. In contrast Doran et al. (2013) found a bolometric luminosity of $\log(L_{\mathrm{bol}}/L_{\odot})$=6.6.

In X-rays R147 is a relatively weak source with 103 net counts. It has a hardness ratio however, of 1.07±0.18, suggesting the source has a hard spectrum.

The variability statistics returned a reduced χ^2=1.40 and KS-test probability of -$\log(P_{\mathrm{KS}})$=0.81, which suggests low/moderate variability. Visual inspection of the light curve however shows it is difficult to assess (see Figure A.1h).

The corrected X-ray luminosity was derived to be $\log(L_{X\mathrm{cor}})$=32.55, using the 1T model in XSPEC. This gives an L_{Xc}/L_{bol} of 0.41×10^{-7}, or L_{Xc}/L_{bol} of 0.23×10^{-7}, using Bestenlehner et al. (2014) or Doran et al. (2013) bolometric luminosities respectively.

At present, the weak detection and low L_{Xc}/L_{bol} is suggestive that R147 is a single star, although the hardness of the spectrum is curious and warrants further investigation. Since the variability is ambiguous we tentatively assign R147 as a binary candidate until more conclusive evidence is produced.

4.3 Discussion

Table 4.5 summarizes the binary properties discussed within this chapter. Prior to this work 7 WR stars had reported orbital periods (R130, R135, Mk39, R140b, R136c, Mk30 & R145). Following this work we are able to confirm the orbital period of R145, identify the period of Mk39, and reveal new determinations for Mk34 and R144.

Table 4.5: Summary of the binarity properties of all WR stars included in the T-ReX sample. L_X/L_{bol} measurements are derived using the bolometric luminosities quoted in column 3 and the corrected X-ray luminosities derived in Chapter 3. Variability is assessed using the reduced χ^2 and KS-test probability results also derived in Chapter 3 and discussed for each source in Section 4.2. A ? response for variability denotes an unclear/uncertain result. Binary periods are taken from the sources indicated in column 9. Binary status is assessed based on the X-Ray work discussed in this chapter, where b, b? and s indicate likely binary, binary candidate, and likely single respectively.

Name	Spectral Type	$Log(L_{bol}/L_{\odot})$	Ref	L_X/L_{bol} $[\times 10^{-7}]$	Hardness Ratio	Variable	Period [days]	Ref	Binary
R130	WN/C + B1I	6.34	(1)	7.08	0.86 ± 0.05	?	4.3125(6)	(2)	b?
R135	WN7h	6.20	(1)	1.55	5.36 ± 1.17	?	2.1110(18)	(2)	b?
VFTS 427	WN8(h)	6.13	(3)	0.46	0.66 ± 0.15	no			s
Mk51	O3.5If/WN7	6.20	(3)	0.27	0.40 ± 0.11	no			s
Mk49	WN6(h)	6.10	(4)	0.56	2.32 ± 0.56	no			s
Mk39	O2.5If/WN6	6.4	(3)	21	0.41 ± 0.01	yes	630	(5)	b
R134	WN7h	6.2	(3)	0.28	1.07 ± 0.28	?			b?
R140a1/a2	WC4 + WN6 + O	6.41	(4)	234	0.35 ± 0.00	yes			b
R140b	WN6 + O5(h)	6.25	(1)	2.57	0.45 ± 0.04	?	2.7586(4)	(1)	b?
R136a1/a2	WN5h + WN5h	7.28	(6)	1.74	0.33 ± 0.01	yes			b?
R136a3/a6	WN5h + O2If	6.79	(6)	0.78	0.38 ± 0.03	?			b?
R136c	WN5h	6.75	(7)	11.2	0.72 ± 0.02	yes	8.2	(8)	b
Mk30	O2If*/WN5	6.16	(1,3)	0.71	0.32 ± 0.05	?	4.6965(2)	(1)	b?
Mk35	O2If*/WN5	6.3	(3)	0.7	0.24 ± 0.04	no			s
Mk34	WN5h + WN5h	6.70	(5)	102	0.70 ± 0.01	yes	155.1(1)	(5)	b
R146	WN5ha	6.29	(3)	1.86	0.25 ± 0.02	?			s
R144	WN5-6h + WN6-7h	6.40	(4)	3.16	0.60 ± 0.03	yes	74.24	(5,9)	b
VFTS 682	WN5h	6.50	(10)	0.83	1.08 ± 0.12	?			s
R145	WN6h + O3.5If*/WN7	6.64	(11)	1.07	0.98 ± 0.07	yes	158.760(17)	(11)	b
R147	WN5h	6.36	(3)	0.41	1.07 ± 0.18	?			b?

1. Shenar et al. (2019); 2. Schnurr et al. (2008); 3. Bestenlehner et al. (2014); 4. Doran et al. (2013); 5. This work; 6. Bestenlehner (private communication); 7. Crowther et al. (2010); 8. Schnurr et al. (2009b); 9. Pollock (private communication); 10. Bestenlehner et al. (2011); 11.Shenar et al. (2017)

As discussed in Section 1.4.3, L_X/L_{bol} measurements are good indicators of colliding wind binaries. With approximately $L_{Xc}/L_{bol}=1\times10^{-7}$ observed for single O stars, we expect a similar limit for WN stars. Using an L_{Xc}/L_{bol} ratio threshold of 1×10^{-7}, 11 out of the 20 sources included in this sample would be considered potential binaries, and of these 8 have derived orbital periods, either from literature or revealed in this work (see Table 4.5). The remaining 3 sources are R140a1/a2, which we are confident is host to either one, if not two, colliding wind binary systems; R136a1/a2, which is a particularly complicated since it is host to multiple sources within a very crowded region; and R146, which is currently thought to be single. We also should note however that using this L_{Xc}/L_{bol} ratio threshold of 1×10^{-7} would exclude Mk30 as a potential binary, however optical monitoring suggests otherwise. From Table 4.5, we find 6 likely single stars, 6 likely binary stars, and 8 potential binary stars. Taking the non-detection of R136b to suggest this WR star is also single gives a binary fraction for the 30 Dor WR stars in the range of 29%–67% based on this X-Ray study.

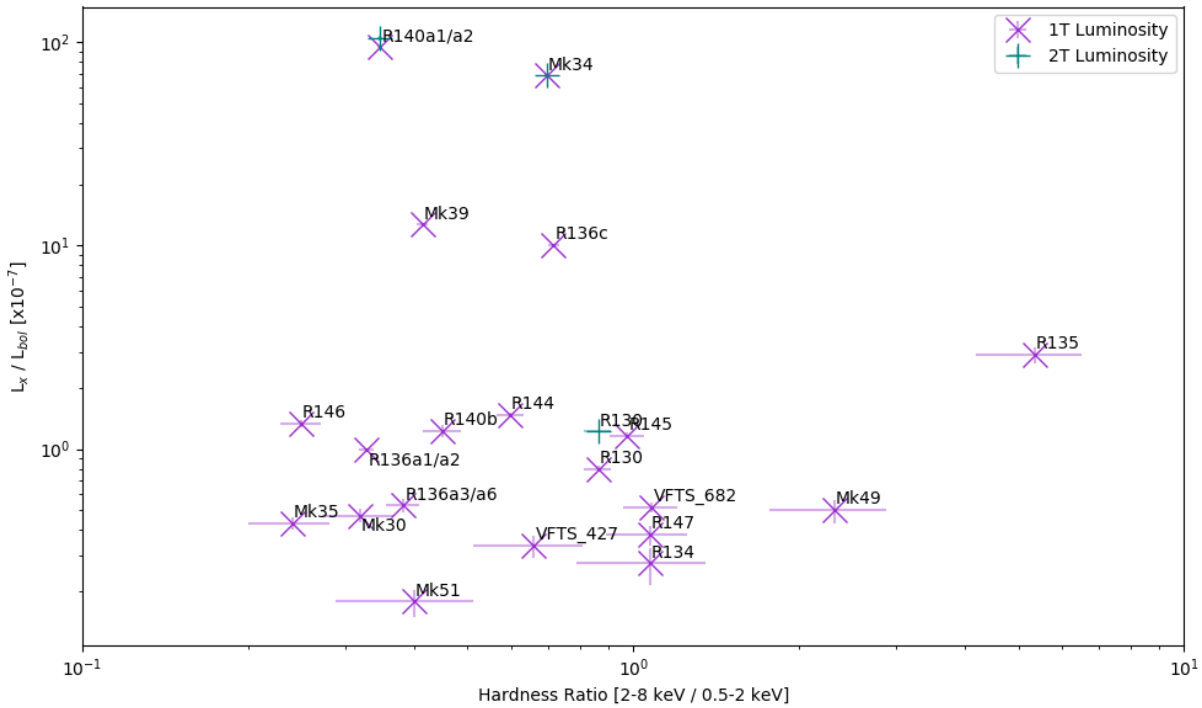

Figure 4.13: Plot showing how the ratio of L_X/L_{bol} varies with hardness for all WR sources in the sample. Corrected X-ray luminosities derived with 1T thermal plasma fits are shown in purple, and corrected X-ray luminosities from 2T thermal plasma fits are shown in blue.

Figure 4.13 shows how the L_X/L_{bol} ratio varies with hardness for each of the WR sources in this sample. For a binary we would expect the source to have a high L_X/L_{bol} ratio and

exhibit a harder spectrum than its single star counterparts, such as WR140 (Pittard & Dougherty, 2006) or WR25 (Pollock & Corcoran, 2006). Whilst this plot shows some clear outliers, it is evident that in reality differentiating binaries is more complicated. Clark et al. (2019) adopt a similar technique, plotting the distribution of WR stars in Wd1 based on hardness and intensity. They too reach similar conclusions to this work, and find that although the brightest, hardest, stars are generally binaries, there are also areas overlap between in the parameter space occupied by binaries and single stars.

R140a1/a2, Mk34, Mk39 and R136c sit significantly higher than the remainder of the sample, occupying a space reserved for those with high L_X/L_{bol} ratios. We are very confident these stars are indeed colliding wind binaries, with orbital periods derived for Mk34 and Mk39 presented here in this work. We do note however, that these sources do not have particularly hard X-ray spectra. In contrast, R135 is a clear outlier when considering spectral hardness. Although optical data reports radial velocity variations for this source, based on the weak X-ray detection and low/moderate X-ray variability, we are cautious to confirm this binary status and instead consider R135 to be a potential binary candidate. This inconsistency would suggest that the hardness ratio is a poor indicator of binarity for WR stars.

With regards to the remainder of the sample, it is very difficult to discriminate between sources since they all occupy the lower left region of Figure 4.13. We know that some of these WRs, such as R140b, R144 and R145, are known binaries, and these sources tend to sit at higher L_X/L_{bol} ratios than the rest of the group, so perhaps this is the key to extracting the binary sources. We should also remember that using the L_X/L_{bol} ratio to differentiate binaries has been investigated using O stars, however there is still the possibility that this relationship is not applicable here. It could be that for main-sequence WR stars, which are essentially an extension of the O star class to higher masses, using the L_X/L_{bol} ratio is relevant, however it may be unsuitable for classical WR stars, especially WC stars.

Nevertheless, we conclude that whilst we are able to confirm some binary sources, and identify others as potential binary candidates, we are reluctant to definitively designate any of the WR stars in the sample as single without a better understanding of single star WR X-ray properties.

Chapter 5

Weighing Melnick 34

Much of the work presented in this Chapter is taken from Tehrani et al. (2019), with additional details added with regards to the observing strategy and data reduction.

5.1 Introduction

Mass is a fundamental property of stars though is often elusive. Robust stellar mass determinations are crucial for deducing a wealth of other stellar properties, such as luminosities and lifetimes. The initial mass function (IMF) describes the distribution of stellar masses and shows that the formation of very massive stars (VMS, >100 $M_\odot$) is exceptionally rare (Vink, 2015).

Due to these complications, we often turn to spectroscopic and evolutionary modelling (e.g. Yusof et al. 2013; Köhler et al. 2015) to determine stellar masses, as discussed in Section 1.6.1. In the high mass regime however, this can lead to ambiguous and controversial results (Crowther et al., 2010; Schneider et al., 2018).

To remedy this we need to verify these models with a robust sample of directly measured masses to act as calibration points. The detached eclipsing binaries catalogue, DEBCat (Southworth, 2015), collates a sample of well-studied spectroscopic binary systems with mass and radius measurements accurate to 2%. Massive stars however, are poorly represented in both visual and spectroscopic searches, with only 3 systems with primary stellar masses greater than 20 $M_\odot$ and none greater than 30 $M_\odot$ appearing in DEBCat.

Within the LMC, a VMS binary has yet to be identified. The most massive double-eclipsing binary currently known is R136-38, an O3 V + O6 V system hosting minimum masses of $M_A \sin^3(i)$=53.8 ± 0.2 $M_\odot$ and $M_B \sin^3(i)$=22.1 ± 0.1 $M_\odot$ respectively (Massey et al., 2002). Both spectroscopic and photometric monitoring reveal a 3.39 day period system, with zero eccentricity and high inclination of 79° ± 1°.

5.1.1 Mk34

Mk34, introduced in Chapter 3, is an X-ray colliding wind binary consisting of a WN5h primary star and an unknown massive companion (Townsley et al., 2006b; Schnurr et al., 2008; Crowther & Walborn, 2011). It was identified as a double-line spectroscopic binary (SB2) by Chené et al. (2011) who obtained a partial radial-velocity curve during spectroscopic monitoring with Gemini/GMOS over 51 days starting in late 2009.

Located on the periphery of R136 at a projected distance of ∼2 pc from the central star R136a1 as shown in Figure 5.1, it is one of the most luminous objects in the LMC, with a luminosity of $\log(L/L_\odot)$=7.05 and an inferred mass of M=390 $M_\odot$ (Hainich et al., 2014),

when considered a single star and using the theoretical M/L relationship from Gräfener et al. (2011).

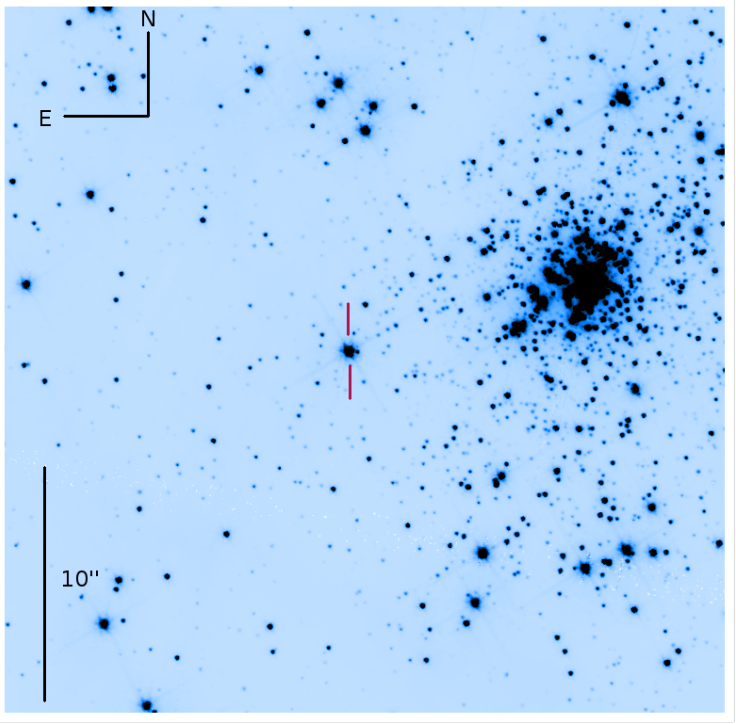

Figure 5.1: HST/WFC3 F555W image of 30 Dor showing the position of Mk34 relative to the central R136 cluster (De Marchi & Panagia, 2014). Field of view shown is 30″× 30″, or 7.3 pc × 7.3 pc, assuming a distance of 50 kpc

X-ray observations revealed a more impressive picture, showcasing Mk34 as the most luminous X-ray source in the 30 Dor nebula, with $\log(L_x)$=35.2 erg s^{-1} (Townsley et al., 2006b). The high X-ray/bolometric luminosity ratio, $L_x/L_{bol} = 3.7 \times 10^{-6}$, prompted the suspicion that Mk34 is a colliding wind binary system. Recurrent X-ray variability, however, had not been observed until recently. The T-ReX programme, discussed in Chapter 3, successfully observed recurrent variability on a 155.1 day X-ray cycle (see Section 4.2.14 and Pollock et al. (2018)), further supporting the binary hypothesis.

To assess the binarity of Mk34 and investigate the system further requires optical data: confirmation of the binary status of the system would provide a unique opportunity to obtain direct mass estimates for VMS in a low-metallicity environment.

In this chapter we report new VLT/UVES optical spectroscopic monitoring of Melnick 34 across a full orbital period, supplemented by archival Gemini/GMOS spectra (Chené et al., 2011). In Section 5.3 we show radial-velocity measurements including the derived orbital properties of the system. In Section 5.5 we present spectral and evolutionary mod-

elling parameters for the system. In Section 5.6 we discuss the limitations and implications of these results, and give brief conclusions in Section 5.7

5.2 Observations

As discussed in Section 4.2.14, the T-ReX data strongly suggested Mk34 was a binary system. To confirm this, we submitted a VLT/UVES proposal requesting 7.5 hours observing time to search for evidence in the optical spectra for a companion. We were awarded this time during observing period 98, which ran from October 1 2016 until March 31 2017.

5.2.1 UVES Observing Schedule

In order to maximise the chance of observing both components of Mk34 whilst still monitoring the system across the full period, the observations were tailored to achieve a high cadence near X-ray maximum, presumed close to periastron, with more sparse sampling during the X-ray quiescent periods.

Based on the 155.1 day X-ray period derived by Pollock et al. (2018) we predicted that, during the P98 observation period, X-ray maxima for Mk34 would fall on October 6 2016 and March 10 2017. We therefore created a schedule of 25 observations, with a higher proportion occurring close to these dates.

To achieve this we used time link containers (TLC). Within a TLC is a group of observations, or OBs, connected by a relative time interval between observing dates. The first OB is given an absolute time interval within which the observation will be taken, however subsequent OBs are assigned a delay window, indicating the amount of time that should elapse before proceeding with next OB. The delay interval is relative to the previous OB, and so this flexibility increases the chance of the observation occurring, however it also means that it is not possible to specify exactly when each observation will be taken.

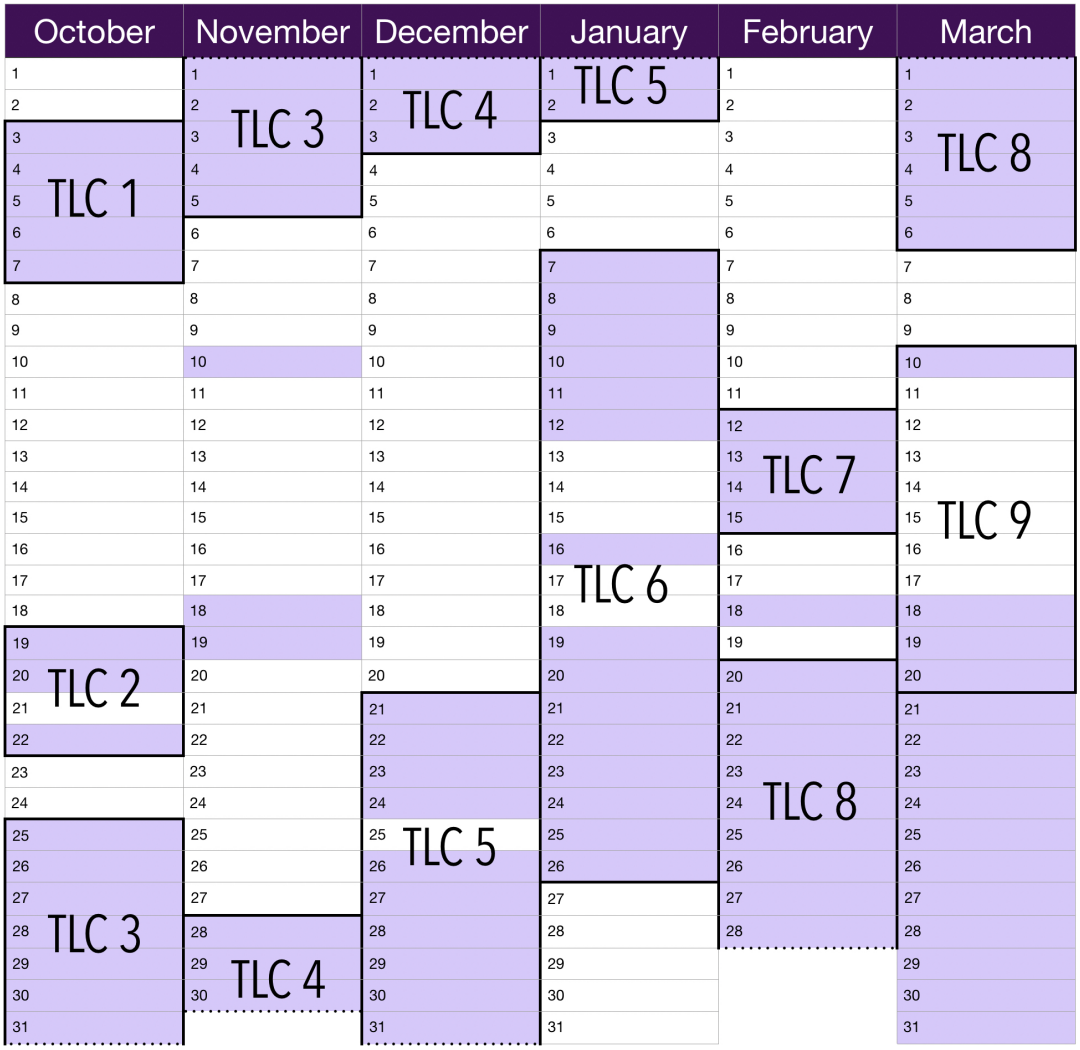

Figure 5.2: Time link container (TLC) schedule for VLT/UVES observations of Mk34. Purple shaded regions highlight dates which UVES was operational in service mode. Bold boxed regions show the range of potential observation dates included within a particular TLC. Table 5.1 gives more details regarding the observations within each TLC.

Figure 5.2 shows an overview of how the TLC were distributed across the observing period. An additional complication during scheduling was the service mode schedule. Since UVES operates in both visitor and service mode, there were restrictions on the nights available for observations. The purple shaded regions in Figure 5.2 highlight when UVES was available for use in service mode, and the black boxes indicate the maximum period over which the TLC could be completed.

Table 5.1 provides additional details for each TLC, such as the number of OB's scheduled to be completed within each TLC, the starting date for the initial observation and the

subsequent delay for following observations.

Table 5.1: Details for each TLC for the VLT/UVES observations of Mk34. OBs column shows how many observations fall within the TLC. Initial OB interval specifies the absolute window within which the first OB of the TLC will be taken. The delay interval specifies the minimum and maximum time for obtaining subsequent OB's within that TLC, relative to the previous OB. Observation window highlights the full potential observing period for that TLC, as shown in Figure 5.2. TLC 10 refers to the additional observations awarded based on two failed OBs from the original run.

TLC	OBs [#]	Initial OB Interval	Delay Interval [days]	Observation Window
1	3	2016-10-03 – 2016-10-04	0.5-2.5	3 – 7 Oct 2016
2	2	2016-10-19 – 2016-10-21	1.5-3.5	19 – 21 Oct 2016
3	4	2016-10-25 – 2016-10-28	1.5-3.5	25 Oct – 5 Nov 2016
4	2	2016-11-28 – 2016-12-02	1.5-4.5	28 Nov – 3 Dec 2016
5	2	2016-12-21 – 2016-12-25	6-10	21 Dec 2016 – 2 Jan 2017
6	2	2017-01-07 – 2017-01-11	12-16	7 – 26 Jan 2017
7	2	2017-02-12 – 2017-02-14	1.5-3.5	12 – 15 Feb 2017
8	6	2017-02-20 – 2017-02-24	1.5-3.5	20 Feb – 6 Mar 2017
9	2	2017-03-10 – 2017-03-11	7.5-10.5	10 – 20 Mar 2017
10	2	2018-01-14 – 2018-01-17	1-3	14 – 20 Jan 2018

Due to the failure of OB 15 and OB 21 to execute, replacement observations were awarded during observing period 100. We scheduled these observations within TLC 10, as shown in Table 5.1, which would coincide with periastron and the days immediately following. A full list of observations can be found in Table 5.2.

5.2.2 UVES Observations

26 epochs of VLT/UVES spectra were obtained in service mode over a 497 day period – from 2016 September 6 to 2018 January 16 (Program–ID 098.D-0108(A), PI Crowther). Observations were taken in the Dichroic 2 instrument mode, giving spectral ranges of 373–499 nm (blue arm), 567–757 nm (red arm lower) and 767–945 nm (red arm upper). The exposure time for each observation was 450 s, with the exception of the first Epoch 0 which was a test run with an exposure time of 120 s, and Epoch 3 which had slightly shorter exposure time of 400 s. A 0.8″ slit was used throughout. The reciprocal dispersion scale

was 0.02–0.03 Å/pixel and the resolution was ∼0.06 Å at 4000 Å and ∼0.09 Å at 5000 Å, with a S/N ratio of 30–40 per resolution element across all epochs. The resultant resolving power was ∼60000 (∼5 km s^{-1}).

Bias, flat-field and ThAr arc calibrations were obtained through the standard calibration routine for service mode by ESO and the data reduction was performed using the ESO pipeline Reflex (Freudling et al., 2013).

The Reflex programme simplifies the extraction and calibration process of UVES data. By selecting the UVES workflow it is possible to provide the tool with a full set of raw and calibration files from which Reflex will return a set of reduced data. To achieve this, Reflex performs a number of operations. First the data are organised and relevant files are located. Next the master calibration files are created, including bias frames, flat fields and line tables from the arc spectra. Using these files a wavelength solution and instrument response are created. The spectra are then extracted and the orders are merged to generate one full spectrum.

Table 5.2: VLT/UVES barycentric radial velocities measured for star A and star B using the N IV 4058 and N V 4945 emission lines. All phase measurements were calculated based on the orbital solution UG1, shown in Table 5.4

VLT/UVES						
		N IV 4058		N V 4945		
Epoch	MJD	RV_A	RV_B	RV_A	RV_B	Phase
		[km s^{-1}]		[km s^{-1}]		
0	57637.41	263 ± 75	258 ± 70	268 ± 80	283 ± 75	0.7816
1	57665.38	428 ± 20	98 ± 20	488 ± 40	128 ± 20	0.9626
2	57666.25	428 ± 20	88 ± 20	508 ± 40	118 ± 20	0.9682
3	57667.21	468 ± 20	73 ± 30	463 ± 35	78 ± 30	0.9745
4	57681.18	343 ± 15	223 ± 15	318 ± 50	338 ± 30	0.0649
5	57684.25	318 ± 20	198 ± 20	332 ± 65	313 ± 45	0.0848
6	57687.32	253 ± 65	238 ± 50	298 ± 50	313 ± 35	0.1046
7	57690.17	158 ± 20	323 ± 15	328 ± 60	343 ± 35	0.1230
8	57692.22	193 ± 15	328 ± 10	308 ± 90	338 ± 60	0.1363
9	57694.22	178 ± 20	333 ± 25	343 ± 65	343 ± 65	0.1492
10	57723.13	238 ± 60	253 ± 45	293 ± 35	298 ± 30	0.3363
11	57725.12	234 ± 45	239 ± 40	304 ± 15	304 ± 15	0.3491
12	57744.21	244 ± 55	249 ± 40	269 ± 40	289 ± 20	0.4727
13	57751.12	290 ± 50	275 ± 35	330 ± 50	320 ± 40	0.5174
14	57761.29	265 ± 35	255 ± 25	275 ± 15	275 ± 15	0.5832
15	57797.03	266 ± 75	251 ± 50	291 ± 60	281 ± 50	0.8145
16	57800.23	276 ± 35	256 ± 35	311 ± 40	271 ± 30	0.8352
17	57806.14	271 ± 60	266 ± 35	441 ± 20	246 ± 25	0.8734
18	57808.03	331 ± 30	221 ± 20	406 ± 45	251 ± 30	0.8856
19	57811.03	366 ± 15	186 ± 25	386 ± 45	186 ± 25	0.9051
20	57815.13	391 ± 20	101 ± 20	411 ± 50	161 ± 30	0.9316
21	57817.01	406 ± 25	131 ± 40	476 ± 45	161 ± 30	0.9437
22	57823.02	461 ± 20	71 ± 20	501 ± 20	111 ± 20	0.9826
23	57831.01	254 ± 45	244 ± 35	279 ± 50	269 ± 40	0.0344
24	58133.17	499 ± 20	74 ± 15	509 ± 10	99 ± 10	0.9895
25	58134.17	519 ± 10	59 ± 20	509 ± 30	69 ± 10	0.9959

5.2.3 GMOS Observations

Archival Gemini-S/GMOS data (Program–ID GS-2009B-Q-32, PI Chené) consist of 22 spectra taken between 2009 December 24 and 2010 February 15. Each observation had an exposure time of 400 s and used a fixed slit width of 0.5″. Here the reciprocal dispersion scale was 0.47 Å/pixel, and the resolution was found to be ∼1.29 Å at 4000 Å and ∼1.16 Å at 5000 Å, corresponding to a much lower resolving power for this data set of ∼3 500. The S/N per resolution element was between 110–170 at 5000 Å, however dropped considerably to 5–30 at 4000 Å.

Similar to the reduction of the GMOS data for IC10, outlined in Section 2.2.2, the Mk34 spectra were bias and flat field corrected using the Gemini GMOS package in IRAF. The spectra were then extracted using the apextract package in IRAF (Tody, 1986). In contrast to the data in Chapter 2, a flux calibration was unnecessary and therefore not performed. A complete list of Gemini/GMOS observations can be found in Table 5.3.

5.2.4 Classification

Figure 5.3 shows a subset of a typical blue UVES spectrum of Mk34 together with a spectrum of the typical WN5h star VFTS 682 from Bestenlehner et al. (2011, 2014) for comparison. Both stars show strong, broad He II 4686 and Balmer series emission, and sharper N IV 4058, N V 4603–20 and N V 4945 emission lines. Upon closer inspection of these narrow lines, we observe two stellar components in a subset of epochs, as shown in Figure 5.4, confirming the SB2 nature of the system. This double emission is brief, occurring in 8 of the 26 epochs observed, covering more than 8 and less than 20 days of the 155 day orbit. For the remainder of the orbit it is not possible to distinguish the two components, suggesting the system is highly eccentric.

The UVES spectra of Mk34 extend beyond this wavelength range, where we also note strong Hα and N IV 7103–7129 emission, and narrow C IV 5801–12 emission. Note that the double emission observed at N IV 7103–7129 can be observed throughout the orbit as this emission is composed of multiple transitions, therefore using this line to trace the stellar radial-velocity curve is difficult and we do not attempt to use it.

When investigating the spectral type of each component we note the N IV 4058 emission is stronger than the N V 4603–20 in both stars, and N III 4640 emission is absent, consistent with a WN5 ionization class as outlined in Smith et al. (1996) and Crowther & Walborn (2011). Also, using the Pickering decrement to search for variations in the strength of the He II (n–4) lines, we note the strong He II 4859 + Hβ and He II 4340 + Hγ emission,

Table 5.3: Archival Gemini S/GMOS barycentric radial velocities measured for star A and star B using the N IV 4058 and N V 4945 emission lines. All phase measurements were calculated based on the orbital solution UG1, shown in Table 5.4

Gemini S/GMOS						
		N IV 4058		N V 4945		
Epoch	MJD	RV_A	RV_B	RV_A	RV_B	Phase
		[km s^{-1}]		[km s^{-1}]		
1	55189.04	399 ± 40	119 ± 30	429 ± 30	169 ± 20	0.9396
2	55189.04	399 ± 40	119 ± 40	429 ± 60	169 ± 30	0.9396
3	55191.21	419 ± 50	99 ± 90	419 ± 30	149 ± 30	0.9536
4	55195.22	489 ± 100	49 ± 130	439 ± 70	69 ± 30	0.9796
5	55196.16	489 ± 40	79 ± 50	459 ± 60	69 ± 40	0.9856
6	55197.32	509 ± 70	-21 ± 40	459 ± 60	69 ± 60	0.9932
7	55198.29	489 ± 80	49 ± 50	509 ± 90	-11 ± 60	0.9994
8	55199.21	489 ± 140	59 ± 130	539 ± 80	39 ± 70	0.0054
9	55207.21	270 ± 100	270 ± 100	300 ± 40	300 ± 40	0.0572
10	55210.11	250 ± 100	250 ± 100	320 ± 60	320 ± 60	0.0759
11	55212.03	260 ± 100	260 ± 100	320 ± 50	320 ± 50	0.0883
12	55213.03	270 ± 110	270 ± 110	310 ± 70	310 ± 70	0.0948
13	55214.24	280 ± 100	280 ± 100	310 ± 70	310 ± 70	0.1027
14	55216.16	280 ± 110	280 ± 110	290 ± 60	290 ± 60	0.1150
15	55225.12	250 ± 110	250 ± 110	310 ± 50	310 ± 50	0.1730
16	55227.11	270 ± 120	270 ± 120	310 ± 60	310 ± 60	0.1859
17	55229.21	280 ± 100	280 ± 100	340 ± 110	340 ± 110	0.1995
18	55236.10	221 ± 200	221 ± 200	311 ± 50	311 ± 50	0.2440
19	55237.10	261 ± 120	261 ± 120	301 ± 60	301 ± 60	0.2505
20	55238.12	281 ± 80	281 ± 80	311 ± 60	311 ± 60	0.2571
21	55241.07	251 ± 200	251 ± 200	311 ± 80	311 ± 80	0.2763
22	55242.12	281 ± 150	281 ± 150	291 ± 70	291 ± 70	0.2830

coupled with the weaker He II 4541 emission. This indicates a clear hydrogen excess and is characteristic of a WN5h designation (Smith et al., 1996). The similarity of the N V/N IV ratio for each star suggests the temperatures of these objects are comparable, and these emission features are common to both components, suggesting that both stars are likely to be of the WN5h spectral type.

We also note a phase-dependent change in the morphology of the Hδ and Hγ emission, which is not present in the VFTS 682 spectrum and therefore not intrinsic to the WN5h spectral type. As shown in Figure 5.5, at times close to periastron the emission is smooth. However, near apastron an additional absorption feature develops superimposed upon the

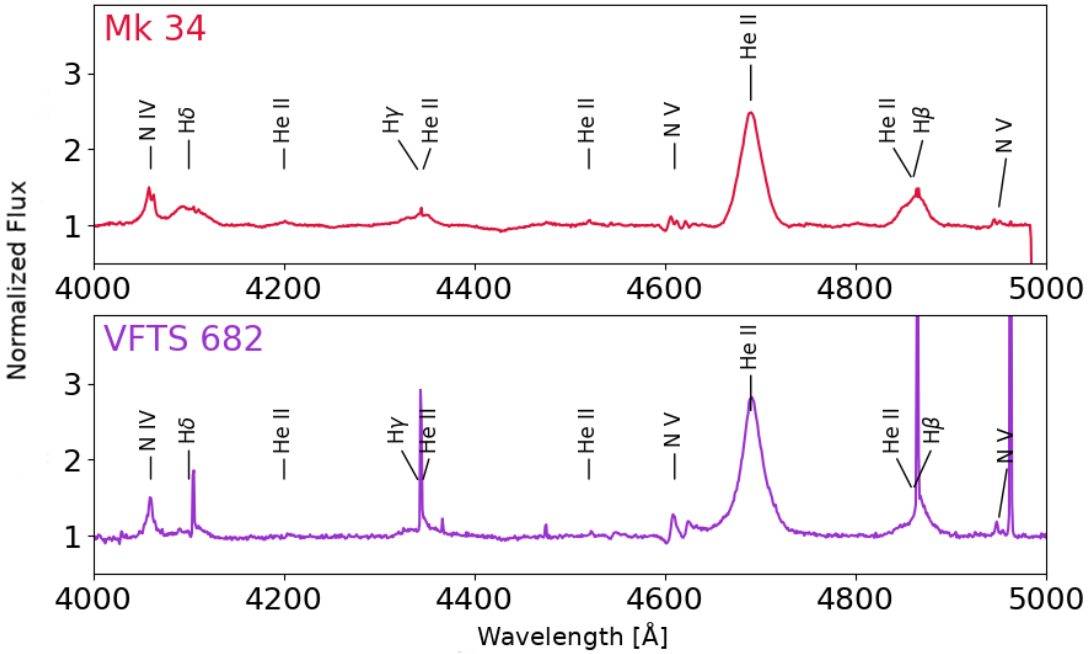

Figure 5.3: Top panel: Epoch 2 of the VLT/UVES data showing the blue spectrum of Mk34. Double-lined emission peaks can be seen in the N IV 4058, N V 4603–20 P Cygni profiles and N V 4945 emission lines confirming the system is an SB2 binary. Bottom panel: VFTS 682 spectrum from Bestenlehner et al. (2011, 2014) classified as a single WN5h star and shown here to demonstrate the similarities between the two spectra, although narrow nebular emission lines are also present here. Relevant emission lines used for classification and radial-velocity measurements have been identified.

emission. Strong Hδ emission may be characteristic of the binary since it is also noted in the known binary R136c (see Chapter 4 and Bestenlehner et al. (2014)), whilst other known single WN5h stars, such as R136a1–3 in the central cluster of 30 Doradus, do not replicate this morphology (Crowther et al., 2010). In general though, the spectrum of Mk34 is morphologically similar to these other known WN5h stars.

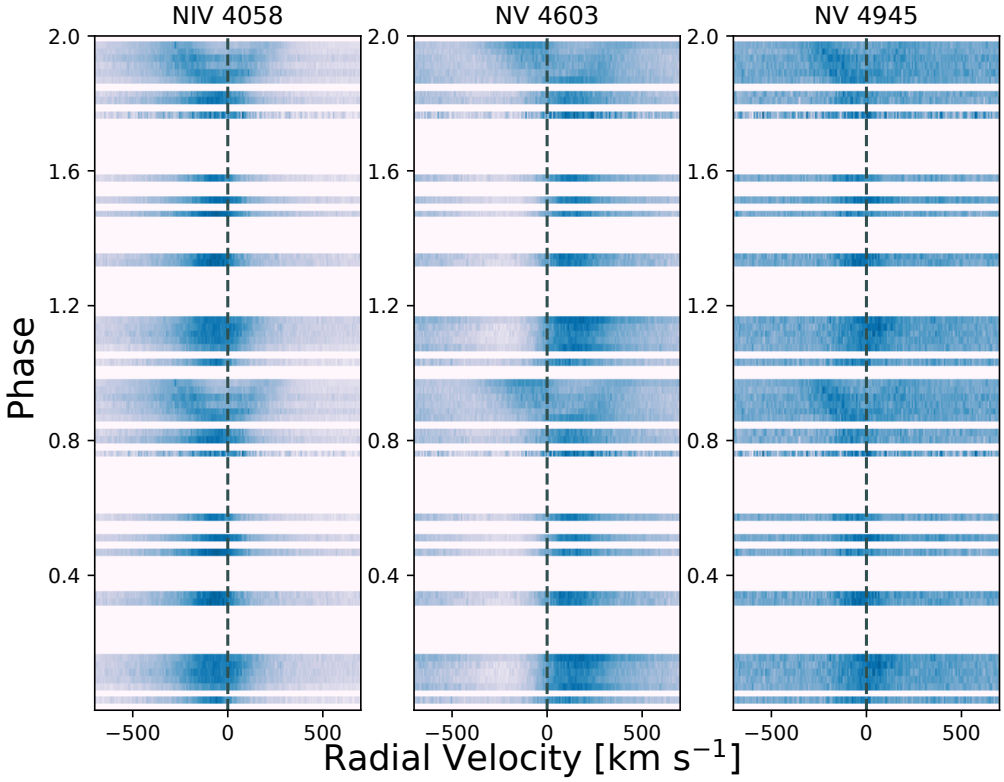

Figure 5.4: Dynamic representation of the evolution of the N IV 4057.7, N V 4603.7 and N V 4944.6 emission-line radial-velocity profiles from the UVES dataset, across two orbital phases, showing the double emission from the two components of Mk34 at phase 0.8-1, from solution UG1. Radial velocities have been corrected for a systemic velocity of 287 km s^{-1}found from solution UG1.

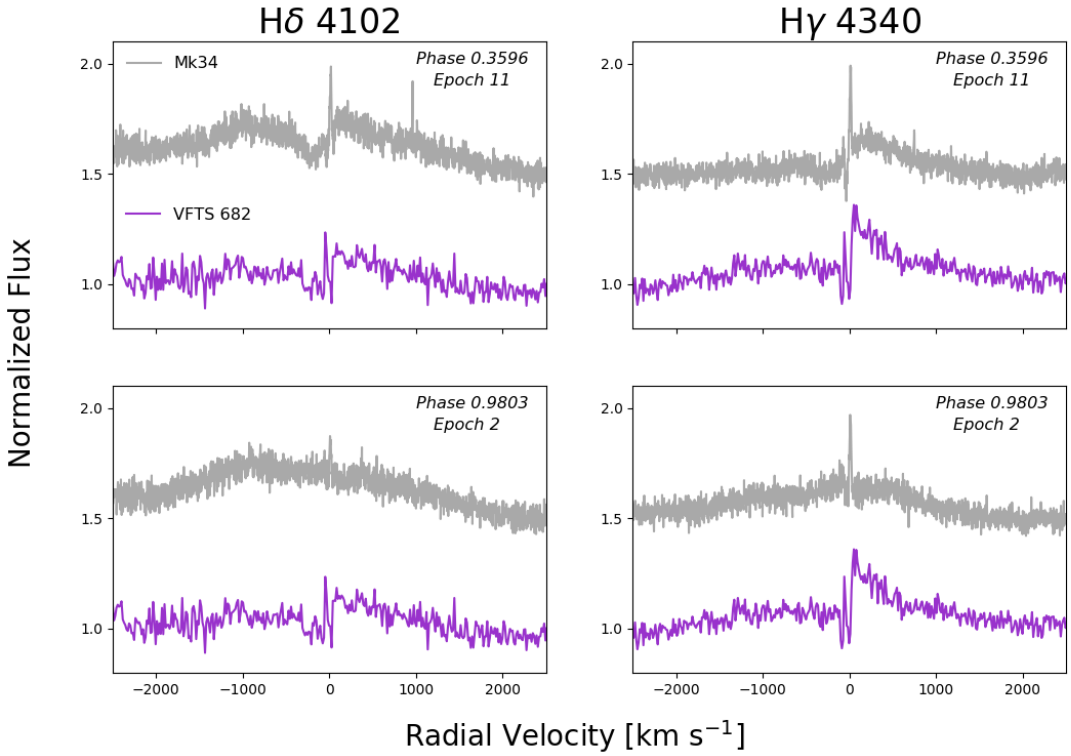

Figure 5.5: A comparison of the Hδ 4101.7 and Hγ 4340.5 emission line profiles at phases close to periastron (Epoch 2) and apastron (Epoch 11). For comparison, matching emission line profiles from the VFTS 682 spectra have also been plotted (Bestenlehner et al., 2011, 2014) to highlight the morphological change in the line profile shape visible at periastron. Nebular emission lines have been removed, using Gaussian profile fits, and a 0.5 vertical offset has been applied to the Mk34 spectrum for clarity. The radial velocities have been corrected for a systemic velocity of 287 km s^{-1}found from solution UG1.

5.3 Orbital Solution

5.3.1 Radial-Velocity Measurement

To reveal the radial-velocity distribution over time we use a template theoretical spectrum of VFTS 682 (WN5h) from Bestenlehner et al. (2011, 2014) to measure the N IV 4058 and N V 4945 emission-line radial velocities. We are restricted to these lines, which are formed in the wind, because no photospheric lines are available for WR stars. We assume that the centroids of the emission lines in the template models accurately reflect the stellar kinematics. Amongst all potential diagnostics, N IV 4058 and N V 4945 originate deep in the stellar wind, with line morphologies lacking complications of P Cygni profiles (e.g. N V 4603-20), therefore we select these lines for our radial-velocity analysis. Figure 5.6 shows a comparison of the line-forming regions for various ions, in particular emphasizing the location of the N IV 4058 and N V 4945 emission line formation, which is much closer to the stellar photosphere (≤ 1.4 R_*) than the He II 4686 line forming region.

The template spectrum was used to measure radial velocities using a simple shift and add method in DIPSO, with each fit being visually examined, for both the UVES and GMOS data sets. The results are recorded in Tables 5.2 to 5.3. It is important to note that due to the poor quality of the GMOS data there is a large degree of uncertainty in the radial velocities measured from this data set, however the longer baseline is useful for helping to constrain the orbital period. We also note a systematic offset between the N IV 4058 and N V 4945 radial velocities, with an average offset of 42 ± 44 km s^{-1}in the UVES data and 33 ± 36 km s^{-1}in the GMOS data which we discuss further in Section 5.5.1.

Figure 5.7 shows an example of this modelling at two extreme stages; at phase ∼0 near periastron when the double-lined emission is very clear and at phase ∼0.4 when emission lines from both stars are blended. Due to the significant intrinsic line widths of both stars involved – FWHM ∼300 km s^{-1}(N IV 4058) and FWHM ∼250 km s^{-1}(N V 4945) – measuring the radial velocities away from periastron proved difficult and therefore they have significant uncertainties, typically ±40 km s^{-1}for UVES, and ±100 km s^{-1}for GMOS.

5.3.2 Orbital Properties

Pollock et al. (2018) established a 155.1 ± 1 day X-ray cycle which was strongly suspected to be the orbital period. Here we can use a combination of the UVES and GMOS data providing a baseline of over 8 years, translating to 19 orbits, better to constrain this period.

To start, we adopt the technique of phase dispersion minimisation (PDM) to identify a range of periods to use as prior probabilities in future analysis. PDM works by varying the

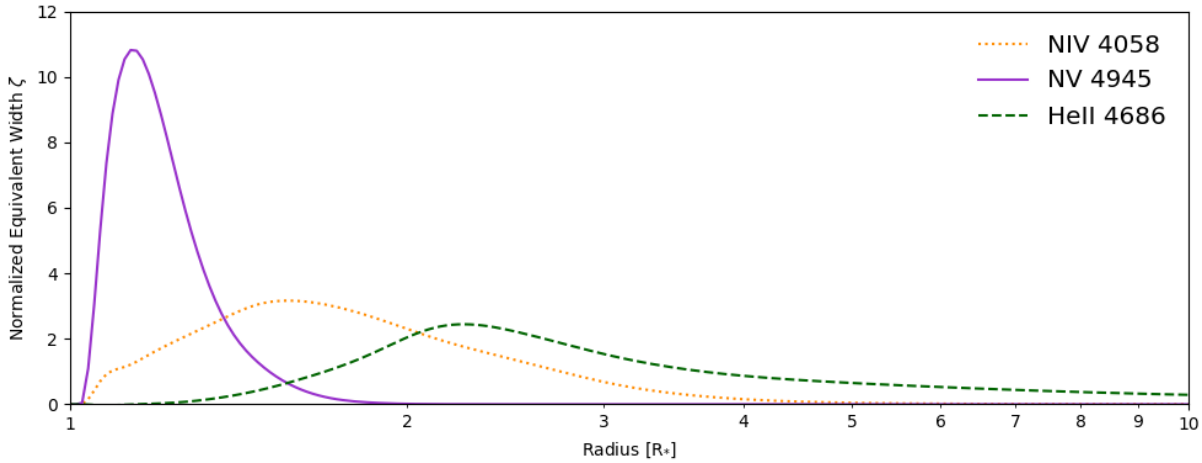

Figure 5.6: A comparison of the position of the line-forming region for various ions showing that the N IV 4058 and N V 4945 emission lines are better tracers of the stellar kinematics than the He II 4686 line which is formed further out in the stellar wind.

period and folding the radial-velocity data in phase before splitting the orbit into bins. We then calculate the variance of the radial velocities within each bin and sum across the full orbit to obtain a total variance. Finally, plotting period against total variance as shown in Figure 5.8 will reveal the most likely period. In this instance, using both the UVES and GMOS data with 20 phase bins, the most likely period was 154.45±1 days.

To obtain a full set of orbital parameters we used Markov Chain Monte Carlo (MCMC) fitting, with a uniform prior distribution for the period of 155 ± 3 days, cautiously guided by the PDM results. This MCMC python code was written by Stuart Littlefair who provided directions on how to use it, and guidance on the following results. During the MCMC fitting we used the averaged radial-velocity measurements of the N IV 4058 and N V 4945 emission lines from the UVES data, and the averaged N IV 4058 and N V 4945 radial velocities from the GMOS data, and applied a barycentric correction to provide 48 epochs of observations available for fitting. The MCMC fitting was carried out twice, once using the combined GMOS and UVES data, and again using only the more reliable UVES measurements, to provide two orbital solutions, solution UG1 and solution U1 respectively. A full set of Keplerian orbital parameters was used in each fit: the semi-amplitudes of the velocities for star A and star B, $K_{\rm A}$ and $K_{\rm B}$ respectively; systemic velocity, γ; eccentricity, e; longitude of periastron, ω; orbital period, P; and time of periastron, T_0); plus a nuisance parameter which was a multiplier for the formal error bars. Uninformative priors were adopted for all parameters, except the period, which for solution UG1 we adopted a uniform probability distribution prior of 155 ± 3 days and, based on the subsequent results of this fit, for

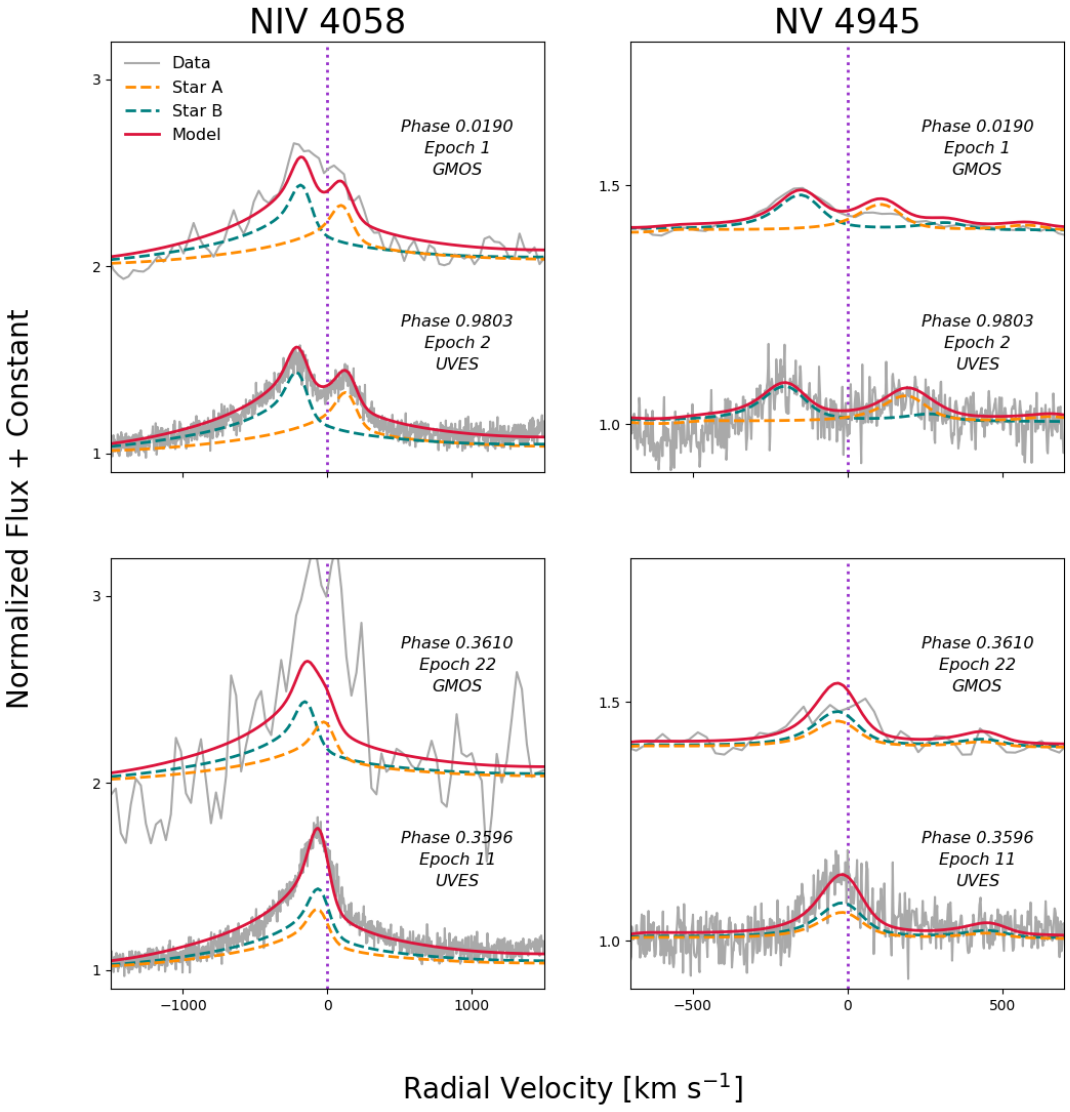

Figure 5.7: A comparison of the GMOS and UVES radial-velocity modelling for the N IV 4058 and N V 4945 emission lines from two different orbital phases to show both double emission and blended epochs. A vertical offset has been introduced to the GMOS data for clarity. The template for both star A and star B has been broadened to account for rotational velocity of ∼125 km s^{-1}. The applied systemic velocity is 287 km s^{-1}found from solution UG1.

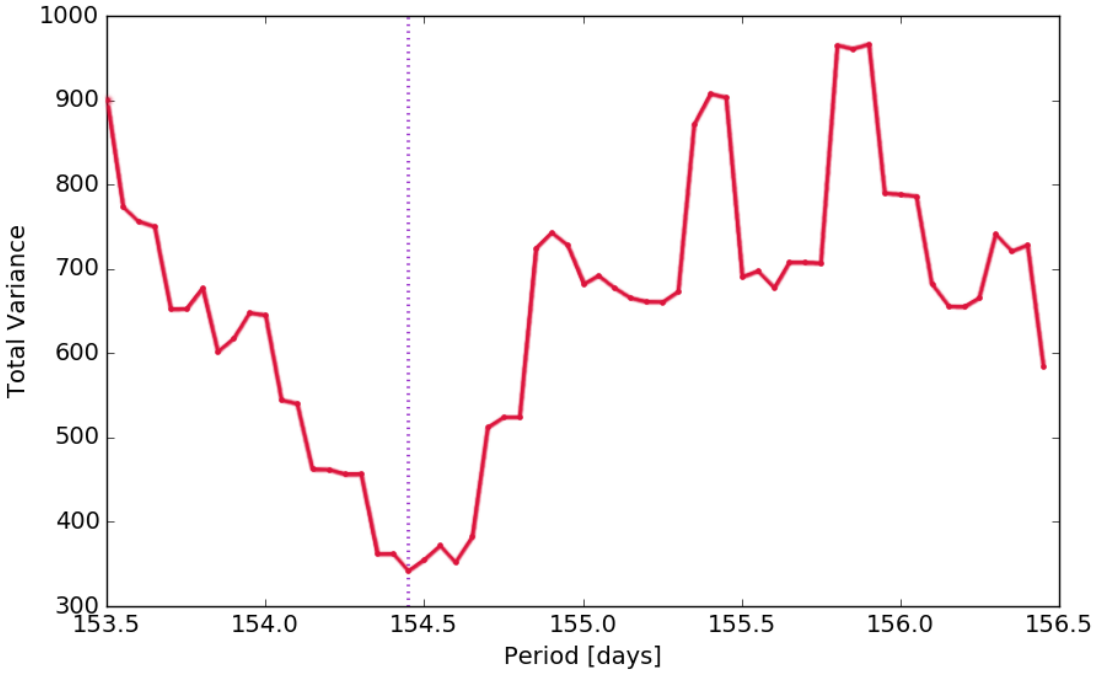

Figure 5.8: Phase dispersed minimisation plot produced from a combination of VLT/UVES and Gemini/GMOS data showing the total variance minimum corresponds to a period of 154.45 days.

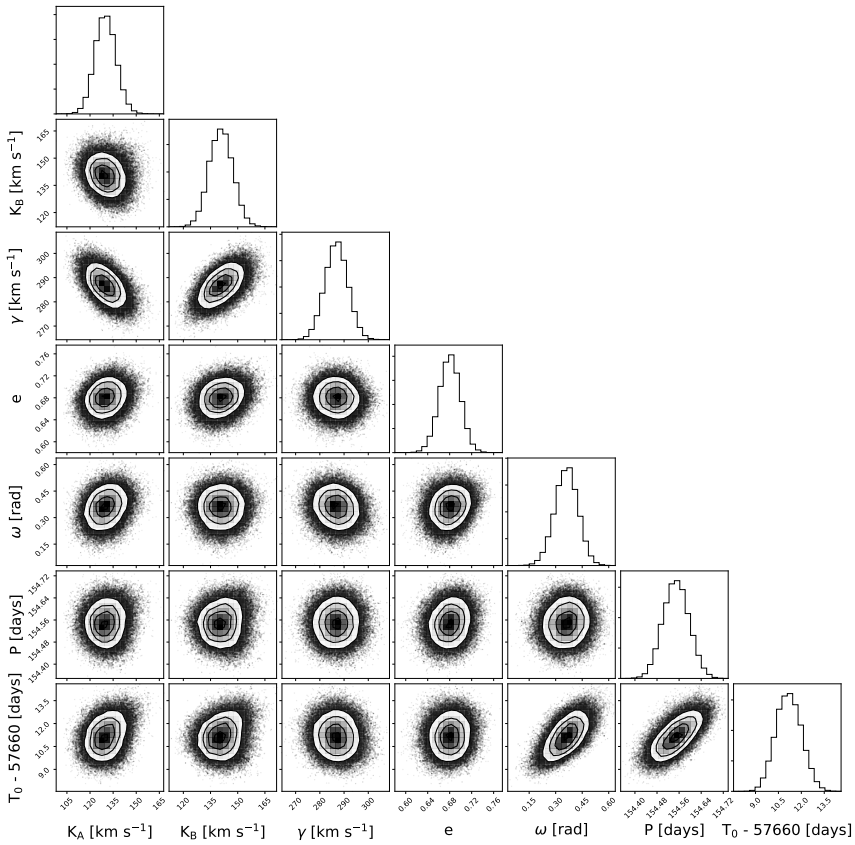

Figure 5.9: Corner plot showing posterior probabilities for solution UG1, where $K_{\rm A}$ and $K_{\rm B}$ are the semi-amplitudes of the velocities for star A and star B respectively, γ is the systemic velocity, e is the eccentricity, omega is the longitude of the periastron, P is the orbital period and $\rm T_0$ is the time of periastron.

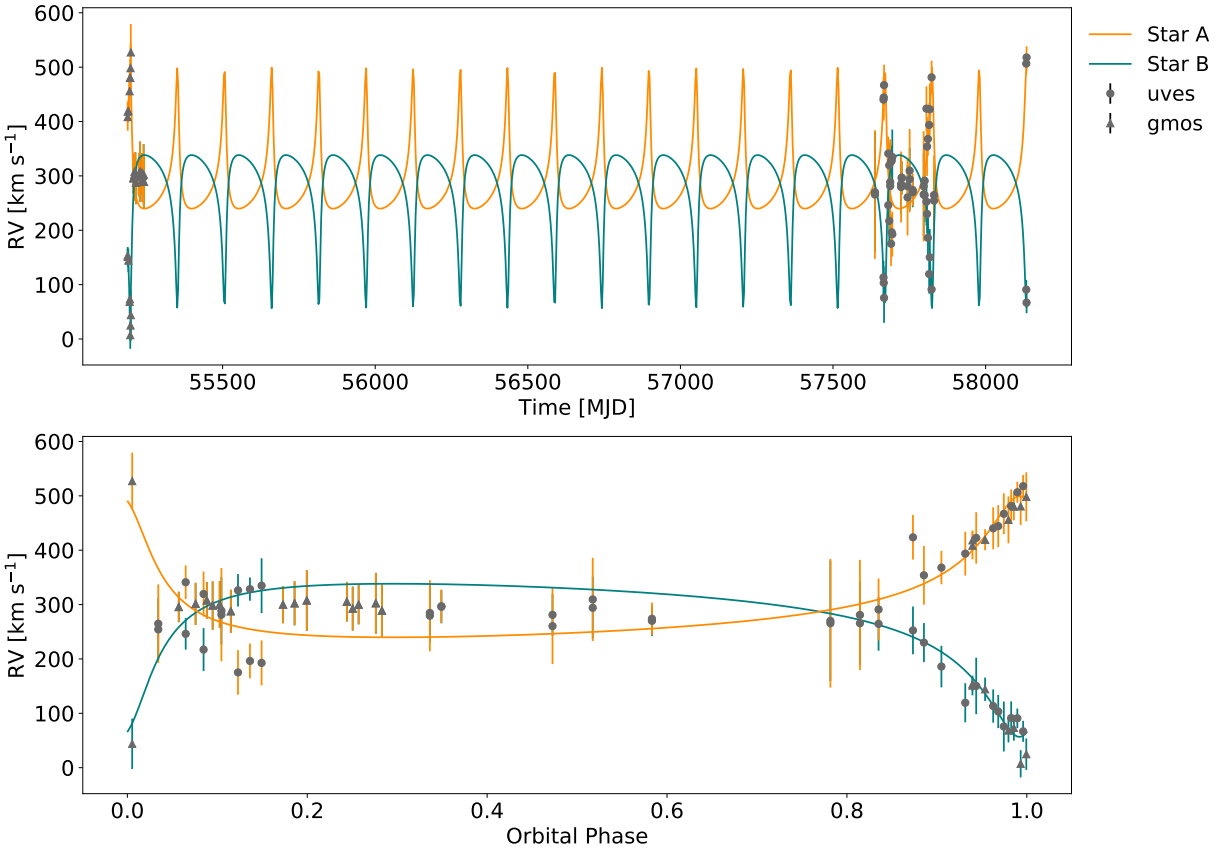

Figure 5.10: Best fitting radial-velocity curve for the VLT/UVES and Gemini/GMOS data providing the parameters for solution UG1. Note that at phases away from periastron it was difficult to differentiate the two stellar components within the blended emission line, which is reflected by the similar radial velocities measured in the middle of the orbital phase.

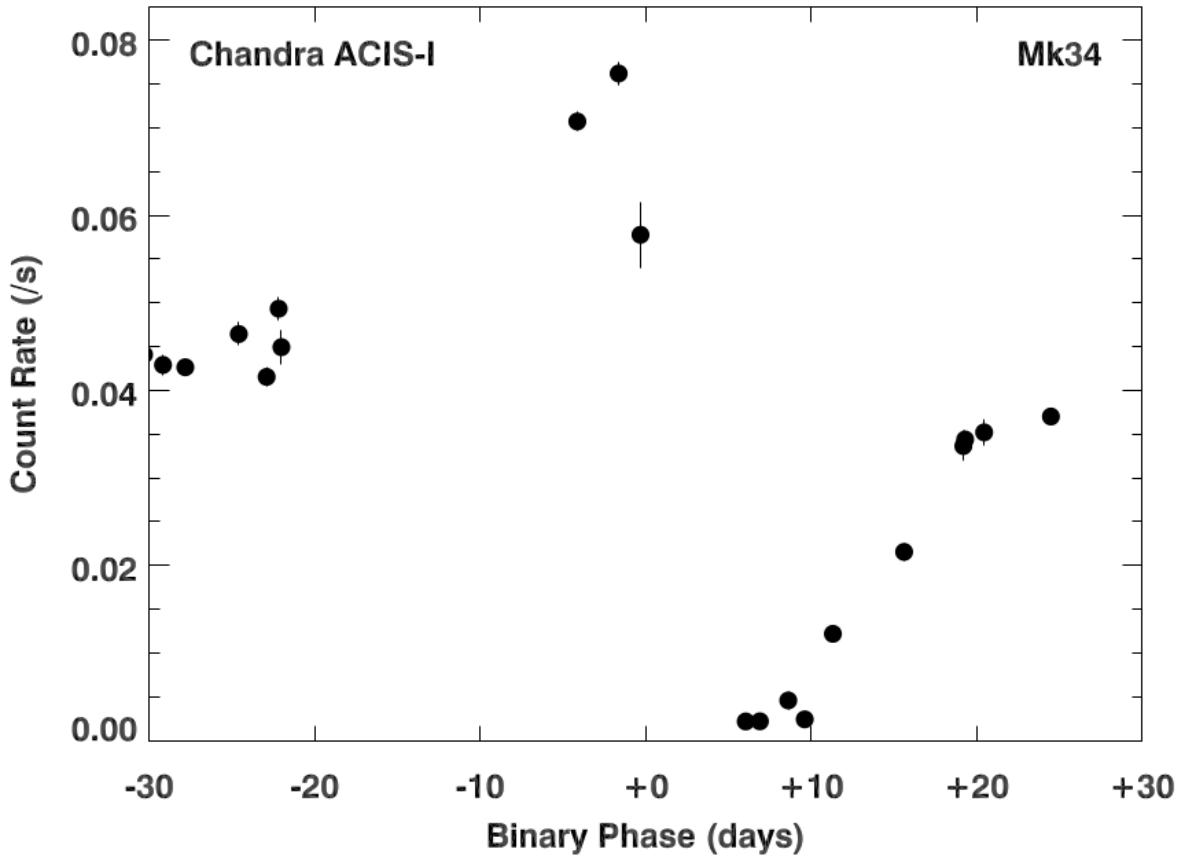

Figure 5.11: Detailed plot of the X-ray variability observed in Pollock et al. (2018) close to periastron, based on the 154.5 day period derived in this work

solution U1 we use a Gaussian prior distribution of 154.5 ± 0.5 days.

Figure 5.9 shows the posterior probability corner plot for solution UG1, demonstrating the credible value range for each orbital parameter. Figure 5.10 shows the radial-velocity curve in time and phase space produced from the MCMC outputs for solution UG1 compared to the observed data. The posterior probability plot and radial-velocity curve for solution U1 can be found in Appendix E (Figure E.1 & Figure E.2). A summary of the associated orbital parameters for these two solutions can be found in Table 5.4 and reveals that for most parameters they are reasonably consistent. Figure 5.11 shows the X-ray light curve from Pollock et al. (2018) using the solution UG1, confirming the X-ray maximum is associated with the periastron of the orbit.

Table 5.4: Orbital parameters derived from radial-velocity fits using the combined VLT/UVES and Gemini/GMOS data (solution UG1) compared with solely the VLT/UVES data (solution U1) and the automated template fitting method (solution U2) discussed in Section 5.3.3. Quoted solutions represent the median of the posterior distributions from MCMC fitting. The error bars represent the 16th and 84th percentiles

Parameter	VLT/UVES & Gemini/GMOS	VLT/UVES	VLT/UVES Automated Fitting		
	Solution UG1	*Solution U1*	*N*IV *4058*	*N*V *4945*	*Solution U2*
$K_{\rm A}$ [km s^{-1}]	130 ± 7	145 ± 10	132 ± 2	141 ± 6	137± 3
$K_{\rm B}$ [km s^{-1}]	141 ± 6	128 ± 9	126 ± 2	126 ± 4	127 ± 2
γ velocity [km s^{-1}]	287 ± 5	277 ± 6	260 ± 1	283 ± 1	271 ± 1
e	0.68 ± 0.02	0.66 ± 0.03	0.764 ± 0.006	0.753 ± 0.011	0.758 ± 0.006
ω [°]	20.9 ± 3.8	28.8 ± 6.6	36.6 ± 0.9	40.1 ± 1.4	38.4 ± 0.8
$P_{\rm orb}$ [days]	154.55 ± 0.05	154.5 ± 0.7	155.03 ± 0.07	155.19 ± 0.12	155.11 ± 0.07
T_0 [MJD]	57671.2 ± 0.9	57672.4 ± 2.0	57670.6± 0.2	57670.8 ± 0.4	57670.7 ± 0.2
q	0.92 ± 0.07	1.13 ± 0.10	1.05 ± 0.02	1.11 ± 0.04	1.08 ± 0.02
$\mathrm{M_A}\sin^3(i)$ [$\mathrm{M_\odot}$]	65 ± 7	64 ± 13	-	-	39 ± 2
$\mathrm{M_B}\sin^3(i)$ [$\mathrm{M_\odot}$]	60 ± 7	73 ± 15	-	-	42 ± 3
$a\sin(i)$ [AU]	2.82 ± 0.09	2.91 ± 0.18	-	-	2.45 ± 0.04

Using the orbital parameter outputs from the MCMC fitting we can infer the minimum mass estimates for each component based on our solutions (Table 5.4) with Equation (5.1).

$$\mathrm{M_{A,B}} \sin^3(i) = \frac{\mathrm{P}}{2\pi G} \, (1 - e^2)^{1.5} \, (\mathrm{K_A} + \mathrm{K_B})^2 \, \mathrm{K_{B,A}} \tag{5.1}$$

Solution UG1 reveals $\mathrm{M_A} \sin^3(i) = 65 \pm 7$ $\mathrm{M_\odot}$ and $\mathrm{M_B} \sin^3(i) = 60 \pm 7$ $\mathrm{M_\odot}$, whereas solution U1 reveals slightly higher determinations of $\mathrm{M_A} \sin^3(i) = 64 \pm 13$ $\mathrm{M_\odot}$ and $\mathrm{M_B} \sin^3(i) = 73 \pm 15$ $\mathrm{M_\odot}$. We do note, however, that these solutions are consistent within the errors. We also note the reversal of the mass ratio between solution UG1 and U1 which is caused by the 10 km $\mathrm{s^{-1}}$shift in the systemic velocity between the two solutions. Minimum semi major axis values are $a \sin^3(i) = 2.82 \pm 0.09$ AU and $a \sin^3(i) = 2.91 \pm 0.18$ AU for solutions UG1,U1 respectively.

5.3.3 Automated Template Fitting

An alternative method for deriving the orbital parameters using an automated template fitting MCMC model was also applied to the UVES data-set. Again this code was provided by Stuart Littlefair who also ran the model and passed on the results. Similar to the previous approach, the model parameters consisted of the Keplerian elements (K_A, K_B, γ, e, ω, P and $\mathrm{T_0}$), a continuum flux ratio parameter of the two stars and a line dilution factor for star B. Uninformative priors were used on all parameters, except the period, which was a Gaussian prior of 154.5 ± 0.5 days, based on solution UG1 and the results from the phase dispersed minimisation. Using these parameters, and the same WN5h template spectrum of VFTS 682 from Bestenlehner et al. (2011, 2014), we produced two scaled and shifted versions of the template to represent star A and star B. We used these templates to fit the N IV 4058 and N V 4945 emission lines separately, however the fit was applied to all 26 epochs of observations simultaneously. We also repeat the fitting from a range of starting points to ensure the results converged.

Figure 5.12 and Figure 5.13 show the best fit models to the N IV 4058 and N V 4945 emission lines respectively. The probability distributions of the orbital parameters resulting from these fits are provided in Figure F.1 in Appendix F. A summary of the best fit orbital solutions for each emission line is included in Table 5.4 together with an average of both emission lines combined (solution U2).

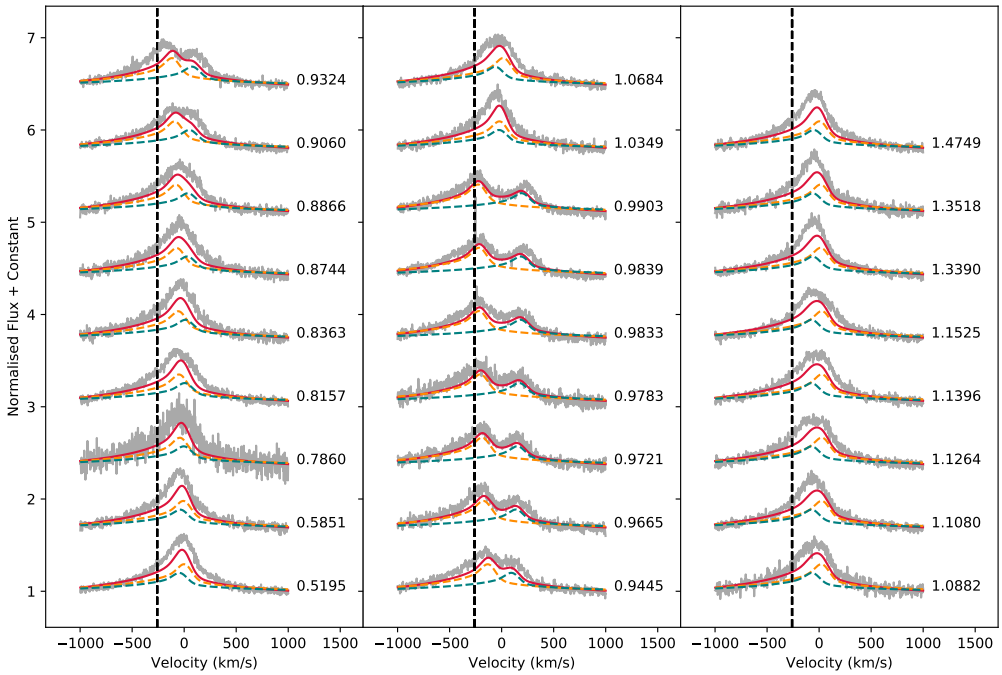

Figure 5.12: Automated template fits of the N IV 4058 emission line for all epochs. The model for star A is shown in orange, star B in green and the combined fit is shown in red. The observed UVES data is shown in grey. The radial-velocity scale is centred such that the systemic velocity is zero and the dashed line corresponds to the rest wavelength of N IV 4058.

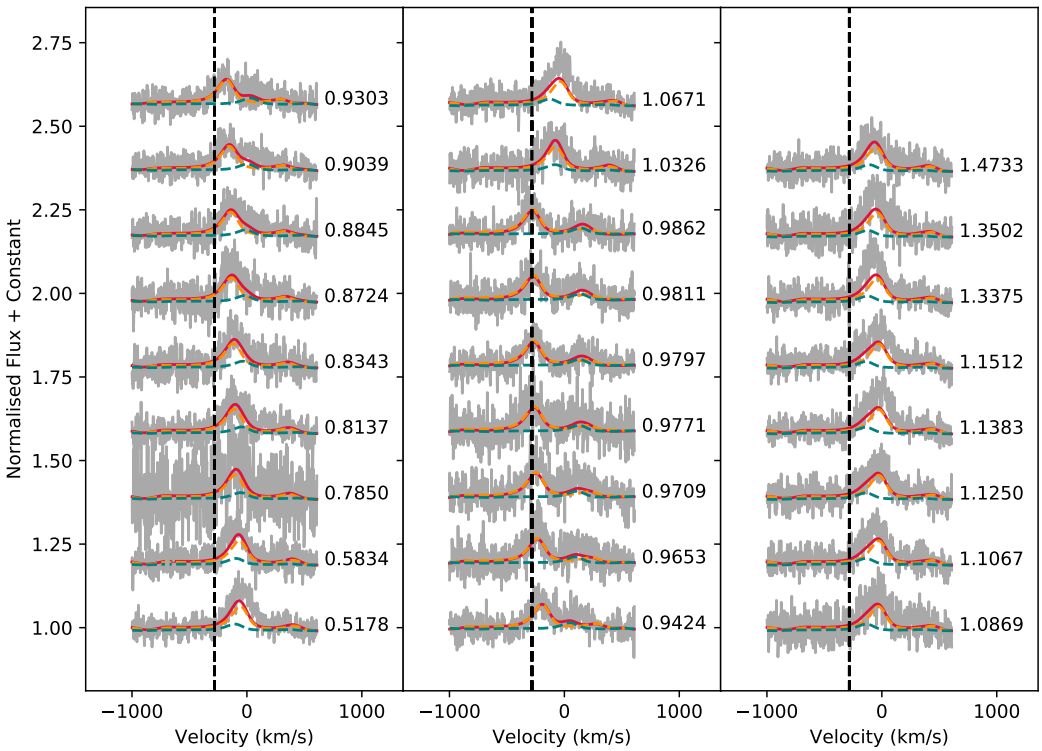

Figure 5.13: Automated template fits of the N v 4945 emission line for all epochs. The model for star A is shown in orange, star B in green and the combined fit is shown in red. The observed UVES data is shown in grey. The radial-velocity scale is centred such that the systemic velocity is zero and the dashed line corresponds to the rest wavelength of N v 4945.

5.4 Relative Photometry

Earlier photometry of the 30 Doradus region by Massey et al. (2002), obtained over a ∼3 week period using HST/STIS, revealed evidence for irregular photometric variations in Mk34. The study notes a repeating periodic dip of ∼0.1 mag in Mk34, following a 20 day period, which is unrelated to the orbital phase.

As part of our observing programme we also requested the UVES acquisition images also be made available, allowing us to perform relative photometry and search for an optical eclipse.

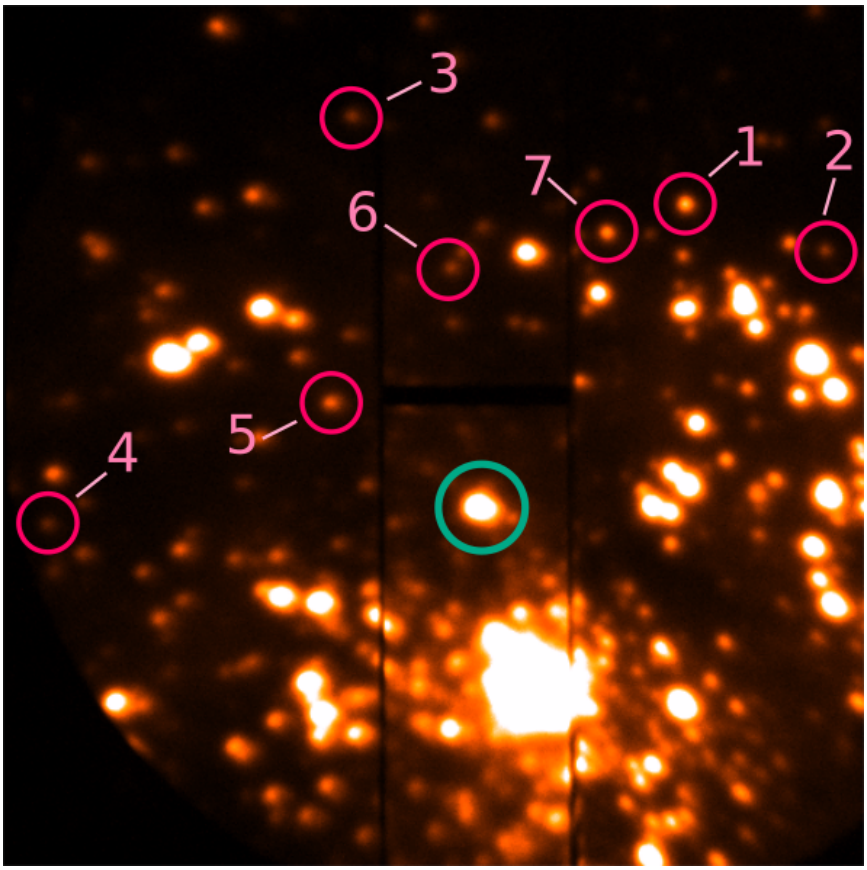

Figure 5.14: VLT/UVES acquisition image of Mk34 during OB10. Positions of the 7 field stars selected for relative photometry are circled in pink. Mk34 is circled in teal. Acquisition images have a field of view of approximately 45″ × 45″, which at a distance of 50 kpc corresponds to ∼11 × 11 pc. In these images east is up and north is to the right.

The sources were extracted using DAOPHOT in the same manner as described in Section 2.2.1, however we did not apply a zero point correction to convert our results to apparent magnitudes. We identified 7 isolated field stars suitable for comparison, as shown in Figure 5.14. We plotted the relative magnitude difference through time to search for

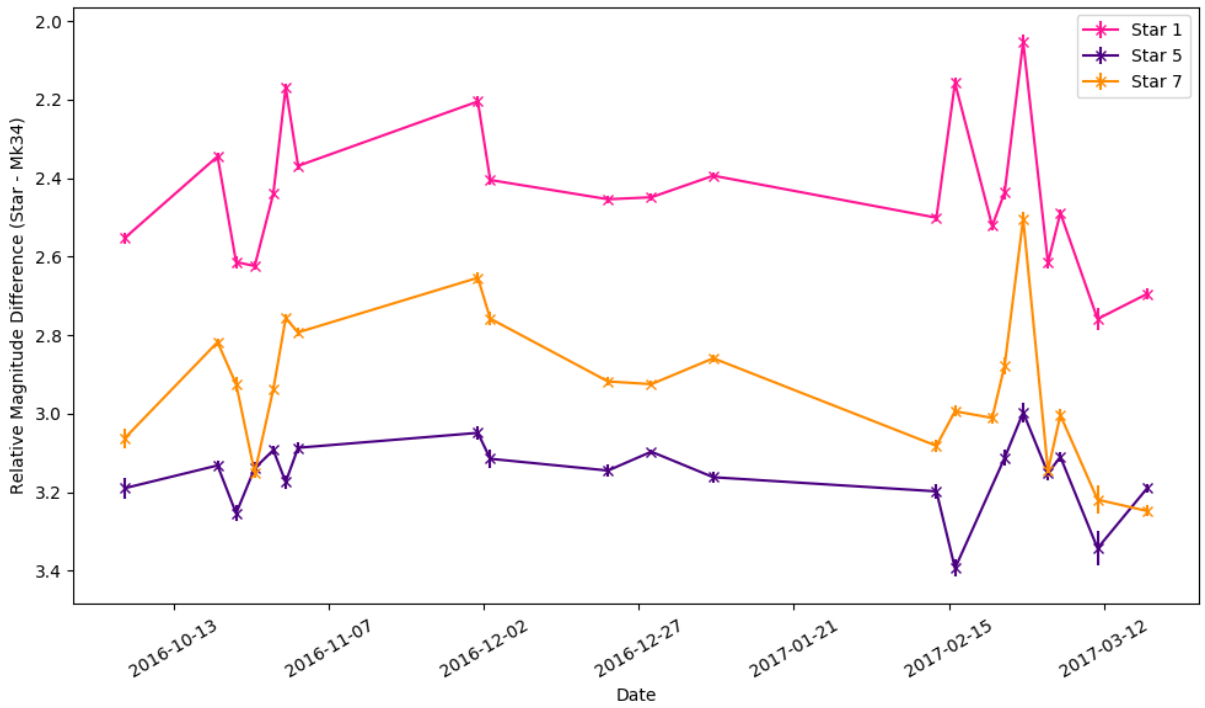

Figure 5.15: Relative magnitude differences between Mk34 and 3 selected field stars showing the apparent variability. Comparison between field stars shows this variability remains and therefore does not help constrain the binarity of Mk34.

variability. As shown in Figure 5.15 the 3 brightest of these stars appeared to show some level of variability, with a scatter of 0.09 – 0.18 mag around the mean. To test the reliability of these data we also performed relative photometry between these stars, which again revealed standard deviation measurements between 0.10 – 0.18 mag.

Unfortunately this would suggest that due to the variable seeing and the crowded region, the relative magnitude variations observed were within the photometric accuracy of ∼0.2 mag achievable with this data.

5.5 Physical and Wind Properties

5.5.1 Spectral Analysis

Both stellar components were identified as WN5h stars using the Bestenlehner et al. (2011, 2014) theoretical template spectrum for VFTS 682. Using the spectral properties of this star as a starting point Joachim Bestenlehner proceeded to compute a grid of models using the non-LTE stellar atmosphere and radiative transfer code CMFGEN (Hillier & Miller,

1998), varying effective temperature (at optical depth τ=2/3), mass loss rates, helium mass fractions, terminal velocities and the β-type velocity law. For this template, we updated the N V model atom better to reflect higher quantum number transitions[1]. In particular, this caused a shift in the N V 4945 emission line centroid of ∼26 km s^{-1}which would reduce the systematic offset between the measured radial velocities of the N IV 4058 and N V 4945 emission lines found in Section 5.2 such that the average differences would fall to 16 km s^{-1}and 7 km s^{-1}for UVES and GMOS respectively. Using the mass ratio deduced from Solution UG1 (M_B/M_A = q = 0.92 ± 0.07) and a specified He abundance, we estimate a luminosity ratio using a theoretical M/L relation (Eqn. 9 of Gräfener et al. 2011) based on this weighting we combine the two spectra and spectral energy distributions (SED) from each star. Using a fitting code provided by Joachim Bestenlehner, which in conjunction with his computed grid of CMFGEN models, allowed us to shift each spectrum in accordance with the radial-velocity measurements recorded from the VLT/UVES data in Tables 5.2 to 5.3 to reproduce the observed spectrum. An example of the combined spectrum fitted to the observed data, along with individual and combined SEDs, is shown in Figure 5.16.

Fits to the N IV 4058, N V 4603-20 P Cygni profile and N V 4945 provided temperature estimates of 53,000 ± 1,200 K for both stars. The He II 4686 and Hα emission line fits were used to deduce mass loss rates and He abundance mass fractions. For star A we find log ($\dot{M}_A/[M_\odot yr^{-1}]$) = −4.88 ± 0.13 and X_{He} = 35 ± 5 %. Similarly for star B we find log ($\dot{M}_B/[M_\odot yr^{-1}]$) = −4.72 ± 0.13 and X_{He} = 35 ± 5 %. We assume a nitrogen-rich, CNO processed atmosphere at 0.5 $Z_\odot$ metallicity, with a fixed nitrogen mass fraction of X_N = 0.35 %. This matched the observed nitrogen intensity and is equivalent to a ∼25x enhanced cosmic LMC nitrogen abundance. The volume filling factor was fixed at f_v = 0.1 which is consistent with the electron scattering wings in the Hα emission. The β-type velocity law was investigated by fitting the line profiles of the Hβ and Hγ lines and we find β ∼1.5 and β ∼2.0 for star A and star B respectively. The terminal velocity was estimated to be 2500 km s^{-1}for both components from fitting the line broadening of Hα and He II 4686.

The combined SED was used to examine the reddening and luminosity of the system. Intrinsic B, V and K-band colours were extracted by convolving the spectra with the corresponding filter function for each respective filter. Literature magnitudes outlined in Table 5.5 were used in combination with these intrinsic magnitudes to derive E(B-V) and E(V-K_s) extinctions, which in turn were used with Equation (5.2), inferred from Maíz Apellániz et al. (2014), to derive a reddening parameter:

[1] https://www.nist.gov/pml/atomic-spectra-database

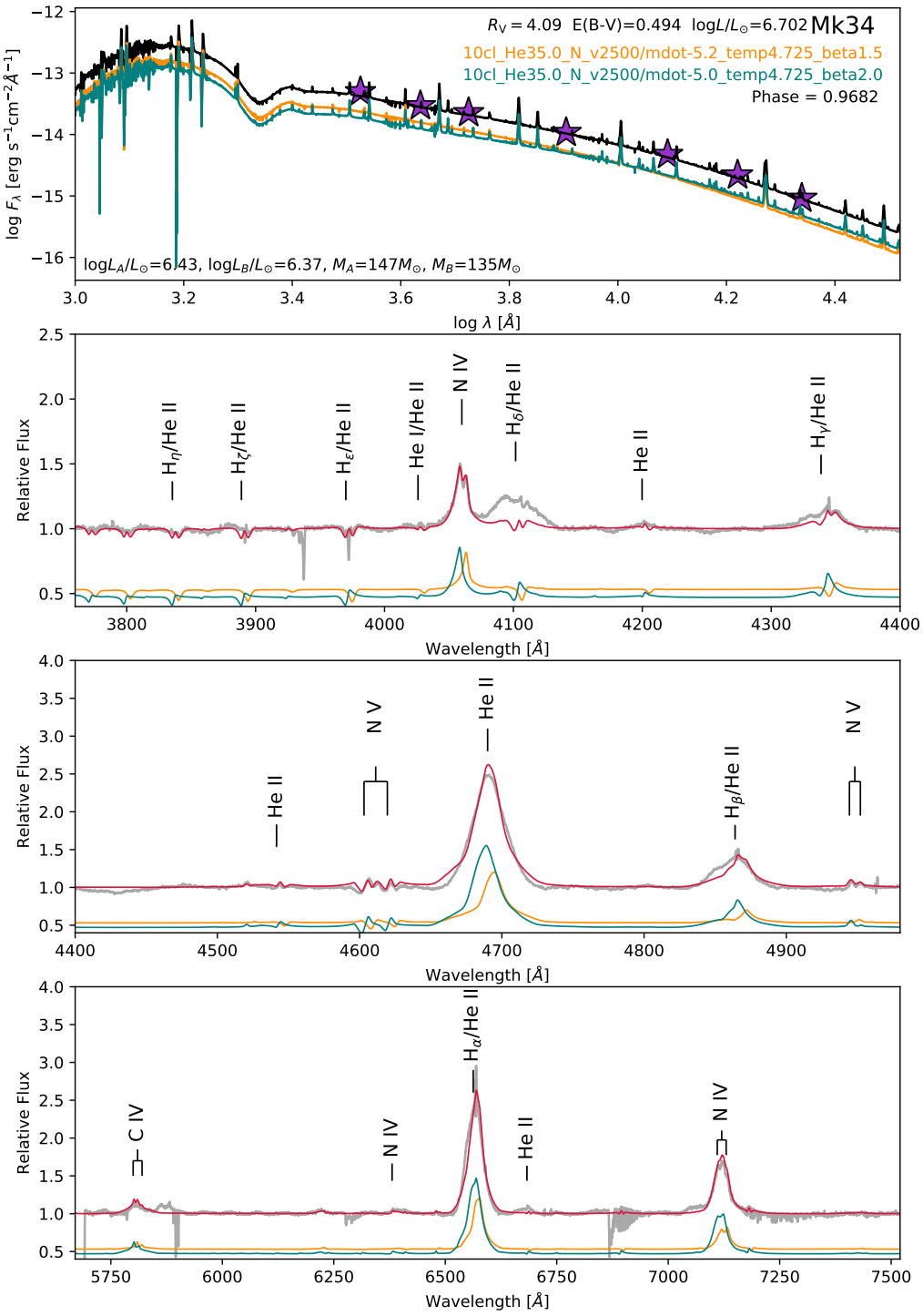

Figure 5.16: Top panel shows the individual reddening corrected model SED for star A (orange) and star B (green) produced by the radiative transfer code CMFGEN, and the combined SED for the system (black). The purple stars correspond to the observed magnitudes in various bands (listed in Table 5.5) used to derive the extinction towards the system. Lower panels show the observed VLT/UVES spectrum of epoch 2 (grey) with the chosen model for star A (orange), star B (green) and the combined model (red) over-plotted. Note the poor fit to the H$\delta$and Hγemission is due to the observed excess in these lines close to periastron, as described in Section 5.2.4

Table 5.5: Mk34 photometry from the literature and the subsequently derived reddening parameters from this work.

Parameter	Value	Reference
U [mag]	12.083	De Marchi et al. (2011)
V [mag]	13.088	De Marchi et al. (2011)
B [mag]	13.388	De Marchi et al. (2011)
I [mag]	12.549	De Marchi et al. (2011)
J [mag]	12.056	Skrutskie et al. (2006)
H [mag]	11.789	Skrutskie et al. (2006)
K_s [mag]	11.68	Crowther et al. (2010)
R_V [mag]	4.09	This work
E(B-V) [mag]	0.49	This work
E(V-K_s) [mag]	1.76	This work
A_V [mag]	2.02	This work
A_{K_s} [mag]	0.26	This work
DM [mag]	18.49	Pietrzyński et al. (2013)
M_V [mag]	−7.42	This work
M_{K_s} [mag]	−7.07	This work

$$R_V = 1.2 \times \frac{E(V\text{-}K_s)}{E(B\text{-}V)} - 0.18. \tag{5.2}$$

We find $R_V = 4.09$, which is typical of other stars in close proximity to R136 (Doran et al., 2013; Gräfener et al., 2011). The model spectrum was then reddened using the extinction law described in Maíz Apellániz et al. (2014) along with our derived extinction and reddening parameters. Following this, we matched the observed K_s-band flux with the reddened model SED, whilst also accounting for the 50 kpc distance to the LMC (Pietrzyński et al., 2013), to derive the absolute luminosity of each component in the system.

Chemically-homogeneous masses[2] were derived from the theoretical mass-luminosity relation from Gräfener et al. (2011), providing an estimate of the mass of each component. We find $M_A = 147 \pm 22$ $M_\odot$ and $M_B = 136 \pm 20$ $M_\odot$ for stars A and B, respectively. We consider the use of a mass-luminosity relationship appropriate, since the low helium abundance of 35 % is evidence that these stars are still on the main sequence. A summary

[2]Conventionally, spectroscopic masses refer to masses derived from a surface gravity estimate. However, in the absence of a clean gravity diagnostic line, throughout this paper we refer to the chemically-homogeneous masses derived from the theoretical mass-luminosity relationship in this section as spectroscopic masses

Table 5.6: Upper panel shows stellar properties derived from spectral modelling of the VLT/UVES spectra using the non-LTE stellar atmosphere code CMFGEN. Spectral masses were derived from the theoretical M/L relation from Gräfener et al. (2011). Lower panel shows stellar properties derived from evolutionary modelling of each component using the BONNSAI statistical analysis code. Luminosity, effective temperature and helium abundance inputs derived from spectral modelling were provided. All evolutionary parameters quote the mode result with the exception of He abundance which refers to the median.

Spectroscopic modelling: CMFGEN		
Parameter	Star A	Star B
T [K]	53000 ± 1200	53000 ± 1200
$\log (L_*/[L_\odot])$	6.43 ± 0.08	6.37 ± 0.08
R $[R_\odot]$	19.3 ± 2.8	18.2 ± 2.7
$\log (\dot{M}_*/[M_\odot yr^{-1}])$	-4.88 ± 0.13	-4.72 ± 0.13
v_∞ [km s^{-1}]	2500 ± 300	2500 ± 300
β (Velocity Law)	1.5	2.0
X_{He} [%]	35 ± 5	35 ± 5
M_{cur} $[M_\odot]$	147 ± 22	136 ± 20
Evolutionary modelling: BONNSAI		
Parameter	Star A	Star B
$\log (L_*/[L_\odot])$	$6.41^{+0.09}_{-0.08}$	$6.35^{+0.08}_{-0.09}$
X_{He} [%]	33^{+3}_{-8}	33^{+3}_{-8}
v_{rot} [km s^{-1}]	240^{+171}_{-20}	250^{+170}_{-29}
T [K]	54388^{+327}_{-822}	54355^{+339}_{-855}
$\log (\dot{M}_*/[M_\odot yr^{-1}])$	$-5.00^{+0.13}_{-0.11}$	$-5.06^{+0.11}_{-0.12}$
Age [Myrs]	0.5 ± 0.3	0.6 ± 0.3
M_{cur} $[M_\odot]$	139^{+21}_{-18}	127^{+17}_{-17}
M_{init} $[M_\odot]$	144^{+22}_{-17}	131^{+18}_{-16}

of the spectral analysis results can be found in Table 5.6.

5.5.2 Evolutionary Modelling

Using the BONNSAI[3] evolutionary modelling code (Schneider et al., 2014) we also derive evolutionary masses for Mk34 based on LMC stellar models (Brott et al., 2011; Köhler et al., 2015). Providing luminosity, effective temperature and helium abundances derived from the spectral analysis the evolutionary modelling returned the parameters summarized in Table 5.6.

We find some differences between spectral and evolutionary modelling but attribute

[3]The BONNSAI web-service is available at www.astro.uni-bonn.de/stars/bonnsai

these to the mass-loss prescription adopted in the BONNSAI analysis, which under-predicts our observed mass-loss rates. To attain the high He abundance selected as a prior, the model requires high rotational velocity rates to enhance the He abundance at the surface of the star. Consequently, the high rotational velocity gives the star a higher effective temperature than expected. In general we cannot confirm the high rotational velocities predicted by the model. We can use the N IV 4058, N V 4603–20 and N V 4945 emission to set good constraints on this parameter, and we find rotational broadening of $\sim$125 km s^{-1}, we cannot discern if this broadening is purely rotational or contaminated by micro and macro turbulence.

The BONNSAI code also provides estimates for the ages and initial masses of the stars. We find consistent stellar ages of $\sim$0.6 $\pm$ 0.3 Myrs for both stars, and current masses of $M_{A(cur)} = 139^{+21}_{-18}$ $M_\odot$, and $M_{B(cur)} = 127^{+17}_{-17}$ $M_\odot$ for star A and star B respectively. These are somewhat lower than the spectral analysis results, which were based on the Gräfener et al. (2011) mass-luminosity relation for chemical homogeneous stars. The initial masses corresponding to the BONNSAI solution are $M_{A(init)} = 144^{+22}_{-17}$ $M_\odot$, and $M_{B(init)} = 131^{+18}_{-16}$ $M_\odot$ for star A and star B respectively.

5.6 Discussion

5.6.1 Melnick 34

In Section 5.3 we have presented three different orbital solutions for Melnick 34 using two alternative methods from which we can confidently conclude that this is an eccentric, massive system with a mass ratio close to unity.

Solutions UG1 and U1 were derived using the same method, and the results show good agreement indicating the method is robust. Similarly, solutions U1 and U2 were derived using the same data, though different methods, and again the results are comparable with the exception of eccentricity. Solution U2 obtains e = 0.758 $\pm$ 0.006, somewhat higher than the e = 0.66 $\pm$ 0.03 found for solution U1. Whilst there are advantages to the automated model fitting, such as the unbiased and systematic nature of the method, we were unable to apply this technique to the GMOS data due to its low S/N ratio. We therefore favour solution UG1 which encompasses all available data, appropriately weighted.

Using these results we can comment on the inclination of the system, by comparing the predicted dynamical masses with the spectroscopic masses derived in Section 5.5.1. Table 5.7 shows how the kinematic masses and periastron distances depend on inclination for solutions UG1 and U2. Recalling the spectroscopic masses of $M_A = 147 \pm 22$ $M_\odot$ and

Table 5.7: A comparison between the stellar masses and periastron distances for Mk34 for various assumed inclination values for both Solution UG1 and Solution U2 orbital properties.

	Solution UG1			*Solution U2*		
Incl	M_A [$M_\odot$]	M_B [$M_\odot$]	a_{peri} [AU]	M_A [$M_\odot$]	M_B [$M_\odot$]	a_{peri} [AU]
80°	68	63	0.91	41	44	0.60
70°	78	72	0.96	47	51	0.63
60°	100	92	1.04	60	65	0.68
50°	144	133	1.18	87	94	0.77
40°	244	225	1.40	147	159	0.92

$M_B = 136 \pm 20$ $M_\odot$, it is apparent from Table 5.7 that solution UG1, with an eccentricity of 0.68, would reproduce the dynamical masses if i ∼50°. In contrast, solution U2, with a higher eccentricity of 0.758, suggests i ∼41° to reconcile the dynamical and spectroscopic masses.

We are in the process of investigating the inclination of the system using X-ray light curve modelling. Another approach would be to search for a visual eclipse, however this would involve obtaining further, very high cadence, optical observations precisely focused on conjunction. Based on solution UG1, the lowest inclination that would produce an eclipse is ∼79°, from which we anticipate the duration of this eclipse to be approximately 16 hours. An inclination of ∼79° would reveal dynamical masses of $M_A = 63$ $M_\odot$ and $M_B = 69$ $M_\odot$, much lower than our spectral modelling estimates, therefore we consider an eclipse to be highly unlikely. Other observations necessary to help constrain the inclination include intensive X-ray monitoring near periastron, which we could combine with Figure 5.11 allowing us to accurately map, and subsequently model, the X-ray variability. Finally, polarimetry observations have proven useful to help measure the inclination of massive binaries, as done by St.-Louis et al. (1993) for WR139.

5.6.2 Colliding Wind Binaries

Table 5.8 provides a comparison between the stellar and orbital properties derived here for Mk34 and other Wolf-Rayet binary systems with a >75 $M_\odot$ primary mass in the Milky Way and LMC. Spectroscopic masses, evolutionary masses and exceptional L_x/L_{bol} discussed in Section 4.2.14 confirms that Mk34 is a high mass colliding wind binary, and most likely the most massive binary known to date. Mk34 is also an excellent candidate for studying the

properties of colliding wind binaries (CWB). Of the systems listed in Table 5.8 only WR21a and WR25 are CWB, making Mk34 a welcome addition at low metallicity, and WR25 is a SB1 system, making mass derivations of the secondary component very uncertain.

Other CWBs outside this group include η Carinae. Again the suitability of this system as the focus of detailed CWB studies is not ideal since the nature of the secondary is uncertain. The SB2 nature of Mk34 has allowed us to thoroughly investigate the orbital properties of this system and produce robust results. The high eccentricity and period encourage obvious wind variations throughout the orbit, which is also useful for studying CWB properties.

Pollock et al. (2018) show a Chandra ACIS-I X-ray image of Mk34 compared with neighbouring stars R136a1–3 and R136c (their Figure 1). It has been proposed that R136a1–3 host stellar masses of 265 $M_\odot$, 195 $M_\odot$, and 135 $M_\odot$ respectively (Crowther et al., 2010) which in turn has sparked discussion regarding the possible binarity of these systems, with mass ratios close to unity. In the binary scenario, R136a1 would be analogous to Mk34 and therefore we would also expect to observe similar X-ray properties if its orbital period were on the order of $\sim$100 days. Based on our results from Chapter 3 and the work from Townsley et al. (2006b) however, we find Mk34 is considerably brighter than the entire R136a cluster at all times due to the colliding wind nature of the system. The lower X-ray flux of R136a supports the interpretation that these stars are single, possess high mass ratios, or large separations for mass ratios close to unity.

Table 5.8: Comparison of stellar and orbital properties of other known massive binary systems in the Large Magellanic Cloud (LMC) and Milky Way (MW).

	LMC			MW				
Property	Melnick 34	R145	R144	NGC3603-A1	F2	WR 20a	WR 21a	WR 25
Ref	[1]	[5]	[8]	[9]	[14]	[15]	[19]	[21]
Sp. Type A	WN5h	WN6h	WN5–6h	WN6ha	WN8–9h	WN6ha[16]	O3/WN5ha	O2.5 If*/WN6[22]
Sp. Type B	WN5h	O3.5 If*/WN7	WN6–7h	WN6ha:	O5–6 Ia	WN6ha[16]	O3Vz((f*))	O2.5 If*/WN6[22]
Period [days]	154.55 ± 0.05	158.76	<370	3.77	10.5	3.69 ± 0.01[17]	31.67 ± 0.01	207.85 ± 0.02
Eccentricity	0.68 ± 0.02	0.788 ± 0.007	-	0	0.05 ± 0.01	0	0.695 ± 0.005	0.50 ± 0.02
Mass Ratio	0.92 ± 0.07	1.01 ± 0.07	1.17 ± 0.06	0.76	0.73 ± 0.07	0.99	0.563 ± 0.025	-
$M_A \sin^3(i)$ [$M_\odot$]	65 ± 7	13.2 ± 1.9	-	99 ± 34	64 ± 9	74.0 ± 4.2	64.4 ± 4.8	-
$M_B \sin^3(i)$ [$M_\odot$]	60 ± 7	13.4 ± 1.9	-	75 ± 21	47 ± 6	73.3 ± 4.2	36.3 ± 1.7	-
Inclination [°]	-	39 ± 6	-	71	67 ± 1	74.5 ± 1.0[17]	-	-
$M_{A(orb)}$ [$M_\odot$]	-	53^{+40}_{-20}	-	116 ± 31	82 ± 12	82.7 ± 5.5	-	-
$M_{B(orb)}$ [$M_\odot$]	-	54^{+40}_{-20}	-	89 ± 16	60 ± 8	81.9 ± 5.5	-	-
Distance [kpc]	50[2]	50[2]	50[2]	7 ± 0.5[10]	8.1	8.0 ± 1.4[18]	4.4[20]	2.3[23]
$M_{A(sp)}$ [$M_\odot$]	147 ± 22	101^{+40}_{-30}	-	120^{+26}_{-17}[11]	-	-	-	-
$M_{B(sp)}$ [$M_\odot$]	136 ± 20	109^{+60}_{-40}	-	92^{+16}_{-15}[11]	-	-	-	-
L_x [$\times 10^{34}$ erg s^{-1}]	1–32[3]	0.6[6]	1[6]	1.7–4.8 [6,12]	-	-	0.1–1.3[3,20]	0.4–0.9[3]
M_v [mag]	−7.42[1,4]	−7.2[7]	−8.2	−7.5[13]	-	−7.04 ± 0.25[18]	−5.9[19,20]	−7.3[24]

1. This work; 2. Pietrzyński et al. (2013); 3. Pollock et al. (2018); 4. De Marchi et al. (2011); 5. Shenar et al. (2017); 6. Townsley (private communication); 7. Schnurr et al. (2009a); 8. Sana et al. (2013a); 9. Schnurr et al. (2008); 10. Moffat (1983); 11. Crowther et al. (2010) 12. Townsley et al. (2014); 13. Drissen et al. (1995); 14. Lohr et al. (2018); 15. Rauw et al. (2005); 16. Rauw et al. (2004); 17. Bonanos et al. (2004); 18. Rauw et al. (2007); 19. Tramper et al. (2016); 20. Rate (private communication); 21. Gamen et al. (2006); 22. Crowther & Walborn (2011); 23. Smith (2006); 24. Hamann et al. (2006)

The colon (:) indicates a highly uncertain measurement

5.6.3 Formation

Our spectroscopic analysis reveals both components of Mk34 are VMS, which prompts the question of how this system formed. Both components are classified as WN5h stars, which are very massive main sequence stars with intrinsically powerful stellar winds. Mk34 lies at a projected distance of ∼2 pc from R136, the dense core of 30 Doradus, whose age is 1.5 ± 0.5 Myr (Crowther et al., 2016). The derived age of Mk34 (∼0.6 Myr) would lead us to favour a scenario in which Mk34 was formed in situ rather than being ejected from this dense core. Proper-motion estimates of this system using Gaia DR2 suggest a ∼30 ± 15 km s^{-1}motion relative to R136 (D. Lennon, private communication). Given the systemic radial velocity of Mk34 from solution UG1, 287 ± 5 km s^{-1}, and the cluster radial velocity of R136, 268 ± 6 km s^{-1}(Hénault-Brunet et al., 2012), we find a relative radial velocity offset of 19 ± 8 km s^{-1}, and therefore a relative 3D velocity of 36 ± 26 km s^{-1}. Considering this relative 3D velocity and the young age of Mk34, the system has traversed 22 ± 19 pc since birth, which exceeds the 2 pc projected distance so is likely inconsistent with a birth environment of R136, preferring a birth in isolation. Here we discuss two potential scenarios from which these massive stars could form:

1. Core fragmentation;
2. Merger of smaller stars.

The core fragmentation mechanism predicts that an initial, bound, proto-stellar core will fragment and collapse to form multiple stars (Goodwin et al., 2007). From this we would expect a small group of stars would form, with a range of stellar masses. Current observations are unable to test a hypothetical low mass population around Mk34. It is also possible, given the close proximity of Mk34 to R136, that the radiation field from stars in R136 heated the neighbouring star formation regions and suppressed the fragmentation of low mass counterparts, instead allowing only the most massive stars to form (Dale et al., 2012, 2013).

The alternative scenario involving merging stars begins in a similar manner to the core fragmentation hypothesis, however rather than the direct formation to the two massive stars we observe today, the cloud instead collapses to form a system with four or more massive stars, each with ∼70 M$_\odot$, which in time undergo mergers to form the current system. Again, this scenario would require an additional low mass population to be present in order to induce the hardening of the quadruple, thereby triggering the mergers. Alternatively, this hardening could be achieved through dynamical friction, where the surrounding ambient

gas applies a braking force to the system and the loss of angular momentum causes the migration of the components inwards, resulting in a merger (Stahler, 2010).

To further investigate the likelihood of the merging scenario compared to core fragmentation limited by a background radiation field, Richard Parker wrote and compiled a Monte Carlo simulation to explore the relative likelihood of forming exactly two ∼130 ± 30 $M_\odot$ stars compared to four ∼70 ± 30 $M_\odot$ stars, providing a rough insight into the more likely formation mechanism. Using a cluster mass function with a slope of −2, across an initial cluster mass range of 50–10,000 $M_\odot$, the simulation randomly sampled the cluster mass function and created a population of stars within each cluster by randomly sampling a Maschberger (2013) IMF, with an initial mass range of 0.1–300 $M_\odot$. In total, 3.76 million clusters were simulated. For full details of this method see Parker & Goodwin (2007).

By counting the number of clusters which successfully formed either exactly two ∼130 ± 30 $M_\odot$ stars or four ∼70 ± 30 $M_\odot$ stars, and no other O-stars (≥17.5 $M_\odot$) we find that both scenarios are unlikely. The formation of two VMS, however, is more favourable than the formation of four massive stars, with probabilities of 0.01 % and 0.0005 % respectively. Figure 5.17 shows a comparison of the results we obtained, showing more clusters forming two VMS rather than four massive stars. We also note that the host cluster masses from which the VMS form are between 420–1200 $M_\odot$. From this we are inclined to conclude that this system is most likely to have formed in-situ, through the direct formation of a low mass cluster including two VMS.

5.6.4 Future Evolution

At present the components of Mk34 orbit in relatively close proximity, with a minimum periastron separation of ∼0.9 AU, however within the next 2-3 Myrs each component will evolve off the main sequence, changing the dynamics of the system. To predict these changes we compare the evolutionary model grids from the Bonn (Köhler et al., 2015) and Geneva (Yusof et al., 2013) codes, based on a star with an initial mass of 150 $M_\odot$ at LMC metallicity (Z=0.006 and Z=0.0047 respectively) and a selected rotational-velocity.

We begin with the model grids by Köhler et al. (2015) which describe the evolution of the star up until core hydrogen burning ceases, which is taken to be when the hydrogen core mass fraction drops below 3%. These models were used in the BONNSAI evolutionary modelling in Section 5.5.2 for which we derived an initial rotational velocity of 250 km s^{-1}, therefore continuing with this particular model suggests the end of the hydrogen burning stage will occur after 2.3 Myrs. During this time the effective temperature of the star will fall to ∼29 kK, causing the radius to swell, reaching ∼78 $R_\odot$. Figure 5.18 shows how the

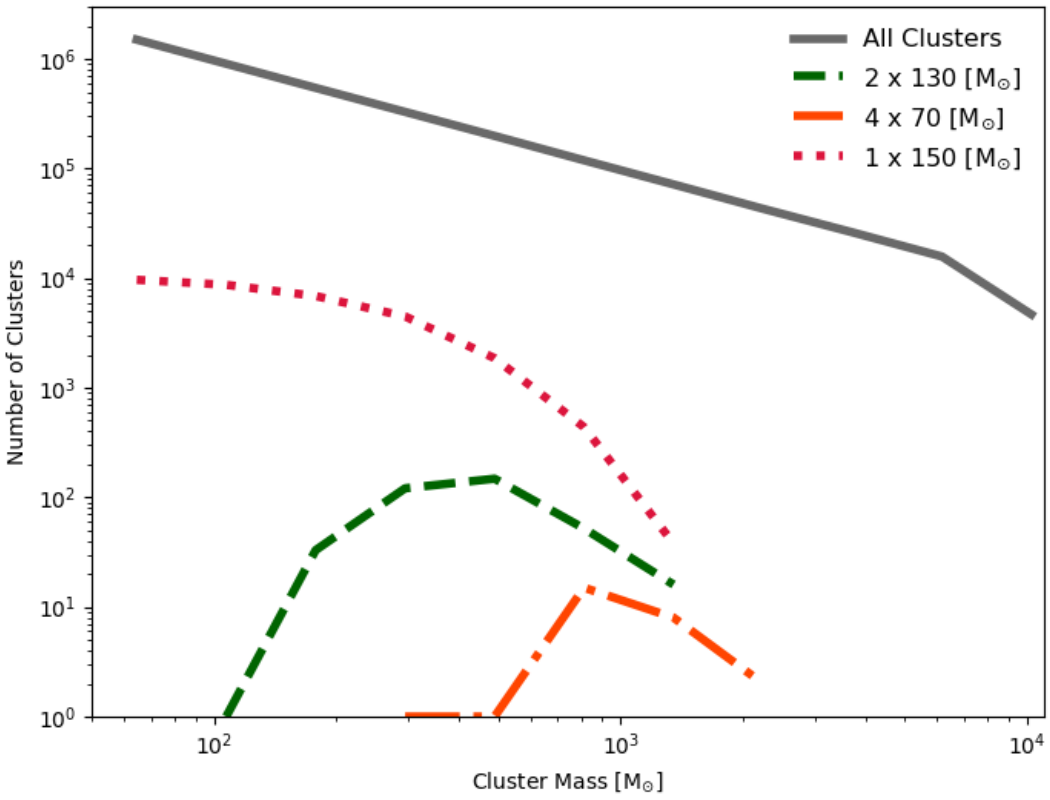

Figure 5.17: The results of the Monte Carlo simulation showing the number of clusters hosting either two ∼130 $M_\odot$ stars (green dashed line), four ∼70 $M_\odot$ stars (orange dot-dashed line), or 1 ∼150 $M_\odot$ star (red dotted line). The likelihood of forming a cluster hosting 2 VMS is slightly higher than forming a cluster of 4 massive stars.

stellar radius evolves through time and can be used to show if Roche lobe overflow and mass transfer in the system would be likely.

For an inclination of 50° we find the current periastron separation to be 254 $R_\odot$ and using Equation (5.3) (Eggleton, 2006), where a is the orbital separation and q is the mass ratio, we find a Roche lobe limit of 386 $R_\odot$. Considering that the periastron distance will change through time, and assuming a non-conservative, fast wind mass-loss mode as parametarised by Postnov & Yungelson (2014), we can derive a Roche lobe limit range based on the initial and final periastron separations at the zero age main-sequence and terminal age main-sequence times respectively. This range corresponds to the shaded region in Figure 5.18, and therefore we can see that, based on the 250 km s^{-1} rotation Köhler et al. (2015) model grid, the primary will not fill its Roche lobe at the end of core hydrogen burning.

$$R_{\rm L} = a\ \frac{0.49{\rm q}^{2/3} + 0.27{\rm q} - 0.12{\rm q}^{4/3}}{0.6{\rm q}^{2/3} + \ln(1 + {\rm q}^{1/3})} \tag{5.3}$$

Assuming no initial rotation, the Köhler et al. (2015) models predict a very similar evolution, with a core-hydrogen burning lifetime of 2.2 Myrs, and an effective temperature of ∼28 kK at the terminal age main sequence, therefore deriving a radius of ∼78 $R_\odot$. Again we can see in Figure 5.18 that an interaction between the two stars is unlikely prior to their post main sequence evolution.

Since the Köhler et al. (2015) model grids terminate at the end of core hydrogen-burning, to understand how the star could progress post-hydrogen core burning, we can use the model grids by Yusof et al. (2013) with two rotational-velocity options; no rotation and a rotational velocity of 404 km s^{-1}.

For single stars in isolation, Yusof et al. (2013) predict that at the end of the core hydrogen burning stage a 150 $M_\odot$ initial mass star at LMC metallicity will have a mass of 66–72 $M_\odot$, depending on rotation. For the model grid with no rotation, hydrogen burning will cease after 2.5 Myrs, during which the effective temperature will have fallen to ∼22 kK, with a radius of ∼126 $R_\odot$. Again, the evolution of the stellar radius through time is shown in Figure 5.18 and it can been seen the expansion does not reach the Roche-lobe limit. Post core hydrogen-burning, there is a brief period of further expansion as can be seen in Figure 5.18, such that the star will fill its Roche-lobe, triggering Roche-lobe overflow and mass transfer onto the secondary. The alternative model grid introduces a rotational velocity of 404 km s^{-1}, and within this scenario the core hydrogen burning phase ends after 2.8 Myrs. Under these initial conditions the effective temperature of the star rises to ∼64 kK, resulting in a reduction of the stellar radius to ∼17 $R_\odot$, suggesting there will be

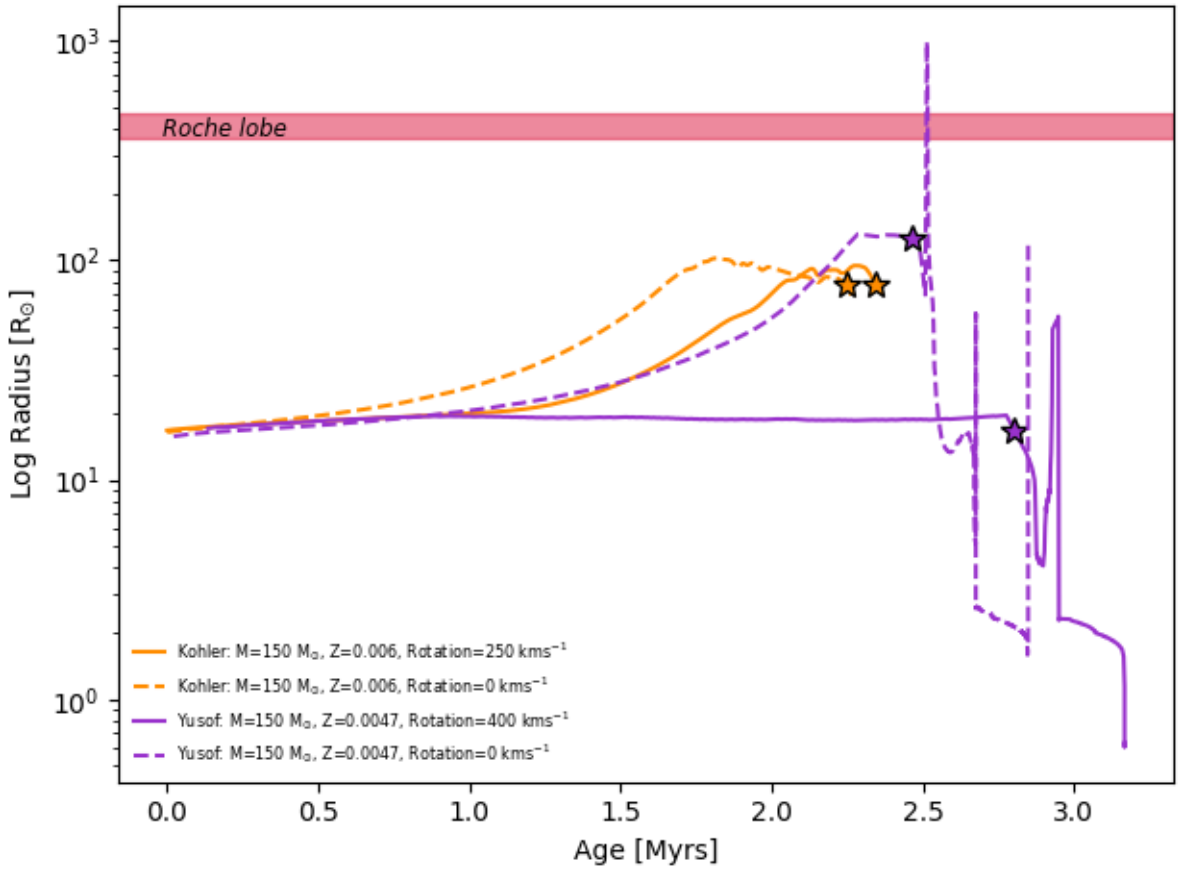

Figure 5.18: The evolution of the stellar radius with time for a 150 $M_{\odot}$star at LMC metallicity, derived from the Köhler et al. (2015) model grids (orange lines) for a star with 250 km s^{-1}rotational velocity (solid line) and a star with no rotation (dashed line). Also included are the Yusof et al. (2013) model grids (purple lines) for a star with a 400 km s^{-1}rotational velocity (solid line) and no rotation (dashed line). The red shaded region represents the Roche lobe radius range of the system between the zero age main sequence and terminal age main sequence, based on an inclination of 50°.

no interaction between the two stars.

Overall it is unlikely that Roche lobe overflow occurs, in which case evolution will proceeds independently. Yusof et al. (2013) predict that at the end of the helium burning stage a 150 $M_\odot$ initial mass star will have a core mass of 43±5 $M_\odot$, and that these stars will end their lives with the direct collapse to a black hole or black hole formation following a weak core collapse supernova. Unfortunately similar models for binary systems are not yet available, though see Kruckow et al. (2018) and Belczynski et al. (2016) for potential massive binary star progenitors of LIGO gravitational wave sources. Under the assumption of single stellar models applying to Mk34, and it surviving two potential supernovae events, this system will progress to be a double stellar-mass black hole binary with a combined mass of ∼90 $M_\odot$. Considering the current gravitational wave catalogue by The LIGO Scientific Collaboration & the Virgo Collaboration (2018), which reveals roughly equal mass BH-BH binary system progenitors, we find that our predicted evolution for Mk34 produces a system with components comparable to that of the gravitational wave source GW170729. We therefore conclude that the ultimate fate of Mk34 could be a black hole merger event, albeit in the far distant future, due to the large separation between these stars.

5.7 Conclusion

Using a combination of VLT/UVES and Gemini/GMOS spectroscopic monitoring we confirm Mk34 is an SB2 binary system, with closer inspection revealing both stars are of WN5h spectral type. Radial-velocity measurements of the N IV 4058 and N V 4945 emission lines reveal a 154.5 day period, eccentric system (e = 0.68 ± 0.02) with a mass ratio of q = 0.92±0.07 as shown in solution UG1. Minimum masses of $M_A \sin^3(i) = 65 \pm 7\ M_\odot$ and $M_B \sin^3(i) = 60 \pm 7\ M_\odot$ were derived for star A and star B respectively. Solution U2 used automated template fitting to the N IV 4058 and N V 4945 emission lines, which produces similar results. Using an average from both emission lines we find a 155.11 day period, an eccentricity of 0.758 ± 0.006 and a mass ratio of 1.08 ± 0.02, which gives minimum masses of $M_A \sin^3(i) = 39 \pm 2\ M_\odot$ and $M_B \sin^3(i) = 42 \pm 3\ M_\odot$.

Spectral modelling using the template spectrum of VFTS 682 unveiled spectroscopic masses of 147 ± 22 $M_\odot$ and 136 ± 20 $M_\odot$ for star A and B respectively. Evolutionary modelling predicted slightly lower mass estimates of $139^{+21}_{-18}\ M_\odot$ and $127^{+17}_{-17}\ M_\odot$ for star A and star B respectively. For consistent dynamical and spectroscopic masses, the inclination of the system would need to be ∼50°, which is currently being investigated through X-ray light curve modelling (Russell et al. in prep).

Overall, Mk34 is an valuable addition to the CWB catalogue, with a high eccentricity producing significant wind variations and reasonable period length allowing detailed monitoring across the full orbit. The predicted masses suggest Mk34 is the highest mass binary system known, and further investigation into the inclination is worthwhile to verify this. Based on an initial rotational velocity of 250 km s^{-1}it is unlikely that in the future these stars will fill their Roche lobes and undergo mass transfer. Both components are, however, likely to evolve through to stellar mass black holes and therefore, should the binary survive, Mk34 will become a double stellar-mass black hole binary and a potential LIGO BH-BH source.

Chapter 6

Summary & Future Work

6.1 Summary

Throughout this work we have investigated the properties of WR stars located within metal-poor Local Group galaxies. In Chapter 2 we aimed to compile a complete survey of the WR population within IC10 from Gemini/GMOS imaging and spectroscopy such that we could investigate these stars at low metallicity.

Our searches were successful, unveiling 3 new confirmed WN stars and a further 7 likely WR candidates. Spectroscopic confirmation is still necessary for these 7 candidates, however upon completion we would consider the IC10 WR survey complete as discussed in Section 2.5.1.

With a nearly complete sample to hand we were able to address one of the main peculiarities regarding IC10, its anomalous WC/WN ratio. Figure 6.1 is an update from Figure 1.18 with the new WC/WN ratio values from Chapter 2 included. We can see here the transition of the IC10 WC/WN ratio to a lower value of 1.0±0.4, found from our work in Chapter 2, as well as the slight shift to higher metallicity also reported. We note that, should the remaining WR candidates be confirmed in the future, that ratio could fall again to 0.70±0.24. We conclude that, since we consider our thorough search of IC10 almost complete, the unusual WC/WN ratio is real and likely a consequence of the high star forming intensity observed within this galaxy.

The binary fraction with the IC10 WR stars was also estimated by searching for a number of binary signatures within the spectra. Three criteria were used; the presence of absorption features from an O star companion, unusual radial velocity shifts and dilution of the emission lines, as outlined in Section 2.4.2. With the condition that a minimum of 2/3 criteria must be satisfied, we find a rough binary fraction of 41%. This is however only a coarse estimate, and a more robust methodology is necessary to properly identify binary systems.

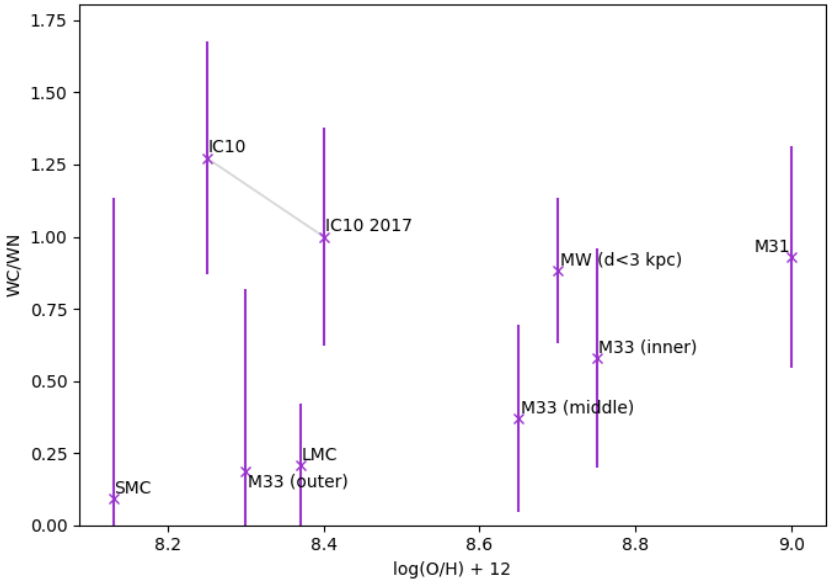

Figure 6.1: The observed WC/WN ratio and metallicity relationship for Local Group galaxies updated from Figure 1.18 to reflect recent findings in Chapter 2. As before, LMC and SMC data are from Neugent et al. (2018) and Massey et al. (2014) respectively, and all other data are from Massey & Johnson (1998).

To further investigate the incidence of binarity in metal poor WR stars, we turned to the 30 Doradus star forming region in the LMC. The Tarantula Revealed by X-rays (T-ReX) survey was a 2 Ms Chandra X-ray visionary programme focussed on producing deep X-ray observations of this region. We utilised this huge dataset and examined the WR population with a view to assessing binary status. In Chapter 3 we reported the X-ray detection of 20/21 WR sources and analysed their X-ray count rates, variability, and hardness. We performed individual 1T XSPEC fitting on all 20 detected sources, and where necessary advanced to 2T XSPEC fits to constrain both observed and corrected X-ray luminosities, in addition to plasma temperatures and stellar column density estimates.

After visual inspection of the X-ray photometry, we note the majority of WR sources reside in relative isolation from other X-ray point sources, with the exception of R136a and R140. We also found 12 out of the 20 brightest X-ray point sources in the T-ReX programme are WR sources.

Based on the X-ray properties derived in Chapter 3, we assessed the binary status of each star in Chapter 4 and, where possible, we took into consideration prior literature findings. For two sources, Mk39 and R144, we have also found complementary optical data to supplement the X-ray results and strengthen support for our binary assessment.

Overall, from X-ray data alone, we concluded that 4 systems (Mk34, R140a1/a2, Mk39,

& R136c) exhibit clear characteristics of colliding wind binary systems, resulting in a minimum binary fraction of 19%, after including R136b as a single star on the basis of its X-ray non-detection. When considering the X-ray results in tandem with the literature results and additional optical data, our assessment rose to 6 clear binaries and 8 binary candidates, giving a binary fraction range of 29% – 67%, again including R136b as a single source. Considering Sana et al. (2013b) derived an intrinsic 30 Dor O-star binary fraction of ∼50% our findings are compelling evidence that a large proportion of O star binaries survive their evolution to the WR phase.

Following our work on the complete 30 Dor WR sample, we initiated a follow-up campaign for one particular source, Mk34, which sparked interest due to its periodic 155.1 ± 0.1 day X-ray variability (Pollock et al., 2018). To confirm the binary nature and constrain the orbital parameters we obtained VLT/UVES optical data, supplemented with archival Gemini/GMOS data which is analysed in Chapter 5. We found radial velocity variations in the N IV and N V emission lines, which confirmed the SB2 status of Mk34, and used these measurements to derive a set of orbital parameters. We found a 154.55 ± 0.05 day orbit and minimum masses of $M_A \sin^3(i) = 65 \pm 7$ $M_\odot$ and $M_B \sin^3(i) = 60 \pm 7$ $M_\odot$ for star A and B respectively.

Spectroscopic modelling with CMFGEN and evolutionary modelling with BONNSAI unveiled theoretical masses of $M_{A(sp)} = 147 \pm 22$ $M_\odot$ and $M_{B(sp)} = 136 \pm 20$ $M_\odot$, and $M_{A(evo)} = 139^{+21}_{-18}$ $M_\odot$ and $M_{B(evo)} = 127^{+17}_{-17}$ $M_\odot$ respectively. To reconcile the observational and theoretical masses requires an inclination measurement of ∼50°, however an estimate of inclination has yet to be obtained. Nevertheless, should an inclination of 50° be established, these results would suggest we have uncovered the most massive binary system measured to date.

6.2 Future Work

There are numerous avenues we can investigate to continue the work undertaken here.

With regards to the work on IC10, whilst we would consider that identification of the WR population is mostly complete, spectroscopic follow-up on the 6 identified WR candidates is still outstanding. Once completed, we can provide robust measurements on spectral type ratios and binary fractions for WR stars in this metal poor galaxy. Improving the binary identification technique would also be useful, as the current method has limitations as discussed in Section 2.4.2. One option would be to obtain optical spectroscopic monitoring observations for the WR stars of IC10, however the high dust extinction towards the galaxy

could hinder the analysis. Alternatively X-ray monitoring could be used to find colliding wind binaries as performed in Chapters 3 to 4, however the high column density towards IC10 would attenuate the soft X-rays and therefore again could impede the analysis.

To complement this work we can extend our search to different galaxies. Other metal-poor galaxies in the Local Group are indeed host to WR stars, however their WR content is thought to be considerably lower, for example NGC6822 is host to 4 WN stars (Armandroff & Massey, 1991) (giving the WC/WN ratio of zero as shown in Figure 6.1) and within IC1613 resides a sole WO star (Tramper et al., 2013).

It is therefore difficult to draw conclusions from their WR populations due to the low numbers. Instead we could search for alternative metal poor galaxies undergoing star-formation located beyond the Local Group, to maximise our chance of observing a significant WR population.

X-ray monitoring is a powerful complementary technique to optical spectroscopy for identifying colliding wind binaries, as demonstrated by our search of the 30 Dor WR stars in Chapters 3 to 4. A natural extension to this work would be to progress our search to include other star-forming regions such as the Galactic cluster Westerlund 1 (Wd1). Its relatively close proximity and high WR content (24 currently confirmed by Crowther et al. (2006)) makes Wd1 an attractive location for a colliding wind binary search, however there is a high column density towards this cluster which will introduce complications during the analysis.

Building on the T-ReX analysis and discussion, it would be useful to constrain orbital periods for the WR stars which exhibit X-ray variability, in particular the 3 remaining WR stars exhibiting high L_{Xc}/L_{bol} ratios; R140a, R136c, and Mk39. As a first approach, we could use phase dispersed minimisation to find potential orbital periods, similar to that outlined in Pollock et al. (2018) which was completed for Mk34. Once potential orbital periods are identified we can constrain them further using targeted optical follow up. Archival VFTS data has allowed us to begin this process for Mk39, as discussed in Section 4.2.6, however this system would still benefit for further optical data to confirm our reported 640 day period, and reduce the associated uncertainty.

In addition to these sources, we also identified R145 and R144 as likely binary systems. R145 has already been investigated in detail by Shenar et al. (2017), however the orbit of R144 remains uncertain. Future optical follow up on R144 to confirm the orbital period suggested in Chapter 4 would therefore be beneficial.

If these follow-up campaigns were successful, we could used the derived orbital properties to help constrain stellar masses for these WR stars. As discussed in Section 5.1, contributing

to the number of directly measured massive stellar masses is crucial for testing theoretical models in this unknown regime.

Within this work the X-ray point sources were extracted through an automated process, but it could also be beneficial to manually process the data for a select few sources. The non-detection of R136b is interesting, especially given its detection in Townsley et al. (2006b). It would, therefore, be useful to test whether this absence of R136b is real. Also, the close proximity of R140a1/a2 and R140b could mean that these systems may benefit from an alternative extraction technique to ensure contamination from either source is minimized. It may also be possible to apply a similar technique to to R136a1/a2 to separate the WR sources here too.

The T-ReX survey catalogues over 4000 X-ray point sources, and whilst we focussed on the WR population, there is also a wealth of other stellar types, including other early-type sources listed in Table C.1. Similar to the analysis outlined in Chapter 3, it would be beneficial to perform a comparable analysis of the OB star population to complement the WR dataset.

Bibliography

Armandroff T. E., Massey P., 1985, ApJ, 291, 685

Armandroff T. E., Massey P., 1991, AJ, 102, 927

Arnaud K. A., 1996, in Jacoby G. H., Barnes J., eds, ASPC Vol. 101, Astronomical Data Analysis Software and Systems V. p. 17

Asplund M., Grevesse N., Sauval A. J., Scott P., 2009, ARA&A, 47, 481

Azzopardi M., Breysacher J., 1979, A&A, 75, 120

Banerjee S., Kroupa P., Oh S., 2012, MNRAS, 426, 1416

Bartzakos P., Moffat A. F. J., Niemela V. S., 2001, MNRAS, 324, 18

Beasor E. R., Davies B., 2018, MNRAS, 475, 55

Belczynski K., Holz D. E., Bulik T., O'Shaughnessy R., 2016, Nature, 534, 512

Berghoefer T. W., Schmitt J. H. M. M., Danner R., Cassinelli J. P., 1997, A&A, 322, 167

Bestenlehner J. M., et al., 2011, A&A, 530, L14

Bestenlehner J. M., et al., 2014, A&A, 570, A38

Bonanos A. Z., et al., 2004, ApJL, 611, L33

Breysacher J., Azzopardi M., Testor G., 1999, A&AS, 137, 117

Broos P. S., Townsley L. K., Feigelson E. D., Getman K. V., Bauer F. E., Garmire G. P., 2010, ApJ, 714, 1582

Broos P. S., et al., 2011, ApJS, 194, 2

Brott I., et al., 2011, A&A, 530, A115

Cairós L. M., Caon N., Weilbacher P. M., 2015, A&A, 577, A21

Cardelli J. A., Clayton G. C., Mathis J. S., 1989, ApJ, 345, 245

Cash W., 1979, ApJ, 228, 939

Castor J. I., Abbott D. C., Klein R. I., 1975, ApJ, 195, 157

Chambers K. C., et al., 2016, preprint, (arXiv:1612.05560)

Chené A.-N., Schnurr O., Crowther P. A., Fernández-Lajús E., Moffat A. F. J., 2011, in Neiner C., Wade G., Meynet G., Peters G., eds, IAU Symposium Vol. 272, Active OB Stars: Structure, Evolution, Mass Loss, and Critical Limits. pp 497–498, doi:10.1017/S174392131101115X

Cherepashchuk A. M., 1976, Soviet Astronomy Letters, 2, 138

Chyży K. T., Drzazga R. T., Beck R., Urbanik M., Heesen V., Bomans D. J., 2016, ApJ, 819, 39

Clark J. S., et al., 2015, A&A, 579, A131

Clark J. S., Ritchie B. W., Negueruela I., 2019, A&A, 626, A59

Cohen M., Barlow M. J., Kuhi L. V., 1975, A&A, 40, 291

Conti P. S., 1984, in Maeder A., Renzini A., eds, IAU Symposium Vol. 105, Observational Tests of the Stellar Evolution Theory. p. 233

Conti P. S., 1991, ApJ, 377, 115

Conti P. S., Massey P., 1989, ApJ, 337, 251

Corcoran M. F., Pollock A. M. T., Hamaguchi K., Russell C., 2011, arXiv e-prints, p. arXiv:1101.1422

Crowther P. A., 2007, ARA&A, 45, 177

Crowther P. A., Bibby J. L., 2009, A&A, 499, 455

Crowther P. A., Hadfield L. J., 2006, A&A, 449, 711

Crowther P. A., Walborn N. R., 2011, MNRAS, 416, 1311

Crowther P. A., Smith L. J., Hillier D. J., Schmutz W., 1995, A&A, 293, 427

Crowther P. A., De Marco O., Barlow M. J., 1998, MNRAS, 296, 367

Crowther P. A., Dessart L., Hillier D. J., Abbott J. B., Fullerton A. W., 2002, A&A, 392, 653

Crowther P. A., Drissen L., Abbott J. B., Royer P., Smartt S. J., 2003, A&A, 404, 483

Crowther P. A., Hadfield L. J., Clark J. S., Negueruela I., Vacca W. D., 2006, MNRAS, 372, 1407

Crowther P. A., Schnurr O., Hirschi R., Yusof N., Parker R. J., Goodwin S. P., Kassim H. A., 2010, MNRAS, 408, 731

Crowther P. A., Hirschi R., Walborn N. R., Yusof N., 2012, in Drissen L., Robert C., St-Louis N., Moffat A. F. J., eds, ASPC Vol. 465, Proceedings of a Scientific Meeting in Honor of Anthony F. J. Moffat. p. 196 (arXiv:1209.6157)

Crowther P. A., et al., 2016, MNRAS, 458, 624

Dale J. E., Ercolano B., Bonnell I. A., 2012, MNRAS, 427, 2852

Dale J. E., Ercolano B., Bonnell I. A., 2013, MNRAS, 431, 1062

De Marchi G., Panagia N., 2014, MNRAS, 445, 93

De Marchi G., et al., 2011, ApJ, 739, 27

De Marco O., Schmutz W., Crowther P. A., Hillier D. J., Dessart L., de Koter A., Schweickhardt J., 2000, A&A, 358, 187

Dessart L., Crowther P. A., Hillier D. J., Willis A. J., Morris P. W., van der Hucht K. A., 2000, MNRAS, 315, 407

Doran E. I., et al., 2013, A&A, 558, A134

Dougherty S. M., Beasley A. J., Claussen M. J., Zauderer B. A., Bolingbroke N. J., 2005, ApJ, 623, 447

Drissen L., Moffat A. F. J., Walborn N. R., Shara M. M., 1995, AJ, 110, 2235

Eenens P. R. J., Williams P. M., 1994, MNRAS, 269, 1082

Eggleton P., 2006, Evolutionary Processes in Binary and Multiple Stars. Cambridge Astrophysics, Cambridge University Press, doi:10.1017/CBO9780511536205

Eldridge J. J., Stanway E. R., 2016, MNRAS, 462, 3302

Esteban C., García-Rojas J., Pérez-Mesa V., 2015, MNRAS, 452, 1553

Evans C. J., et al., 2011, A&A, 530, A108

Fahed R., et al., 2011, MNRAS, 418, 2

Feast M. W., Thackeray A. D., Wesselink A. J., 1960, MNRAS, 121, 337

Feldmeier A., Puls J., Pauldrach A. W. A., 1997, A&A, 322, 878

Figer D. F., 2005, Nature, 434, 192

Filippenko A. V., 1997, ARAA, 35, 309

Fitzpatrick E. L., Savage B. D., 1984, ApJ, 279, 578

Foellmi C., Moffat A. F. J., Guerrero M. A., 2003a, MNRAS, 338, 360

Foellmi C., Moffat A. F. J., Guerrero M. A., 2003b, MNRAS, 338, 1025

Freudling W., Romaniello M., Bramich D. M., Ballester P., Forchi V., García-Dabló C. E., Moehler S., Neeser M. J., 2013, A&A, 559, A96

Fukui Y., et al., 2018, ApJ, 859, 166

Galama T. J., et al., 1998, Nature, 395, 670

Gamen R., et al., 2006, A&A, 460, 777

García-Lorenzo B., Cairós L. M., Caon N., Monreal-Ibero A., Kehrig C., 2008, ApJ, 677, 201

Garnett D. R., 1990, ApJ, 363, 142

Georgy C., Ekström S., Meynet G., Massey P., Levesque E. M., Hirschi R., Eggenberger P., Maeder A., 2012, A&A, 542, A29

Georgy C., Ekström S., Hirschi R., Meynet G., Groh J. H., Eggenberger P., 2015, in Wolf-Rayet Stars: Proceedings of an International Workshop held in Potsdam. pp 229–232 (arXiv:1508.04650)

Gieles M., 2009, MNRAS, 394, 2113

Gonçalves D. R., Teodorescu A. M., Alves-Brito A., Méndez R. H., Magrini L., 2012, MNRAS, 425, 2557

González Delgado R. M., Leitherer C., Heckman T. M., 1999, ApJS, 125, 489

Goodwin S. P., Kroupa P., Goodman A., Burkert A., 2007, Protostars and Planets V, pp 133–147

Götberg Y., de Mink S. E., Groh J. H., Kupfer T., Crowther P. A., Zapartas E., Renzo M., 2018, A&A, 615, A78

Gräfener G., Koesterke L., Hamann W.-R., 2002, A&A, 387, 244

Gräfener G., Vink J. S., de Koter A., Langer N., 2011, A&A, 535, A56

Gregory P. C., Scott W. K., Douglas K., Condon J. J., 1996, ApJS, 103, 427

Hadfield L. J., van Dyk S. D., Morris P. W., Smith J. D., Marston A. P., Peterson D. E., 2007, MNRAS, 376, 248

Hainich R., et al., 2014, A&A, 565, A27

Hamann W.-R., Gräfener G., 2003, A&A, 410, 993

Hamann W.-R., Gräfener G., Liermann A., 2006, A&A, 457, 1015

Hamann W. R., et al., 2019, A&A, 625, A57

Hénault-Brunet V., et al., 2012, A&A, 546, A73

Herbig G. H., 1995, ARA&A, 33, 19

Herwig F., Blöcker T., Langer N., Driebe T., 1999, A&A, 349, L5

Hillier D. J., 1991, A&A, 247, 455

Hillier D. J., Miller D. L., 1998, ApJ, 496, 407

Hjorth J., et al., 2003, Nature, 423, 847

Hodge P., Lee M. G., 1990, PASP, 102, 26

Homeier N. L., Blum R. D., Conti P. S., Damineli A., 2003, A&A, 397, 585

Hook I. M., Jørgensen I., Allington-Smith J. R., Davies R. L., Metcalfe N., Murowinski R. G., Crampton D., 2004, PASP, 116, 425

Huchra J. P., Vogeley M. S., Geller M. J., 1999, ApJS, 121, 287

Humphreys R. M., Davidson K., 1994, PASP, 106, 1025

Hunter D. A., Shaya E. J., Holtzman J. A., Light R. M., O'Neil Earl J. J., Lynds R., 1995, ApJ, 448, 179

Iben Icko J., Livio M., 1993, PASP, 105, 1373

Janka H.-T., 2017, Neutrino-Driven Explosions. p. 1095, doi:10.1007/978-3-319-21846-5˙109

Kennicutt R. C. J., 1984, ApJ, 287, 116

Kennicutt Jr. R. C., 1988, ApJ, 334, 144

Kennicutt Jr. R. C., 1998, ApJ, 498, 541

Kennicutt Jr. R. C., Bresolin F., Bomans D. J., Bothun G. D., Thompson I. B., 1995, AJ, 109, 594

Kennicutt Jr. R. C., Lee J. C., Funes J. G., J. S., Sakai S., Akiyama S., 2008, ApJS, 178, 247

Kochanek C. S., et al., 2017, PASP, 129, 104502

Koenigsberger G., Morrell N., Hillier D. J., Gamen R., Schneider F. R. N., González-Jiménez N., Langer N., Barbá R., 2014, AJ, 148, 62

Köhler K., et al., 2015, A&A, 573, A71

Koornneef J., 1982, A&A, 107, 247

Kraus S., et al., 2009, A&A, 497, 195

Kroupa P., 2001, MNRAS, 322, 231

Kruckow M. U., Tauris T. M., Langer N., Kramer M., Izzard R. G., 2018, MNRAS, 481, 1908

Lada C. J., Lada E. A., 2003, ARAA, 41, 57

Lamers H. J. G. L. M., Cassinelli J. P., 1999, Introduction to Stellar Winds

Lamers H. J. G. L. M., Levesque E. M., 2017, Understanding Stellar Evolution, doi:10.1088/978-0-7503-1278-3.

Lamers H. J. G. L. M., Maeder A., Schmutz W., Cassinelli J. P., 1991, ApJ, 368, 538

Langer N., 1989, A&A, 210, 93

Lebouteiller V., Bernard-Salas J., Brandl B., Whelan D. G., Wu Y., Charmandaris V., Devost D., Houck J. R., 2008, ApJ, 680, 398

Leitherer C., et al., 1999, ApJS, 123, 3

Lequeux J., Peimbert M., Rayo J. F., Serrano A., Torres-Peimbert S., 1979, A&A, 80, 155

Levesque E. M., 2010, in Leitherer C., Bennett P. D., Morris P. W., Van Loon J. T., eds, ASPC Vol. 425, Hot and Cool: Bridging Gaps in Massive Star Evolution. p. 103 (arXiv:0911.4720)

Lohr M. E., Clark J. S., Najarro F., Patrick L. R., Crowther P. A., Evans C. J., 2018, preprint, (arXiv:1804.05607)

Lucy L. B., 1982, ApJ, 255, 286

Lucy L. B., Solomon P. M., 1970, ApJ, 159, 879

Lucy L. B., White R. L., 1980, ApJ, 241, 300

MacFadyen A. I., Woosley S. E., 1999, ApJ, 524, 262

Maeder A., 1991, A&A, 242, 93

Maíz Apellániz J., et al., 2014, A&A, 564, A63

Marchenko S. V., et al., 2003, ApJ, 596, 1295

Maschberger T., 2013, MNRAS, 429, 1725

Massey P., Armandroff T., 1995, AJ, 109, 2470

Massey P., Holmes S., 2002, ApJL, 580, L35

Massey P., Hunter D. A., 1998, ApJ, 493, 180

Massey P., Johnson O., 1998, ApJ, 505, 793

Massey P., Armandroff T. E., Conti P. S., 1992, AJ, 103, 1159

Massey P., Penny L. R., Vukovich J., 2002, ApJ, 565, 982

Massey P., Puls J., Pauldrach A. W. A., Bresolin F., Kudritzki R. P., Simon T., 2005, ApJ, 627, 477

Massey P., Neugent K. F., Morrell N., Hillier D. J., 2014, ApJ, 788, 83

Massey P., Neugent K. F., Morrell N. I., 2015a, in Hamann W.-R., Sander A., Todt H., eds, Wolf-Rayet Stars: Proceedings of an International Workshop held in Potsdam, Germany, 1–5 June 2015. Edited by Wolf-Rainer Hamann, Andreas Sander, Helge Todt. Universitätsverlag Potsdam, 2015., p.35-42. pp 35–42 (arXiv:1507.07297)

Massey P., Neugent K. F., Morrell N., 2015b, ApJ, 807, 81

Mauron N., Josselin E., 2011, A&A, 526, A156

McConnachie A. W., 2012, AJ, 144, 4

Melnick J., 1985, A&A, 153, 235

Meynet G., Maeder A., 2005, A&A, 429, 581

Moffat A. F. J., 1983, A&A, 124, 273

Moffat A. F. J., 1989, ApJ, 347, 373

Moffat A. F. J., Niemela V. S., 1984, ApJ, 284, 631

Moffat A. F. J., Seggewiss W., 1986, ApJ, 309, 714

Moffat A. F. J., Niemela V. S., Phillips M. M., Chu Y.-H., Seggewiss W., 1987, ApJ, 312, 612

Mokiem M. R., et al., 2007, A&A, 473, 603

Morgan W. W., Keenan P. C., Kellman E., 1943, An atlas of stellar spectra, with an outline of spectral classification

Muench A., Getman K., Hillenbrand L., Preibisch T., 2008, Star Formation in the Orion Nebula I: Stellar Content. p. 483

Najarro F., Geballe T. R., Figer D. F., de la Fuente D., 2017, ApJ, 845, 127

Nazé Y., et al., 2011, ApJS, 194, 7

Neugent K., Massey P., 2019, Galaxies, 7, 74

Neugent K. F., Massey P., Morrell N., 2012a, AJ, 144, 162

Neugent K. F., Massey P., Georgy C., 2012b, ApJ, 759, 11

Neugent K. F., Massey P., Hillier D. J., Morrell N., 2017, ApJ, 841, 20

Neugent K. F., Massey P., Morrell N., 2018, ApJ, 863, 181

North J. R., Tuthill P. G., Tango W. J., Davis J., 2007, MNRAS, 377, 415

Nugis T., Lamers H. J. G. L. M., 2000, A&A, 360, 227

O'Connor E., Ott C. D., 2011, ApJ, 730, 70

O'Connor E., Ott C. D., 2013, ApJ, 762, 126

Oey M. S., Clarke C. J., 2005, ApJL, 620, L43

Osterbrock D. E., 1989, Astrophysics of gaseous nebulae and active galactic nuclei

Osterbrock D. E., Ferland G. J., 2006, Astrophysics of gaseous nebulae and active galactic nuclei

Owocki S. P., Castor J. I., Rybicki G. B., 1988, ApJ, 335, 914

Paczyński B., 1967, AcA, 17, 355

Paczyński B., 1971, ARA&A, 9, 183

Pallavicini R., Golub L., Rosner R., Vaiana G. S., Ayres T., Linsky J. L., 1981, ApJ, 248, 279

Panagia N., Felli M., 1975, A&A, 39, 1

Parker J. W., 1993, AJ, 106, 560

Parker R. J., Goodwin S. P., 2007, MNRAS, 380, 1271

Pettini M., Pagel B. E. J., 2004, MNRAS, 348, L59

Pietrzyński G., et al., 2013, Nature, 495, 76

Pittard J. M., Dougherty S. M., 2006, MNRAS, 372, 801

Plucinsky P. P., Bogdan A., Marshall H. L., Tice N. W., 2018, in Space Telescopes and Instrumentation 2018: Ultraviolet to Gamma Ray. p. 106996B (arXiv:1809.02225), doi:10.1117/12.2312748

Podsiadlowski P., 2001, in Podsiadlowski P., Rappaport S., King A. R., D'Antona F., Burderi L., eds, ASPC Vol. 229, Evolution of Binary and Multiple Star Systems. p. 239

Pollock A. M. T., 1987, ApJ, 320, 283

Pollock A. M. T., Corcoran M. F., 2006, A&A, 445, 1093

Pollock A. M. T., Crowther P. A., Tehrani K., Broos P. S., Townsley L. K., 2018, MNRAS, 474, 3228

Portegies Zwart S. F., Pooley D., Lewin W. H. G., 2002, ApJ, 574, 762

Portegies Zwart S. F., McMillan S. L. W., Gieles M., 2010, ARA&A, 48, 431

Postnov K. A., Yungelson L. R., 2014, LRR, 17, 3

Prestwich A. H., et al., 2007, ApJL, 669, L21

Prilutskii O. F., Usov V. V., 1976, Soviet Astronomy, 20, 2

Prinja R. K., Barlow M. J., Howarth I. D., 1990, ApJ, 361, 607

Ramirez-Agudelo O. H., et al., 2013, VizieR Online Data Catalog, pp J/A+A/560/A29

Ramírez-Agudelo O. H., et al., 2017, A&A, 600, A81

Rauw G., et al., 2004, A&A, 420, L9

Rauw G., et al., 2005, A&A, 432, 985

Rauw G., Manfroid J., Gosset E., Nazé Y., Sana H., De Becker M., Foellmi C., Moffat A. F. J., 2007, A&A, 463, 981

Richer M. G., et al., 2001, A&A, 370, 34

Rosen S. R., et al., 2016, A&A, 590, A1

Royer P., Smartt S. J., Manfroid J., Vreux J.-M., 2001, A&A, 366, L1

Russell S. C., Dopita M. A., 1990, ApJS, 74, 93

Sana H., et al., 2012, Science, 337, 444

Sana H., et al., 2013a, MNRAS, 432, L26

Sana H., et al., 2013b, A&A, 550, A107

Sander A., Shenar T., Hainich R., Gímenez-García A., Todt H., Hamann W.-R., 2015, A&A, 577, A13

Sander A. A. C., Hamann W. R., Todt H., Hainich R., Shenar T., Ramachandran V., Oskinova L. M., 2019, A&A, 621, A92

Sanna N., et al., 2008, ApJL, 688, L69

Schaerer D., Maeder A., 1992, A&A, 263, 129

Schaerer D., Vacca W. D., 1998, ApJ, 497, 618

Schlafly E. F., Finkbeiner D. P., 2011, ApJ, 737, 103

Schmutz W., et al., 1997, A&A, 328, 219

Schneider F. R. N., Langer N., de Koter A., Brott I., Izzard R. G., Lau H. H. B., 2014, A&A, 570, A66

Schneider F. R. N., et al., 2018, preprint, (arXiv:1801.03107)

Schnurr O., Moffat A. F. J., St-Louis N., Morrell N. I., Guerrero M. A., 2008, MNRAS, 389, 806

Schnurr O., Moffat A. F. J., Villar-Sbaffi A., St-Louis N., Morrell N. I., 2009a, MNRAS, 395, 823

Schnurr O., Chené A. N., Casoli J., Moffat A. F. J., St-Louis N., 2009b, MNRAS, 397, 2049

Schwartz D. A., 2014, Review of Scientific Instruments, 85, 061101

Seaton M. J., 1979, MNRAS, 187, 73

Selman F., Melnick J., Bosch G., Terlevich R., 1999, A&A, 341, 98

Seward F. D., Forman W. R., Giacconi R., Griffiths R. E., Harnden Jr. F. R., Jones C., Pye J. P., 1979, ApJL, 234, L55

Shappee B. J., et al., 2014, ApJ, 788, 48

Shara M. M., Moffat A. F. J., Smith L. F., Niemela V. S., Potter M., Lamontagne R., 1999, AJ, 118, 390

Shenar T., et al., 2016, A&A, 591, A22

Shenar T., et al., 2017, A&A, 598, A85

Shenar T., et al., 2019, arXiv e-prints, p. arXiv:1905.09296

Shi F., Kong X., Li C., Cheng F. Z., 2005, A&A, 437, 849

Sidoli F., Smith L. J., Crowther P. A., 2006, MNRAS, 370, 799

Silverman J. M., Filippenko A. V., 2008, ApJ, 678, L17

Simón-Díaz S., Herrero A., Esteban C., Najarro F., 2006, A&A, 448, 351

Skinner S., Güdel M., Schmutz W., Zhekov S., 2006, Astrophys Space Sci, 304, 97

Skinner S. L., Zhekov S. A., Güdel M., Schmutz W., Sokal K. R., 2010, AJ, 139, 825

Skrutskie M. F., et al., 2006, AJ, 131, 1163

Smartt S. J., 2009, ARA&A, 47, 63

Smartt S. J., Crowther P. A., Dufton P. L., Lennon D. J., Kudritzki R. P., Herrero A., McCarthy J. K., Bresolin F., 2001, MNRAS, 325, 257

Smith N., 2006, MNRAS, 367, 763

Smith N., 2014, ARA&A, 52, 487

Smith N., Conti P. S., 2008, ApJ, 679, 1467

Smith N., Tombleson R., 2015, MNRAS, 447, 598

Smith L. F., Shara M. M., Moffat A. F. J., 1990, ApJ, 358, 229

Smith L. F., Shara M. M., Moffat A. F. J., 1996, MNRAS, 281, 163

Smith N., Li W., Filippenko A. V., Chornock R., 2011, MNRAS, 412, 1522

Sokasian A., Yoshida N., Abel T., Hernquist L., Springel V., 2004, MNRAS, 350, 47

Southworth J., 2015, in Rucinski S. M., Torres G., Zejda M., eds, ASPC Vol. 496, Living Together: Planets, Host Stars and Binaries. p. 164

St.-Louis N., Moffat A. F. J., Lapointe L., Efimov Y. S., Shakhovskoj N. M., Fox G. K., Piirola V., 1993, ApJ, 410, 342

Stahler S. W., 2010, MNRAS, 402, 1758

Stetson P. B., 1987, PASP, 99, 191

Stevens I. R., Blondin J. M., Pollock A. M. T., 1992, ApJ, 386, 265

Sukhbold T., Woosley S. E., 2014, ApJ, 783, 10

Tan J. C., Beltrán M. T., Caselli P., Fontani F., Fuente A., Krumholz M. R., McKee C. F., Stolte A., 2014, in Beuther H., Klessen R. S., Dullemond C. P., Henning T., eds, Protostars and Planets VI. p. 149 (arXiv:1402.0919), doi:10.2458/azu˙uapress˙9780816531240-ch007

Tehrani K., Crowther P. A., Archer I., 2017, MNRAS, 472, 4618

Tehrani K. A., Crowther P. A., Bestenlehner J. M., Littlefair S. P., Pollock A. M. T., Parker R. J., Schnurr O., 2019, MNRAS, 484, 2692

The LIGO Scientific Collaboration the Virgo Collaboration 2018, preprint, (arXiv:1811.12907)

Tody D., 1986, in Crawford D. L., ed., Proc. SPIE Vol. 627, Instrumentation in astronomy VI. p. 733, doi:10.1117/12.968154

Townsley L. K., Broos P. S., Feigelson E. D., Brandl B. R., Chu Y.-H., Garmire G. P., Pavlov G. G., 2006a, AJ, 131, 2140

Townsley L. K., Broos P. S., Feigelson E. D., Garmire G. P., Getman K. V., 2006b, AJ, 131, 2164

Townsley L. K., Broos P. S., Garmire G. P., Bouwman J., Povich M. S., Feigelson E. D., Getman K. V., Kuhn M. A., 2014, ApJS, 213, 1

Tramper F., et al., 2013, A&A, 559, A72

Tramper F., Sana H., Fitzsimons N. E., de Koter A., Kaper L., Mahy L., Moffat A., 2016, MNRAS, 455, 1275

Tully R. B., et al., 2013, AJ, 146, 86

Tumlinson J., et al., 2002, ApJ, 566, 857

Vacca W. D., Conti P. S., 1992, ApJ, 401, 543

Vanbeveren D., De Loore C., Van Rensbergen W., 1998, A&ARv, 9, 63

Vink J. S., ed. 2015, Very Massive Stars in the Local Universe Astrophysics and Space Science Library Vol. 412, doi:10.1007/978-3-319-09596-7.

Vink J. S., de Koter A., 2005, A&A, 442, 587

Vuong M. H., Montmerle T., Grosso N., Feigelson E. D., Verstraete L., Ozawa H., 2003, A&A, 408, 581

Walborn N. R., 1977, ApJ, 215, 53

Walborn N. R., 1982, ApJ, 256, 452

Walborn N. R., et al., 2014, VizieR Online Data Catalog, pp J/A+A/564/A40

Weidner C., Kroupa P., 2004, MNRAS, 348, 187

Weidner C., Kroupa P., 2006, MNRAS, 365, 1333

Weigelt G., Baier G., 1985, A&A, 150, L18

Weisskopf M. C., Brinkman B., Canizares C., Garmire G., Murray S., Speybroeck L. P. V., 2002, PASP, 114, 1

Westerlund B. E., 1990, A&A Rev., 2, 29

Whitmore B. C., Zhang Q., Leitherer C., Fall S. M., Schweizer F., Miller B. W., 1999, AJ, 118, 1551

Wilcots E. M., Miller B. W., 1998, AJ, 116, 2363

Williams P., 2011, Bulletin de la Societe Royale des Sciences de Liege, 80, 595

Williams P. M., Antonopoulou E., 1981, MNRAS, 196, 915

Williams P. M., van der Hucht K. A., The P. S., 1987a, QJRAS, 28, 248

Williams P. M., van der Hucht K. A., The P. S., 1987b, A&A, 182, 91

Wolf C., Rayet G., 1867, Comptes Rendus, 65, 292

Wolter H., 1952, Annalen der Physik, 445, 94

Woosley S. E., 1993, ApJ, 405, 273

Wray J. D., Corso G. J., 1972, ApJ, 172, 577

Wright A. E., Barlow M. J., 1975, MNRAS, 170, 41

Yusof N., et al., 2013, MNRAS, 433, 1114

Zhang Q., Fall S. M., 1999, ApJ, 527, L81

de Jager C., Nieuwenhuijzen H., van der Hucht K. A., 1988, A&AS, 72, 259

de Vaucouleurs G., de Vaucouleurs A., Corwin Jr. H. G., Buta R. J., Paturel G., Fouqué P., 1991, Third Reference Catalogue of Bright Galaxies. Volume I: Explanations and references. Volume II: Data for galaxies between 0^h and 12^h. Volume III: Data for galaxies between 12^h and 24^h.. Springer-Verlag

van Loon J. T., Cioni M. R. L., Zijlstra A. A., Loup C., 2005, A&A, 438, 273

van der Hucht K. A., 2001, New A Rev, 45, 135

Appendix A

T-ReX: X-ray Variability

X-ray variability plots for the 20 WR sources detected in T-ReX, showing the variation in corrected count rate against time. The main T-ReX campaign is supplement with three additional archival X-ray observations. The dashed line indicated the mean count rate for each source, as discussed in Section 3.4.

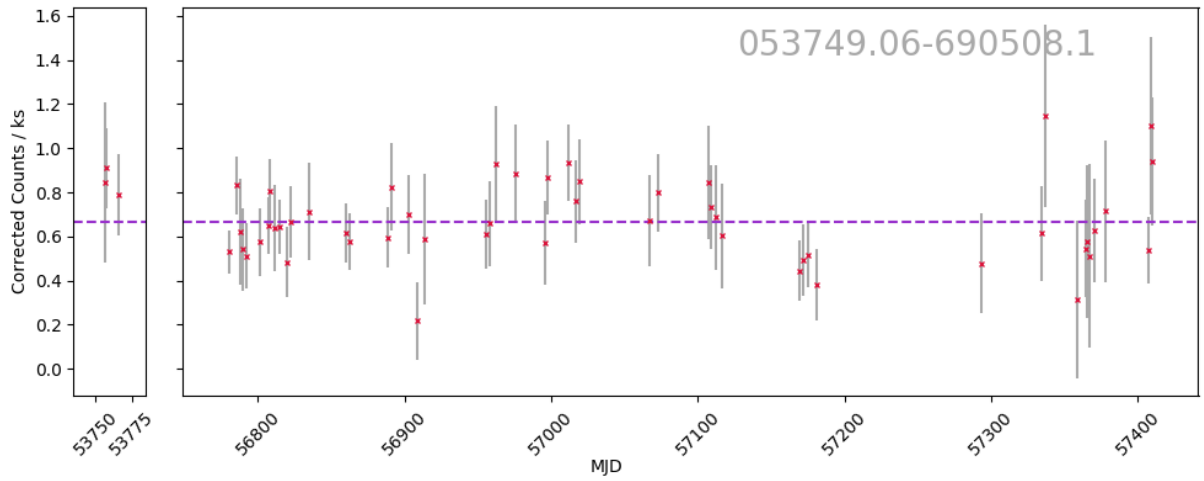

Figure A.1a: Plots of X-ray variability against time for all WR stars within the T-ReX sample.

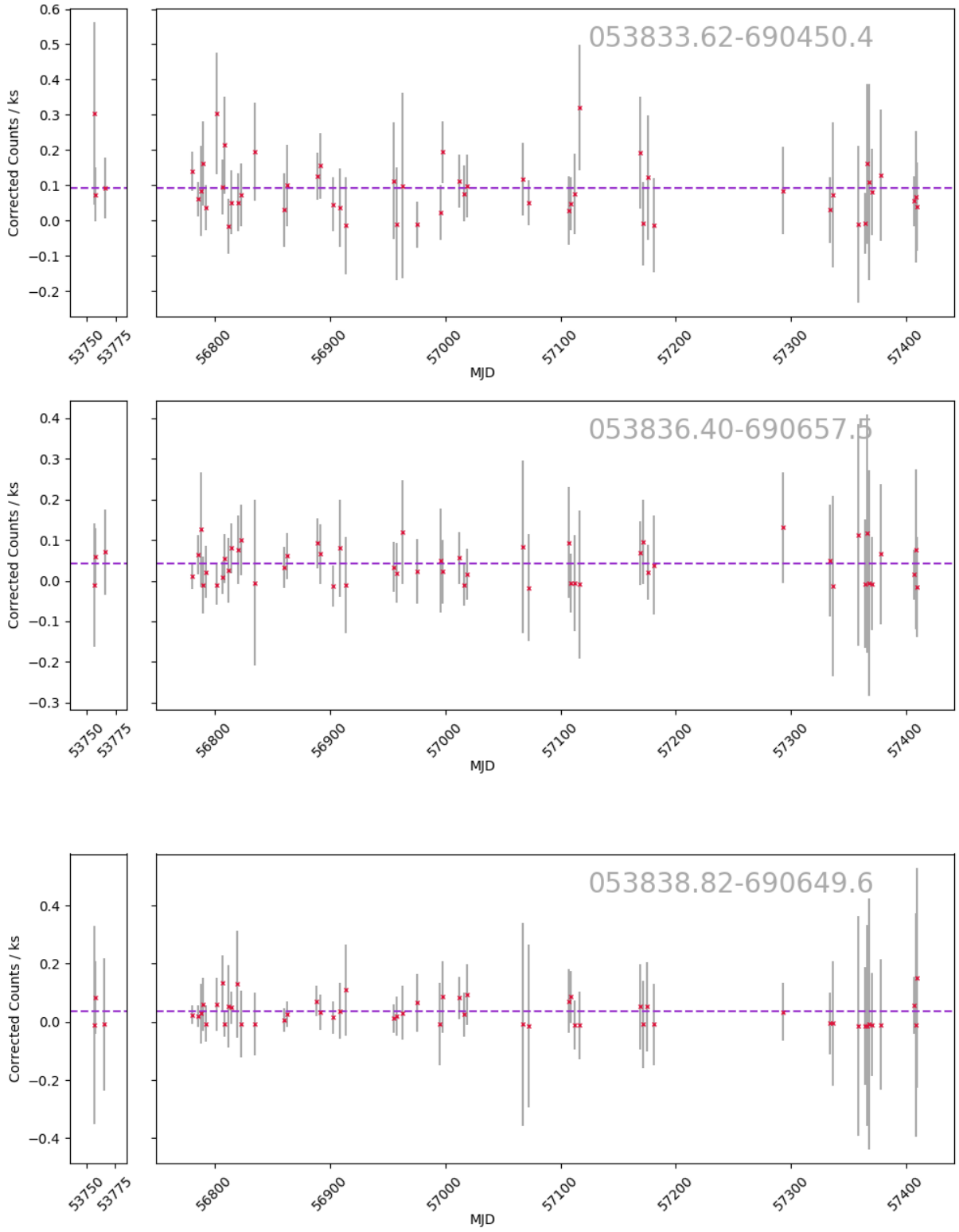

Figure A.1b: Plots of X-ray variability against time for all WR stars within the T-ReX sample.

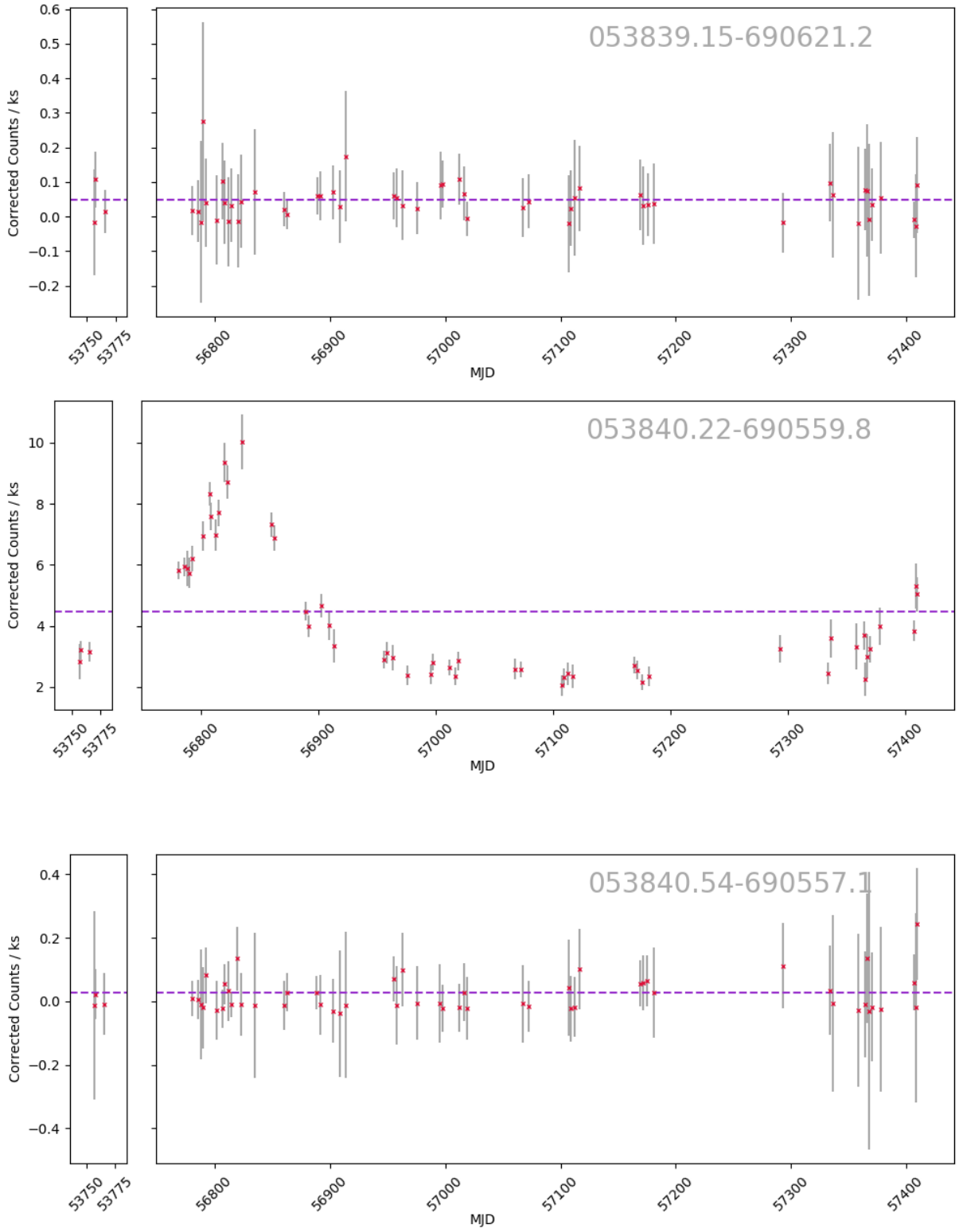

Figure A.1c: Plots of X-ray variability against time for all WR stars within the T-ReX sample.

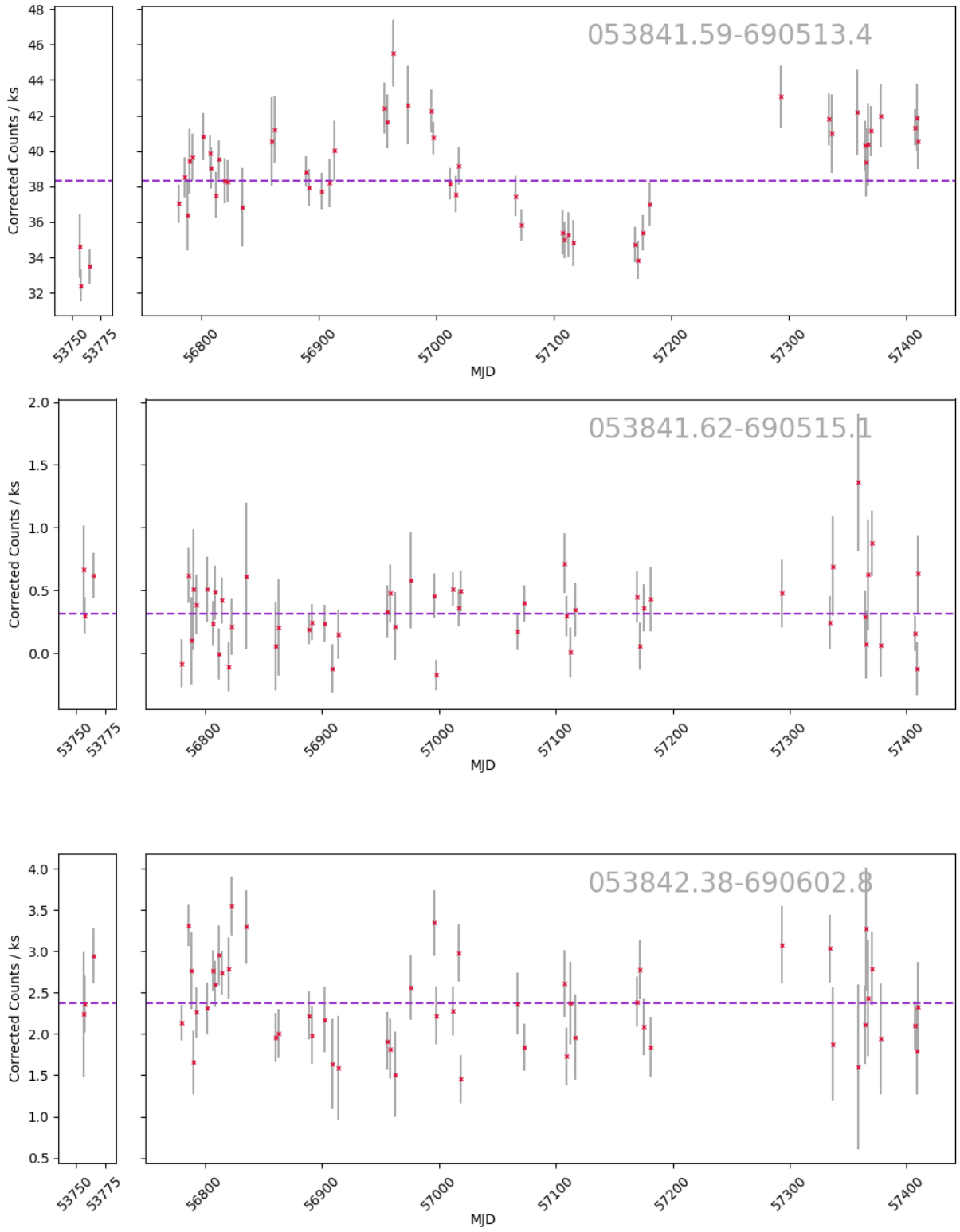

Figure A.1d: Plots of X-ray variability against time for all WR stars within the T-ReX sample.

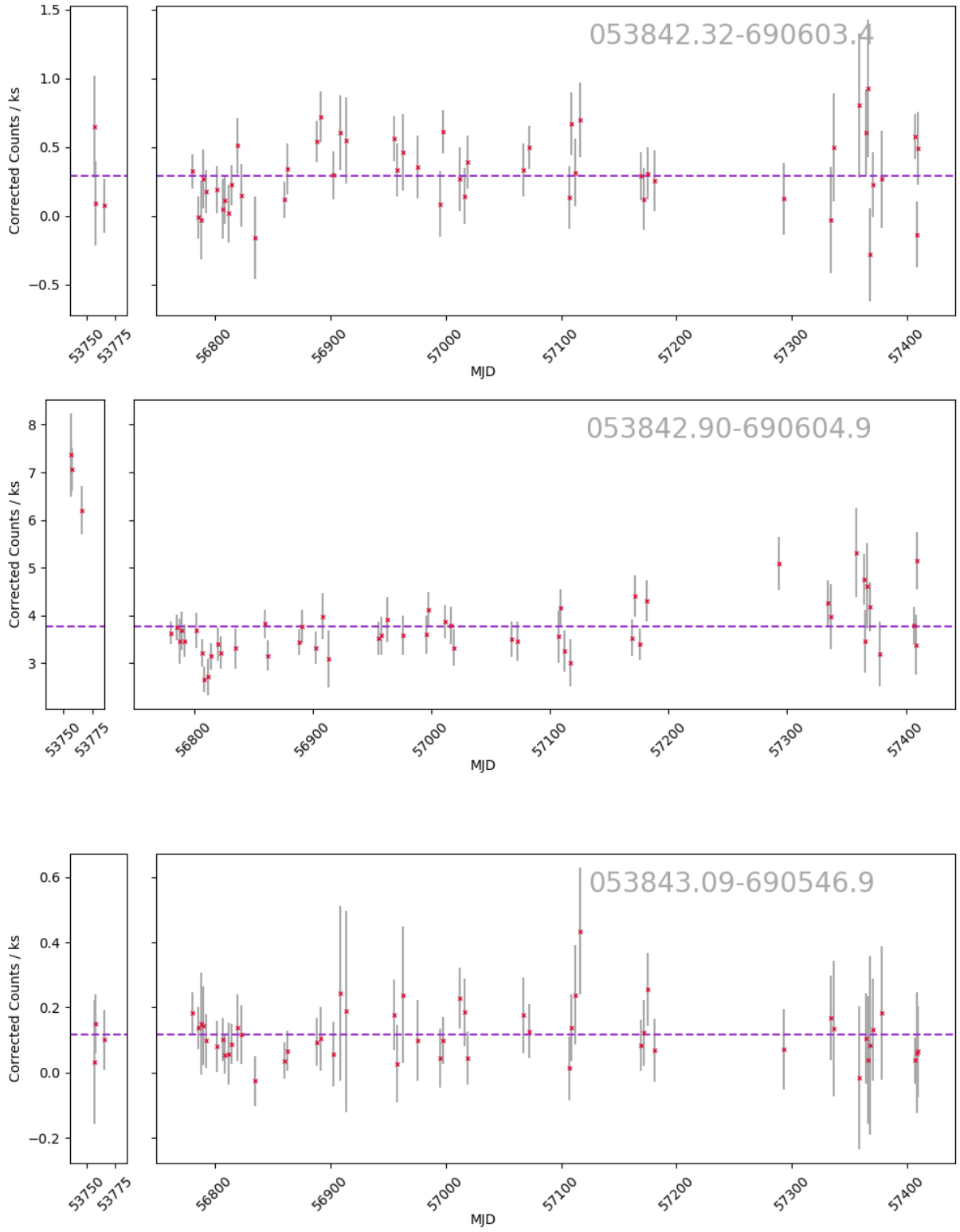

Figure A.1e: Plots of X-ray variability against time for all WR stars within the T-ReX sample.

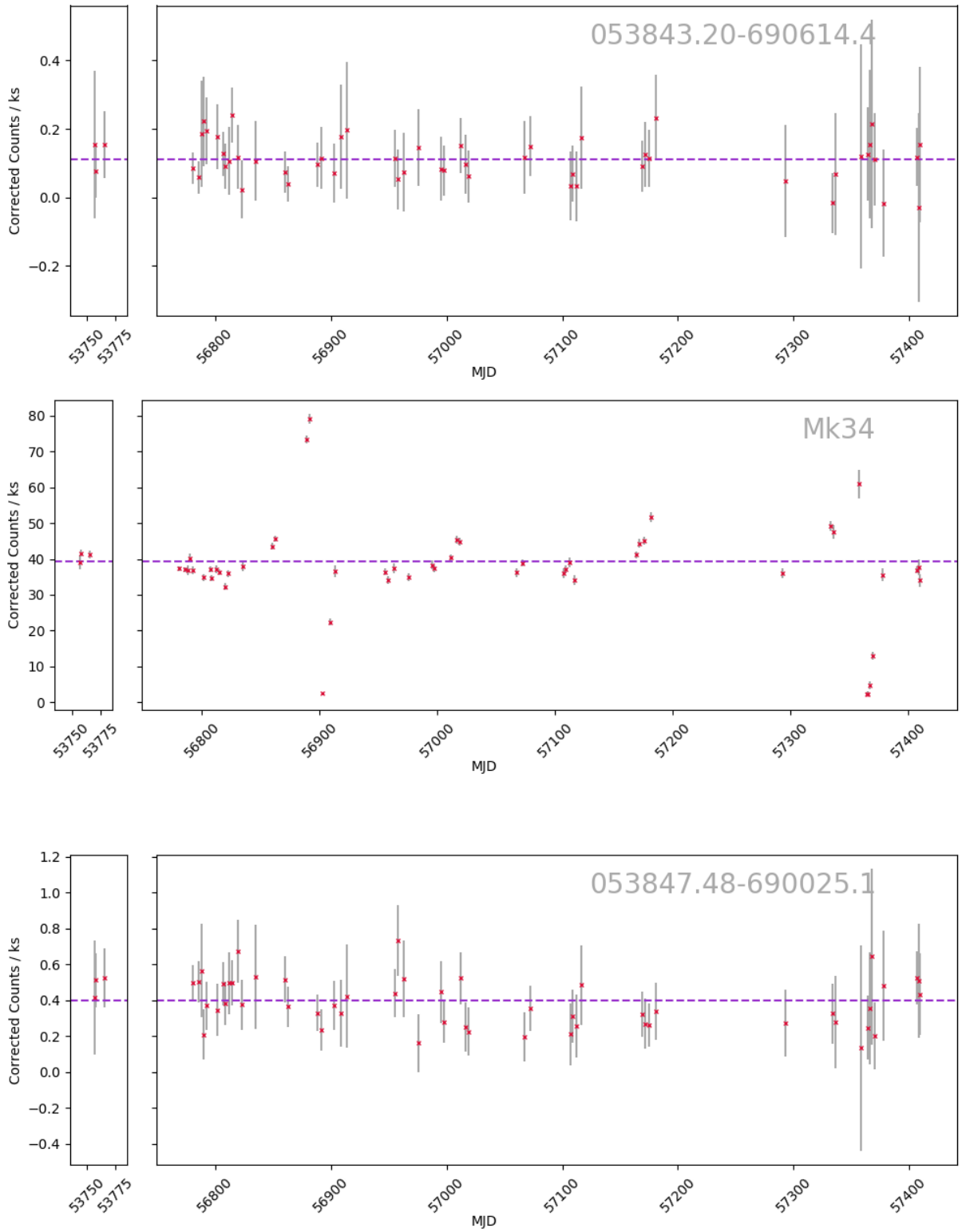

Figure A.1f: Plots of X-ray variability against time for all WR stars within the T-ReX sample.

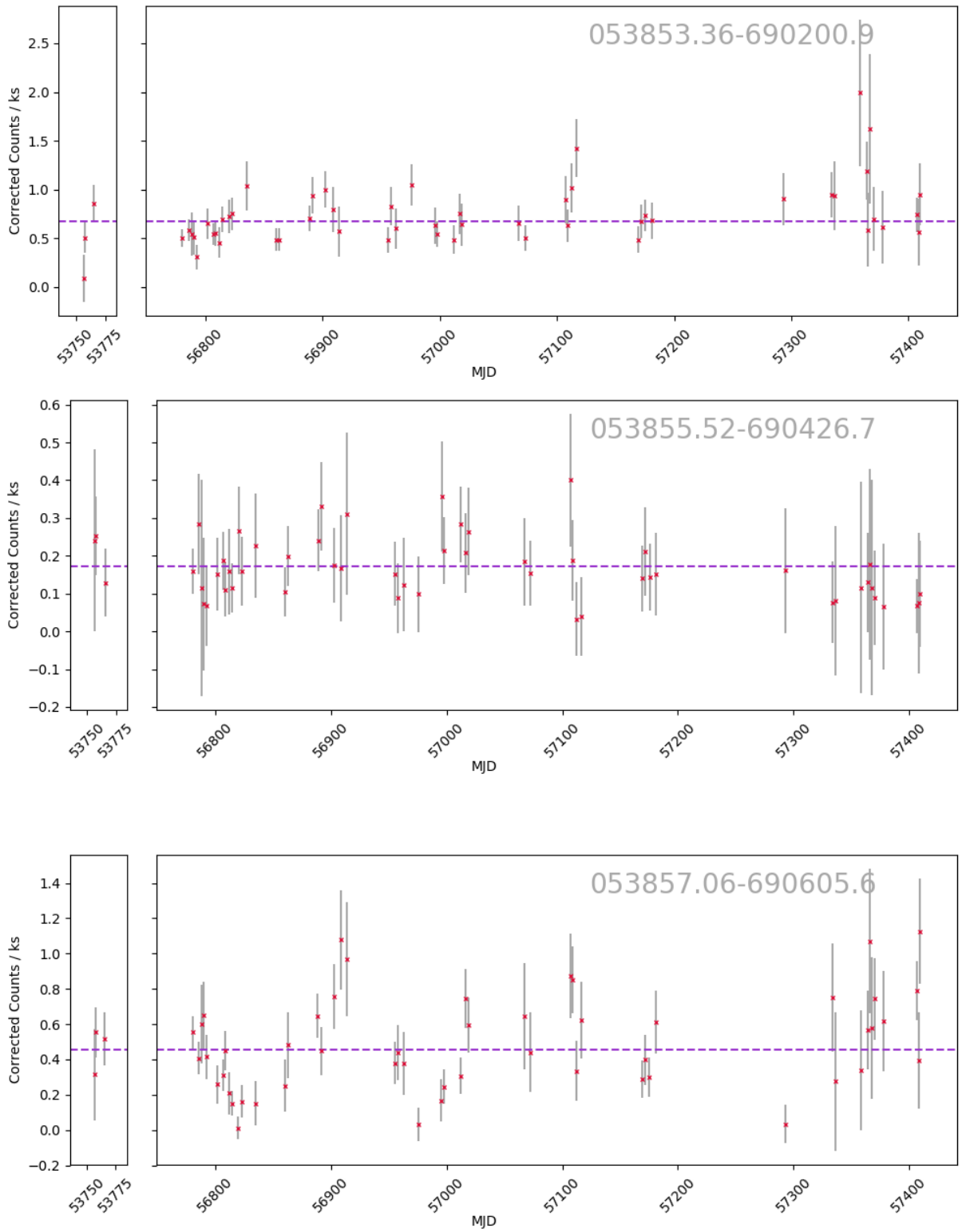

Figure A.1g: Plots of X-ray variability against time for all WR stars within the T-ReX sample.

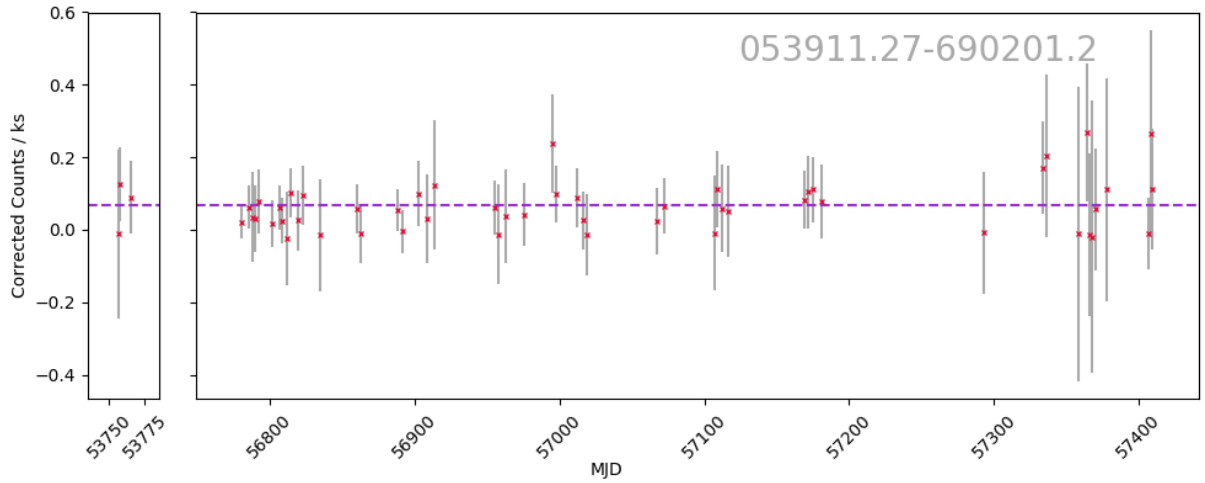

Figure A.1h: Plots of X-ray variability against time for all WR stars within the T-ReX sample.

Appendix B

T-ReX: 1T XSPEC Fitting

Single temperature plasma XSPEC fits to all 20 WR sources observed within T-ReX. The XSPEC spectral fitting process is described in Section 3.6 and the final fitting parameters are summarized in Table 3.6.

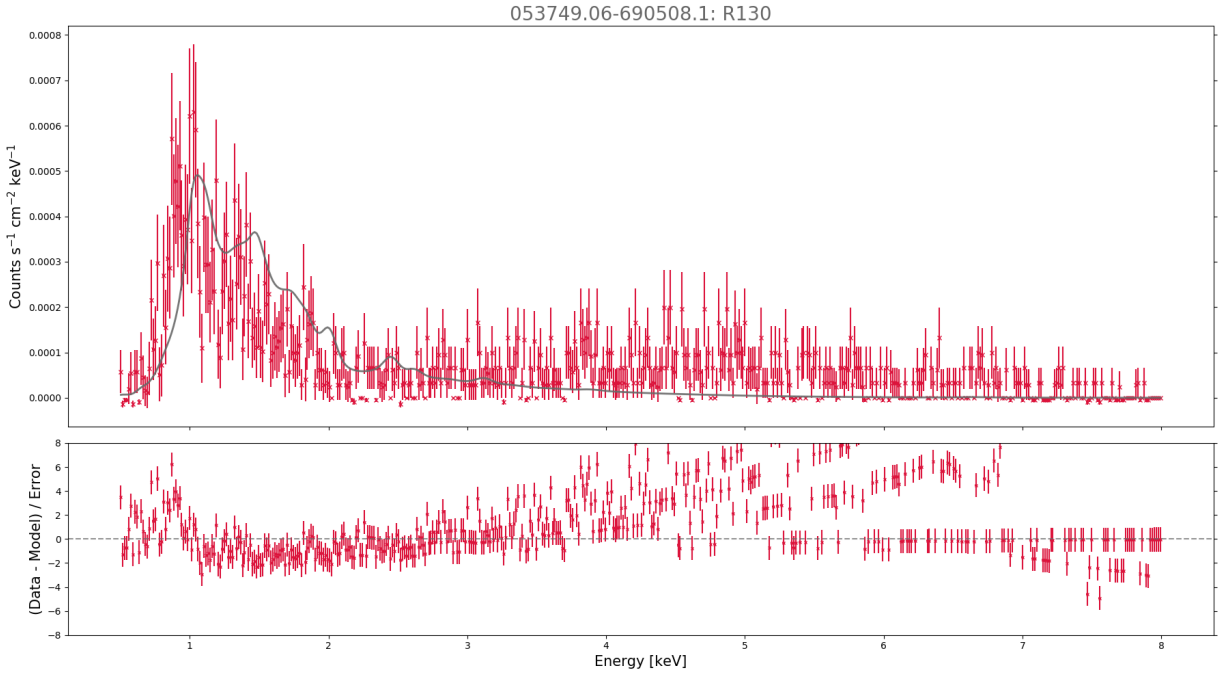

Figure B.1a: 1T plasma XSPEC fits to all WR sources in the sample. Red lines show the observed data and grey lines show the best 1T model fit. Fitting parameters are shown in Table 3.6.

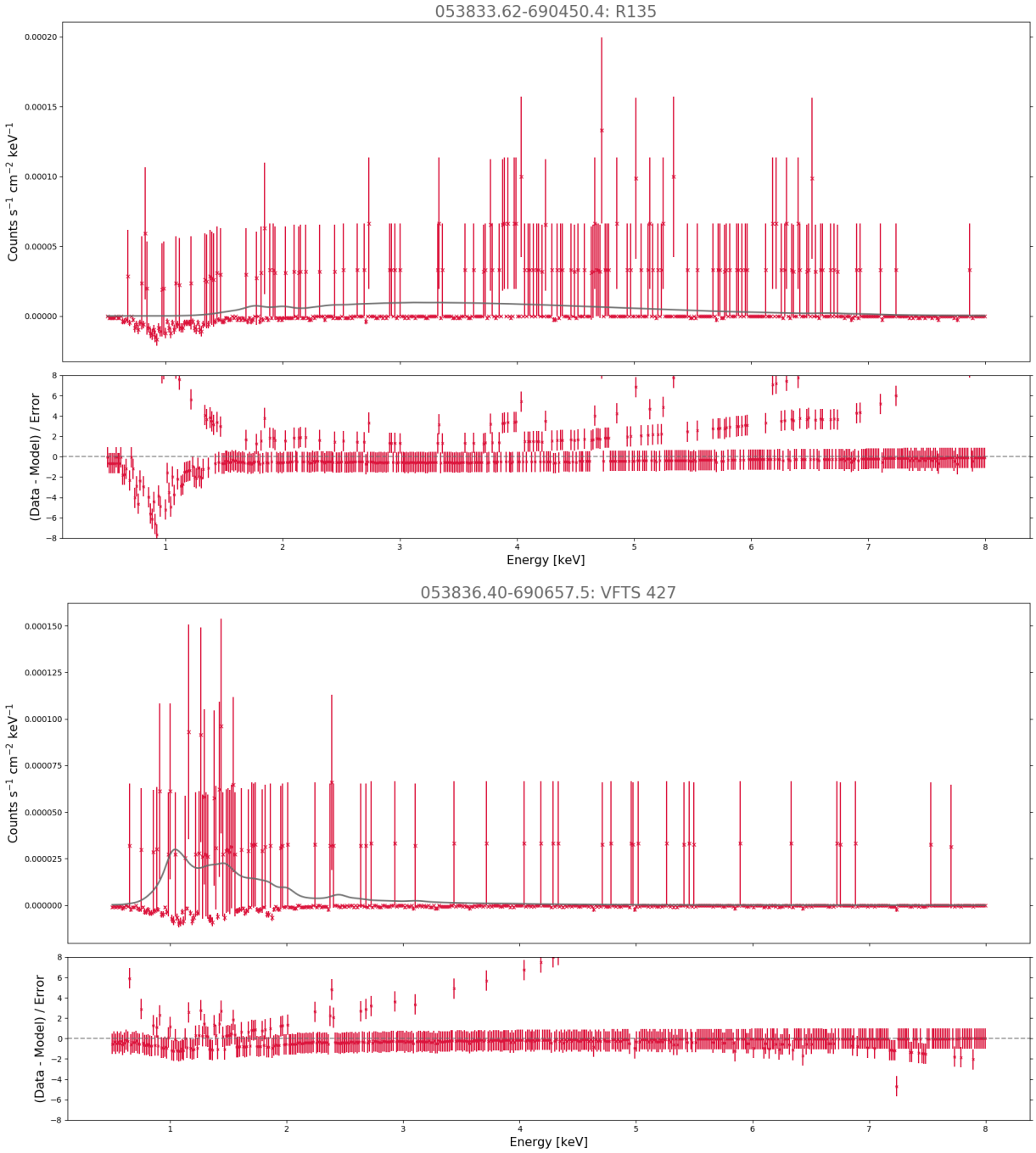

Figure B.1b: 1T plasma XSPEC fits to all WR sources in the sample. Red lines show the observed data and grey lines show the best 1T model fit. Fitting parameters are shown in Table 3.6.

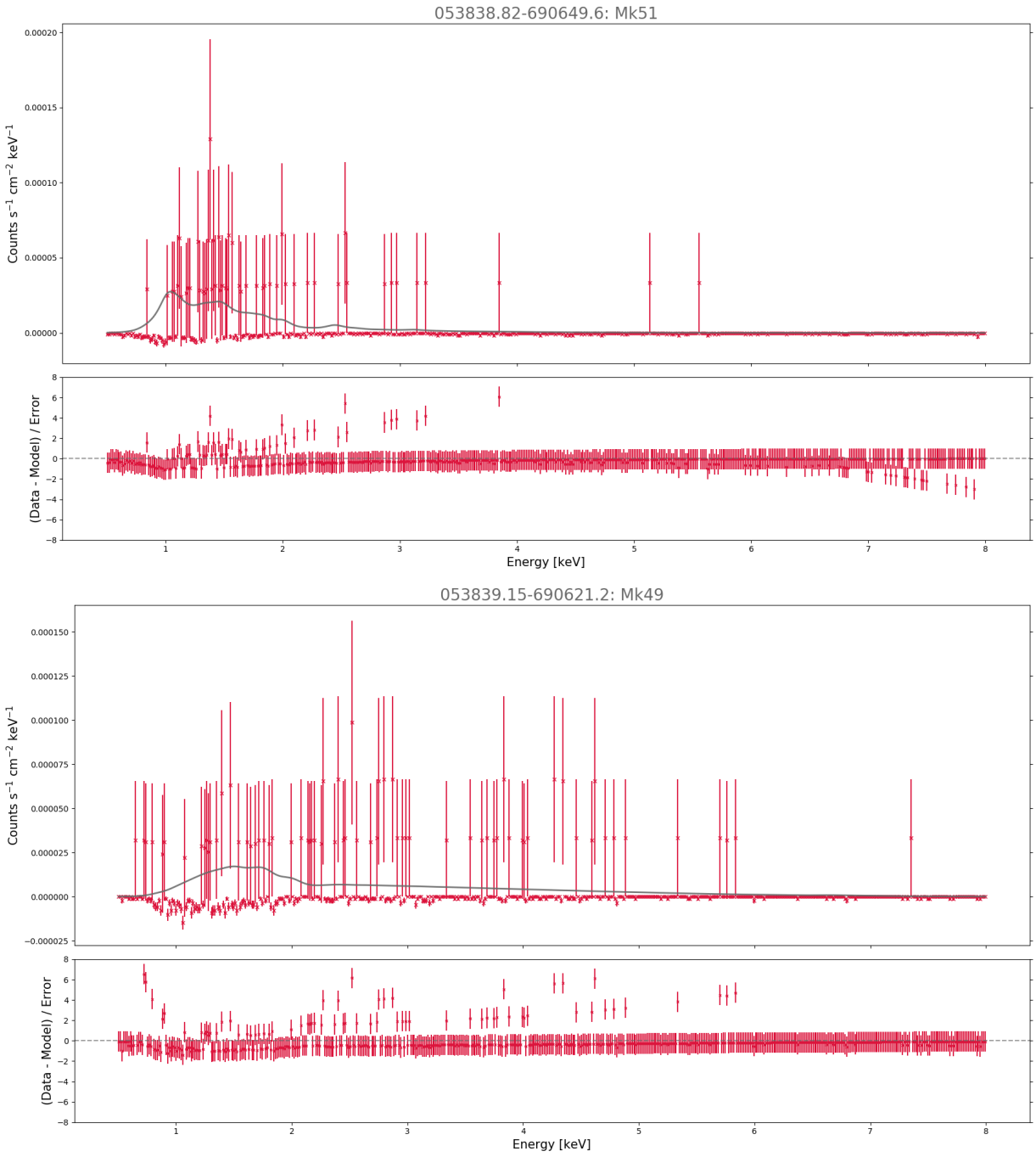

Figure B.1c: 1T plasma XSPEC fits to all WR sources in the sample. Red lines show the observed data and grey lines show the best 1T model fit. Fitting parameters are shown in Table 3.6.

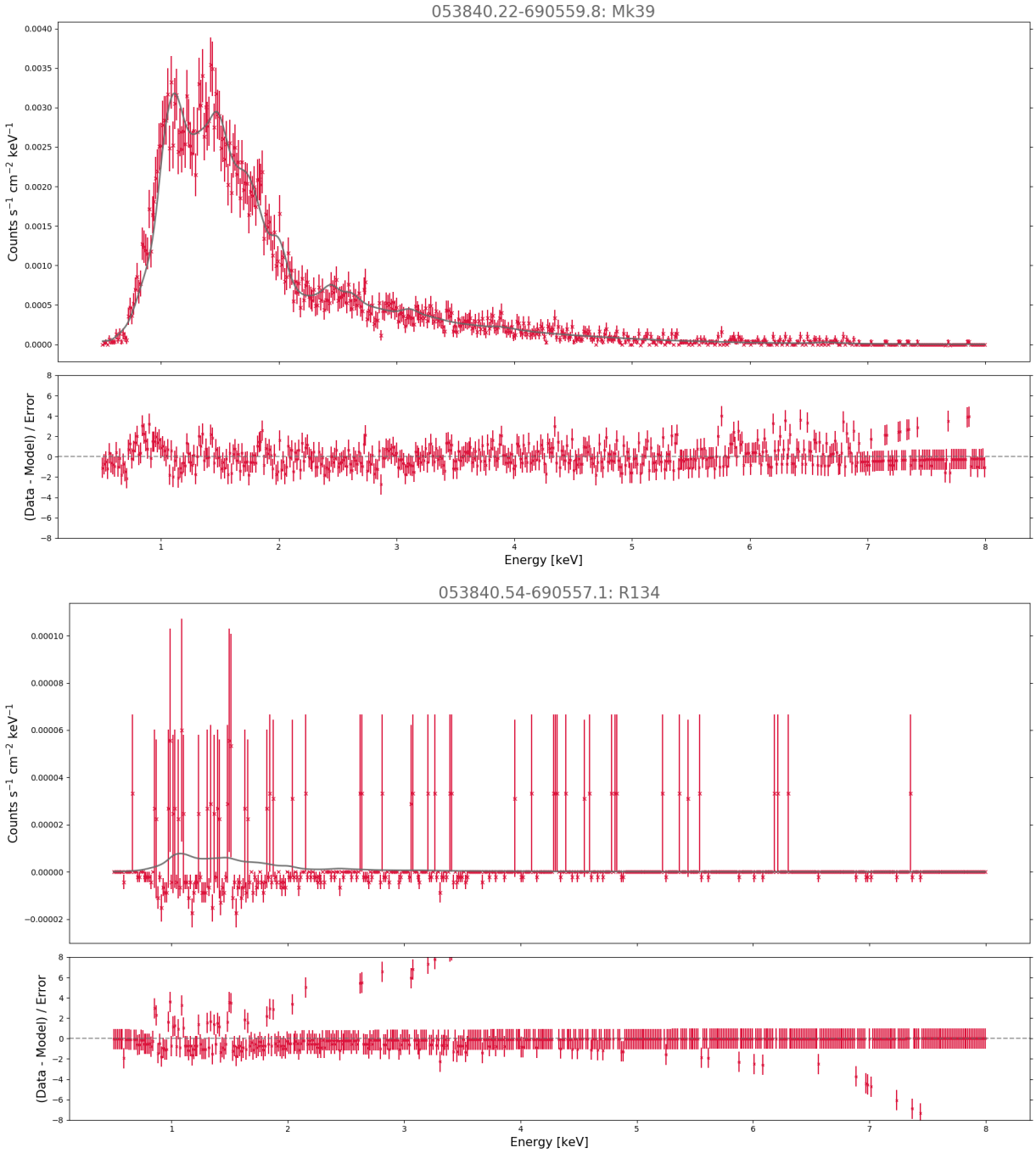

Figure B.1d: 1T plasma XSPEC fits to all WR sources in the sample. Red lines show the observed data and grey lines show the best 1T model fit. Fitting parameters are shown in Table 3.6.

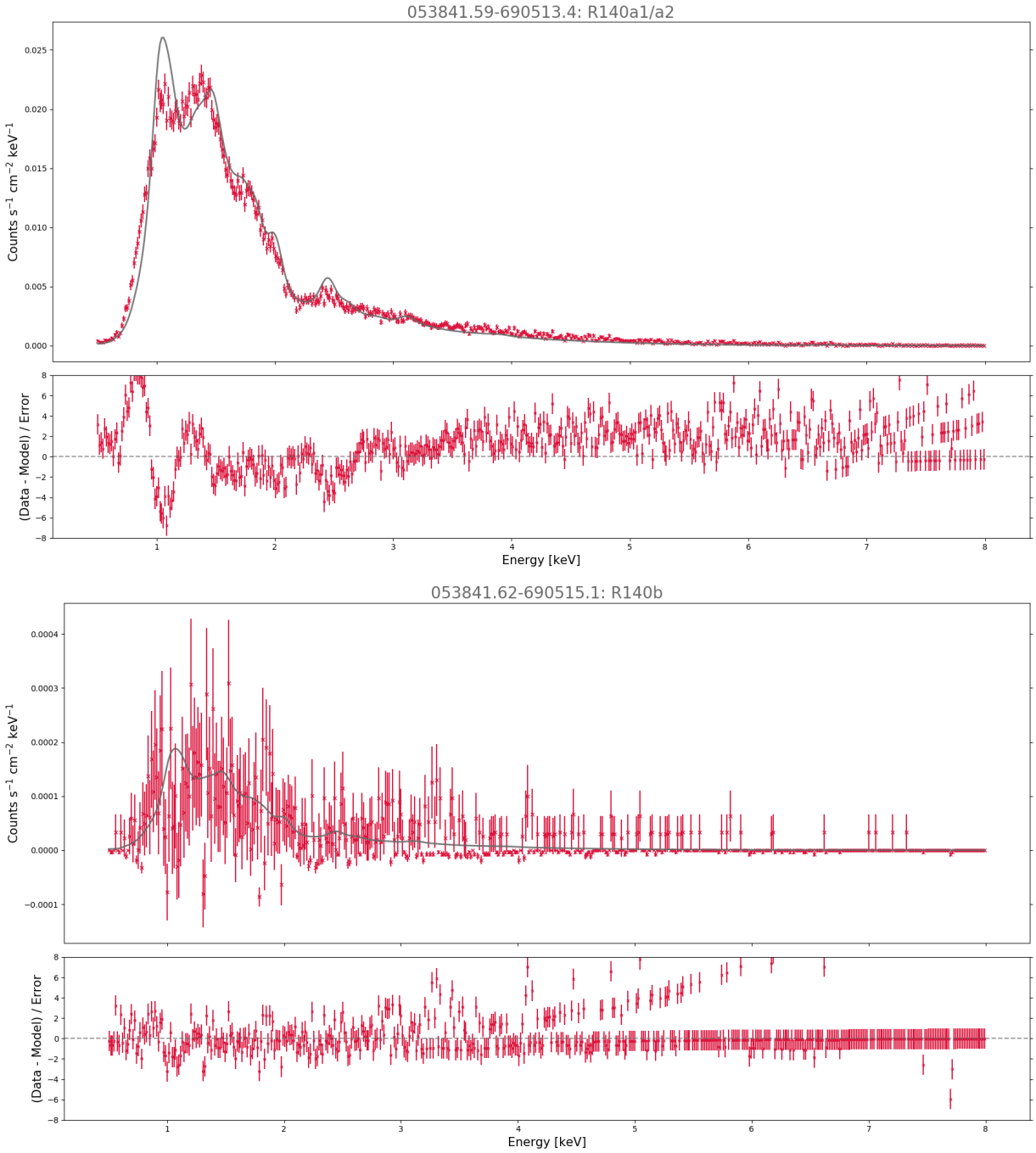

Figure B.1e: 1T plasma XSPEC fits to all WR sources in the sample. Red lines show the observed data and grey lines show the best 1T model fit. Fitting parameters are shown in Table 3.6.

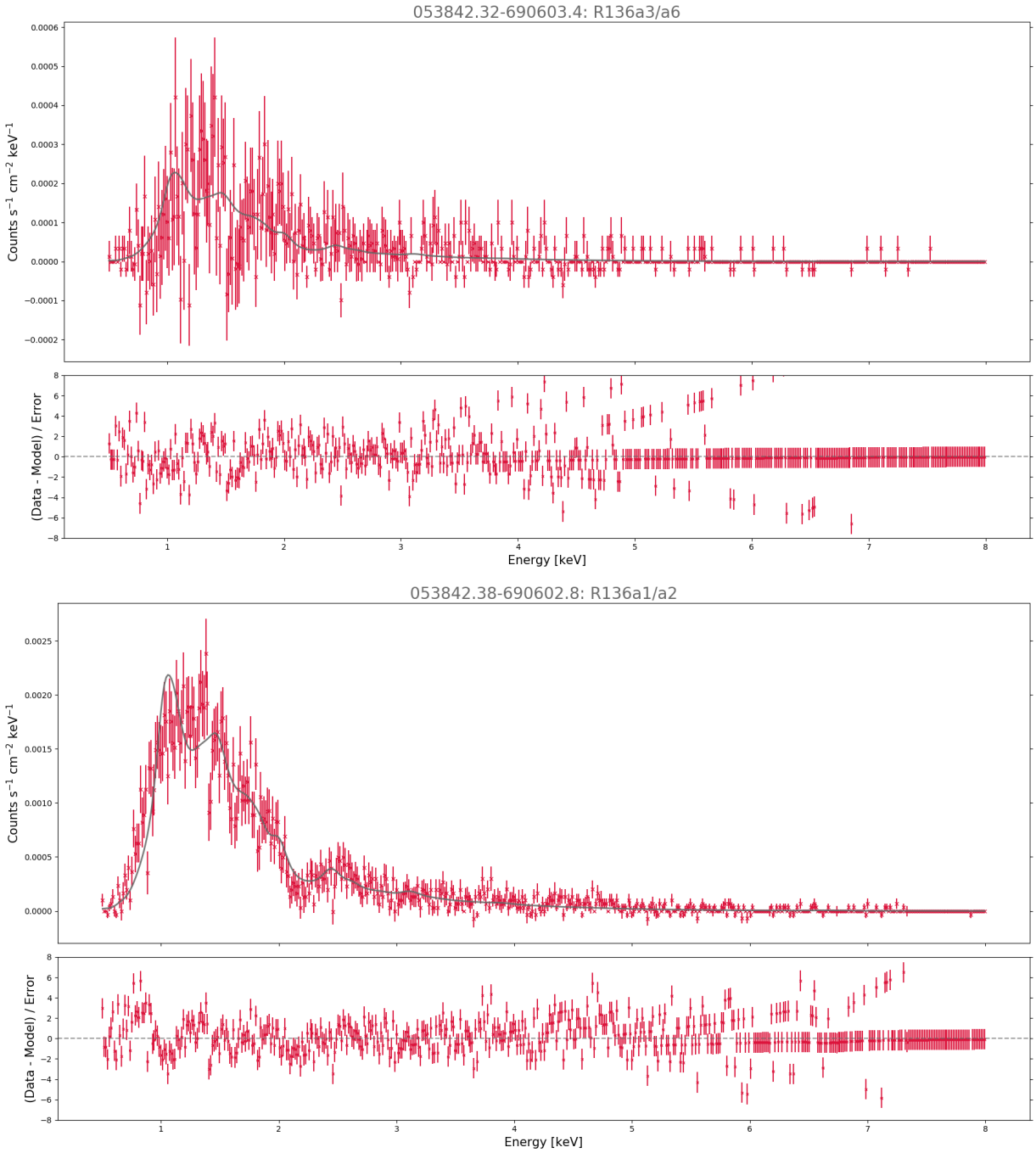

Figure B.1f: 1T plasma XSPEC fits to all WR sources in the sample. Red lines show the observed data and grey lines show the best 1T model fit. Fitting parameters are shown in Table 3.6.

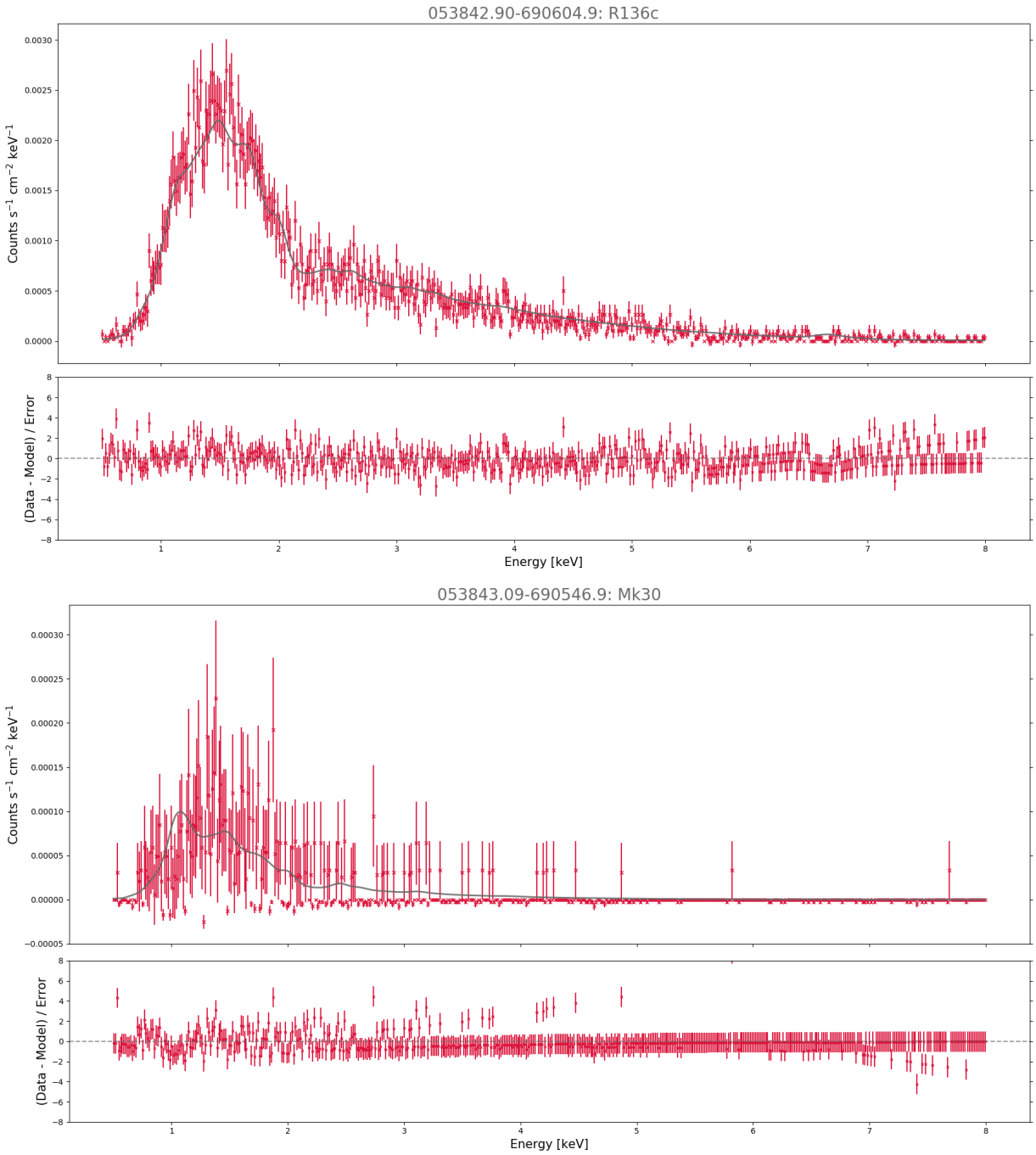

Figure B.1g: 1T plasma XSPEC fits to all WR sources in the sample. Red lines show the observed data and grey lines show the best 1T model fit. Fitting parameters are shown in Table 3.6.

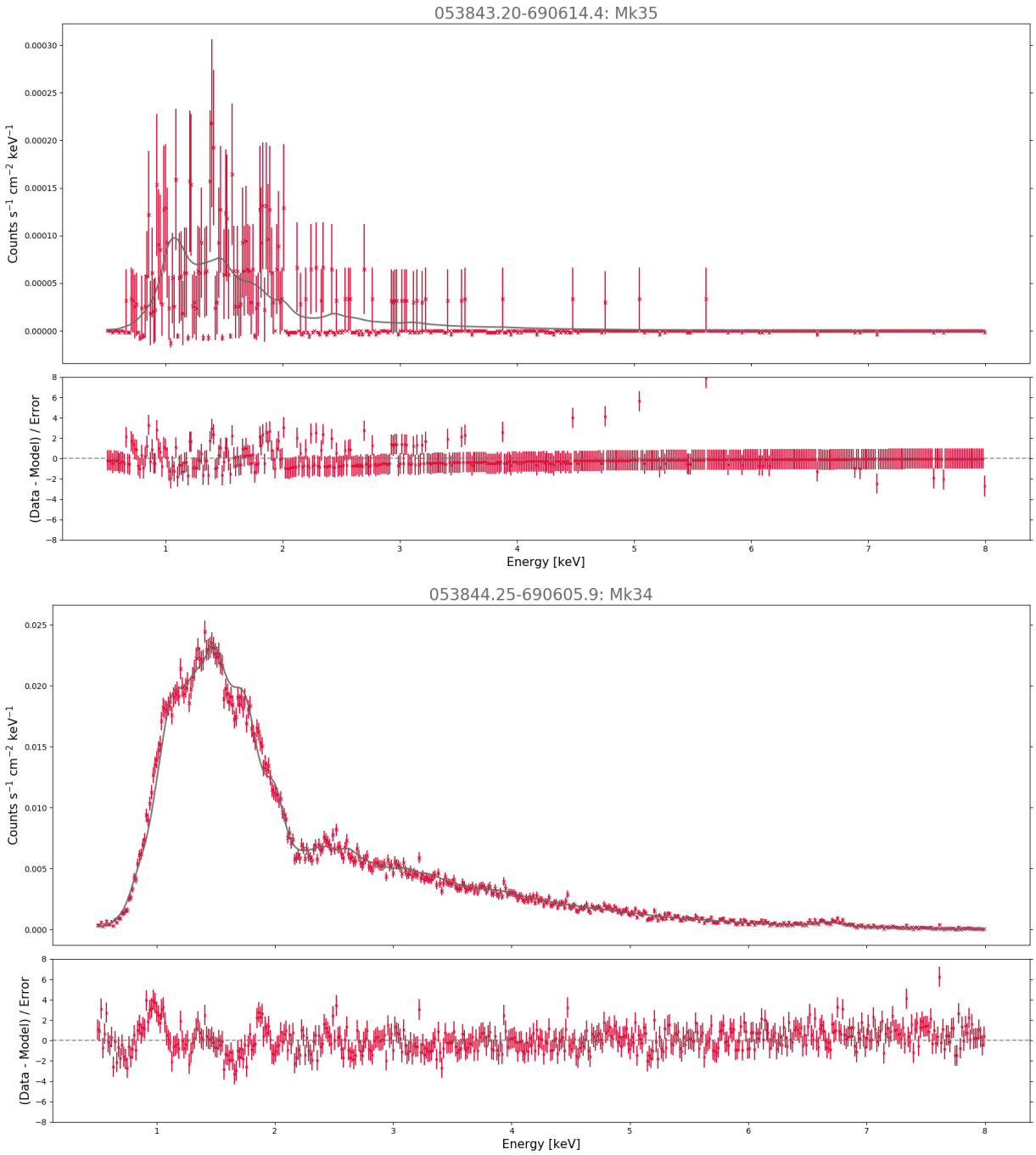

Figure B.1h: 1T plasma XSPEC fits to all WR sources in the sample. Red lines show the observed data and grey lines show the best 1T model fit. Fitting parameters are shown in Table 3.6.

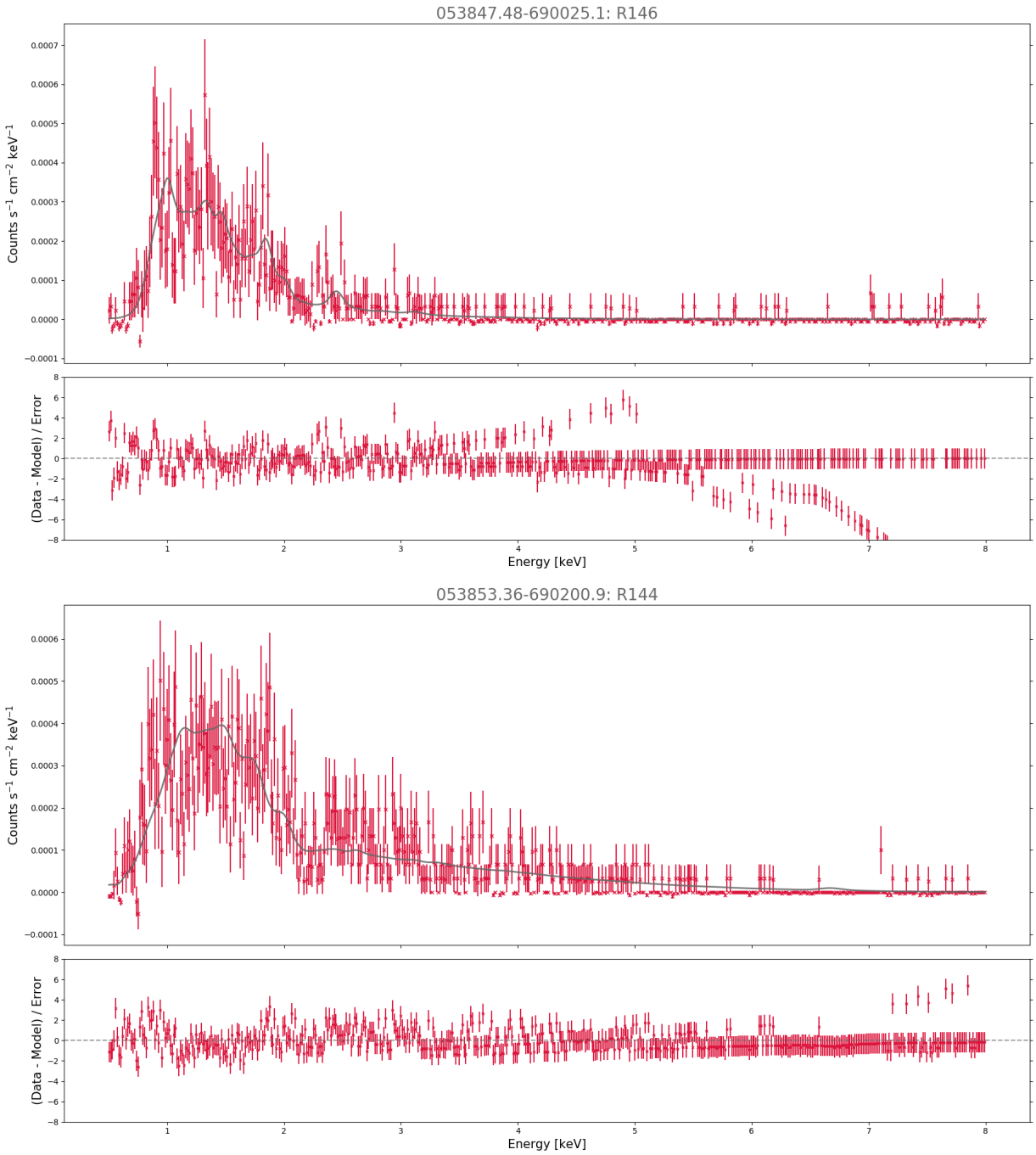

Figure B.1i: 1T plasma XSPEC fits to all WR sources in the sample. Red lines show the observed data and grey lines show the best 1T model fit. Fitting parameters are shown in Table 3.6.

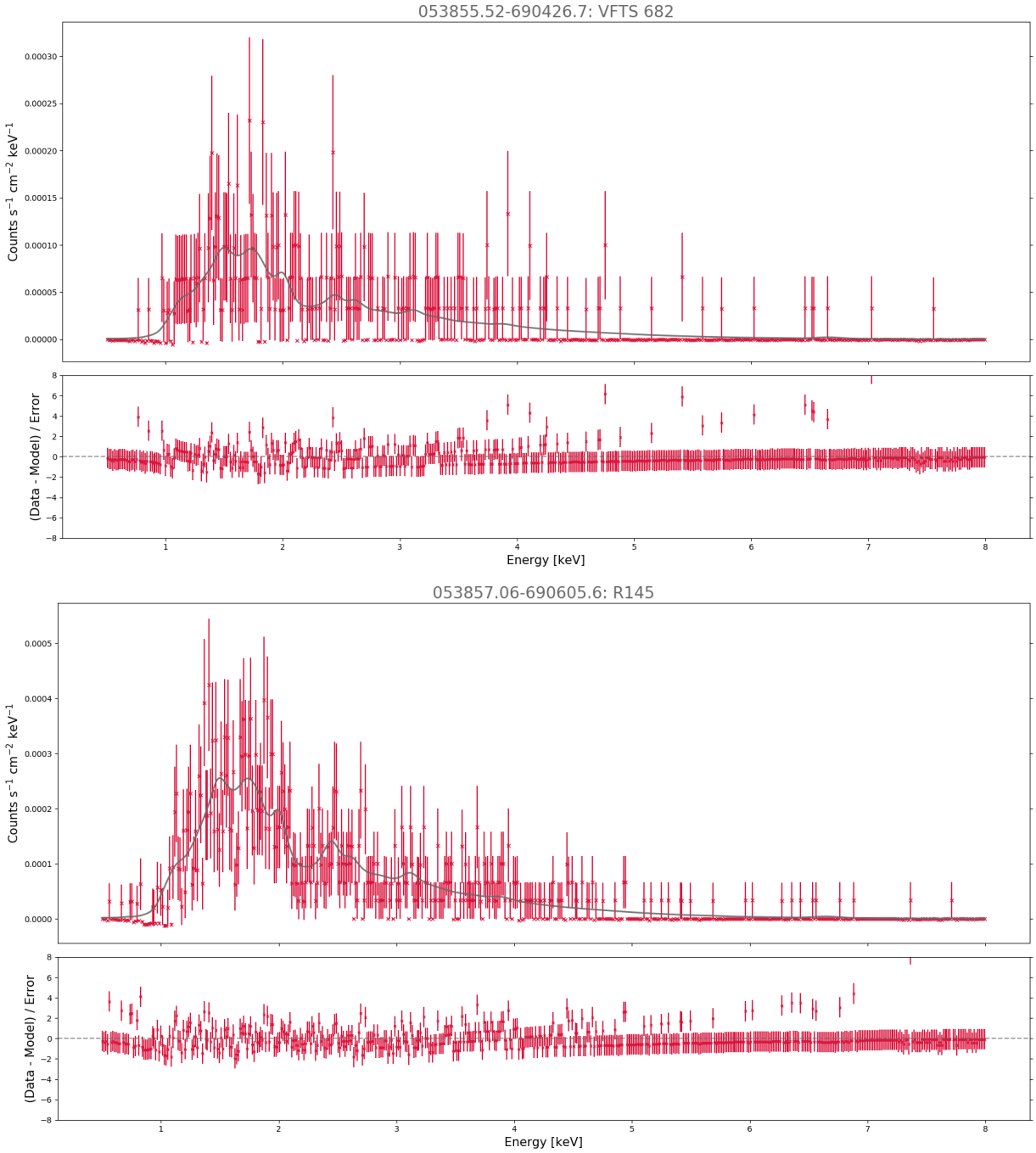

Figure B.1j: 1T plasma XSPEC fits to all WR sources in the sample. Red lines show the observed data and grey lines show the best 1T model fit. Fitting parameters are shown in Table 3.6.

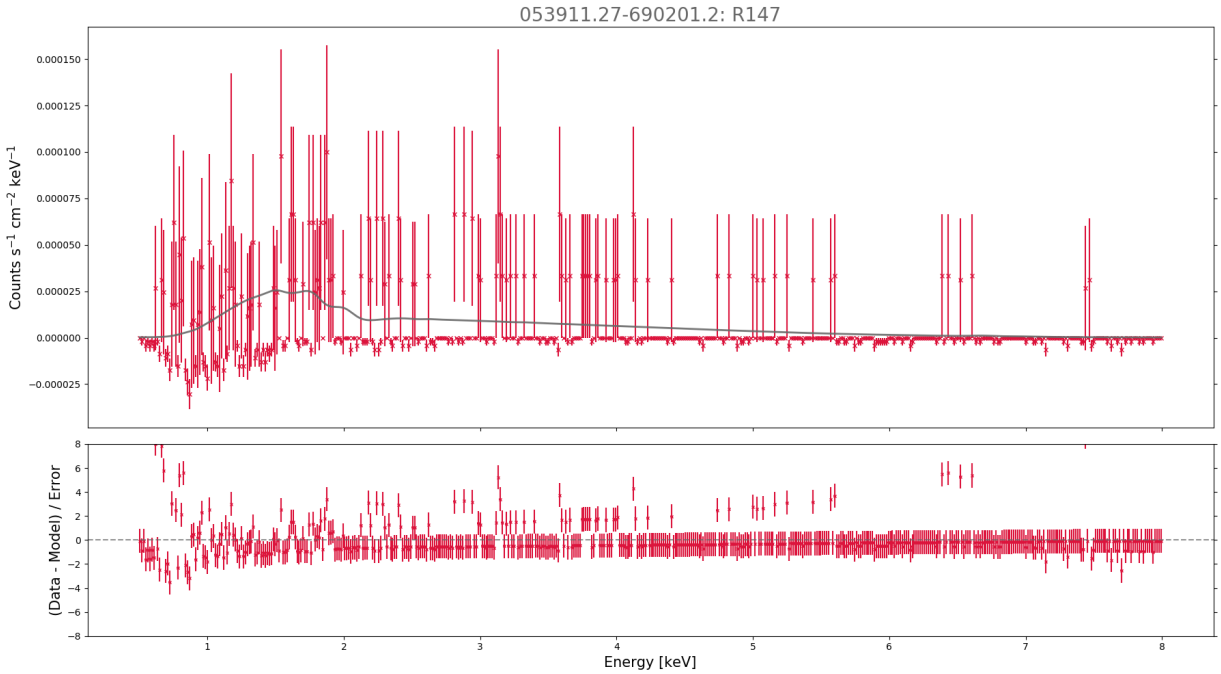

Figure B.1k: 1T plasma XSPEC fits to all WR sources in the sample. Red lines show the observed data and grey lines show the best 1T model fit. Fitting parameters are shown in Table 3.6.

Appendix C

Early Type Sources in T-ReX

Table C.1: All early type sources detected in T-ReX, sorted by X-ray net counts. WR stars included in this work have been highlighted in pink. Table was compiled by Crowther (private communication). Alias names refer to the following references: (R#) Feast et al. (1960); (M#) Melnick (1985); (R136#) Weigelt & Baier (1985); (P#) Parker (1993); (H#) Hunter et al. (1995); (S#) Selman et al. (1999).

CXOU J	Net Counts	Spectral Type	VFTS	Doran	Other Alias
05:38:44.25-69:06:05.9	74355	WN5+WN5	-	770	Mk34, S17, H8
05:38:41.59-69:05:13.3	54061	WC4+WN6+O	507	543/544	R140a1/a2
05:38:33.43-69:11:59.0	22011	O9III	399	372	
05:38:40.22-69:05:59.8	7979	O2.5If/WN6	482	480	Mk39
05:38:42.90-69:06:04.9	6961	WN5	1025	706	R136c
05:38:42.38-69:06:02.8	4368	WN5+WN5+O	-	630/633	R136a1/a2/a4/a5/a7/a8
05:38:44.12-69:05:56.6	2187	O3III	-	765	Mk33Sa, S44, H18
05:38:44.33-69:05:54.7	1869	O3If	-	775	Mk33Na, S33, H16
05:38:42.34-69:04:58.1	1683	O6.5I+O6I	527	620	R139
05:38:53.36-69:02:00.9	1262	WN5-6+WN6-7	-	916	R144
05:37:49.06-60:05:08.1	1177	WN/C+B1I	-	185	R130
05:38:42.11-69:05:55.2	947	O2If	-	580	Mk42
05:38:57.06-69:06:05.6	784	WN5+O3If/WN	695	938	R145
05:38:47.48-69:00:25.1	696	WN5	617	862	R146
05:38:42.65-69:06:02.9	516	O2If	-	682	H36
05:38:42.23-69:06:03.4	492	WN5+O2If	-	613/642	R136a3/a6, H6/H20
05:38:41.49-69:05:56.9	492	O3V	-	539	S53, H289
05:38:41.62-69:05:15.1	395	WN6+O	509	545	R140b
05:38:42.08-69:06:02.2	338	O3V+O3V	-	576	H42
05:38:55.52-69:04:26.7	302	WN5	682	928	

CXOU J	Net Counts	Spectral Type	VFTS	Doran	Other Alias
05:38:42.49-69:06:04.3	245	O2V	-	652	H31
05:38:38.02-69:05:43.3	216	O3-4V+O4-7V	445	424	
05:38:43.09-69:05:46.9	205	O2If/WN5	542	727	Mk30
05:38:43.20-69:06:14.4	201	O2If/WN5	545	736	Mk35
05:38:41.87-69:06:14.4	193	O2-4.5	1017	561	S88, H44
05:37:59.53-69:09:01.5	191	O4V+O5V	217	235	
05:38:42.01-69:06:07.6	175	O3III	1019	568	
05:38:13.97-69:07:47.7	169	O3III-I	267	276	
05:38:42.09-69:05:45.5	160	O6II-I+O5.5	522	578	S134, H82
05:38:52.72-69:06:43.3	151	O7II	664	909	Mk4
05:38:33.82-69:09:57.1	147	O3.5V	404	377	
05:38:33.62-69:04:50.4	139	WN7	402	375	R135
05:38:40.70-69:05:56.9	126	B?	-	497	S162, H106
05:38:43.67-69:05:47.8	116	O3V	1031	751	
05:38:41.55-69:05:19.4	106	ON2V	506	542	Mk25
05:39:11.27-69:02:01.2	102	WN5	758	1001	R147
05:38:42.37-69:06:15.1	95	O4If	1022	637	Mk37, S28, H14
05:38:44.93-69:05:54.1	94	O3V	-	800	S83, H43
05:38:41.52-69:06:01.0	94	O2-4.5+	1014	540	
05:38:41.21-69:02:58.3	93	O6.5V+O6.5V	500	525	
05:38:44.23-69:05:47.1	85	O8III	1034	769	Mk32, S21, H13
05:38:28.43-69:11:19.4	74	O4.5V+O5.5V	352	333	
05:38:41.74-69:06:25.0	72	O2V-III	512	555	S68

CXOU J	Net Counts	Spectral Type	VFTS	Doran	Other Alias
05:38:43.04-69:06:11.2	71	O2-4.5V	1026	718	Mk35N, S76, H41
05:38:42.27-69:06:04.9	70	O9.5V	-	612	H121
05:37:08.89-69:07:20.9	68	O2III-If	16	18	
05:38:36.40-69:06:57.5	67	WN8	427	402	Mk53
05:38:46.17-69:06:17.2	66	O3III	599	840	S40
05:38:40.17-69:05:51.2	66	O3-6V	-	475	S105, H63
05:38:39.15-69:06:21.2	65	WN6	-	443	Mk49
05:38:39.36-69:06:06.5	64	O2V+	468	451	Mk36
05:38:23.69-69:05:03.4	59	O8II-III	333	318	R133
05:38:45.69-69:06:22.5	54	B0.2Ia	591	825	Mk12
05:38:38.82-69:06:49.6	50	O3.5If/WN7	457	435	Mk51
05:38:45.11-69:05:08.4	49	O3-6V	-	810	S116
05:38:44.55-69:04:51.1	47	O3III	566	783	Mk23
05:38:43.29-69:06:16.4	45	O3.5-4.5	1028	739	Mk35S
05:38:40.79-69:05:25.1	44	O5-6V	-	502	S80
05:38:42.17-69:06:01.6	42	O6V	-	589	H75
05:38:42.05-69:06:14.3	39	O4If	1021	575	Mk37Wa, H11
05:38:40.80-69:06:03.4	35	B[e]	1003	499	
05:38:40.54-69:05:57.1	34	WN6	1001	493	R134
05:37:52.08-69:04:39.5	32	B1V	186	205	
05:38:46.26-69:05:59.3	32	O5-6V	601	842	Mk14N
05:39:10.87-69:06:13.7	32	O3V	755	996	
05:38:41.16-69:05:49.3	32	???	-	521	H517

CXOU J	Net Counts	Spectral Type	VFTS	Doran	Other Alias
05:38:42.23-69:06:00.5	32	???	-	604	H127
05:38:39.59-69:05:59.3	31	O-type	-	458	S255, H157
05:38:42.35-69:06:00.1	31	???	-	636	H170
05:38:42.21-69:08:32.5	29	O8.5I	526	594	P925
05:38:38.76-69:06:13.0	29	O5V	455	432	S108
05:38:13.20-69:05:36.2	29	OB?	-	273	
05:38:38.51-69:06:21.8	27	O9.7III+O7	450	428	Mk50
05:38:43.44-69:05:42.0	27	???	1030	-	
05:38:44.41-69:05:36.2	27	O4III	562	778	Mk26, S32
05:39:39.79-69:04:30.5	26	O5-6V	830	1076	P2270
05:38:45.24-69:05:46.3	25	O7V	585	813	S31
05:38:44.57-69:05:12.4	24	O6-8V	564	784	S253
05:39:39.84-69:06:09.4	23	O-type	-	472	S151
05:38:46.49-69:04:28.0	22	O4III	603	847	Mk10
05:38:40.92-69:05:54.9	22	O-type	-	508	S155, H95
05:38:46.82-69:06:03.0	21	O4III	608	852	Mk14
05:38:39.72-69:06:08.7	20	O-type	-	461	S144, H138
05:38:44.97-69:05:07.8	20	O9:	579	802	S171
05:38:48.07-69:04:42.4	19	O2V	621	866	
05:38:42.67-69:06:35.9	19	O3V+OB	532	684	S104
05:38:45.86-69:05;5 0.8	19	O-type	-	831	S114
05:38:35.56-69:06:05.5	17	O-type	416	390	S93
05:38:42.35-69:06:02.2	17	O6.5V	-	614	H30

CXOU J	Net Counts	Spectral Type	VFTS	Doran	Other Alias
05:38:39.04-69:06:59.0	16	O7.5V+O7.5V	460	439	S278
05:38:37.44-69:05:50.7	15	???	-	415	
05:38:45.07-69:05:09.8	15	???	-	807	S676
05:38:32.51-69:04:31.9	14	O9IV	386	361	Mk58
05:38:51.03-69:06:20.3	14	B2Ip+O9III	652	897	Mk5
05:38:36.31-69:06:08.1	13	O-type	-	398	S82
05:38:32.33-69:05:23.6	12	O4-5V	385	358	S84
05:38:33.59-69:05:22.0	11	O9.7	400	-	S227
05:38:58.73-69:05:23.7	11	O6-7V	706	946	P1838
05:38:42.87-69:04:33.3	11	B1.5V?	-	708	P1004
05:38:37.68-69:05:42.3	10	O-type	-	417	S123
05:38:35.94-69:06:09.2	10	B0.5Ia	420	395	Mk54
05:38:39.72-69:06:23.7	10	O-type	-	462	S75
05:38:34.58-69:06:05.7	7	O7-8V	410	384	S288
05:38:34.76-69:05:00.7	7	B1-3V-III	411	-	
05:38:42.64-69:05:36.7	7	O6-7V	-	677	S71
05:39:07.45-69:04:20.3	5	???	-	990	P2021
05:38:35.68-69:06:17.6	2	B2Ib	417	391	S204

Appendix D

Mk39: VFTS Optical Spectra

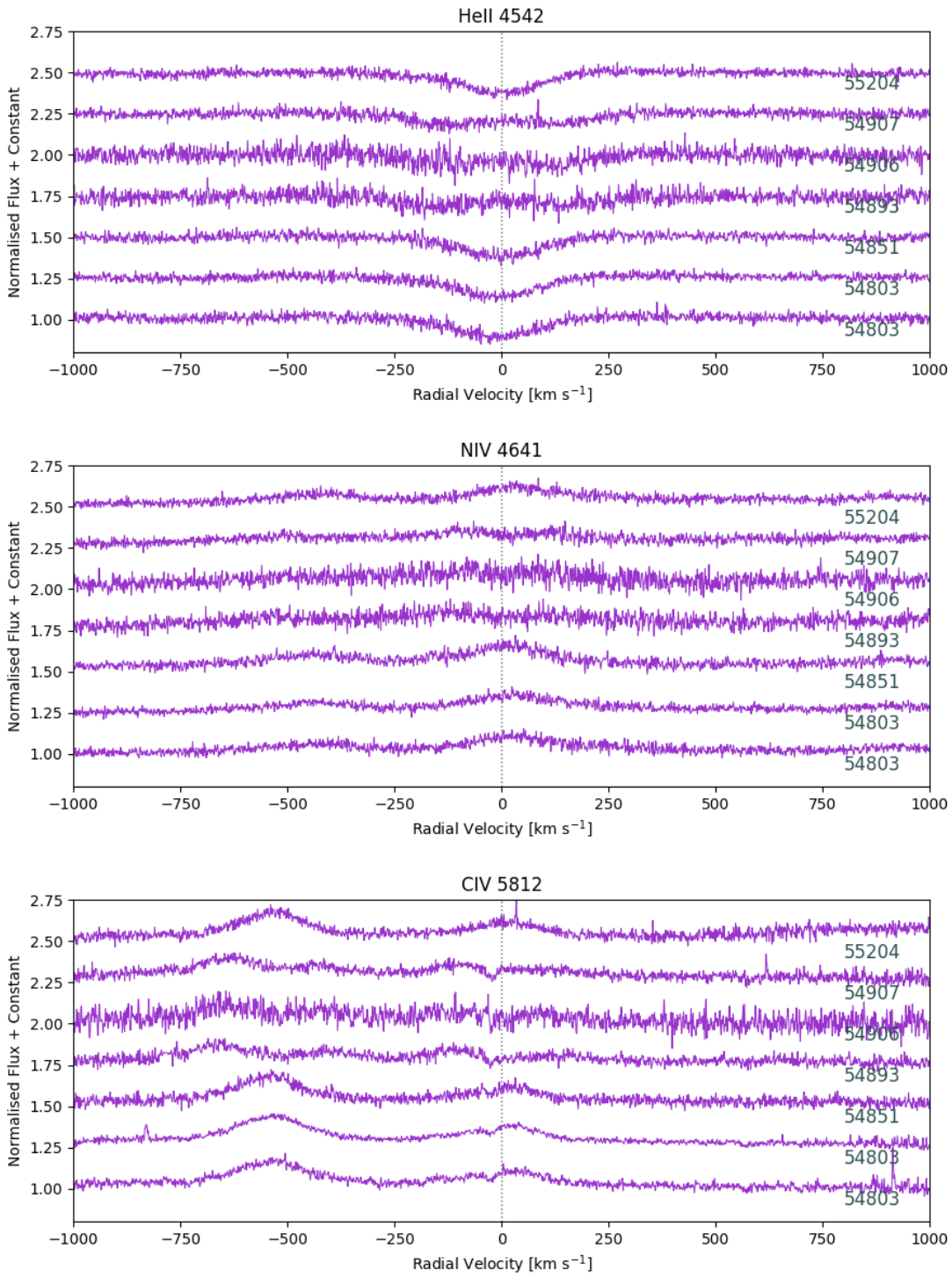

Figure D.1: Radial velocity variations in optical emission/absorption lines using VFTS data of Mk39. Spectra are plotted in chronological order with the observation MJD noted within the figure. Spectra are offset for clarity. The radial-velocity scale is centred such that the reference velocity (taken here to be 250 km s^{-1}) is zero and the dashed line corresponds to the rest wavelength of each emission line.

Appendix E

Mk34: Orbital Properties – Solution U1

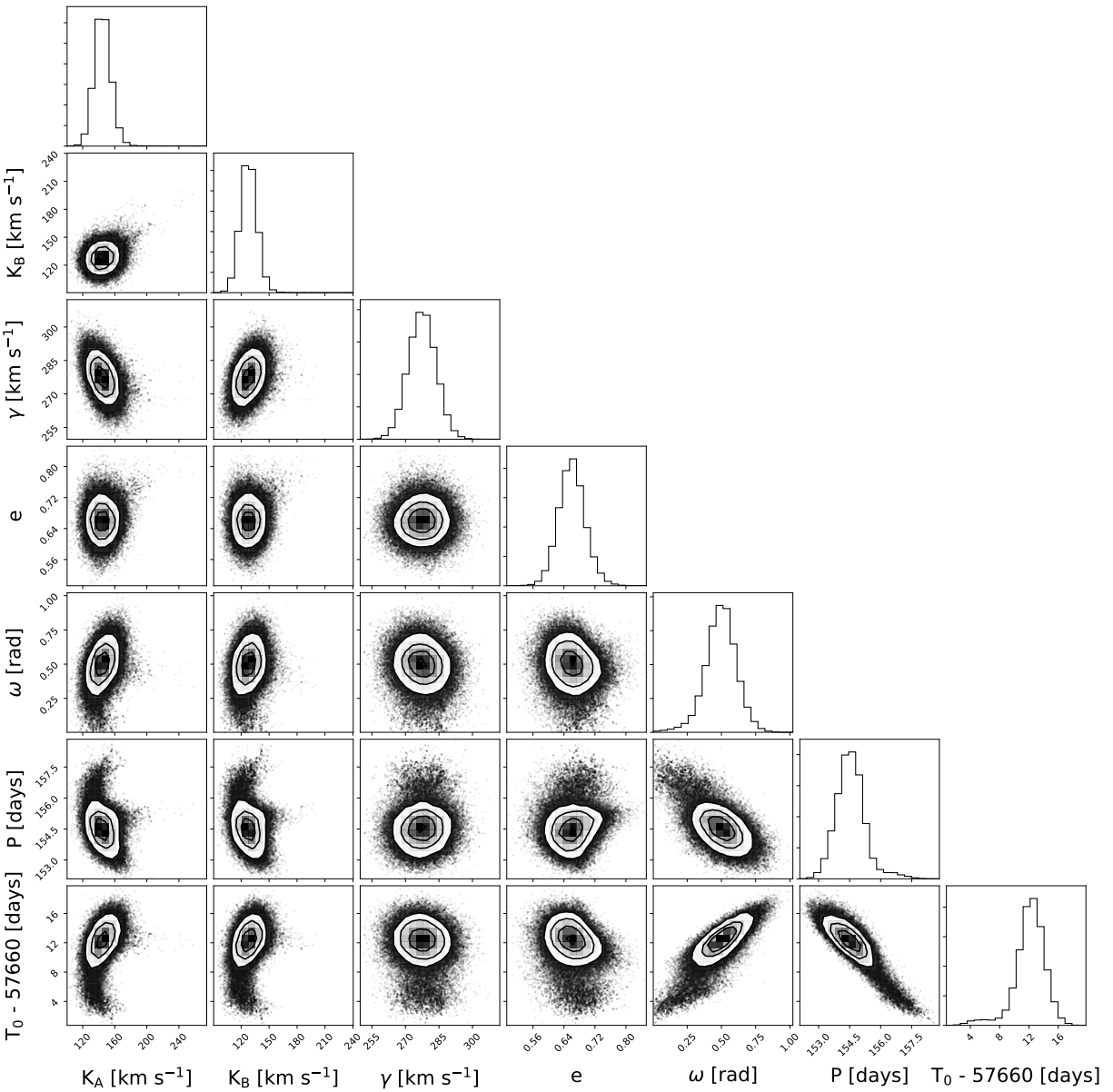

Figure E.1: Corner plot showing posterior probabilities for solution U1, where K_{A} and K_{B} are the semi-amplitudes of the velocities for star A and star B respectively, γ is the systemic velocity, e is the eccentricity, omega is the longitude of the periastron, P is the orbital period and T_0 is the time of periastron.

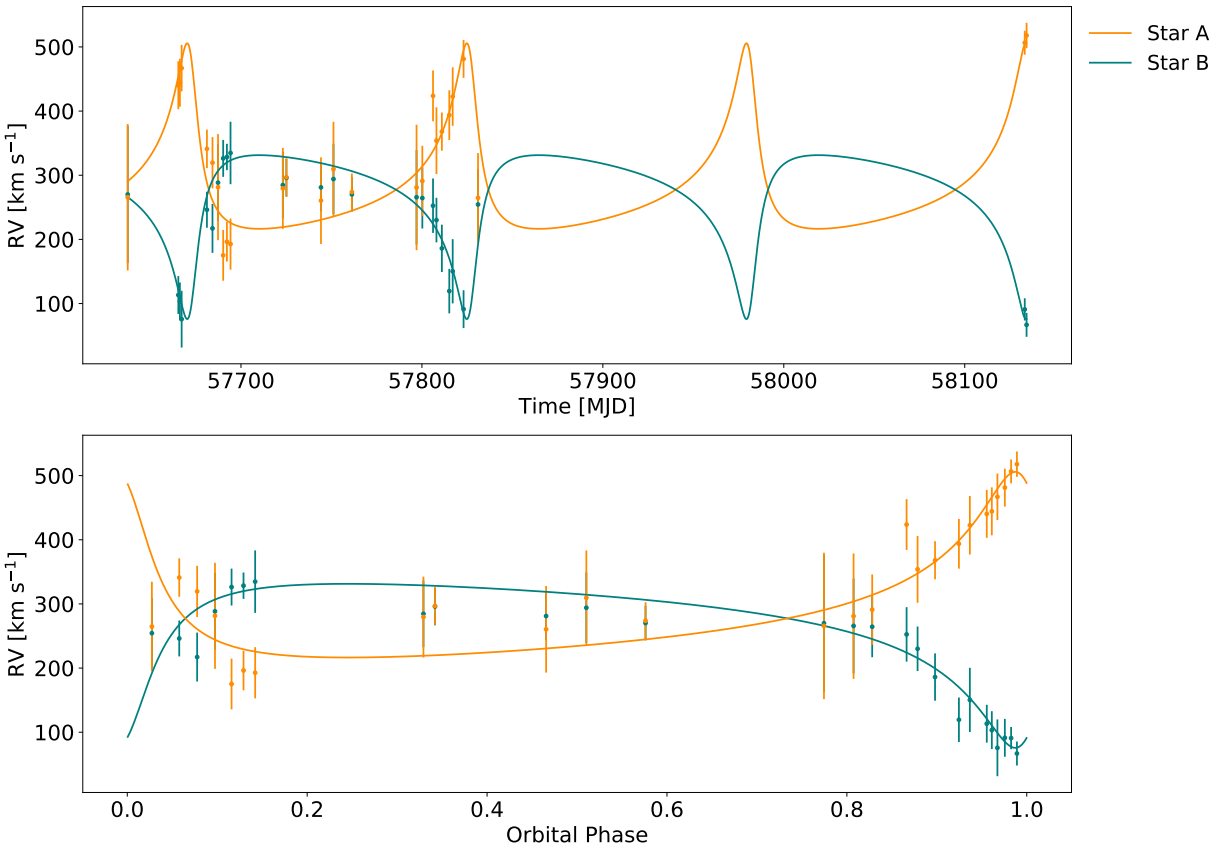

Figure E.2: Best fitting radial-velocity curve for the VLT/UVES data providing the parameters for solution U1.

Appendix F

Mk34: Orbital Properties – Solution U2

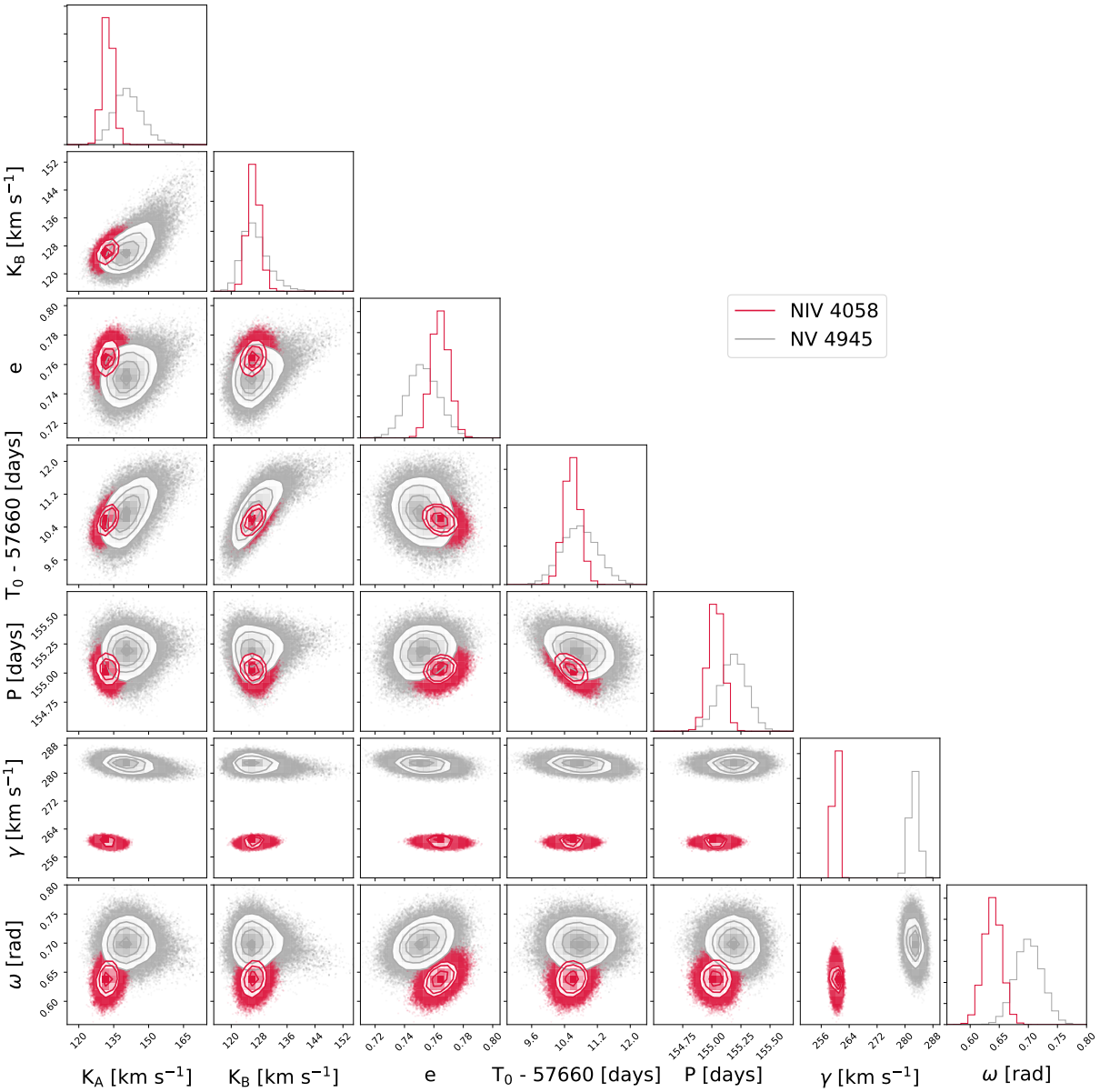

Figure F.1: Corner plot showing a comparison of the posterior probabilities for the automated template fitting of the N IV 4058 emission line (pink contours) and N V 4945 emission line (grey contours) using the VFTS 682 template from Bestenlehner et al. (2014), where K_A and K_B are the semi-amplitudes of the velocities for star A and star B respectively, e is the eccentricity, T_0 is the time of periastron, P is the orbital period, γ is the systemic velocity and ω is the longitude of the periastron. The results of this fitting were combined to produce solution U2